

Optical Control of Magnetic Feshbach Resonances by Closed-Channel Electromagnetically Induced Transparency

by

Arunkumar Jagannathan

Department of Physics
Duke University

Date: _____

Approved:

John E. Thomas, Supervisor

Robert P. Behringer

Gleb Finkelstein

Thomas Mehen

Mark C. Kruse

Dissertation submitted in partial fulfillment of the requirements for the degree of
Doctor of Philosophy in the Department of Physics
in the Graduate School of Duke University
2016

ABSTRACT

Optical Control of Magnetic Feshbach Resonances by
Closed-Channel Electromagnetically Induced Transparency

by

Arunkumar Jagannathan

Department of Physics
Duke University

Date: _____

Approved:

John E. Thomas, Supervisor

Robert P. Behringer

Gleb Finkelstein

Thomas Mehen

Mark C. Kruse

An abstract of a dissertation submitted in partial fulfillment of the requirements for
the degree of Doctor of Philosophy in the Department of Physics
in the Graduate School of Duke University
2016

Copyright © 2016 by Arunkumar Jagannathan
All rights reserved except the rights granted by the
Creative Commons Attribution-Noncommercial Licence

Abstract

Optical control of interactions in ultracold gases opens new fields of research by creating “designer” interactions with high spatial and temporal resolution. However, previous optical methods using single optical fields generally suffer from atom loss due to spontaneous scattering. This thesis reports new optical methods, employing two optical fields to control interactions in ultracold gases, while suppressing spontaneous scattering by quantum interference. In this dissertation, I will discuss the experimental demonstration of two optical field methods to control narrow and broad magnetic Feshbach resonances in an ultracold gas of ^6Li atoms. The narrow Feshbach resonance is shifted by 30 times its width and atom loss suppressed by destructive quantum interference. Near the broad Feshbach resonance, the spontaneous lifetime of the atoms is increased from 0.5 ms for single field methods to 400 ms using our two optical field method. Furthermore, I report on a new theoretical model, the continuum-dressed state model, that calculates the optically induced scattering phase shift for both the broad and narrow Feshbach resonances by treating them in a unified manner. The continuum-dressed state model fits the experimental data both in shape and magnitude using only one free parameter. Using the continuum-dressed state model, I illustrate the advantages of our two optical field method over single-field optical methods.

For the cutest munchkin in the town of Cary

Contents

Abstract	iv
List of Tables	xi
List of Figures	xii
Acknowledgements	xvi
1 Introduction	1
1.1 Magnetic Feshbach resonances in ultracold atoms	3
1.2 Why do we need optical control of interactions?	6
1.3 Optical control of interactions in ultracold atoms	8
1.4 Advantages of our two-field optical methods	12
1.5 Dissertation organization	15
2 Theory of Collisional Feshbach Resonances	17
2.1 Feshbach resonance in ${}^6\text{Li}$	21
2.2 Continuum-dressed state treatment of Feshbach resonance	23
2.3 Dressed continuum state $ E_k\rangle$	24
2.3.1 Magnetic Feshbach resonance induced phase shift $\tilde{\Delta}$	32
2.3.2 Zero energy scattering length a	33
2.3.3 Effective range r_e	36
2.4 Dressed bound state $ E\rangle$	36
2.5 Properties of dressed states $ E\rangle$ and $ E_k\rangle$	40

2.5.1	Orthogonality of $ E\rangle$ and $ E_k\rangle$	40
2.5.2	Z(B) - Singlet character in dressed bound state $ E\rangle$	44
2.5.3	C(B) - Total probability of $ g_1\rangle$ to be in the dressed continuum	47
2.5.4	Z(B) and C(B) near the broad and narrow Feshbach resonance in ${}^6\text{Li}$	54
2.5.5	Molecular binding energy E_m	54
2.6	Summary: Physical significance of the dressed states $ E\rangle$ and $ E_k\rangle$. .	58
2.6.1	Above Feshbach resonance - BCS side	58
2.6.2	Below Feshbach resonance - BEC side	59
3	Continuum-Dressed State Model	61
3.1	Two-field optical method: Level scheme	62
3.2	Bare-state basis and continuum-dressed state basis	63
3.3	Optical control: Continuum-dressed basis	65
3.3.1	Adiabatic approximation	67
3.4	Scattering state wave function	69
3.5	Evaluating the energy denominator $D(E, E_K)$	73
3.5.1	Dressed bound state shift I_E	76
3.5.2	Dressed continuum state shift I_{E_K}	78
3.6	Evaluation of the optically induced phase shift ϕ	88
3.7	Evaluation of the total phase shift δ	90
4	Continuum-Dressed Model Predictions	92
4.1	Two-body loss rate constant K_2	92
4.2	Procedure for calculating K_2	95
4.3	Two-body loss rate K_2 near broad Feshbach resonance	97
4.3.1	Two-body loss rate K_2 for different Rabi frequencies Ω_2	100
4.3.2	Two-body loss rate K_2 vs Rabi frequency Ω_1	101

4.3.3	Two-body loss rate K_2 vs ratio of Rabi frequencies Ω_1/Ω_2 . . .	101
4.3.4	Two-body loss rate K_2 vs detuning Δ_2	102
4.4	Two-body loss rate K_2 near narrow Feshbach resonance	104
4.4.1	Shift of the narrow Feshbach resonance vs Rabi frequency Ω_1 .	105
4.4.2	EIT loss suppression near narrow Feshbach resonance	106
4.5	Zero energy scattering length a	108
4.5.1	Zero energy scattering length a near the broad Feshbach resonance	111
4.5.2	Zero energy scattering length a near the narrow Feshbach resonance	113
4.6	Effective range r_e	114
4.7	Two-field optical method near the narrow Feshbach resonance	116
4.8	Two-field optical method near the broad Feshbach resonance	119
4.9	Evaluation of optically induced atom loss from K_2	122
5	Experimental Methods	125
5.1	Laser cooling and trapping of atoms	125
5.1.1	^6Li oven - Generating the atoms	126
5.1.2	Zeeman slower and the “slower” beam - Initial cooling	126
5.1.3	Magneto-optical trap - Precooling	128
5.1.4	Far off-resonance trap (FORT) - Evaporative cooling	129
5.1.5	Imaging the atom cloud	132
5.2	Experimental setup for two-field optical method	134
5.2.1	Basic experimental setup	135
5.2.2	Frequency stabilization of lasers using PDH lock	138
5.2.3	Locking the FP cavity using iodine saturation absorption spectroscopy	141
5.2.4	Frequency offset lock between the reference and the control laser	142

5.2.5	Spectral filtering of optical fields	145
5.2.6	Illuminating the atoms with optical fields	146
5.3	Measurement of density and temperature of the atom cloud	147
5.3.1	Measurement of trap frequencies of atoms in a CO ₂ dipole trap	147
5.3.2	Measurement of the trap oscillation frequencies for the com- bined CO ₂ dipole and red trap	149
5.3.3	Measurement of temperature of the atom cloud	152
5.3.4	Measurement of density of the atom cloud	154
5.4	Determination of the Rabi frequencies	155
5.5	Measurement of the transition frequencies	156
5.6	Measurement of three-body recombination loss near the narrow Fesh- bach resonance	159
6	Results and Conclusion	162
6.1	Shifting the narrow Feshbach resonance using a single-optical field . .	164
6.2	Comparison of single-field loss data with the continuum-dressed state model near the narrow Feshbach resonance	169
6.3	Two-field loss suppression near the narrow Feshbach resonance	170
6.4	Comparison of two-field loss suppression data with the continuum- dressed state model near the narrow Feshbach resonance	173
6.5	Two-field loss suppression near broad Feshbach resonance	175
6.6	Comparison of two-field loss suppression data with the continuum- dressed state model near the broad Feshbach resonance	177
6.7	Increasing the spontaneous lifetime of atoms near the broad Feshbach resonance	178
6.8	Summary and future experiments	179
A	Evaluation of phase shift Δ due to magnetic Feshbach resonance	181
B	Evaluation of contour integral for solving $\tilde{I}_{E_k}^b$ near the broad Fesh- bach resonance	186

Bibliography	189
Biography	195

List of Tables

2.1	Magnetic Feshbach resonances in ${}^6\text{Li}$ for s-wave collisions	35
4.1	Energy states for closed channel EIT	98
4.2	Zero energy detunings for closed channel EIT	99
6.1	Single-field shift of narrow Feshbach resonance	169

List of Figures

1.1	Magnetic Feshbach resonance in ultracold gases	4
1.2	Zero energy scattering length near a magnetic Feshbach resonance. . .	4
1.3	Basic level scheme for optical Feshbach resonance (OFR).	8
1.4	Basic level scheme for Raman-coupled optical Feshbach resonance (OFR).	10
1.5	Level scheme for single-field optical method to control interactions. .	11
1.6	Closed-channel EIT method to control interactions in ultracold gases.	13
2.1	Magnetic Feshbach resonance in ${}^6\text{Li}$	18
2.2	Zero energy scattering length a as a function of magnetic field for the broad Feshbach resonance and the narrow Feshbach resonance in ${}^6\text{Li}$	19
2.3	Transformation from bare states to dressed states.	23
2.4	Contour Integral for I_1	31
2.5	Contour Integral for $\Sigma_E(k)$	51
2.6	$Z(B)$ and $C(B)$ for the broad Feshbach resonance and the narrow Feshbach resonance in ${}^6\text{Li}$	55
2.7	Binding energy E_m in units of E_{bg} near the broad Feshbach resonance in ${}^6\text{Li}$	57
3.1	Basic level scheme for the two-field optical technique.	63
3.2	Level schemes in “bare-state” and “continuum-dressed-state” bases. .	64
3.3	Contour Integral for I_1	72
3.4	Plot of $f_c(\tilde{\Delta}_0, \epsilon, x')$ as a function of x for the case $\epsilon \ll 1$ when $\Delta_0 = 2.1$.	81

3.5	Comparison of exact shift evaluated numerically and analytic shift for broad and narrow Feshbach resonance	87
4.1	Two-body loss rate K_2 near the broad Feshbach resonance at $B = 825$ G as a function of single-photon detuning Δ_e	99
4.2	Two-body loss rate K_2 vs single photon detuning Δ_e for fixed Ω_1 . . .	100
4.3	Two-body loss rate K_2 vs single photon detuning Δ_e for fixed Ω_2 . . .	101
4.4	Two-body loss rate K_2 vs single photon detuning Δ_e for Ω_1/Ω_2	102
4.5	Two-body loss rate K_2 vs single photon detuning Δ_e at $B = 825$ G for $ \Delta_2 < 2\gamma_e$	102
4.6	Two-body loss rate K_2 vs single photon detuning Δ_e at $B = 825$ G for $ \Delta_2 > 2\gamma_e$	103
4.7	Shifting the narrow Feshbach resonance using a single optical field. . .	104
4.8	Shifting the narrow Feshbach resonance at 543.2 G for $\Omega_1 = 1\gamma_e$, $\Omega_2 = 2\gamma_e$, and $\Omega_2 = 3\gamma_e$	106
4.9	EIT loss suppression at the broad peak near the narrow Feshbach resonance.	107
4.10	EIT loss suppression at the narrow peak near the narrow Feshbach resonance.	108
4.11	EIT loss suppression plot in Fig. 4.10 expanded around the suppression region.	109
4.12	Zero energy scattering length a and K_2 versus single photon detuning Δ_e near the Broad Feshbach resonance at 825 G.	112
4.13	Zero energy scattering length and corresponding K_2 versus B-field near the narrow Feshbach resonance.	113
4.14	Effective range versus control beam detuning Δ_e for the two-field method.	115
4.15	Zero energy scattering length and corresponding K_2 versus B-field near the narrow Feshbach resonance.	116
4.16	Zero energy scattering length a and corresponding K_2 versus two-photon detuning δ_e near the narrow Feshbach resonance	117

4.17	Zero energy scattering length a and two-body loss rate coefficient K_2 as function of ω_1 (detuning Δ_e).	119
4.18	Two-body loss rate constant K_2 versus zero energy scattering length a for single-field and two-field optical methods.	120
5.1	Experimental setup for initial cooling of ${}^6\text{Li}$ atoms.	127
5.2	Experimental setup for evaporative cooling of ${}^6\text{Li}$ atoms in a CO_2 optical dipole trap and absorption imaging using a resonant beam. . .	130
5.3	Absorption image of an atom cloud evaporative cooled at 832 G. . . .	133
5.4	Basic level scheme for the two-field optical technique.	134
5.5	Experimental setup for two-field optical control.	136
5.6	Frequency discriminator error signal (screenshot) using PDH lock. . .	140
5.7	Frequency discriminator error signal (screenshot) from iodine saturation absorption spectroscopy.	142
5.8	Basic schematic for the frequency offset lock.	143
5.9	Frequency discriminator error signal (screenshot) from the frequency offset lock.	144
5.10	Parametric resonance to measure trap oscillation frequencies of atoms in an optical dipole trap.	148
5.11	Atom cloud images in dipole trap dipole and red (EIT beam) trap. . .	150
5.12	Single field atom loss spectra as a function of single photon detuning Δ_e	157
5.13	Loss suppression near the broad Feshbach resonance as a function of single photon detuning Δ_e	158
5.14	Three-body recombination loss near the narrow Feshbach resonance at 543.2 G.	160
6.1	Basic level scheme for closed-channel EIT technique.	163
6.2	Single-field loss spectra near the narrow Feshbach resonance with the three body loss peak and three body loss peak removed.	164
6.3	Level scheme for the single-field optical experiment near the narrow Feshbach resonance.	165

6.4	Shifting the narrow Feshbach resonance at 543.2 G using a single optical field.	168
6.5	Level scheme for EIT loss suppression near the narrow Feshbach resonance at the broad peak and the narrow peak.	170
6.6	Loss suppression using the two-field optical technique.	172
6.7	Level scheme for loss suppression near the broad Feshbach resonance at 840 G	175
6.8	Two-field optical loss suppression near the broad Feshbach resonance.	176
6.9	Increasing the spontaneous lifetime of atoms near the broad Feshbach resonance using closed-channel EIT	178
B.1	Contour Integral for $I(q, x)$	186

Acknowledgements

I would like to thank my advisor Dr. John Thomas for his support and supervision. John has always been a constant source of encouragement, which was instrumental in driving me forward even when things were not going as planned. His open minded approach to new ideas and down to earth mentality have made my PhD experience a very enjoyable one. In the current age, where graduate student life is “expected” to be tiresome with inhumane working hours and ill-treatment from supervisors, which I have personally heard from many of my friends, John treats every single member in the group with respect and ensures that everyone truly enjoys what they are pursuing. During my course of stay in our research group, I have learned far more important things in life from John than my PhD research.

I am indebted to Ethan and James for teaching me our atom trapping and cooling system when I entered our research group as an amateur. In the midst of completing the experiment for his PhD work, Ethan answered all my questions with utmost patience and provided clear supervision on some of the most basic optical techniques. I learned to independently operate the main cooling and trapping system under the supervision of James and he did an excellent job in teaching me all the nuances of our 20 year old system, including the much complicated operation of the ultra “unstable” dye laser system. When we moved from Duke to NC state, James single handedly implemented the entire control system in our lab and has always provided a helping hand in several difficult situations. I have always enjoyed having “science”

fights with James, expecting “science” to be the ultimate winner, without which I am fairly confident I would not have completed my PhD.

I have read several thesis acknowledgements, where people say, “This would not be possible without the support of my wife.” In my case, this statement is literally and absolutely true, as Nithya joined our research group an year after me. We both worked on the same experiments, which ultimately yielded results thereby providing a path for me to successfully graduate. She has been a great wife, good friend, fantastic co-worker, and her acumen in implementing optical and electronic systems is second to none. I am glad, I graduated without getting a divorce due to “physics” fights, which John feared to be a real possibility.

I would like to specially thank Ilya who has helped and advised in numerous situations from implementing complex RF experiments to checking the basic alignment of CO₂ beam. I have always been amazed by his attention to detail and his thorough “physical” insight. I would also like to thank Haibin who taught me several important aspects of my experiment.

This acknowledgement would not be complete without mentioning the people that made my entry into Duke a reality. My journey from Umass lowell to Duke would not have been possible without the constant encouragement of Dr. James Egan, the former chair of Umass lowell’s physics department and my favorite teacher of all time. I am indebted to Dr. Albert Altman, who taught me Mathematical Methods, and highly discouraged me from becoming a string theorist, thereby saving me from falling into a perilous abyss. My special thanks to Dr. Jayant Kumar, who made me realize that optics is so much fun. I would also like to thank Dr. Kunat Sebastian, my research advisors at UML, Dr. Andrew Gatesman and Dr. Robert Giles for their support and encouragement.

My friends and family has always been supportive of my endeavors. I would like to thank my brother, Dr. Madhan Mohan, the most intelligent person that I have

seen till date. His passion for physics is highly infectious and has greatly influenced me as a kid. Although growing up along side such an individual can be demanding sometimes, I whole heartedly believe that I would not have been a physicist without his influence and motivation. I would like to specially thank my friend, tennis partner and coach Ravi Dhulipala, with whom I have had the most stimulating conversations. Playing tennis with Ravi was essential in keeping myself sane and staying focussed on my PhD research. I also would like to thank my tennis idol, Roger Federer, from whom I learned the concept of serenity and the sense of “looseness” even under extreme pressure situations, both in tennis and real life. My very special thanks to Mr. Alagarsamy, a great person and a fantastic individual, who helped me pursue my dreams, including funding my first plane ticket to America, when I was almost bankrupt.

I will conclude my acknowledgement with one of my favorite quotes from John. Once John said, “I think we should hire Tom Cruise as our Post-Doc, because we do impossible experiments.” May be we should.

Introduction

Controlling interactions in ultracold gases is essential for emulating intriguing systems in nature, ranging from exotic nuclear matter such as neutron stars to high temperature superconductors. Ultracold gases with tunable interactions are studied by utilizing collisional (Feshbach) resonances [1]. A Feshbach resonance occurs when the energy of the two-atom scattering state is tuned into resonance with a molecular bound state. Typically, external magnetic fields are used to control interactions in an ultracold gas near Feshbach resonances. However, in order to control interactions with high spatial and temporal resolution, the use of optical techniques becomes inevitable. Optical control of interactions in an ultracold gas offers tantalizing possibilities for creating “designer” two-body interactions. Unfortunately, previously reported optical methods [2, 3, 4, 5, 6, 7, 8, 9, 10, 11, 12] suffer from spontaneous scattering which limits the tunability of interactions. This dissertation reports on the demonstration of new optical methods that uses two optical fields to control interactions near collisional (Feshbach) resonances while suppressing spontaneous scattering by destructive quantum interference.

In order to understand optical control of two-body scattering parameters in an

ultracold gas, we begin with the discussion of the scattering amplitude in a collision between two particles. At ultracold temperatures, low energy s-wave collisions are dominant. The s-wave scattering amplitude

$$f(k) = \frac{e^{2i\delta(k)} - 1}{2ik} = \frac{1}{k \cot \delta(k) - ik}, \quad (1.1)$$

where $\delta(k)$ is the relative momentum dependent scattering phase shift.

In early studies of low energy s-wave scattering in nuclear physics, Schwinger [13, 14] used variational methods to derive the relationship between the scattering phase shift $\delta(k)$ and the relative momentum k as $k \rightarrow 0$

$$k \cot \delta(k) \cong -\frac{1}{a} + \frac{k^2}{2} r_e, \quad (1.2)$$

where a is the zero energy s-wave scattering length and r_e is the effective range. The real part of a determines the zero-energy elastic cross section and the imaginary part of a determines the inelastic cross section. The two field optical method [15] induces narrow optical features in the scattering phase shift $\delta(k)$ thereby allowing “designer” control of elastic scattering length and inelastic loss. Furthermore, the relative kinetic energy $\hbar^2 k^2/m$ of the colliding particles leads to energy-dependent optical detuning of these narrow features, producing a rapid k^2 dependence in the scattering phase shift $\delta(k)$, allowing the tunability of effective range.

By controlling both the zero energy scattering length and the effective range, our two-optical field methods will open new fields of research, which include the systematic study of non-equilibrium phenomena in strongly correlated Bose and Fermi gases [16], a new paradigm for neutron matter, where the s-wave scattering length, the effective range, and the interparticle spacing are in the correct proportions [17], and the creation of new scale-invariant dimer pairs using scattering lengths that vary linearly in space [18]. Control of the effective range may stabilize trimer formation near p-wave resonances [19].

Implementation of optical control methods requires an understanding of the optically-induced level structure and energy shifts, which depend on the relative momentum of a colliding atom pair. I present a new theoretical model, the continuum-dressed state model, which provides a comprehensive treatment for calculating the scattering phase shift, taking into account the relative momentum dependence of the colliding atoms. The predicted relative-momentum averaged loss spectra agree in shape and magnitude with data for both broad and narrow resonances, substantiating the new theoretical approach. These results pave the way for predicting two-body scattering parameters for experiments employing optically controlled interactions.

1.1 Magnetic Feshbach resonances in ultracold atoms

A Feshbach resonance in a ultracold gas occurs when the energy of a pair of unbound colliding atoms is degenerate with a quasi-bound molecular state [1]. At a Feshbach resonance, the scattering length diverges, thereby leading to strong interactions. At resonance, the scattering length no longer plays any role in the description of the gas. The only length scales that remain are the average distance between the atoms and the thermal De Broglie wavelength. This technique of tuning the interactions of atoms near a Feshbach resonance using external magnetic fields is denoted as magnetic Feshbach resonance (MFR).

Fig. 1.1 (a,b) illustrates the concept of a magnetic Feshbach resonance. The unbound colliding atom pair resides in an energetically allowed scattering channel $|T, k\rangle$ called the open channel, where k indicates the relative momentum of the colliding atom pair and T indicates the spin state of the colliding atom pair. The molecular bound state $|g_1\rangle$, which is not energetically accessible, resides in the closed channel. If the open channel and closed channels have different magnetic moments, the open and closed channels can be tuned using external magnetic fields to be degenerate creating a Feshbach resonance at the resonance magnetic field B_{res} ,

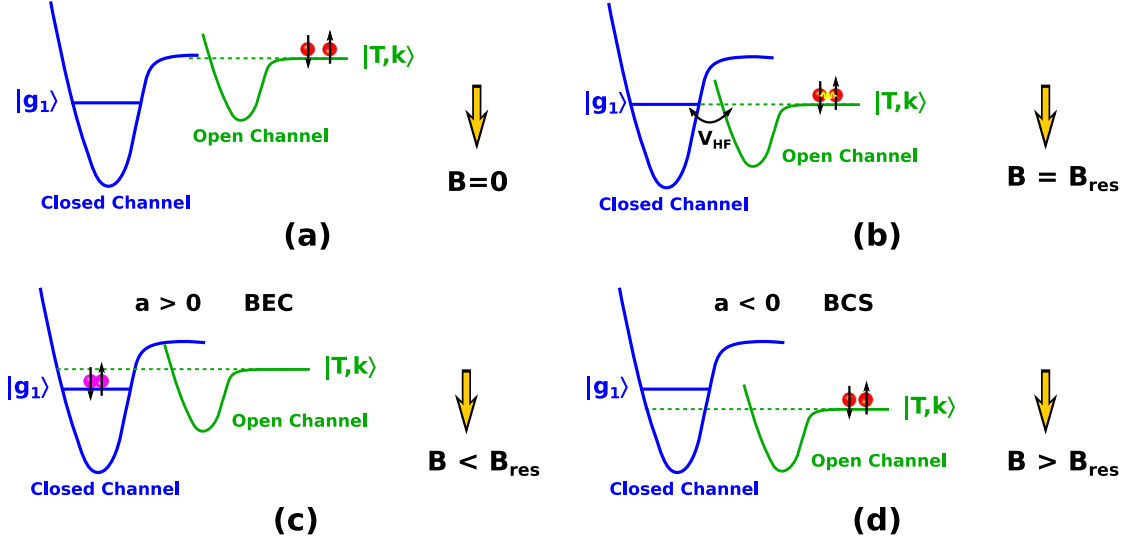


FIGURE 1.1: Magnetic Feshbach resonance arises due to the coupling between the molecular bound state $|g_1\rangle$ and the scattering continuum $|T, k\rangle$. Down arrow indicates that increasing the magnetic field tunes the energy of the scattering continuum downward. (a) At $B = 0$, the energetically accessible scattering state $|T, k\rangle$ (open channel) of the unbound free atom pair is higher in energy than the molecular bound state. (b) At $B = B_{res}$, the molecular bound state is degenerate with the scattering continuum which leads to Feshbach resonance due to the presence of hyperfine coupling V_{HF} between them. (c) At $B < B_{res}$, BEC side of the Feshbach resonance (d) At $B > B_{res}$, BCS side of the Feshbach resonance.

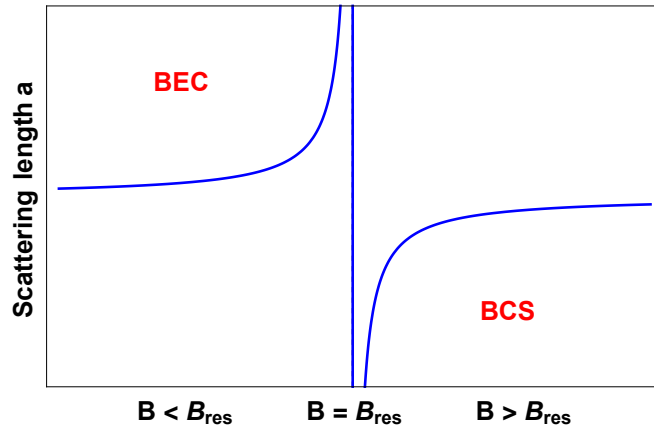


FIGURE 1.2: Zero energy scattering length a near a magnetic Feshbach resonance. When $B = B_{res}$, the scattering length diverges and leads to strong interactions. When $B < B_{res}$, BEC side of the Feshbach resonance, where the scattering length is positive and the interactions are repulsive. When $B > B_{res}$, BCS side of the Feshbach resonance, where the scattering length is negative and interactions are attractive.

due to the hyperfine coupling between the open and closed channels.

Fig. 1.2 shows zero energy scattering length near a magnetic Feshbach resonance. At the Feshbach resonance $B = B_{res}$, the scattering length diverges leading to strong interactions. For magnetic fields below the resonance magnetic field, $B < B_{res}$, the scattering length is positive and interactions are repulsive. For magnetic fields above the resonance magnetic field $B > B_{res}$, the scattering length is negative and interactions are attractive.

In Fermi gases, when the scattering length is positive, unbound atom pairs with opposite spins can form a BEC of molecules [20, 21] by three-body recombination and populates the molecular bound state $|g_1\rangle$, Fig. 1.1(c). This regime is called the BEC side of the resonance. Above the Feshbach resonance, when the scattering length is negative, unbound free atom pairs in the presence of other fermions can form Cooper pairs due to the presence of weak attractions between them, Fig. 1.1(d). This regime is called the BCS side of the resonance, as the BCS theory of superconductivity is required to explain the physics in this regime.

Over the past several years magnetic Feshbach resonances have been extensively used and have yielded several important observations in the study of ultracold gases with tunable interactions [1]. In Bose gases, Feshbach resonances were used to create an atomic Bose-Einstein condensate (BEC) of ^{85}Rb [22] and ^{133}Cs [23]. Feshbach resonances were used to tune the interaction on a stable BEC from repulsive to attractive resulting in condensate collapse and has led to the observation of bright matter-wave solitons in ^7Li [24, 25]. Ultracold molecules of ^{85}Rb were produced using oscillatory magnetic fields [26] near a Feshbach resonance. In addition, using Feshbach resonances to turn off interactions near a zero-crossing of the scattering length is important in fields such as atom interferometry. Using a non-interacting BEC, long lived Bloch oscillations have been observed in ^{133}Cs [27] and ^{39}K [28]. More recently, Feshbach resonances in ultracold cesium were used to observe Efimov

trimers [29, 30], a theoretical prediction [31] which was made over half a century ago, that would have been impossible had it not been for the ability to magnetically tune the interactions.

In Fermi gases, pioneering work utilizing Feshbach resonances has been done by our group [32, 33, 34], including the first observation of a strongly-interacting degenerate Fermi gas in ${}^6\text{Li}$ in 2003 [35, 32]. Other pioneering works using Feshbach resonances in ${}^6\text{Li}$ include the observation of vortices and superfluidity [36, 37], superfluid phase transition [38], sound propagation [39], universal quantum viscosity [34], and evidence of collective excitations near a BEC-BCS crossover [40, 41]. A Bose-Einstein condensate of ${}^6\text{Li}_2$ ultracold molecules was produced using three-body recombination near a Feshbach resonance [42]. Using Feshbach resonances, a strongly-interacting Fermi gas was realized in ${}^{40}\text{K}$ by Jin's group at JILA [43]. The same research group also demonstrated the creation of a BEC of molecules in ${}^{40}\text{K}$ by adiabatically sweeping the magnetic field through the Feshbach resonance into the BEC regime [44].

1.2 Why do we need optical control of interactions?

Although magnetically tunable interactions near Feshbach resonances have been instrumental in driving the burgeoning field of ultracold atoms into uncharted territories, it suffers from some drawbacks. One of the main disadvantages of using magnetic fields to control interactions is the lack of spatial resolution since large and bulky coils are used to generate the required high magnetic fields. Therefore, it is not possible to have spatially selective control of interactions within an atom cloud which is only a few hundred microns in size.

For example, exotic atomic systems such as a strongly interacting system sandwiched between two non-interacting systems, cannot be realized using magnetic Feshbach resonances. However, as the size of optical beams can be modulated on a

sub-wavelength scale, optical fields can provide high-resolution spatial control of interactions in ultracold gases. Encouraged by the potential of using optical beams to induce spatial variations in the scattering length, many theoretical proposals have been put forth, including the observation of Hawking radiation from acoustic black holes [45] and controllable soliton emission in atomic Bose-Einstein condensates [46].

Another disadvantage of using magnetic fields to control interactions is its slow tunability. Magnetic fields in general are generated by driving a current through a coil. The high inductance of these coils limits the rate at which the magnetic field can be changed. Several groups [26, 47, 48] have demonstrated tunabilities on a time scale of sub-milliseconds by using a set of two coils, a high inductance primary coil and a low inductance auxiliary coil. The primary coil generates the high magnetic field but does not tune the magnetic field. The auxiliary coil is used for tuning the magnetic field. However, tuning interactions in the timescale of milliseconds is still insufficient to pursue experiments towards studies of non-equilibrium thermodynamics in interacting Fermi gases which involves rapid changes in the system parameters.

For example, the natural time scale in a Fermi gas is the “Fermi time”, τ_F , which is defined as the time taken by a fermion with the Fermi velocity v_F to move a De Broglie wavelength λ_F . For a Fermi Energy, $E_F \approx k_B \times 1\mu\text{K}$, the Fermi time is in the order of $\hbar/E_F \sim 10\mu\text{s}$ [49]. In order to control interactions on a time scale faster than the Fermi time, the use of optical techniques becomes inevitable. Optical fields can be used to tune interactions in a few nanoseconds as the tuning rate is only limited by the switching time of an optical switch, such as an acousto-optical or electro-optical modulator.

1.3 Optical control of interactions in ultracold atoms

The concept of using optical methods to control interactions was proposed even before the realization of a Bose-Einstein condensate [50, 51]. As we saw from the illustration for a magnetic Feshbach resonance in Fig. 2.1, the change in scattering length in a unbound pair of atoms was brought by coupling the atom pair colliding state to a bound molecular state. In a magnetic Feshbach resonance, the bound state is chosen to be one of the vibrational states in the ground potential of the closed channel. Similarly, the scattering length can also be changed by coupling unbound colliding atom pairs to the electronically excited bound vibrational state of the open channel by applying laser light Fig. 1.3. The phenomenon by which unbound colliding atom pairs can be coupled to a bound state by the application of light is called photoassociation [52]. One of the very first demonstrations of using optical fields to control interactions utilized a photoassociation resonance [4]. This resonance is also called as optical Feshbach resonance (OFR).

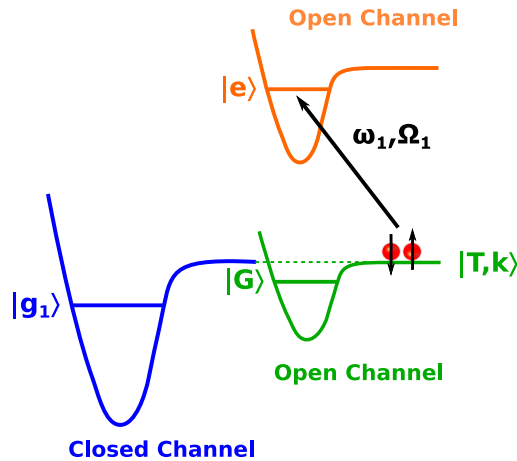


FIGURE 1.3: Basic level scheme for optical Feshbach resonance (OFR) to control interactions as illustrated in Ref. [4, 6]. An optical field with frequency ω_1 and Rabi frequency Ω_1 couples the scattering continuum $|T, k\rangle$ in the open channel to the bound excited state $|e\rangle$ in the open channel.

Fig. 1.3 illustrates the concept of optical Feshbach resonance . In OFR, laser light

of frequency ω_1 and Rabi frequency Ω_1 couples the unbound free atom pairs in the open channel to the excited vibrational state of the closed channel. Note that this technique completely ignores the magnetic Feshbach resonance and does not utilize the bound state in the closed channel. It is a stand alone optical technique that only acts on the open channel. The very first observation of OFR was reported by Fatemi and coworkers in an ultracold gas of sodium vapor [4]. However, they did not demonstrate the tunability of the scattering length associated with an optical Feshbach resonance.

The first demonstration of tuning the scattering length using OFR was reported by M. Theis and coworkers [6] in a ^{87}Rb Bose condensate using the scheme illustrated in Fig. 1.3. They were able to tune the scattering length from $10 a_0$ to $190 a_0$, where a_0 is the Bohr radius. One of the major drawbacks of optical control techniques is atom loss through spontaneous scattering. As atoms are excited from the ground state of the open channel to the excited vibrational bound state of the open channel, they spontaneously decay to *all* allowed lower energy vibrational states leading to atom loss. The atom loss is characterized by the two-body loss rate coefficient K_2 given in cm^3/s . M.Theis and coworkers were able to attain a $K_2 \approx 10^{-10} \text{ cm}^3/\text{s}$. To put that number into perspective, if we have a Bose-Einstein condensate at typical densities of 10^{14} cm^{-3} , the lifetime of the atoms would be $100 \mu\text{s}$. In other words, experiments using OFR should be done within $100 \mu\text{s}$, which is a severe limitation on the proposed next generation experiments.

In order to increase the lifetime of the atoms by suppressing spontaneous scattering, M.Theis and coworkers adopted a two-field technique that used two-photon Raman coupling [7] as illustrated in Fig. 1.4. In a Raman-coupled OFR, in addition to the ω_1 optical field, a second optical field with frequency ω_2 and Rabi frequency Ω_2 couples the ground vibrational state $|G\rangle$ in the open channel to the excited vibrational state in the open channel. Both the optical fields, ω_1 and ω_2 are far detuned

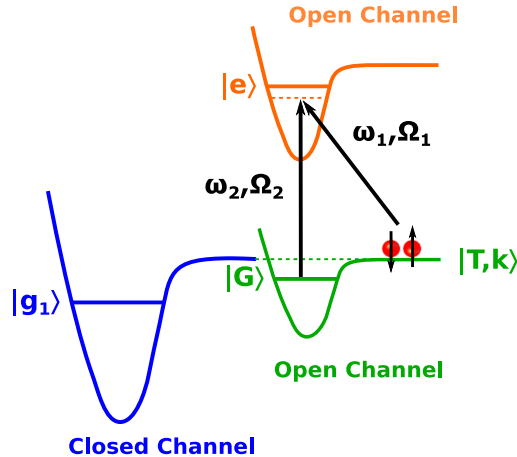


FIGURE 1.4: Basic level scheme for Raman-coupled optical Feshbach resonance (OFR) to control interactions as illustrated in Ref. [7]. An optical field with frequency ω_1 and Rabi frequency Ω_1 couples the scattering continuum $|T, k\rangle$ in the open channel to the bound excited state $|e\rangle$ in the open channel. A second optical field with frequency ω_2 and Rabi frequency Ω_2 couples the ground molecular state $|G\rangle$ in the open channel to the bound excited state $|e\rangle$ in the open channel. Both optical fields are detuned from the excited state and absorption occurs due to two-photon Raman coupling.

from the excited state. Two-photon Raman coupling is a well known process in atomic physics where atoms absorb two-photons to couple from the ground state to the excited state through a virtual state. Compared to the experiment done using a single optical field in Ref. [6], M.Theis and coworkers were not able to demonstrate net improvement in the lifetime of the atoms for a given tunability in the scattering length.

A major breakthrough in this field occurred when Bauer and coworkers used an optical field acting on the closed channel to tune the scattering length near a magnetic Feshbach resonance [9]. The basic level scheme for this technique is illustrated in Fig. 1.5. A single optical field with frequency ω_1 , Rabi frequency Ω_1 , and detuning Δ couples the ground vibrational state $|g_1\rangle$ in the closed channel to the excited vibrational state $|e\rangle$ in the closed channel. Note that the molecular bound state $|g_1\rangle$ is responsible for the Feshbach resonance.

The ω_1 field creates a light shift Σ_{opt} proportional to $\Omega_1^2/4\Delta$ of the state $|g_1\rangle$ thereby changing the position of the magnetic Feshbach resonance. By using mag-

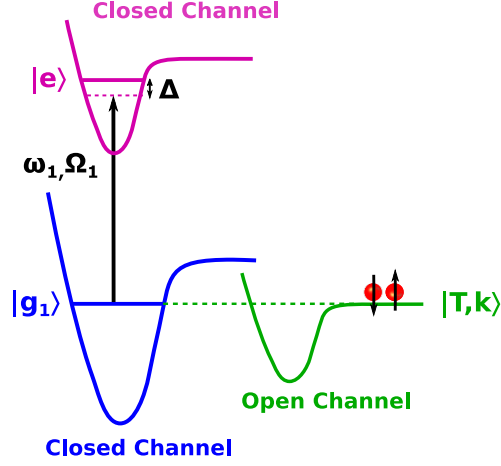


FIGURE 1.5: Level scheme for single-field optical method to control interactions as illustrated in Ref. [9]. An optical field with frequency ω_1 and Rabi frequency Ω_1 couples the ground vibrational state $|g_1\rangle$ in the closed channel to the bound excited state $|e\rangle$ in the closed channel.

netic fields, the open channel is initially tuned near degeneracy with state $|g_1\rangle$. The ω_1 field is then applied to tune the state $|g_1\rangle$ to be degenerate with the open channel. Bauer and coworkers were able to demonstrate tunability in the scattering length of $200 a_0$ with a two-body loss rate constant $K_2 \approx 10^{-11} \text{cm}^3/\text{s}$, an order of improvement compared to Ref. [6, 7].

Note that, unlike OFR, the optical fields in this technique does not interact directly with the free atoms in the open channel. The optical fields interact only with the closed channel and is merely involved in creating a light shift of the state $|g_1\rangle$, which is responsible for the Feshbach resonance. Also, this technique is not a stand alone optical technique to control interactions. It uses optical fields to tune the interactions near a magnetic Feshbach position by light shifting the state $|g_1\rangle$.

For the single-field optical technique like the one used in Ref. [9], the loss rate is proportional to $\Omega_1^2/4\Delta^2$ and the shift is proportional to $\Omega_1^2/4\Delta$. Therefore, larger

detunings can improve the lifetime of the atoms at the cost of reduced tunability. In a follow up experiment [12], Bauer and coworkers demonstrated an order of improvement in two body loss rate constant $K_2 \approx 10^{-12} \text{ cm}^3/\text{s}$ for the same tunability of $200 a_0$ by using an optical field with large detuning and high intensity. However, intense optical fields can create unwanted dipole trapping potential of the atoms, which limits the usability of this technique. Following Bauer and coworkers, a similar experiment was done in Fermi gases by Fu and coworkers in ultracold ^{40}K [10].

More recently, Clark and coworkers used ultracold cesium atoms to demonstrate that by tuning the wavelength of the ω_1 laser (Fig. 1.5) to the so called “magic” wavelength, the effect of optical dipole potential on the atoms can be completely nullified [11]. By choosing the “magic” wavelength in between the D_1 and D_2 atomic transition lines of cesium, Ref. [11] showed the net optical dipole potential on the atoms is canceled by quantum interference. Note that this technique is exactly similar to the one reported in Ref. [12], minus the effect of the dipole trapping potential. Ref. [11] demonstrated light shift of the Feshbach resonance by 38 mG, corresponding to a scattering length change from $0 a_0$ upto $180 a_0$ with a lifetime of 100 ms. They further demonstrated spatial and temporal control of scattering length by monitoring condensate dynamics and using intermodulation spectroscopy [26], respectively.

1.4 Advantages of our two-field optical methods

The fundamental problem with the use of single-field optical methods is spontaneous scattering, which limits the tunability of interactions. As we saw in the previous section, single-field methods relies on large detunings to suppress atom loss. Although this approach can work in atomic species with very narrow Feshbach resonances, it is not generally applicable to any moderate width Feshbach resonances. For example, Ref. [11] utilized a d-wave Feshbach resonance in cesium with a resonance width of 157 mG. Using a far-detuned single-optical field, Ref. [11] demonstrated shifting

of the Feshbach resonance by tens of mG with a lifetime of 100 ms. However, to control interactions in atomic species like ${}^6\text{Li}$ which has a broad Feshbach resonance with a width of 300 G cannot be controlled by a single field. The only way to tune interactions in ${}^6\text{Li}$ is to use a near resonant light. However, as we have seen from our prior discussion, near resonant light creates atom loss by spontaneous scattering. So the question is, how do we use near resonant light to create a large change in the scattering length and suppress atom loss at the same time?

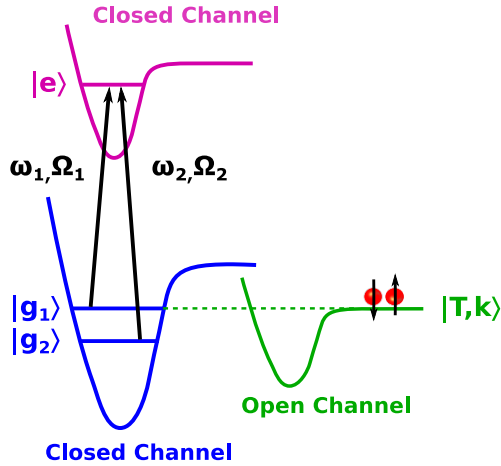


FIGURE 1.6: Our closed-channel EIT method to control interactions in ultracold gases. An optical field with frequency ω_1 and Rabi frequency Ω_1 couples the ground vibrational state $|g_1\rangle$ in the closed channel to the bound excited state $|e\rangle$ in the closed channel. A second optical field with frequency ω_2 and Rabi frequency Ω_2 couples the lower lying ground molecular state $|g_2\rangle$ in the closed channel to the bound excited state $|e\rangle$ in the closed channel.

A theoretical proposal from our group [49, 53] suggested that two-optical fields could be applied to the closed channel to suppress loss through electromagnetically induced transparency (EIT). Our closed-channel EIT method is illustrated in Fig. 1.6. In addition to the ω_1 field, a second optical field ω_2 couples the lower lying vibrational bound state $|g_2\rangle$ in the closed channel to the excited vibrational state $|e\rangle$ in the closed channel. The ω_1 field is a near-resonant optical field that induces changes in the scattering length by light shifting the state $|g_1\rangle$ and the ω_2 field suppresses

loss through destructive quantum interference. Electromagnetically induced transparency (EIT) [54, 55] is a well known technique in the field of quantum optics where atomic absorption due to an optical field is suppressed by the use of another optical field that creates a transparency window in the absorption spectra of the atoms.

In addition to suppressing atom loss, our closed-channel EIT method has other major advantages compared to single-field methods. Using closed-channel EIT, a small change in the frequency of either the ω_1 field or ω_2 field creates narrow features in the relative momentum k dependence of the scattering phase shift δ . Therefore, we can tune the scattering length by changing the frequency of the optical fields, thereby avoiding any net change in the optical dipole trapping potential. Since single-field methods use large detunings to avoid atom loss, small changes in frequency of the optical field will have negligible effect on the scattering length. The only “knob” for controlling the interactions in single-field methods is the intensity of the optical beam. However, changing the intensity of the optical beam to control interactions might cause adverse effects of creating unwanted trapping potential on the atoms.

My PhD work primarily focused on building an optical system that experimentally demonstrates the use of closed-channel EIT to optically control interactions in ultracold gases. In the work presented here, I will demonstrate that using closed-channel EIT, the spontaneous lifetime of atoms near a broad Feshbach resonance in ${}^6\text{Li}$ is increased from 0.5 ms for single-field methods to 400 ms using our two-field methods. I will further demonstrate that the narrow Feshbach resonance in ${}^6\text{Li}$ can be shifted by 3 G, about 30 times its width, while suppressing atom loss.

I will also present a new theoretical model, the continuum-dressed state model to calculate the momentum dependent optically induced scattering phase shift of the colliding atom pair. Previous theoretical approaches from our group [49, 53] and others [9, 56] are valid for narrow Feshbach resonances with weak hyperfine coupling between the scattering continuum and the molecular bound state. However, for

Feshbach resonances with strong hyperfine coupling, Ref. [9, 49, 53, 56] does not predict the correct behavior. Therefore, I developed a new theoretical model that provides a comprehensive treatment by treating both the broad and narrow Feshbach resonances in a unified manner.

The validity of the continuum-dressed state model is tested by comparing our data. The continuum-dressed state model fits the data both in magnitude and shape using only one fitting parameter. The continuum-dressed state model is one of the important results reported in this thesis as it provides a general prescription to calculate the scattering phase shift for optical control experiments.

1.5 Dissertation organization

In the next chapter, I will introduce the basic theory of collisional Feshbach resonances. I will derive the scattering state wavefunction and the scattering phase shift due to a magnetic Feshbach resonance.

In chapter 3, I will develop the continuum-dressed state model for optical control of interactions. Using the continuum-dressed state model, I will derive the relative momentum dependent optically induced scattering phase shift

In chapter 4, I will use optically induced phase shift derived using the continuum-dressed state model in chapter 3 to derive the two-body loss rate constant K_2 , zero energy s-wave scattering length a , and the effective range r_e . I will further show the predictions of the continuum dressed state model for closed-channel EIT control of interactions near the broad and narrow Feshbach resonances in ${}^6\text{Li}$.

In chapter 5, I will briefly discuss the experimental setup used in our laboratory to create a ultracold gas of ${}^6\text{Li}$ atoms and explain in detail the optical system that I designed and built to demonstrate the closed-channel EIT in an ultracold gas of ${}^6\text{Li}$ atoms.

In chapter 6, I will discuss the experimental results for the closed-channel EIT

experiment near the broad and narrow Feshbach resonances in ${}^6\text{Li}$. I will use the continuum-dressed state model to fit our experimental data, demonstrating the validity of the continuum-dressed state model in accurately predicting momentum-dependant scattering phase shift. Furthermore, I will summarize my entire work and discuss future directions of this project.

2

Theory of Collisional Feshbach Resonances

In two-atom scattering, a collisional Feshbach resonance occurs when the total energy of a pair of free unbound atoms is tuned into resonance with a molecular bound state, Fig. 2.1. This leads to a resonant enhancement of the scattering cross section where the scattering length diverges. The energetically accessible scattering channel of the free unbound atoms is called the open channel. The atom-pair enters and exits in this channel. The molecular bound state is not energetically accessible by the free unbound atoms and resides in the energetically closed channel. The open channel state can be tuned using an external magnetic field to be degenerate with the closed channel molecular state thereby creating a Feshbach resonance due to the hyperfine coupling between the open and closed channels. This method of using magnetic fields to induce a collisional resonance is called a magnetic Feshbach resonance.

The expression for the zero energy s-wave scattering length a near a magnetic Feshbach resonance is given by [1]

$$a = a_{bg} - |a_{bg}| \frac{\Delta B}{B - B_{res}}, \quad (2.1)$$

where a_{bg} is the background scattering length, ΔB is the width of the resonance,

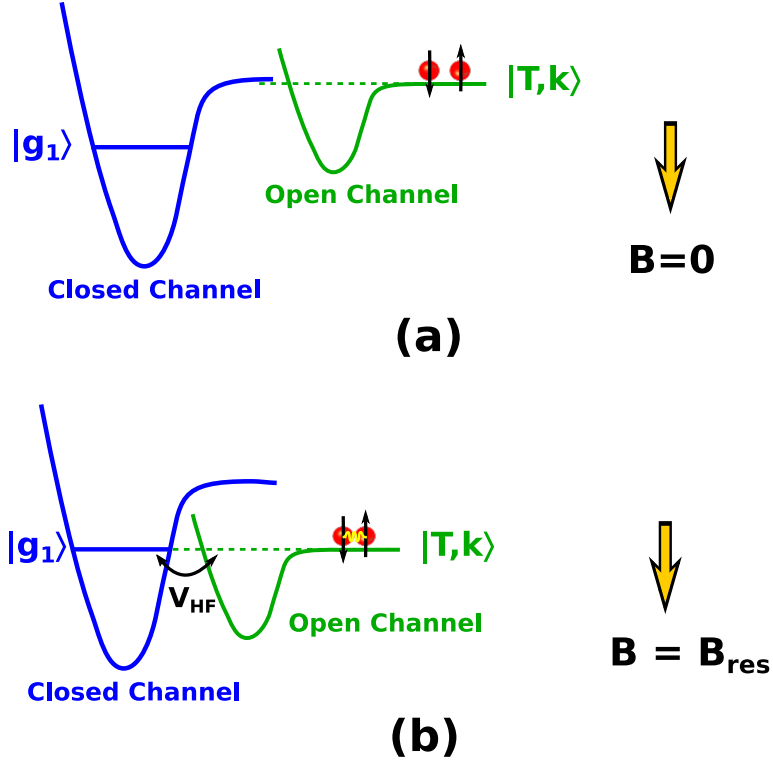


FIGURE 2.1: Magnetic Feshbach resonance arises due to the coupling between the molecular bound state $|g_1\rangle$ and the scattering continuum $|T, k\rangle$. Down arrow indicates that increasing the magnetic field tunes the energy of the scattering continuum downward. (top) At $B = 0$, the energetically accessible scattering state $|T, k\rangle$ (open channel) of the unbound free atom pair is higher in energy than the molecular bound state. (bottom) At $B = B_{res}$, the molecular bound state is degenerate with the scattering continuum which leads to Feshbach resonance due to the presence of hyperfine coupling between them.

B_{res} is the resonance magnetic field, and B is the magnetic field. From Eq. 2.1, we can see that when $B = B_{res}$, the scattering length a diverges.

The lowest two hyperfine states in ${}^6\text{Li}$ (see section 2.1) have a broad Feshbach resonance at 832.2 G with width $\Delta B = 300$ G [57, 58] and a narrow Feshbach resonance at 543.2 G with width $\Delta B = 0.1$ [59]. Fig. 2.2 shows the plot of the scattering length (Eq. 2.1) for the case of broad Feshbach resonance (Fig. 2.2 top) and narrow Feshbach resonance (Fig. 2.2 bottom) in ${}^6\text{Li}$. The background scattering lengths a_{bg} in Eq. 2.1 given in terms of the Bohr radius a_0 for the broad and narrow

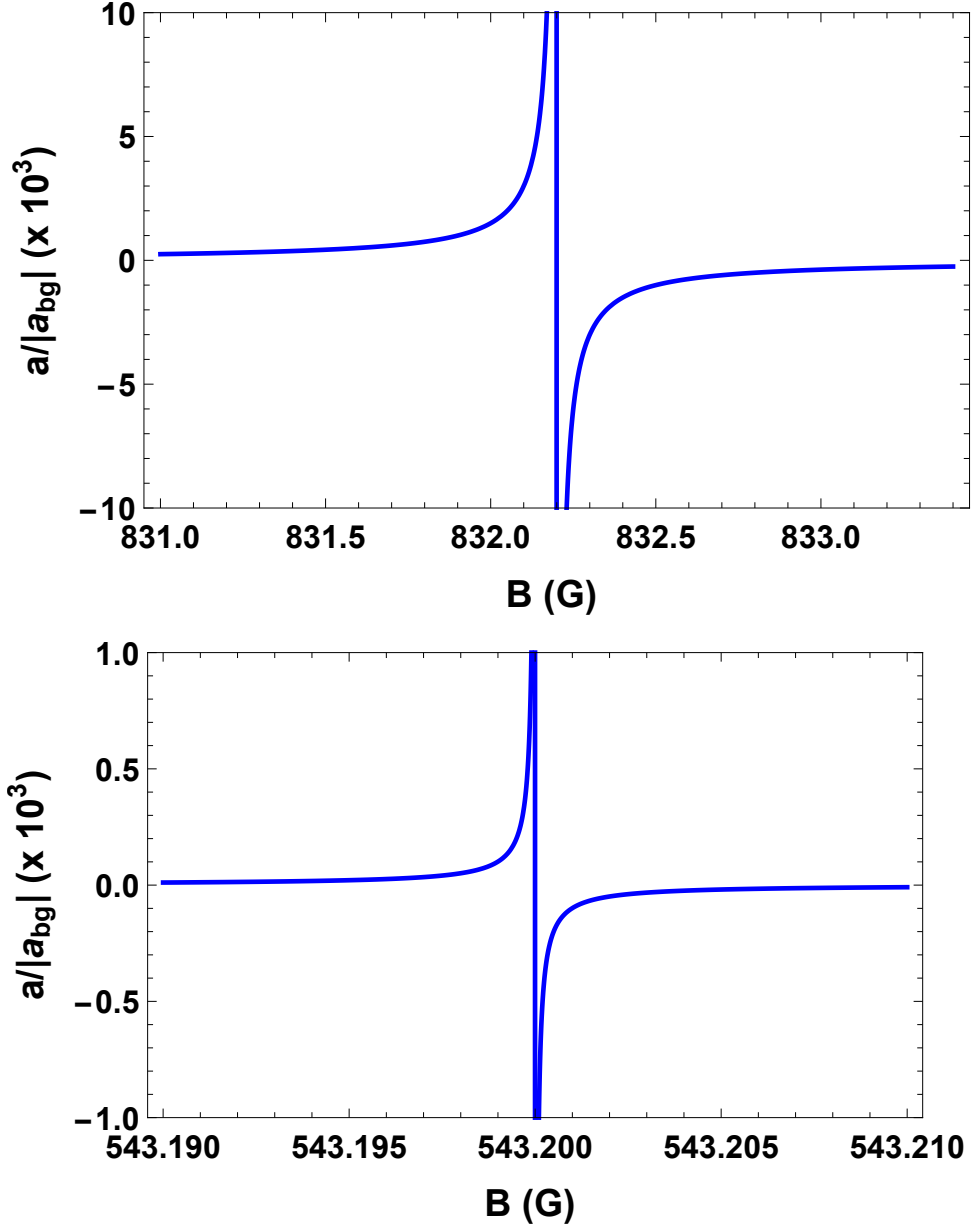


FIGURE 2.2: Zero energy scattering length a in units of background scattering length a_{bg} as a function of magnetic field for the broad Feshbach resonance (top) and the narrow Feshbach resonance (bottom). The background scattering length a_{bg} for broad and narrow Feshbach resonance in ${}^6\text{Li}$ is $-1450 a_0$ and $62 a_0$, respectively.

Feshbach resonances in ${}^6\text{Li}$ are $-1450 a_0$ and $62 a_0$, respectively.

The region to the left of the resonance where $B < B_{res}$ is called the BEC side, since a BEC (Bose-Einstein condensate) of molecules can be created at sufficiently

low temperatures. The region to the right of the resonance where $B > B_{res}$ is called the BCS side, where BCS (Bardeen-Cooper-Schrieffer) theory is required to explain the formation of Cooper pairs at low temperatures.

On the BEC side, the scattering length is positive and the interactions between the atoms are repulsive. Also, the triplet continuum $|T, k\rangle$ lies in energy above the molecular bound state $|g_1\rangle$. The unbound free atom pairs in $|T, k\rangle$ can form molecules by three body recombination. The molecules can decay into the bound state $|g_1\rangle$, forming a BEC of ${}^6\text{Li}$ atoms. At low temperatures, when the thermal energy is less than the binding energy of the molecules, the molecular population is stable i.e., the molecules cannot break into free atom pairs and decay back into the continuum, which lies higher in energy.

On the BCS side, the scattering length is negative and the interaction between the atoms are attractive. The triplet continuum $|T, k\rangle$ lies lower in energy than the molecular bound state $|g_1\rangle$. In the presence of other fermions i.e., in the so called “Fermi sea”, two fermions with weak attractive interactions between them can form Cooper pairs by weakly coupling to $|g_1\rangle$ that lies above $|T, k\rangle$. The formation of Cooper pairs can occur only at very low temperatures due to the presence of weak coupling between the pairs. Two-body physics cannot be used to study the interactions and many-body physics is required to explain the physics on the BCS side.

In this chapter, we will formally derive the theory of magnetic Feshbach resonances and derive the scattering parameters such as the scattering length a and the effective range r_e . In our theoretical treatment, we study the mixing between the scattering continuum in the open channel and the molecular bound state near a Feshbach resonance using a “dressed state” picture, where the molecular bound state is considered to be “dressed” by the scattering continuum due to the hyperfine mixing between them. Although several theoretical treatments for Feshbach resonances in

ultracold gases have been reported over the past decade [1, 60], we will show that our treatment of Feshbach resonances using these dressed states provides a simple and intuitive picture of the exotic physics near a magnetic Feshbach resonance. In the next section, we will consider the Feshbach resonances in ${}^6\text{Li}$.

2.1 Feshbach resonance in ${}^6\text{Li}$

${}^6\text{Li}$ is a fermion with 3 electrons, 3 protons, and 3 neutrons. The nuclear spin is $I = 1$. The electronic ground state of ${}^6\text{Li}$ has a total electronic spin angular momentum of $S = 1/2$ and total electronic orbital momentum of $L = 0$. Hence, the total angular momentum F takes the values, $F = 1/2$ and $F = 3/2$. In the absence of external magnetic field, the $F = 1/2$ state is two-fold degenerate corresponding to $m_f = 1/2, -1/2$ and the $F = 3/2$ state is four-fold degenerate corresponding to $m_f = -3/2, -1/2, 1/2, 3/2$. The application of a bias magnetic field breaks this degeneracy and gives rise to six hyperfine states, conventionally labeled as $|1\rangle, |2\rangle, |3\rangle, |4\rangle, |5\rangle$, and $|6\rangle$ in the order of increasing energy. The electronic structure of ${}^6\text{Li}$ is covered extensively in all previous thesis in our group. I therefore suggest the reader to refer to older thesis [61] in our group to get a detailed understanding about the hyperfine states in ${}^6\text{Li}$.

In our laboratory, experiments using ultracold atoms are done using a 50-50 mixture of the two lowest hyperfine states of ${}^6\text{Li}$, namely, states $|1\rangle$ and $|2\rangle$. We will now discuss the two-atom states responsible for the broad and narrow Feshbach resonances in ${}^6\text{Li}$. In the $|m_s, m_I\rangle$ basis, where m_s is the electronic spin projection quantum number and m_I is the nuclear spin projection quantum number, the lowest energy hyperfine state $|1\rangle$ is a superposition of $|1/2, 0\rangle$ and $| -1/2, 1\rangle$ and the second lowest energy hyperfine state $|2\rangle$ is a superposition of $|1/2, -1\rangle$ and $| -1/2, 0\rangle$.

In low energy s-wave collisions of atoms in a $|1\rangle - |2\rangle$ mixture, where one atom is in $|1\rangle$ and the other atom is in $|2\rangle$, the total magnetic quantum number $M = 0$ is

conserved in a bias magnetic field B_z . In the $|S, m_s; I, m_I\rangle$ basis, where S is the total electronic spin quantum number and I is the total nuclear spin quantum number of the two-atom system, there are five states for $M = 0$. These include two singlet states, $|0, 0; 0, 0\rangle$ and $|0, 0; 2, 0\rangle$ and three triplet states, $|1, -1; 1, 1\rangle$, $|1, 0; 1, 0\rangle$, and $|1, 1; 1, -1\rangle$.

The triplet state $|1, 0; 1, 0\rangle$ does not tune with the magnetic field ($m_s = 0$) and the triplet state $|1, 1; 1, -1\rangle$ tunes upward with magnetic field ($m_s = +1$). The only triplet state that tunes downward with magnetic field is $|1, -1; 1, 1\rangle$ ($m_s = -1$). For the Feshbach resonances in ${}^6\text{Li}$, the energy of the triplet state has to be tuned downward to be degenerate with the bound singlet vibrational state, Fig. 2.1. Hence, the triplet state $|1, -1; 1, 1\rangle$ which tunes downward with magnetic field is responsible for the Feshbach resonance in ${}^6\text{Li}$. We write the incoming triplet state as

$$|T\rangle = |1, -1; 1, 1\rangle. \quad (2.2)$$

The Zeeman-hyperfine energy of this triplet state is

$$E_T = -\frac{a_{HF}}{2} - 2\mu_B B \quad (2.3)$$

where $a_{HF} = h \times 152.1$ MHz is the hyperfine coupling constant, $\mu_B = 1.4$ MHz/G is the Bohr magnetron, and B is the magnetic field.

It has sometimes been reported in the literature that one of the two singlet states is responsible for the broad Feshbach resonance and the other singlet state is responsible for the narrow Feshbach resonance [62]. Recent work [49, 53] from our group with rigorous evaluation of the energy shifts due to singlet-triplet mixing near a Feshbach resonance has made this argument invalid. As reported in [49, 53], a superposition of two singlet states $|g_1^n\rangle$, is responsible for the narrow Feshbach resonance at 543.2 G. The state $|g_1^n\rangle$ has zero first order hyperfine mixing with the triplet state $|1, -1; 1, 1\rangle$ but has a second order mixing through the triplet state

$|1, 0; 1, 0\rangle$. We write

$$|g_1^n\rangle = \frac{1}{3}|0, 0; 0, 0\rangle + \frac{2\sqrt{2}}{3}|0, 0; 2, 0\rangle \quad (2.4)$$

The singlet state that is orthogonal to $|g_1^n\rangle$, namely $|g_1^b\rangle$, is responsible for the broad Feshbach resonance at 832.2 G. We write

$$|g_1^b\rangle = \frac{2\sqrt{2}}{3}|0, 0; 0, 0\rangle - \frac{1}{3}|0, 0; 2, 0\rangle \quad (2.5)$$

The singlet-triplet hyperfine coupling for the broad Feshbach resonance is $V_{HF}/\hbar = 131.6$ MHz and for the narrow Feshbach resonance is $V_{HF}/\hbar = 5.9$ MHz.

In the general treatment of the Feshbach resonance presented in the rest of the chapter, both the narrow Feshbach resonance singlet state $|g_1^n\rangle$ and the broad Feshbach resonance singlet state $|g_1^b\rangle$ will be collectively called $|g_1\rangle$. As we have established the relevant states involved in the Feshbach resonance of ${}^6\text{Li}$, we will proceed to construct a theoretical framework, which we use to derive the scattering parameters.

2.2 Continuum-dressed state treatment of Feshbach resonance

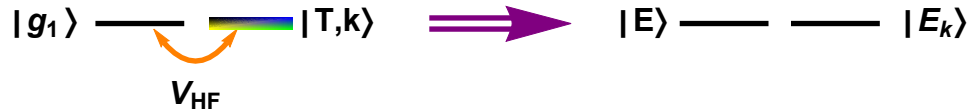


FIGURE 2.3: Transformation from bare states (left) to dressed states (right). The bare singlet bound state $|g_1\rangle$ and bare triplet continuum $|T, k\rangle$ with hyperfine mixing V_{HF} , leads to two dressed states, namely, the dressed bound state $|E\rangle$ and dressed continuum state $|E_k\rangle$.

As mentioned in the previous section, the hyperfine coupling between the singlet ground state $|g_1\rangle$ and the triplet state $|T, k\rangle$ causes a Feshbach resonance. In our theoretical approach, we treat the hyperfine mixing between the singlet bound state $|g_1\rangle$ and the triplet continuum $|T, k\rangle$ in the “dressed state” picture, where $|g_1\rangle$ gets

“dressed” by $|T, k\rangle$. The dressing of $|g_1\rangle$ by $|T, k\rangle$ leads to two dressed states, namely, the dressed continuum $|E_k\rangle$ and the dressed bound state $|E\rangle$ (Fig. 2.3). Hence, both the dressed continuum $|E_k\rangle$ and the dressed bound state $|E\rangle$ are superpositions of $|g_1\rangle$ and $|T, k\rangle$.

We will study the Feshbach resonance by first deriving the wavefunction of the dressed continuum state $|E_k\rangle$ and the dressed bound state $|E\rangle$.

2.3 Dressed continuum state $|E_k\rangle$

We write $|E_k\rangle$ as a superposition of $|g_1\rangle$ and $|T, k\rangle$,

$$|E_k\rangle = c_1 |g_1\rangle + c_T(k) |T, k\rangle + \sum_{k' \neq k} c_T(k') |T, k'\rangle, \quad (2.6)$$

where $|T, k\rangle$ represents the chosen incoming triplet scattering state with relative momentum $\hbar k$ and $|T, k'\rangle$ represents all other triplet scattering states in the continuum with relative momentum $\hbar k'$. Here, $c_T(k)$ is the probability amplitude of the chosen input state $|T, k\rangle$, $c_T(k')$ is the probability amplitude of the rest of the continuum $|T, k'\rangle$, and c_1 is the probability amplitude of the bound state $|g_1\rangle$.

Writing the basis states in Eq. 2.6 in terms of the factored spin and relative momentum part filtered, we have

$$|E_k\rangle = c_1 |s\rangle |v\rangle + c_T(k) |T\rangle |k\rangle + \sum_{k' \neq k} c_T(k') |T\rangle |k'\rangle, \quad (2.7)$$

where $|s\rangle$ is the spin singlet state for $|g_1\rangle$ and $|v\rangle$ is the vibrational bound state for $|g_1\rangle$.

The Hamiltonian of the system can be written in terms of the singlet state $|s\rangle$ and the triplet continuum $|T\rangle$ states,

$$H = E_{g_1} |s\rangle \langle s| + \left(E_T + \frac{\hbar^2 k^2}{m} \right) |T\rangle \langle T| + V_{HF} (|s\rangle \langle T| + |T\rangle \langle s|), \quad (2.8)$$

where E_{g_1} is the energy of the ground singlet bound state, $E_T = -a_{HF}/2 - 2\mu_B B$ is the energy of the triplet continuum, $\hbar^2 k^2/m$ is the relative kinetic energy between two particles ($\mu = m/2$ is the reduced mass), and V_{HF} is the hyperfine coupling between the ground singlet state $|s\rangle$ and the triplet continuum $|T\rangle$.

Using the Schrödinger equation, we have

$$H|E_k\rangle = E_k|E_k\rangle, \quad (2.9)$$

where E_k is the total energy of the selected input state, given by

$$E_k = E_T + \frac{\hbar^2 k^2}{m}. \quad (2.10)$$

We solve for the probability amplitudes in $|E_k\rangle$ by taking the projections of the basis states onto Eq. 2.9. Projecting onto $|s\rangle|v\rangle$, and using Eq. 2.7 and Eq. 2.8, gives

$$(E_k - E_{g_1}) c_1 = V_{HF} \langle v|k\rangle c_T(k) + \sum_{k' \neq k} V_{HF} \langle v|k\rangle c_T(k'), \quad (2.11)$$

where $\langle v|k\rangle$ is the spatial overlap integral of the vibrational bound state wavefunction with bare triplet continuum eigenstate.

Defining $V_{HF} \langle v|k\rangle = \hbar g^*(k)$ in Eq. 2.11, we have

$$(E_k - E_{g_1}) c_1 = \hbar g^*(k) c_T(k) + \sum_{k' \neq k} \hbar g^*(k') c_T(k'). \quad (2.12)$$

Similarly, projecting Eq. 2.9 onto $|T, k'\rangle$ on Eq. 2.9 and using Eq. 2.7 and Eq. 2.8, we have

$$c_T(k') = \frac{\hbar g(k')}{(E_k - E'_k)} c_1; \quad \text{for } k' \neq k. \quad (2.13)$$

Substituting Eq. 2.13 in Eq. 2.12, yields

$$(E_k - E_{g_1}) c_1 = \hbar g^*(k) c_T(k) + \sum_{k' \neq k} \frac{|\hbar g(k')|^2}{(E_k - E'_k)} c_1. \quad (2.14)$$

Rewriting Eq. 2.14, in terms of the input amplitude $c_T(k)$

$$c_1 = \frac{\hbar g^*(k)}{E_k - E_{g_1} - \Sigma_E(k)} c_T(k), \quad (2.15)$$

where $\Sigma_E(k)$ is the energy shift given by

$$\Sigma_E(k) = \sum_{k' \neq k} \frac{|\hbar g(k')|^2}{(E_k - E'_k)}. \quad (2.16)$$

Substituting Eq. 2.15 in Eq. 2.13, we write $c_T(k')$ in terms of the input amplitude $c_T(k)$

$$c_T(k') = c_T(k) \frac{\hbar g^*(k)}{E_k - E_{g_1} - \Sigma_E(k)} \frac{\hbar g(k')}{(E_k - E'_k)} \quad (2.17)$$

Using Eq. 2.17 in Eq. 2.6, we obtain the dressed continuum state

$$|E_k\rangle = c_1 |g_1\rangle + c_T(k) \left\{ |T, k\rangle + |T, k'\rangle \frac{\hbar g^*(k)}{E_k - E_{g_1} - \Sigma_E(k)} \sum_{k' \neq k} \frac{\hbar g(k')}{(E_k - E'_k)} \right\}. \quad (2.18)$$

As $r \rightarrow \infty$, the molecular wavefunctions vanish since $\langle r \rightarrow \infty | v \rangle = 0$ and only the triplet continuum part of the wavefunction survives. Hence, taking the projection of Eq. 2.18 onto $|r \rightarrow \infty\rangle$,

$$\begin{aligned} \psi_{E_k}(r \rightarrow \infty) &= c_T(k) \left\{ \langle r \rightarrow \infty | k \rangle \right. \\ &\quad \left. + \frac{\hbar g^*(k)}{E_k - E_{g_1} - \Sigma_E(k)} \sum_{k' \neq k} \frac{\hbar g(k')}{(E_k - E'_k)} \langle r \rightarrow \infty | k' \rangle \right\}. \quad (2.19) \end{aligned}$$

As $|r \rightarrow \infty\rangle$, we can write the bare continuum state wave function $\langle r | k \rangle$ for box normalization as

$$\langle r \rightarrow \infty | k \rangle = \frac{1}{\sqrt{V}} \frac{\sin(kr + \delta_{bg})}{kr}, \quad (2.20)$$

where V is the box normalization volume and δ_{bg} is the background phase shift.

Using the effective range expansion [13, 14], the phase shift δ_{bg} for $k \rightarrow 0$ obeys,

$$k \cot \delta_{bg} = -\frac{1}{a_{bg}} + \frac{k^2}{2} r_{bg}, \quad (2.21)$$

where a_{bg} is the background scattering length and r_{bg} is the background effective range.

Substituting Eq. 2.20 in Eq. 2.19, we get

$$\begin{aligned} \psi_{E_k}(r \rightarrow \infty) &= \frac{c_T(k)}{kr\sqrt{V}} \left\{ \sin(kr + \delta_{bg}) \right. \\ &+ \left. \frac{\hbar k g^*(k)}{E_k - E_{g_1} - \Sigma_E(k)} \sum_{k' \neq k} \frac{\hbar g(k')}{(E_k - E'_k)} \frac{\sin(kr' + \delta_{bg}(k'))}{k'} \right\}. \end{aligned} \quad (2.22)$$

We define the continuum normalized overlap integral

$$\hbar \tilde{g}(k) = \sqrt{\frac{V}{(2\pi)^3}} \hbar g(k) = V_{HF} \langle \tilde{k} | v \rangle, \quad (2.23)$$

which is independent of the volume V . We convert the summations in Eq. 2.22 into integrals by using

$$\sum_{k' \neq k} \rightarrow \mathcal{P} \int d^3k' \frac{V}{(2\pi)^3} = \mathcal{P} \int_0^\infty dk' 4\pi k'^2 \frac{V}{(2\pi)^3}, \quad (2.24)$$

where \mathcal{P} signifies the principal part ($k' \neq k$). Using Eq. 2.23 and Eq. 2.24 in Eq. 2.22, yields

$$\psi_{E_k}(r \rightarrow \infty) = \frac{c_T(k)}{kr\sqrt{V}} \left\{ \sin(kr + \delta_{bg}) - \frac{k}{E_k - E_{g_1} - \Sigma_E(k)} I_1 \right\}, \quad (2.25)$$

where I_1 is

$$I_1 = 4\pi \mathcal{P} \int_0^\infty dk' k'^2 \frac{\hbar^2 \tilde{g}^*(k) \tilde{g}(k')}{(E'_k - E_k)} \frac{\sin[k'r + \delta_{bg}(k')]}{k'}. \quad (2.26)$$

Substituting $E_k = E_T + \hbar^2 k^2/m$ in Eq. 2.26, yields

$$I_1 = 4\pi \mathcal{P} \int_0^\infty dk' k'^2 \frac{\hbar^2 \tilde{g}^*(k) \tilde{g}(k')}{\frac{\hbar^2}{m} (k'^2 - k^2)} \frac{\sin[k'r + \delta_{bg}(k')]}{k'} \quad (2.27)$$

We will now determine I_1 using a complex integral approach and substitute the result back into Eq. 2.25 to derive the dressed triplet scattering state wave function. From the effective range expansion of $\delta_{bg}(k)$ in Eq. 2.21, we know that $\delta_{bg}(k')$ is an odd function of k' , because the right hand side of Eq. 2.21 is even in k . Then, the functions $\tilde{g}(k)$ and $\tilde{g}(k')$ are even functions in k' because Eq. 2.20 is even in k' . Hence, the function $\sin[k'r + \delta_{bg}(k')]/k'$ is also an even function in k' , making the total integrand in Eq. 2.27 even in k' . Therefore, we symmetrize the limits of the integration and rewrite Eq. 2.27,

$$I_1 = 2\pi m \left[\text{Im} \left\{ P \int_{-\infty}^{\infty} \frac{dk' k'}{(k'^2 - k^2)} \tilde{g}^*(k) \tilde{g}(k') e^{ik'r + \delta_{bg}(k')} \right\} \right]. \quad (2.28)$$

The first step in using the complex integral approach is to evaluate the poles of the integrand in Eq. 2.28. The overlap integral $\hbar \tilde{g}^*(k)$ can be evaluated using a simple model for the bound state wavefunction as shown in Ref. [49], where

$$\langle r|v\rangle = \frac{1}{\sqrt{2\pi R}} \frac{e^{-r/R}}{r}. \quad (2.29)$$

The continuum normalized wave function for $r \rightarrow \infty$ is,

$$\langle r|\tilde{k}\rangle = \frac{1}{\sqrt{(2\pi)^3}} \frac{\sin(kr + \delta_{bg})}{kr}. \quad (2.30)$$

From Eq. 2.29 and Eq. 2.30, overlap integral $\langle \tilde{k}|v\rangle$ is given by

$$\begin{aligned}
\langle \tilde{k}|v\rangle &= \int_0^\infty dr 4\pi r^2 \frac{1}{\sqrt{2\pi R}} \frac{e^{-r/R}}{r} \frac{1}{\sqrt{(2\pi)^3}} \frac{\sin(kr + \delta_{bg})}{kr} \\
&= \text{Im} \left[\frac{1}{k\pi\sqrt{R}} \int_0^\infty dr e^{i(kr + \delta_{bg})} e^{-r/R} \right] \\
&= \text{Im} \left[\frac{e^{i\delta_{bg}}}{k\pi\sqrt{R}} \int_0^\infty dr e^{ikr} e^{-r/R} \right] \\
&= \text{Im} \left[\frac{e^{i\delta_{bg}}}{k\pi\sqrt{R}} \left[\frac{R}{1 - ikR} \right] \right] \\
&= \text{Im} \left[\frac{e^{i\delta_{bg}}}{k\pi\sqrt{R}} \left[\frac{R(1 + ikR)}{1 + k^2 R^2} \right] \right] \\
&= \text{Im} \left[\frac{\cos \delta_{bg} + i \sin \delta_{bg}}{k\pi\sqrt{R}} \left[\frac{R(1 + ikR)}{1 + k^2 R^2} \right] \right] \\
&= \left[\frac{kR^2 \cos \delta_{bg} + R \sin \delta_{bg}}{k\pi\sqrt{R}(1 + k^2 R^2)} \right] \tag{2.31}
\end{aligned}$$

For broad Feshbach resonances, where the effective range r_e is small, we can ignore the k^2 terms in the effective range expansion in Eq. 2.21 and write

$$\tan \delta_{bg} = -k a_{bg} \tag{2.32}$$

From Eq. 2.32, it follows

$$\sin \delta_{bg} = -\frac{k a_{bg}}{\sqrt{1 + k^2 a_{bg}^2}} \tag{2.33}$$

$$\cos \delta_{bg} = \frac{1}{\sqrt{1 + k^2 a_{bg}^2}} \tag{2.34}$$

Using Eq. 2.33 and Eq. 2.34 in Eq. 2.31, we obtain

$$\langle \tilde{k}|v\rangle = \left[\frac{kR^2 - kRa_{bg}}{k\pi\sqrt{R}(1 + k^2 R^2) \sqrt{1 + k^2 a_{bg}^2}} \right] \tag{2.35}$$

Further reduction of Eq. 2.35, yields

$$\langle \tilde{k}|v\rangle = \frac{R^{3/2}}{\pi} \frac{1}{\sqrt{1+k^2 a_{bg}^2}} \frac{1-a_{bg}/R}{1+k^2 R^2} \quad (2.36)$$

From Eq. 2.36 and Eq. 2.23, it follows

$$|\hbar\tilde{g}(k)|^2 = \frac{R^3}{\pi^2} \frac{V_{HF}^2}{1+k^2 a_{bg}^2} \frac{(1-a_{bg}/R)^2}{(1+k^2 R^2)^2} \quad (2.37)$$

For $a_{bg} \gg R$, as in the case of broad Feshbach resonance where $a_{bg} = -1405 a_0$, the factor $k^2 a_{bg}^2$ dominates over $k^2 R^2$. Therefore, using $1 - a_{bg}/R \approx -a_{bg}/R$ in the numerator and $1 + k^2 R^2 \approx 1$ in the denominator of Eq. 2.37, we obtain

$$|\hbar\tilde{g}(k)|^2 = \frac{V_{HF}^2 R}{\pi^2} \frac{|a_{bg}|^2}{1+k^2 a_{bg}^2} \quad (2.38)$$

From Eq. 2.38, we take

$$\hbar\tilde{g}(k') = \frac{V_{HF}}{\pi} \left(\frac{a_{bg}^2 R}{1+(k' a_{bg})^2} \right)^{\frac{1}{2}}. \quad (2.39)$$

From Eq. 2.39, we can write

$$\tilde{g}(k') = \frac{\tilde{g}(0)}{\sqrt{1+(k' a_{bg})^2}}, \quad (2.40)$$

where

$$\tilde{g}(0) = \frac{V_{HF} (a_{bg}^2 R)^{\frac{1}{2}}}{\pi}. \quad (2.41)$$

We write $e^{i\delta_{bg}}$ as,

$$e^{i\delta_{bg}} = \frac{1+i \tan \delta_{bg}}{\sqrt{1+\tan^2 \delta_{bg}}}. \quad (2.42)$$

From the effective range expansion in Eq. 2.21, ignoring higher order terms in k , we write

$$\tan \delta_{bg} = -k a_{bg}. \quad (2.43)$$

From Eq. 2.40 - Eq. 2.43, we obtain

$$\tilde{g}(k')e^{i\delta_{bg}} = \tilde{g}(0) \frac{1 - ik a_{bg}}{1 + (k a_{bg})^2} = \frac{\tilde{g}(0)}{1 + ik a_{bg}}. \quad (2.44)$$

From Eq. 2.44, we see that the function $\tilde{g}(k')e^{i\delta_{bg}}$ has no poles on the real axis. For poles on either upper half or lower half of the imaginary axis, $k' = \pm iq$, where $q > 0$, and $e^{ik'r}$ takes the form $e^{-|q|r}$ in the convergent half-plane. Therefore, as $r \rightarrow \infty$, $e^{ik'r} \rightarrow 0$. Hence, as $r \rightarrow \infty$, only poles on real axis $k' = \pm k$ contribute for the integral in Eq. 2.28. Therefore, using Fig. 2.5 to evaluate the principal part,

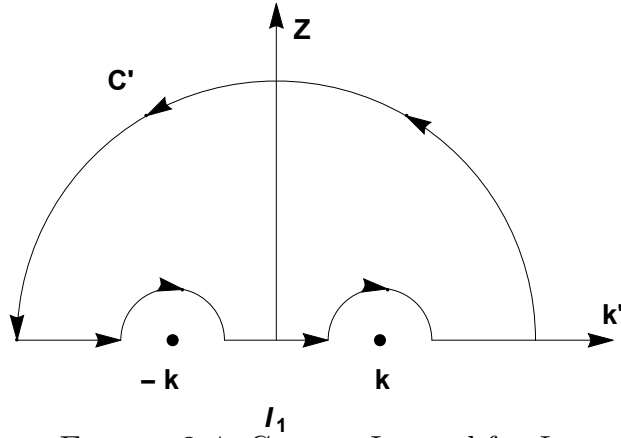


FIGURE 2.4: Contour Integral for I_1

$$I_1 - \pi i [Res(k) + Res(-k)] \rightarrow 0 \quad \text{as} \quad r \rightarrow \infty.$$

Using Cauchy residue theorem, Eq. 2.28 becomes

$$\begin{aligned} I_1 &= 2\pi m |\tilde{g}(k)|^2 \operatorname{Im} \left\{ \pi i \frac{k' - k}{k' - k} \frac{k'}{k' + k} e^{ik'r + \delta_{bg}(k')} \Bigg|_{k' \rightarrow k} \right\} \\ &+ 2\pi m |\tilde{g}(k)|^2 \operatorname{Im} \left\{ \pi i \frac{k' + k}{k' + k} \frac{k'}{k' - k} e^{ik'r + \delta_{bg}(k')} \Bigg|_{k' \rightarrow -k} \right\}. \end{aligned} \quad (2.45)$$

Hence Eq. 2.45 yields

$$I_1 = 2\pi m |\tilde{g}(k)|^2 \pi \cos(kr + \delta_{bg}). \quad (2.46)$$

Substituting Eq. 2.46 in Eq. 2.25, we obtain

$$\psi_{E_k}(r \rightarrow \infty) = \frac{c_T(k)}{kr\sqrt{V}} \left\{ \sin(kr + \delta_{bg}) - \frac{2\pi^2 m k |\tilde{g}(k)|^2}{E_k - E_{g_1} - \Sigma_E(k)} \cos(kr + \delta_{bg}) \right\}. \quad (2.47)$$

Eq. 2.47 is the expression for the wavefunction of the dressed continuum scattering state. We will use normalization of Eq. 2.47 to find the amplitude $c_T(k)$ of the chosen input state, the zero energy scattering length a , and the effective range r_e .

2.3.1 Magnetic Feshbach resonance induced phase shift $\tilde{\Delta}$

As $r \rightarrow \infty$, the scattering state wavefunction, which is purely triplet in nature, will accumulate a phase shift $\tilde{\Delta}$ induced by the magnetic Feshbach resonance. In this section, we will evaluate the phase shift $\tilde{\Delta}$ due to the Feshbach resonance. Furthermore, we will also evaluate the probability amplitude $c_T(k)$ of the triplet scattering state so that the scattering state wavefunction in Eq. 2.47 is normalized .

From Eq. 2.20, the asymptotic form of the scattering state wavefunction in the presence of a magnetic Feshbach resonance, must take the form

$$\psi_{E_k}(r \rightarrow \infty) = \frac{1}{\sqrt{V}} \frac{1}{kr} \sin(kr + \delta_{bg} + \tilde{\Delta}). \quad (2.48)$$

Expanding Eq. 2.48,

$$\psi_{E_k}(r \rightarrow \infty) = \frac{1}{\sqrt{V}} \frac{1}{kr} \left\{ \cos \tilde{\Delta} \sin(kr + \delta_{bg}) + \sin \tilde{\Delta} \cos(kr + \delta_{bg}) \right\}. \quad (2.49)$$

Comparing Eq. 2.49 with Eq. 2.47, we have

$$c_T(k) = \cos \tilde{\Delta} \quad (2.50)$$

$$-c_T(k) \left(\frac{2\pi^2 m k |\tilde{g}(k)|^2}{E_k - E_{g_1} - \Sigma_E(k)} \right) = \sin \tilde{\Delta} \quad (2.51)$$

From Eq. 2.50, we have

$$|c_T(k)|^2 = \cos^2 \tilde{\Delta} = \frac{1}{1 + \tan^2 \tilde{\Delta}}. \quad (2.52)$$

Dividing Eq. 2.51 by Eq. 2.50,

$$\tan \tilde{\Delta} = -\frac{2\pi^2 m k |\tilde{g}(k)|^2}{E_k - E_{g_1} - \Sigma_E(k)} = \frac{1}{\cot \tilde{\Delta}}. \quad (2.53)$$

Eq. 2.53 is the expression for phase shift $\tilde{\Delta}$ due to the magnetic Feshbach resonance.

Using Eq. 2.53 in Eq. 2.52, we obtain

$$|c_T(k)|^2 = \frac{[E_k - E_{g_1} - \Sigma_E(k)]^2}{[E_k - E_{g_1} - \Sigma_E(k)]^2 + [2\pi^2 m k |\tilde{g}(k)|^2]^2}. \quad (2.54)$$

2.3.2 Zero energy scattering length a

In this section, we will derive the expression for zero energy scattering length near a magnetic Feshbach resonance using the expression for the phase shift $\tilde{\Delta}$ derived in the previous section. From Eq. 2.53, we have

$$k \cot \tilde{\Delta} = -\frac{E_k - E_{g_1} - \Sigma_E(k)}{2\pi^2 m |\tilde{g}(k)|^2}. \quad (2.55)$$

Using the effective range expansion in Eq. 2.21 for the phase shift induced by the magnetic Feshbach resonance $\tilde{\Delta}$, we obtain

$$k \cot \tilde{\Delta} = \frac{-1}{\tilde{a}} + \frac{k^2}{2} \tilde{r}_e, \quad (2.56)$$

where \tilde{a} is the zero scattering length due to the magnetic Feshbach resonance and \tilde{r}_e is the corresponding effective range. From Eq. 2.48, the total phase shift Δ is given by

$$\Delta = \tilde{\Delta} + \delta_{bg}. \quad (2.57)$$

Using Eq. 2.57, we can write the total phase shift Δ as

$$k \cot \Delta = \frac{(k \cot \tilde{\Delta})(k \cot \delta_{bg}) - k^2}{k \cot \tilde{\Delta} + k \cot \delta_{bg}}. \quad (2.58)$$

Substituting $k \cot \tilde{\Delta}$ from Eq. 2.55 and $k \cot \delta_{bg}$ from Eq. 2.21 in Eq. 2.58, yields for $k \rightarrow 0$

$$a = \tilde{a} + a_{bg}. \quad (2.59)$$

From Eq. 2.10, we know $E_k = E_T$ for the case $k = 0$. Comparing Eq. 2.55 and Eq. 2.56 and substituting $E_k = E_T$ for $k = 0$, we obtain the zero energy scattering length due to the magnetic Feshbach resonance

$$\tilde{a} = \frac{2\pi^2 m |\tilde{g}(0)|^2}{E_T - E_{g_1} - \Sigma_E(0)}. \quad (2.60)$$

Since the energy of the triplet state is

$$E_T = -\frac{a_{HF}}{2} - 2\mu_B B, \quad (2.61)$$

we know that at resonance when $B = B_{res}$, the energy of the triplet state can be written as

$$(E_T)_{res} = -\frac{a_{HF}}{2} - 2\mu_B B_{res}. \quad (2.62)$$

Further, we know that the scattering length $\tilde{a} \rightarrow \infty$ at resonance, implying the denominator in Eq. 2.60 goes to zero. Hence, at resonance

$$(E_T)_{res} - E_{g_1} - \Sigma_E(0) = 0. \quad (2.63)$$

Substituting Eq. 2.62 in Eq. 2.63, yields

$$(E_T)_{res} = E_{g_1} + \Sigma_E(0) = -\frac{a_{HF}}{2} - 2\mu_B B_{res}. \quad (2.64)$$

From Eq. 2.61 and Eq. 2.64, we have

$$E_T - E_{g_1} - \Sigma_E(0) = -2\mu_B(B - B_{res}). \quad (2.65)$$

We define the width of the resonance ΔB as

$$2\mu_B|a_{bg}|\Delta B = 2\pi^2 m |\tilde{g}(0)|^2. \quad (2.66)$$

Using Eq. 2.65 and Eq. 2.66 in Eq. 2.60, the resonant part of the scattering length is then

$$\tilde{a} = -|a_{bg}| \frac{\Delta B}{(B - B_{res})}. \quad (2.67)$$

Using Eq. 2.67 in Eq. 2.59, we obtain the zero-energy scattering length

$$a = a_{bg} - |a_{bg}| \frac{\Delta B}{B - B_{res}}. \quad (2.68)$$

Eq. 2.68 is the standard expression for zero-energy scattering length for a magnetic Feshbach resonance [1] that was introduced at the start of the chapter. The resonance position B_{res} , width ΔB , background scattering length a_{bg} , and the hyperfine coupling V_{HF} for various resonances in ${}^6\text{Li}$ for s-wave collisions are given in Table. 2.1.

Table 2.1: Magnetic Feshbach resonances in ${}^6\text{Li}$ for s-wave collisions [49, 57, 58, 59]

Mixture	$B_{res}(G)$	ΔB	$a_{bg}(a_0)$	$V_{HF}(MHz)$
1-2(B)	834	300	-1405	-131.6
1-2(N)	543	0.1	+62	-5.9
1-3	690	122	-1727	76.0
2-3	811	222	-1490	107.5

2.3.3 Effective range r_e

In this section, we derive the expression for the effective range r_e . We use the effective range expansion in Eq. 2.21 to write the phase shift $\tilde{\Delta}$ induced by the Feshbach resonance in terms of the resonant scattering length \tilde{a} and the effective range \tilde{r}_e ,

$$k \cot \tilde{\Delta} = \frac{-1}{\tilde{a}} + \frac{k^2}{2} \tilde{r}_e. \quad (2.69)$$

For $k \rightarrow 0$, expanding $k \cot \tilde{\Delta}$ in Eq. 2.56 to the order k^2 ,

$$k \cot \tilde{\Delta} = -\frac{1}{\tilde{a}} + \frac{k^2}{2} \tilde{r}_e = -\frac{E_T - E_{g1} - \Sigma_E(0)}{2\pi^2 m |\tilde{g}(0)|^2} - \frac{\frac{\hbar^2 k^2}{m}}{2\pi^2 m |\tilde{g}(0)|^2}. \quad (2.70)$$

In the above equation, only the kinetic energy term in k^2 survives and other k^2 terms in the expansion cancel [49]. Comparing k^2 terms in Eq. 2.70 and Eq. 2.69 yields

$$\tilde{r}_e = -\frac{\hbar^2}{\pi^2 m^2 |\tilde{g}(0)|^2}. \quad (2.71)$$

Substituting Eq. 2.66 in Eq. 2.71, we obtain

$$\tilde{r}_e = -\frac{\hbar^2}{m\mu_B |a_{bg}| \Delta B}. \quad (2.72)$$

From Eq. 2.72, we can see that for large ΔB , such as the broad resonance in ${}^6\text{Li}$, the effective range is small and for small ΔB , such as the narrow resonance in ${}^6\text{Li}$, the effective range is large. For the broad Feshbach resonance at 832.2 G and the narrow Feshbach resonance at 543.2 G in ${}^6\text{Li}$, $r_e \simeq -1 a_0$ and $-7 \times 10^4 a_0$, respectively.

2.4 Dressed bound state $|E\rangle$

In the previous section, we derived the wavefunction for the dressed continuum scattering state $|E_k\rangle$ and used it to derive the scattering length a and the effective range

r_e . In this section, we will study the dressed bound state $|E\rangle$. The dressed bound state can be written as

$$|E\rangle = C_s |s\rangle |v\rangle + \sum_{all\ k} C_T(k) |T\rangle |k\rangle, \quad (2.73)$$

where C_s is the probability amplitude of $|E\rangle$ to be in the bare molecular bound state $|g_1\rangle$ and $C_T(k)$ is the probability amplitude of $|E\rangle$ to be in the bare continuum $|T, k\rangle$.

Note that capital letters, C_s and $C_T(k)$, are used to denote the probability amplitudes in $|E\rangle$ and small letters, c_s and $c_T(k)$, are used to denote the probability amplitudes in $|E_k\rangle$, since $C_s \neq c_s$ and $C_T(k) \neq c_T(k)$.

We recall from previous section, that the hamiltonian can be written as

$$H = E_{g_1} |s\rangle\langle s| + \left(E_T + \frac{\hbar^2 k^2}{m} \right) |T\rangle\langle T| + V_{HF} (|s\rangle\langle T| + |T\rangle\langle s|), \quad (2.74)$$

Using the Schrödinger equation, we have

$$H|\psi_E\rangle = E|\psi_E\rangle. \quad (2.75)$$

where E is the energy of the dressed bound state. We solve for the probability amplitudes in $|E\rangle$ by taking the projections of basis states on Eq. 2.75. For $|s\rangle|v\rangle$, using Eq. 2.74 and Eq. 2.73, this gives

$$(E - E_{g_1})C_s = \sum_{all\ k} V_{HF} \langle v|k\rangle C_T(k). \quad (2.76)$$

Substituting Eq. 2.23 in Eq. 2.76

$$(E - E_{g_1})C_s = \sum_{all\ k} V_{HF} \langle v|k\rangle C_T(k) = \sum_{all\ k} \hbar g^*(k) C_T(k). \quad (2.77)$$

where from Eq. 2.23, we know

$$\hbar g(k) \equiv V_{HF} \langle k|v\rangle. \quad (2.78)$$

We solve for the probability amplitude $C_T(k)$ by taking the projections of $|k'\rangle$ on Eq. 2.75. Using Eq. 2.74 and Eq. 2.73, we get

$$E C_T(k') = V_{HF} C_s \langle k'|v\rangle + \left(E_T + \frac{\hbar^2 k'^2}{m} \right) C_T(k'). \quad (2.79)$$

Substituting Eq. 2.78 in Eq. 2.79, yields

$$\left(E - E_T - \frac{\hbar^2 k^2}{m} \right) C_T(k) = \hbar g(k) C_s. \quad (2.80)$$

Substituting Eq. 2.80 in Eq. 2.77, we get

$$(E - E_{g_1}) C_s = \sum_{all\ k} \frac{|\hbar g(k)|^2}{\left(E - E_T - \frac{\hbar^2 k^2}{m} \right)} C_s. \quad (2.81)$$

We define the energy shift of the bound state $\Sigma(E)$

$$\Sigma(E) \equiv E - E_{g_1} = \sum_{all\ k} \frac{|\hbar g(k)|^2}{\left(E - E_T - \frac{\hbar^2 k^2}{m} \right)}. \quad (2.82)$$

We convert the summation into integral in Eq. 2.82,

$$\Sigma(E) = \int d^3 \vec{k} \frac{|\hbar \tilde{g}(k)|^2}{\left(E - E_T - \frac{\hbar^2 k^2}{m} \right)} = \int dk\ 4\pi k^2 \frac{|\hbar \tilde{g}(k)|^2}{\left(E - E_T - \frac{\hbar^2 k^2}{m} \right)}, \quad (2.83)$$

where the continuum normalized overlap integral $\tilde{g}(k)$ is defined by

$$\hbar \tilde{g}(k) = \sqrt{\frac{V}{(2\pi)^3}} \hbar g(k) = V_{HF} \langle \tilde{k}|v\rangle. \quad (2.84)$$

Using the normalization for the state $|E\rangle$ in Eq. 2.73, we have

$$\langle E|E\rangle = 1 = |C_s|^2 + \sum_k |C_T(k)|^2. \quad (2.85)$$

Substituting Eq. 2.80 in Eq. 2.85

$$|C_s|^2 \left[1 + \sum_k \frac{|\hbar\tilde{g}(k)|^2}{(E - E_T - \frac{\hbar^2 k^2}{m})^2} \right] = 1. \quad (2.86)$$

Converting the summation into integral using box normalization in Eq. 2.86, yields

$$|C_s|^2 \left[1 + \int d^3\vec{k} \frac{|\hbar\tilde{g}(k)|^2}{(E - E_T - \frac{\hbar^2 k^2}{m})^2} \right] = 1. \quad (2.87)$$

Using Eq. 2.83, we see that

$$\frac{\partial\Sigma(E)}{\partial E} = - \int d^3\vec{k} \frac{|\hbar\tilde{g}(k)|^2}{(E - E_T - \frac{\hbar^2 k^2}{m})^2}. \quad (2.88)$$

Substituting Eq. 2.88 in Eq. 2.87,

$$|C_s|^2 \left[1 - \frac{\partial\Sigma(E)}{\partial E} \right] = 1. \quad (2.89)$$

From Eq. 2.89, we obtain

$$|C_s|^2 = \left[1 - \frac{\partial\Sigma(E)}{\partial E} \right]^{-1} \equiv Z, \quad (2.90)$$

where Z is the probability of $|g_1\rangle$ to be in the dressed bound state $|E\rangle$.

The dressed bound state in Eq. 2.73 can be written as

$$|\psi_E\rangle = C_s \left[|s\rangle |v\rangle + \sum_{all\ k} \frac{C_T(k)}{C_s} |T\rangle |k\rangle \right]. \quad (2.91)$$

Substituting $C_T(k)$ from Eq. 2.80 in Eq. 2.91, yields

$$|\psi_E\rangle = C_s \left[|s\rangle |v\rangle + \sum_{all\ k} \frac{\hbar g(k)}{(E - E_T - \frac{\hbar^2 k^2}{m})} |T\rangle |k\rangle \right] \quad (2.92)$$

where C_s is given in Eq. 2.90. Eq. 2.92 gives the wavefunction of the dressed bound state $|E\rangle$.

2.5 Properties of dressed states $|E\rangle$ and $|E_k\rangle$

In this section, we will use the wavefunction of the dressed bound state $|E\rangle$ and dressed continuum state $|E_k\rangle$ derived in the previous sections to study the properties of dressed states, namely, the orthogonality of the states $|E\rangle$ and $|E_k\rangle$, the probability of the singlet molecular state $|g_1\rangle$ in the dressed bound state $|E\rangle$, the total probability of the singlet molecular state $|g_1\rangle$ to be in the dressed continuum states, and the molecular binding energy associated with the dressed bound state $|E\rangle$.

2.5.1 Orthogonality of $|E\rangle$ and $|E_k\rangle$

In this section, we will prove that the dressed states $|E\rangle$ and $|E_k\rangle$ form an orthogonal set. From Eq. 2.73, we can write the dressed bound state as

$$|E\rangle = C_s |s, v\rangle + \sum_{k'} C_T(k') |T, k'\rangle, \quad (2.93)$$

where the probability amplitude $C_T(k')$ can be written in terms of C_s using Eq. 2.80 as

$$C_T(k') = \frac{\hbar g(k')}{E - E_T - \frac{\hbar^2 k'^2}{m}} C_s. \quad (2.94)$$

Using Eq. 2.93 in Eq. 2.94 and using the definition of Z in Eq. 2.90, we rewrite Eq. 2.94 as

$$|E\rangle = \sqrt{Z} \left[|s, v\rangle + \sum_{k'} \frac{\hbar g(k')}{E - E_T - \frac{\hbar^2 k'^2}{m}} |T, k'\rangle \right]. \quad (2.95)$$

Rewriting the second term with the summation over all k' in Eq. 2.95 separated into a k term and a $k' \neq k$ term, we get

$$|E\rangle = \sqrt{Z} \left[|s, v\rangle + \frac{\hbar g(k)}{E - E_T - \frac{\hbar^2 k^2}{m}} |T, k\rangle + \sum_{k' \neq k} \frac{\hbar g(k')}{E - E_T - \frac{\hbar^2 k'^2}{m}} |T, k'\rangle \right]. \quad (2.96)$$

Similarly, we use Eq. 2.7 to write the dressed continuum state

$$|E_k\rangle = c_1(k) |s, v\rangle + c_T(k) |T, k\rangle + \sum_{k' \neq k} c_T(k') |T, k'\rangle. \quad (2.97)$$

Using Eq. 2.15 and Eq. 2.17, we write the probability amplitudes

$$c_T(k' \neq k) = \frac{\hbar g(k')}{E_k - E_T - \frac{\hbar^2 k'^2}{m}} c_1(k). \quad (2.98)$$

$$c_1(k) = \frac{\hbar g^*(k)}{E_k - E_{g_1} - \Sigma_E(k)} c_T(k). \quad (2.99)$$

Substituting Eq. 2.98 and Eq. 2.99 in Eq. 2.97, yields

$$|E_k\rangle = c_1 \left[|s, v\rangle + \frac{E_k - E_{g_1} - \Sigma_E(k)}{\hbar g^*(k)} |T, k\rangle + \sum_{k' \neq k} \frac{\hbar g(k')}{E_k - E_T - \frac{\hbar^2 k'^2}{m}} |T, k'\rangle \right] \quad (2.100)$$

Using Eq. 2.96 and Eq. 2.100, we obtain

$$\begin{aligned} \langle E|E_k\rangle &= c_1 \sqrt{Z} \left[1 + \frac{\hbar g^*(k)}{E - E_T - \frac{\hbar^2 k^2}{m}} \frac{E_k - E_{g_1} - \Sigma_E(k)}{\hbar g^*(k)} \right. \\ &\quad \left. + \sum_{k' \neq k} \frac{\hbar g^*(k')}{E - E_T - \frac{\hbar^2 k'^2}{m}} \frac{\hbar g(k')}{E_k - E_T - \frac{\hbar^2 k'^2}{m}} \right]. \end{aligned} \quad (2.101)$$

Substituting $E_k = E_T + \hbar^2 k^2/m$ in Eq. 2.101, we have

$$\langle E|E_k\rangle = c_1 \sqrt{Z} \left[1 + \frac{E_k - E_{g_1} - \Sigma_E(k)}{E - E_k} + \sum_{k' \neq k} \frac{|\hbar g(k')|^2}{(E - E'_k)(E_k - E'_k)} \right] \quad (2.102)$$

The third term with summation over $k' \neq k$ in Eq. 2.102 can be written as

$$\sum_{k' \neq k} \frac{|\hbar g(k')|^2}{(E - E'_k)(E_k - E'_k)} = \frac{1}{E - E_k} \left[\sum_{k' \neq k} \frac{|\hbar g(k')|^2}{(E_k - E'_k)} - \sum_{k' \neq k} \frac{|\hbar g(k')|^2}{(E - E'_k)} \right]. \quad (2.103)$$

Rewriting the second term in Eq. 2.103,

$$\begin{aligned} \sum_{k' \neq k} \frac{|\hbar g(k')|^2}{(E - E'_k)(E_k - E'_k)} &= \frac{1}{E - E_k} \left[\sum_{k' \neq k} \frac{|\hbar g(k')|^2}{(E_k - E'_k)} \right. \\ &\quad \left. - \sum_{\text{all } k'} \frac{|\hbar g(k')|^2}{(E - E'_k)} + \frac{|\hbar g(k)|^2}{(E - E_k)} \right]. \end{aligned} \quad (2.104)$$

From Eq. 2.16 and Eq. 2.82 we recall that the energy shift of the dressed continuum and the energy shift of the dressed bound state is defined as

$$\Sigma_E(k) \equiv \sum_{k' \neq k} \frac{|\hbar g(k')|^2}{E_k - E'_k}. \quad (2.105)$$

$$\Sigma(E) \equiv \sum_{\text{all } k} \frac{|\hbar g(k)|^2}{(E - E_k)}. \quad (2.106)$$

Substituting Eq. 2.105 and Eq. 2.106 in Eq. 2.104,

$$\sum_{k' \neq k} \frac{|\hbar g(k')|^2}{(E - E'_k)(E_k - E'_k)} = \frac{1}{E - E_k} \left[\Sigma_E(k) - \Sigma(E) + \frac{|\hbar g(k)|^2}{(E - E_k)} \right]. \quad (2.107)$$

Substituting Eq. 2.107 in Eq. 2.102, yields

$$\begin{aligned} \langle E|E_k \rangle &= c_1 \sqrt{Z} \left[1 + \frac{E_k - E_{g_1} - \Sigma_E(k)}{E - E_k} + \frac{1}{E - E_k} [\Sigma_E(k) - \Sigma(E)] \right. \\ &\quad \left. + \frac{|\hbar g(k)|^2}{(E - E_k)^2} \right]. \end{aligned} \quad (2.108)$$

Simplifying Eq. 2.108,

$$\langle E|E_k \rangle = \sqrt{Z} c_1 \left[1 + \frac{E_k - E_{g_1} - \Sigma(E)}{E - E_k} + \frac{|\hbar g(k)|^2}{(E - E_k)^2} \right]. \quad (2.109)$$

Using $\Sigma(E) = E - E_{g_1}$ (Eq. 2.82) in Eq. 2.109,

$$\langle E|E_k \rangle = \sqrt{Z} c_1 \left[1 + \frac{E_k - E}{E - E_k} + \frac{|\hbar g(k)|^2}{(E - E_k)^2} \right]. \quad (2.110)$$

The first two terms cancel, so that

$$\langle E|E_k\rangle = \sqrt{Z} c_1 \frac{|\hbar g(k)|^2}{(E - E_k)^2}. \quad (2.111)$$

From Eq. 2.15 and Eq. 2.54, we can write the probability

$$|c_1|^2 = \frac{|\hbar g(k)|^2}{[E_k - E_{g_1} - \Sigma_E(k)]^2 + [2\pi^2 m k |\tilde{g}(k)|^2]}. \quad (2.112)$$

Using $\Sigma(E) = E - E_{g_1}$ (Eq. 2.82) in Eq. 2.112,

$$|c_1|^2 = \frac{|\hbar g(k)|^2}{[E_k - E + \Sigma(E) - \Sigma_E(k)]^2 + [2\pi^2 m k |\tilde{g}(k)|^2]}. \quad (2.113)$$

Using Eq. 2.105 and Eq. 2.106, we get

$$|c_1|^2 = \frac{|\hbar g(k)|^2}{\left[(E_k - E) + \frac{|\hbar g(k)|^2}{(E - E_k)^2} \right]^2 + [2\pi^2 m k |\tilde{g}(k)|^2]}, \quad (2.114)$$

where the factor $2\pi^2 m k |\tilde{g}(k)|^2$ is finite as the volume $V \rightarrow 0$.

From Eq. 2.86 and Eq. 2.90, we write the singlet molecular fraction Z as

$$Z = \frac{1}{1 + \sum_{k'} \frac{|\hbar g(k')|^2}{(E - E_{k'})^2}}. \quad (2.115)$$

We further recall from Eq. 2.23, that the continuum normalized overlap integral $\tilde{g}(k)$ is related to $g(k)$ by the relation

$$|\hbar g(k)|^2 = \frac{(2\pi)^3}{V} |\hbar \tilde{g}(k)|^2. \quad (2.116)$$

In Eq. 2.114, the factor $2\pi^2 m k |\tilde{g}(k)|^2$ is finite. For the case, $E \neq E_k$ and Z finite, $|\hbar g(k)|^2 \rightarrow 0$ as $V \rightarrow \infty$, Hence

$$\langle E|E_k\rangle \rightarrow 0 \quad \text{for} \quad E \neq E_k. \quad (2.117)$$

For the case $E \rightarrow E_k$,

$$\frac{1}{(E - E_k)^2} \rightarrow 0, \quad (2.118)$$

keeping the dominant term we write $|c_1^2|$ and the singlet fraction Z using Eq. 2.114 and Eq. 2.115 as

$$|c_1|^2 = \frac{|\hbar g(k)|^2}{\left[\frac{|\hbar g(k)|^2}{(E - E_k)}\right]^2}, \quad (2.119)$$

and

$$Z = \frac{1}{\frac{|\hbar g(k)|^2}{(E - E_k)^2}}. \quad (2.120)$$

Hence, for the case $E \rightarrow E_k$, using Eq. 2.119 and Eq. 2.120 in Eq. 2.111, we get

$$\lim_{E \rightarrow E_k} \langle E | E_k \rangle = \frac{1}{\frac{|\hbar g(k)|}{|E - E_k|}} \frac{|\hbar g(k)|}{|E - E_k|} \frac{|\hbar g(k)|^2}{(E - E_k)^2} = 1. \quad (2.121)$$

Using Eq. 2.117 and Eq. 2.121, we obtain

$$\langle E | E_k \rangle = \delta_{k,k'} \quad (2.122)$$

2.5.2 $Z(B)$ - Singlet character in dressed bound state $|E\rangle$

In this section, we will evaluate the probability $Z(B)$ of finding the singlet molecular state $|g_1\rangle$ in the dressed continuum state $|E\rangle$. We can see from Eq. 2.73 and Eq. 2.90 that the probability Z of the singlet state $|g_1\rangle$ in the dressed bound state $|E\rangle$ is given by

$$Z = |\langle g_1 | E \rangle|^2 = |C_s|^2 = \left[1 - \frac{\partial \Sigma(E)}{\partial E}\right]^{-1}. \quad (2.123)$$

Z is the amount of singlet character in the dressed molecules that populates the dressed bound state $|E\rangle$ on the BEC side of the resonance.

We recall from Eq. 2.83 that the bound state shift $\Sigma(E)$ is given by

$$\Sigma(E) = \int_0^\infty dk 4\pi k^2 \frac{|\hbar\tilde{g}(k)|^2}{(E - E_T - \frac{\hbar^2 k^2}{m})}. \quad (2.124)$$

From Eq. 2.30, we know that $\tilde{g}(k)$ is an even function in k . Hence, the integrand in Eq. 2.124 is an even function in k . Therefore, symmetrizing the integration limits,

$$\Sigma(E) = \int_{-\infty}^\infty dk 2\pi k^2 \frac{|\hbar\tilde{g}(k)|^2}{(E - E_T - \frac{\hbar^2 k^2}{m})}. \quad (2.125)$$

From Eq. 2.38, we know

$$|\hbar\tilde{g}(k)|^2 = \frac{V_{HF}^2}{\pi^2} \frac{a_{bg}^2 R}{1 + (ka_{bg})^2}. \quad (2.126)$$

Using Eq. 2.126 in Eq. 2.125, yields

$$\Sigma(E) = 2\pi \int_{-\infty}^\infty \frac{dk k^2}{(E - E_T - \frac{\hbar^2 k^2}{m})} \frac{a_{bg}^2 R}{1 + (ka_{bg})^2} \frac{V_{HF}^2}{\pi^2}. \quad (2.127)$$

Substituting $x = k|a_{bg}|$ and defining $E_{bg} = \hbar^2/ma_{bg}^2$ in Eq. 2.127, we get

$$\Sigma(E) = \frac{2}{\pi} |V_{HF}|^2 \frac{R}{|a_{bg}|} \int_{-\infty}^\infty \frac{dx x^2}{1 + x^2} \frac{1}{E - E_T - E_{bg}x^2}. \quad (2.128)$$

Simplification of Eq. 2.128, yields

$$\Sigma(E) = -\frac{2}{\pi} \frac{|V_{HF}|^2}{E_{bg}} \frac{R}{|a_{bg}|} \int_{-\infty}^\infty \frac{dx x^2}{1 + x^2} \frac{1}{\frac{E_T - E}{E_{bg}} + x^2}. \quad (2.129)$$

Now we will evaluate the integral in Eq. 2.129. We define $q^2 \equiv (E_T - E)/E_{bg}$ in Eq. 2.129. Evaluating the integral for $q^2 > 0$ i.e., $E < E_T$ for a bound state, we have

$$\int_{-\infty}^\infty \frac{dx x^2}{1 + x^2} \frac{1}{q^2 + x^2} = \frac{\pi}{1 + q}. \quad (2.130)$$

Substituting Eq. 2.130 in Eq. 2.129, yields

$$\Sigma(E) = -\frac{2}{\pi} \frac{|V_{HF}|^2}{E_{bg}} \frac{R}{|a_{bg}|} \frac{\pi}{1 + \sqrt{\frac{E_T - E}{E_{bg}}}}. \quad (2.131)$$

so that

$$\Sigma(E) = -\frac{2R}{|a_{bg}|} \frac{|V_{HF}|^2}{E_{bg}} \frac{1}{1 + \sqrt{\frac{E_T - E}{E_{bg}}}}. \quad (2.132)$$

From Eq. 2.66, we know that the width ΔB is written as

$$2\mu_B |a_{bg}| \Delta B = 2\pi^2 m |\tilde{g}(0)|^2. \quad (2.133)$$

Hence

$$2\mu_B \Delta B = \frac{2\pi^2 m |\tilde{g}(0)|^2}{|a_{bg}|}. \quad (2.134)$$

From Eq. 2.126, we write

$$|\hbar \tilde{g}(0)|^2 = \frac{V_{HF}^2}{\pi^2} a_{bg}^2 R. \quad (2.135)$$

Using Eq. 2.135 in Eq. 2.134 and using $E_{bg} = \hbar^2 / m a_{bg}^2$, yields

$$2\mu_B \Delta B = \frac{2\pi^2 m |\tilde{g}(0)|^2}{|a_{bg}|} = \frac{2R}{|a_{bg}|} \frac{|V_{HF}|^2}{E_{bg}}. \quad (2.136)$$

Substituting Eq. 2.136 in Eq. 2.132, we obtain a compact expression for the energy shift of the dressed bound state

$$\Sigma(E) = \frac{-2\mu_B \Delta B}{1 + \sqrt{\frac{E_T - E}{E_{bg}}}}. \quad (2.137)$$

From Eq. 2.123, we know that the singlet molecular fraction is given by

$$Z = |\langle g_1 | E \rangle|^2 = |C_s|^2 = \left[1 - \frac{\partial \Sigma(E)}{\partial E} \right]^{-1}. \quad (2.138)$$

From Eq. 2.137, we get

$$\frac{\partial \Sigma(E)}{\partial E} = -\frac{2\mu_B \Delta B}{(1 + \sqrt{\frac{E_T - E}{E_{bg}}})^2} \sqrt{\frac{E_T - E}{E_{bg}}} \frac{1}{2(E_T - E)}. \quad (2.139)$$

Substituting Eq. 2.139 in Eq. 2.138, we obtain

$$Z = \frac{1}{1 + \frac{\mu_B \Delta B}{E_{bg}} \sqrt{\frac{E_{bg}}{E_T - E}} \frac{1}{(1 + \sqrt{\frac{E_T - E}{E_{bg}}})^2}}. \quad (2.140)$$

Eq. 2.140 gives the probability of singlet molecular ground state $|g_1\rangle$ to be in the dressed bound state $|E\rangle$.

2.5.3 $C(B)$ - Total probability of $|g_1\rangle$ to be in the dressed continuum

In this section, we will evaluate the total probability $C(B)$ of the singlet molecular state $|g_1\rangle$ to be in the dressed continuum. From the completeness relationship of singlet state $|g_1\rangle$, we can write

$$|\langle E|g_1\rangle|^2 + \sum_k |\langle E_k|g_1\rangle|^2 = 1. \quad (2.141)$$

Using Eq. 2.123, we rewrite Eq. 2.141 as,

$$Z(B) + C(B) = 1, \quad (2.142)$$

where

$$C(B) = \sum_k |\langle E_k|g_1\rangle|^2. \quad (2.143)$$

Here, both Z and C is written with the explicit magnetic field dependency as $Z(B)$ and $C(B)$, respectively. Now, we proceed to evaluate $C(B)$. We convert the summation into integral and including the box normalization factor V , we have

$$C(B) = \frac{V}{(2\pi)^3} \int_0^\infty 4\pi k^2 dk |\langle E_k|g_1\rangle|^2 = \int_0^\infty 4\pi k^2 dk |\langle g_1|\tilde{E}_k\rangle|^2, \quad (2.144)$$

where \tilde{E}_k is the box normalized dressed continuum state and $\langle E_k | g_1 \rangle = \langle g_1 | E_k \rangle^*$.

We know from Eq. 2.6, the overlap $\langle g_1 | E_k \rangle$ is given by the probability amplitude c_1 . From Eq. 2.6 and Eq. 2.15, we get

$$c_1 = \frac{\hbar g^*(k)}{E_k - E_{g_1} - \Sigma_E(k)} c_T(k) = \langle g_1 | E_k \rangle. \quad (2.145)$$

From Eq. 2.145, it follows

$$|\langle g_1 | E_k \rangle|^2 = \frac{|\hbar g(k)|^2}{[E_k - E_{g_1} - \Sigma_E(k)]^2} |c_T(k)|^2. \quad (2.146)$$

From Eq. 2.23, we get the box normalized overlap integral

$$|\tilde{g}(k)|^2 \equiv \frac{V}{(2\pi)^3} |g(k)|^2. \quad (2.147)$$

Using Eq. 2.147 in Eq. 2.146, we can write

$$|\langle g_1 | \tilde{E}_k \rangle|^2 \equiv \frac{V}{(2\pi)^3} |\langle g_1 | E_k \rangle|^2 = \frac{|\hbar \tilde{g}(k)|^2 |c_T(k)|^2}{[E_k - E_{g_1} - \Sigma_E(k)]^2}. \quad (2.148)$$

Substituting the value of $c_T(k)$ from Eq. 2.54 in Eq. 2.148,

$$|\langle g_1 | \tilde{E}_k \rangle|^2 = \frac{|\hbar \tilde{g}(k)|^2}{[E_k - E_{g_1} - \Sigma_E(k)]^2 + [2\pi^2 m k |\tilde{g}(k)|^2]^2}. \quad (2.149)$$

Substituting Eq. 2.149 in Eq. 2.144, yields

$$C(B) = \int_0^\infty 4\pi k^2 dk \frac{|\hbar \tilde{g}(k)|^2}{[E_k - E_{g_1} - \Sigma_E(k)]^2 + [2\pi^2 m k |\tilde{g}(k)|^2]^2}. \quad (2.150)$$

Next we proceed to write $C(B)$ in Eq. 2.150 in terms of the width ΔB and the resonance position B_{res} of the Feshbach resonance. We define

$$x \equiv k |a_{bg}| \quad (2.151)$$

$$E_{bg} \equiv \frac{\hbar^2}{ma_{bg}^2} \quad (2.152)$$

Then the dressed continuum energy can be written as

$$E_k = E_T + \frac{\hbar^2 k^2}{m} = E_T + E_{bg} x^2, \quad (2.153)$$

We first proceed to evaluate the numerator $|\hbar \tilde{g}(k)|^2$ in Eq. 2.150. Substituting $x \equiv k|a_{bg}|$ in Eq. 2.40, we get

$$|\tilde{g}(k)|^2 = \frac{|\tilde{g}(0)|^2}{1 + x^2}. \quad (2.154)$$

From Eq. 2.66, we know

$$2\mu_B |a_{bg}| \Delta B = 2\pi^2 m |\tilde{g}(0)|^2, \quad (2.155)$$

Substituting Eq. 2.155 in Eq. 2.154, we get the numerator in Eq. 2.150

$$|\hbar \tilde{g}(k)|^2 = \frac{\hbar^2 \mu_B \Delta B |a_{bg}|}{\pi^2 m (1 + x^2)}. \quad (2.156)$$

Next we proceed to find the denominator in Eq. 2.150. We recall from Eq. 2.65,

$$E_T - E_{g_1} - \Sigma_E(0) = -2\mu_B (B - B_{res}). \quad (2.157)$$

We define Δ_0 as

$$\Delta_0 \equiv \frac{2\mu_B (B - B_\infty)}{\hbar}. \quad (2.158)$$

Substituting Eq. 2.158 in Eq. 2.157, yields

$$E_T - E_{g_1} - \Sigma_E(0) = -\hbar \Delta_0. \quad (2.159)$$

Using Eq. 2.153, we can write

$$E_k - E_{g_1} - \Sigma_E(k) = E_T - E_{g_1} + E_{bg} x^2 - \Sigma_E(k). \quad (2.160)$$

Using Eq. 2.159 in Eq. 2.160 , we can write

$$E_k - E_{g_1} - \Sigma_E(k) = -\hbar \Delta_0 + \Sigma_E(0) + E_{bg}x^2 - \Sigma_E(k). \quad (2.161)$$

We need to evaluate the energy shift of the dressed continuum state $\Sigma_E(k)$ to proceed further. From Eq. 2.16, we know

$$\Sigma_E(k) = \sum_{k' \neq k} \frac{|\hbar g(k')|^2}{(E_k - E'_k)}. \quad (2.162)$$

We change the summation in Eq. 2.162 into an integral,

$$\Sigma_E(k) = \mathcal{P} \int_{-\infty}^{\infty} dk' 4\pi k'^2 \frac{|\hbar \tilde{g}(k')|^2}{(E_k - E'_k)}. \quad (2.163)$$

Substituting $E_k = \hbar^2 k^2/m$ and $E'_k = \hbar^2 k'^2/m$ in Eq. 2.163,

$$\Sigma_E(k) = \mathcal{P} \int_{-\infty}^{\infty} dk' 4\pi k'^2 \frac{m |\tilde{g}(k')|^2}{(k^2 - k'^2)}. \quad (2.164)$$

From Eq. 2.38, we know for $|a_{bg}| \gg R$,

$$|\hbar \tilde{g}(k')|^2 = \frac{V_{HF}^2 R}{\pi^2} \frac{|a_{bg}|^2}{1 + k'^2 a_{bg}^2} \quad (2.165)$$

Substituting Eq. 2.165 in Eq. 2.164,

$$\Sigma_E(k) = 4\pi m \frac{V_{HF}^2 R |a_{bg}|^2}{\pi^2 \hbar^2} \left[\mathcal{P} \int_{-\infty}^{\infty} dk' \frac{k'^2}{(k^2 - k'^2)} \frac{1}{1 + k'^2 a_{bg}^2} \right]. \quad (2.166)$$

$$\Sigma_E(k) = 4\pi m \frac{V_{HF}^2 R}{\pi^2 \hbar^2} \left[\mathcal{P} \int_{-\infty}^{\infty} dk' \frac{k'^2}{(k^2 - k'^2)} \frac{1}{(k' + i/a_{bg})(k' - i/a_{bg})} \right]. \quad (2.167)$$

There are four poles in the integral for k' in Eq. 2.166, namely, $k' = \pm k$ and $k' = \pm i/a_{bg}$. Using the contour integration method, we choose the upper half of

the imaginary plane and evaluate the integral by calculating the residues of the poles encompassed by the contour integral. The residues for $k' = \pm k$ cancel. For a_{bg} negative, we can write $a_{bg} = -|a_{bg}|$, so that the only pole that contributes is $k' = i/|a_{bg}|$. Hence,

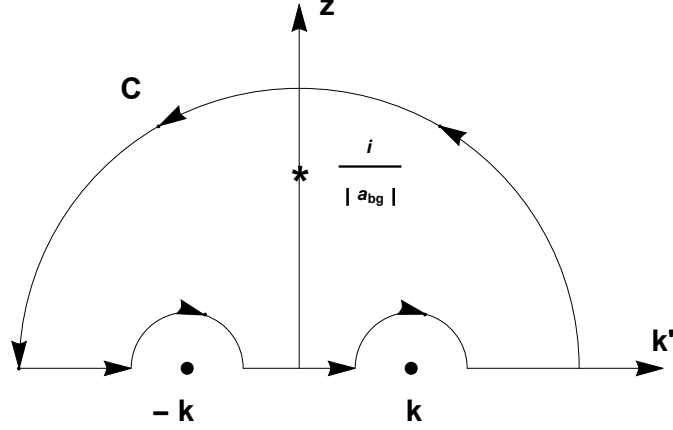


FIGURE 2.5: Contour Integral for $\Sigma_E(k)$

$$\begin{aligned}
\Sigma_E(k) &= 4\pi m \frac{V_{HF}^2 R}{\pi^2 \hbar^2} \pi i \left[\lim_{k' \rightarrow i/|a_{bg}|} \frac{k'^2}{(k^2 - k'^2)} \frac{(k' - i/|a_{bg}|)}{(k' + i/|a_{bg}|)(k' - i/|a_{bg}|)} \right] \\
&= 4\pi m \frac{V_{HF}^2 R}{\pi^2 \hbar^2} \pi i \left[\frac{(i/|a_{bg}|)^2}{(k^2 - (i/|a_{bg}|)^2)} \frac{1}{(i/|a_{bg}| + i/|a_{bg}|)} \right] \\
&= -2\pi^2 m \frac{V_{HF}^2 R}{\pi^2 \hbar^2} \frac{|a_{bg}|}{(1 + k^2 a_{bg}^2)} \tag{2.168}
\end{aligned}$$

Comparing Eq. 2.168 with Eq. 2.165, we obtain

$$\Sigma_E(k) = -\frac{2\pi^2 m |\tilde{g}(k)|^2}{|a_{bg}|} \tag{2.169}$$

From Eq. 2.165, we know

$$\tilde{g}(k) = \frac{\tilde{g}(0)}{\sqrt{1 + k^2 a_{bg}^2}} \tag{2.170}$$

Substituting Eq. 2.170 in Eq. 2.169,

$$\Sigma_E(k) = -\frac{2\pi^2 m |\tilde{g}(0)|^2}{|a_{bg}| (1 + k^2 a_{bg}^2)} \quad (2.171)$$

From the definition of the width of the resonance in Eq. 2.66,

$$2\mu_B |a_{bg}| \Delta B = 2\pi^2 m |\tilde{g}(0)|^2. \quad (2.172)$$

Substituting Eq. 2.172 in Eq. 2.171, we obtain

$$\Sigma_E(k) = -\frac{2\mu_B \Delta B}{1 + k^2 a_{bg}^2}. \quad (2.173)$$

Substituting $x = k|a_{bg}|$ in Eq. 2.174, we get

$$\Sigma_E(k) = -\frac{2\mu_B \Delta B}{1 + x^2}. \quad (2.174)$$

Hence

$$\Sigma_E(0) = -2\mu_B \Delta B. \quad (2.175)$$

We also define

$$\tilde{\Delta}_0 \equiv \frac{B - B_{res}}{\Delta B}. \quad (2.176)$$

$$\epsilon \equiv \frac{E_{bg}}{2\mu_B \Delta B}, \quad (2.177)$$

where $E_{bg} = \hbar^2/m a_{bg}^2$ is defined in Eq. 2.152. Substituting Eq. 2.174 to Eq. 2.177 in Eq. 2.161, yields

$$E_k - E_{g_1} - \Sigma_E(k) = 2\mu_B \Delta B \left[-\tilde{\Delta}_0 + \epsilon x^2 - \frac{x^2}{1 + x^2} \right]. \quad (2.178)$$

We define

$$\tilde{\Delta}_0(x) \equiv \tilde{\Delta}_0 - \epsilon x^2. \quad (2.179)$$

Substituting Eq. 2.179 in Eq. 2.178, we get

$$E_k - E_{g_1} - \Sigma_E(k) = 2\mu_B \Delta B \left[-\tilde{\Delta}_0(x) - \frac{x^2}{1+x^2} \right]. \quad (2.180)$$

We write $2\pi^2 m k |\tilde{g}(k)|^2$ using Eq. 2.40 as

$$2\pi^2 m k |\tilde{g}(k)|^2 = \frac{2\pi^2 m x |\tilde{g}(0)|^2}{|a_{bg}|(1+x^2)}. \quad (2.181)$$

Using Eq. 2.66 in Eq. 2.181, yields

$$2\pi^2 m k |\tilde{g}(k)|^2 = 2\mu_B \Delta B \left[\frac{x}{1+x^2} \right]. \quad (2.182)$$

Substituting Eq. 2.156, Eq. 2.180, and Eq. 2.182 in Eq. 2.150, and changing the integral in k to an integral in x by using $x = k|a_{bg}|$, we have

$$C(B) = \int_0^\infty dx \frac{4\pi x^2}{|a_{bg}|^3} \frac{\frac{\hbar^2}{2\pi^2 m} \frac{|a_{bg}|}{2\mu_B \Delta B} \frac{1}{1+x^2}}{\left[\tilde{\Delta}_0(x) + \frac{x^2}{1+x^2} \right]^2 + \left[\frac{x}{1+x^2} \right]^2}. \quad (2.183)$$

Using Eq. 2.177 and Eq. 2.179 in Eq. 2.183 yields

$$C(B) = \epsilon \frac{2}{\pi} \int_0^\infty \frac{dx x^2}{[\tilde{\Delta}_0 - \epsilon x^2]^2 + x^2 [1 + \tilde{\Delta}_0 - \epsilon x^2]^2}. \quad (2.184)$$

$C(B)$ in Eq. 2.184 gives the total probability of the singlet molecular ground $|g_1\rangle$ to be in the dressed continuum.

2.5.4 $Z(B)$ and $C(B)$ near the broad and narrow Feshbach resonance in ${}^6\text{Li}$

In this section, we will study the behavior of $Z(B)$ and $C(B)$ near the broad and narrow Feshbach resonance in ${}^6\text{Li}$ and test the validity of the expressions $Z(B)$ and $C(B)$ by comparing them with the completeness relationship of singlet state the $|g_1\rangle$.

From the completeness relationship of singlet state $|g_1\rangle$ in Eq. 2.142, we know

$$Z(B) + C(B) = 1, \quad (2.185)$$

where $C(B)$ is given in Eq. 2.184 and $Z(B)$ is given in Eq. 2.140.

Fig. 2.6 shows the plot of $Z(B)$ (Eq. 2.140) and $C(B)$ (Eq. 2.184) for the broad Feshbach resonance and the narrow Feshbach resonance in ${}^6\text{Li}$ near 832.2 G and 543.2 G, respectively. The black horizontal dashed line is the sum of $Z(B)$ and $C(B)$. We can see that the sum adds to 1, as it should, substantiating the expressions for $Z(B)$ and $C(B)$ derived in this section.

Also, we can see that $Z(B) = 0$ above resonance due to the absence of the bound state. Hence, above resonance, there is no singlet molecular population. However, above resonance $C(B) \rightarrow 1$ indicating that the dressed continuum state $|E_k\rangle$ has a strong admixture of the singlet state $|g_1\rangle$. Furthermore, we can also see that in the case of broad Feshbach resonance, $Z(B) \rightarrow 1$ as $B \rightarrow 400$ G, which is similar to the results reported in [60]. The behavior of $Z(B)$ and $C(B)$ as a function of the magnetic field derived from the dressed states $|E_k\rangle$ and $|E\rangle$ is one of the most important results of our theory.

2.5.5 *Molecular binding energy E_m*

In the previous section, we used the singlet bound state wave function to derive the singlet molecular fraction Z . In this section, we will derive the molecular binding energy E_m of the singlet molecules.

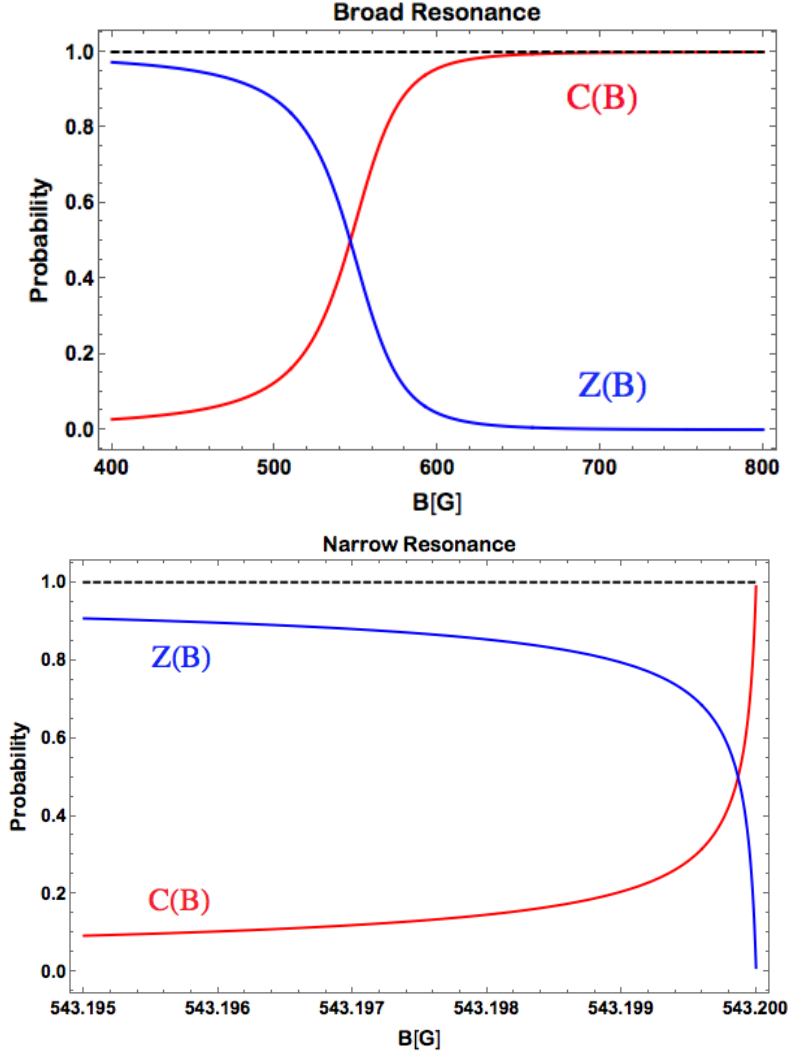


FIGURE 2.6: $Z(B)$ (blue curve) and $C(B)$ (red curve) for the broad Feshbach resonance (top) and the narrow Feshbach resonance (bottom) in ${}^6\text{Li}$.

We define the molecular binding energy $E_m > 0$ as

$$E_m = E_T - E. \quad (2.186)$$

Substituting Eq. 2.186 in Eq. 2.82 for energy shift of the bound state,

$$E_T - E_{g_1} - E_m = \Sigma(E). \quad (2.187)$$

We rewrite Eq. 2.187 by adding and subtracting the zero momentum energy shift of

the dressed continuum $\Sigma_E(0)$

$$-E_m = E_{g_1} - E_T + \Sigma_E(0) + \Sigma(E) - \Sigma_E(0). \quad (2.188)$$

We recall from Eq. 2.157 and Eq. 2.158 that

$$E_{g_1} - E_T + \Sigma_E(0) = 2\mu_B(B - B_\infty) = \hbar \Delta_0. \quad (2.189)$$

Substituting Eq. 2.189 in Eq. 2.188, we get

$$-E_m = \hbar \Delta_0 - \Sigma_E(0) + \Sigma(E). \quad (2.190)$$

Using $\Sigma_E(0) = -2\mu_B \Delta B$ (Eq. 2.175) and Eq. 2.137, we can write the energy shift of the dressed bound state $\Sigma(E)$ in terms of the zero momentum energy shift $\Sigma_E(0)$ as

$$\Sigma(E) = \frac{\Sigma_E(0)}{1 + \sqrt{\frac{E_T - E}{E_{bg}}}}. \quad (2.191)$$

Substituting Eq. 2.191 in Eq. 2.190, yields

$$-E_m = \hbar \Delta_0 - \Sigma_E(0) \left[1 - \frac{1}{1 + \sqrt{\frac{E_T - E}{E_{bg}}}} \right]. \quad (2.192)$$

Using Eq. 2.186 in Eq. 2.192,

$$-E_m = \hbar \Delta_0 - \Sigma_E(0) \frac{\sqrt{\frac{E_m}{E_{bg}}}}{1 + \sqrt{\frac{E_m}{E_{bg}}}}. \quad (2.193)$$

Dividing Eq. 2.193 by E_{bg} where $E_{bg} = \hbar^2/ma_{bg}^2$, yields

$$-\frac{E_m}{E_{bg}} = \frac{\hbar \Delta_0}{E_{bg}} - \frac{\Sigma_E(0)}{E_{bg}} \frac{\sqrt{\frac{E_m}{E_{bg}}}}{1 + \sqrt{\frac{E_m}{E_{bg}}}}. \quad (2.194)$$

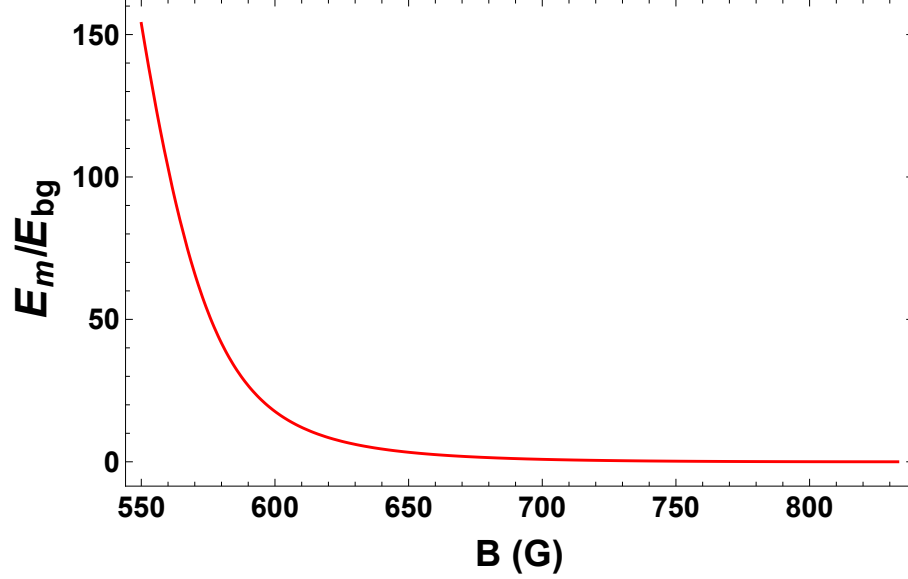


FIGURE 2.7: Binding energy E_m in units of E_{bg} near the broad Feshbach resonance in ${}^6\text{Li}$ ($\epsilon = 0.00036$) by self consistently solving Eq. 2.198.

Using $\tilde{E}_m = E_m/E_{bg}$ in Eq. 2.194, we have

$$-\tilde{E}_m = \frac{\hbar \Delta_0}{E_{bg}} - \frac{\Sigma_E(0)}{E_{bg}} \frac{\sqrt{\tilde{E}_m}}{1 + \sqrt{\tilde{E}_m}}. \quad (2.195)$$

Using Eq. 2.158 and Eq. 2.175, we rewrite Eq. 2.195 as

$$-\tilde{E}_m = \frac{2\mu_B(B - B_\infty)}{E_{bg}} + \frac{2\mu_B \Delta B}{E_{bg}} \frac{\sqrt{\tilde{E}_m}}{1 + \sqrt{\tilde{E}_m}}. \quad (2.196)$$

Using $\epsilon \equiv E_{bg}/2\mu_B \Delta B$ (Eq. 2.177) in Eq. 2.195,

$$-\tilde{E}_m = \frac{1}{\epsilon} \frac{2\mu_B(B - B_\infty)}{2\mu_B \Delta B} + \frac{1}{\epsilon} \frac{2\mu_B \Delta B}{2\mu_B \Delta B} \frac{\sqrt{\tilde{E}_m}}{1 + \sqrt{\tilde{E}_m}}. \quad (2.197)$$

Using $\tilde{\Delta}_0$ defined in Eq. 2.176 in Eq. 2.197, we obtain finally

$$\epsilon \tilde{E}_m + \tilde{\Delta}_0 + \frac{\sqrt{\tilde{E}_m}}{1 + \sqrt{\tilde{E}_m}} = 0 \quad (2.198)$$

We can evaluate the molecular binding energy for $B < B_{res}$ ($\tilde{\Delta}_0 < 0$) by self consistently solving Eq. 2.198 for \tilde{E}_m as a function of $\tilde{\Delta}_0$. Fig. 2.7 shows a plot of binding energy E_m as a function of the magnetic field near the broad Feshbach resonance ($\epsilon = 0.00036$) in ${}^6\text{Li}$.

2.6 Summary: Physical significance of the dressed states $|E\rangle$ and $|E_k\rangle$

In this section, I will discuss the physical significance of the dressed states $|E\rangle$ and $|E_k\rangle$ and further argue that the dressed states are not just chosen for mathematical convenience but have real physical meaning based on the results reported by [63].

Let me start by summarizing the big picture that has led us here. We started with the bare states responsible for the Feshbach resonance, namely, the bound singlet state $|g_1\rangle$ and the triplet continuum $|T, k\rangle$. The mixing of $|g_1\rangle$ with $|T, k\rangle$ due to hyperfine coupling leads to a Feshbach resonance. We treated this mixing using the continuum-dressed state picture, where the mixing of $|g_1\rangle$ with $|T, k\rangle$ leads to two dressed states, namely, the dressed continuum $|E_k\rangle$ and the dressed bound state $|E\rangle$. The atoms are initially prepared in the triplet continuum $|T, k\rangle$. However, near the Feshbach resonance, a fraction of the atoms, will populate the dressed bound state $|E\rangle$ and form singlet ground state dressed molecules. The amount of singlet character in the dressed molecules is given by $Z(B)$. The remaining fraction of unbound free atoms populates the dressed continuum states.

2.6.1 Above Feshbach resonance - BCS side

Above the Feshbach resonance (Fig. 2.6), $Z(B) \rightarrow 0$ and $C(B) \rightarrow 1$, indicating the absence of dressed bound state $|E\rangle$. Therefore, above the Feshbach Resonance, there are no singlet dressed molecules. However, since $C(B) \rightarrow 1$, the free atoms in dressed continuum states will have singlet character associated with them. This is easily verified by a simple experiment where an optical field illuminates the atoms to

couple the dressed continuum to the singlet excited state. If there is no admixture of $|g_1\rangle$ with $|E_k\rangle$, there should be no excitation of the atoms to the excited state, since a transition from the spin “triplet” state to the spin “singlet” state is forbidden by the selection rules. However, as reported in [63] and later in this thesis, the free atoms which are originally prepared in the “triplet” state are pumped to a “singlet” excited state due to the strong admixture of singlet state $|g_1\rangle$ with dressed continuum $|E_k\rangle$. This process, where free atoms in the continuum, are coupled to an excited bound state through an optical field is called photoassociation. Above the Feshbach resonance, photoassociation causes atom loss, as the atoms in the dressed continuum state are pumped into the singlet excited state and are subsequently lost due to spontaneous scattering to different lower lying vibrational states.

2.6.2 Below Feshbach resonance - BEC side

Below the Feshbach resonance, at low temperatures, a fraction of the total atoms populates the dressed bound state $|E\rangle$ forming dressed molecules and the remaining fraction remains as free atoms in the dressed continuum state. The amount of singlet character in the dressed molecules is given by $Z(B)$. In order to observe the singlet molecular fraction in the dressed bound state, experiments should be done at low temperatures, such that the thermal energy does not break the molecular pairs causing them to decay into the dressed continuum as free atoms. Below the Feshbach resonance, when an optical field is shined on the atoms to couple the dressed continuum to the singlet excited state, atom loss occurs due to the following

- (i) Photoassociation of free atoms from the dressed triplet continuum to the bound singlet excited state
- (ii) Pumping of singlet ground state molecules from the dressed bound state to the singlet excited state.

In the above two processes, the transition rate for the photoassociation of free

atoms is much slower compared to the direct pumping of singlet molecules, since the molecules reside in the dressed bound state $|E\rangle$ which is predominantly singlet in character and the free atoms reside in the dressed continuum states. This was clearly observed in the experiment done by [63], where they observe, at low temperatures, both a slow photoassociation loss and a fast decay due to the pumping of singlet molecules to the singlet excited state.

In summary, the dressed state $|E\rangle$ exists only below the Feshbach resonance on the BEC side and is populated by singlet ground state molecules. The dressed state $|E_k\rangle$ exists both below (BEC side) and above (BCS side) the magnetic Feshbach resonance and is populated by free unbound atoms which have a admixture of singlet character.

In the next chapter, the dressed states $|E\rangle$ and $|E_k\rangle$ will further be used as the basis states for the continuum-dressed state model of optical control. We will use the continuum-dressed state model to study a two-field optical method in detail to control interactions in an ultracold Fermi gas near a magnetic Feshbach resonance.

Continuum-Dressed State Model

In this chapter, we introduce the basic level scheme for the two-field optical method to control magnetic Feshbach resonances and a new theoretical model to calculate the scattering phase shift. Implementation of optical control methods requires an understanding of the optically-induced level structure and energy shifts, which depend on the relative momentum of a colliding atom pair.

In optical control of interactions, optical fields couple the singlet ground molecular state that has an hyperfine coupling to the triplet continuum to an excited molecular state (Chapter 1). Previous work from this group as well as other groups used a bare-state basis to determine the scattering state from which the scattering phase shift in the presence of optical fields is calculated [9, 49, 53, 56]. A central assumption in this approach is that the probability amplitude of the excited state tracks the probability amplitude of the ground state, permitting the adiabatic elimination of the excited state. This assumption is valid when the hyperfine coupling V_{HF}/h between the triplet continuum and the singlet ground state is small compared to the linewidth of the excited molecular state γ_e . For example, in the case of the narrow Feshbach resonance in ${}^6\text{Li}$ at 543.2 G, where $V_{HF}/h = 5.9$ MHz and $\gamma_e = 11.8$ MHz, we

can use the bare-state basis to solve for the scattering state. However, for broad Feshbach resonances like the resonance in ${}^6\text{Li}$ at 832.2 G where $V_{HF}/h = 131.6$ MHz, this approach breaks down, because adiabatic elimination of the excited state is no longer valid and leads to predictions that are in strong disagreement with the measurements [49].

In order to circumvent this problem, we introduce a continuum-dressed state model where the eigenstate basis is constructed as a result of “dressing” the bare-state basis by the hyperfine interaction. As the “continuum-dressed” basis already includes the hyperfine coupling in the eigenstate basis of the unperturbed Hamiltonian, the validity of the adiabatic elimination becomes independent of V_{HF} . In addition, the continuum-dressed state model provides a comprehensive treatment in calculating the scattering phase shift taking into account the relative momentum dependence, which can be different for broad and narrow Feshbach resonances. Using the continuum-dressed state basis, we solve the time dependent Schrödinger equation and determine the optically induced phase shift ϕ and the total phase shift δ , which is the sum of optically induced phase shift ϕ and the phase shift Δ due to the magnetic Feshbach resonance (chapter 2 Eq. 2.53).

3.1 Two-field optical method: Level scheme

The basic level scheme for the two-field optical technique is shown in Fig. 5.4. An optical field with Rabi frequency Ω_1 and frequency ω_1 couples the ground vibrational state $|g_1\rangle$ of the singlet ${}^1\Sigma_g^+$ potential to the excited vibrational state $|e\rangle$ of the singlet ${}^1\Sigma_u^+$ potential. A second optical field with Rabi frequency Ω_2 and frequency ω_2 couples a lower lying ground vibrational state $|g_2\rangle$ to the excited vibrational state $|e\rangle$. The ω_1 beam results in a light shift of state $|g_1\rangle$ as well as atom loss due to photoassociation from the triplet continuum $|T, k\rangle$, which is hyperfine coupled to $|g_1\rangle$ and hence optically coupled to the excited state $|e\rangle$. The ω_2 beam suppresses atom

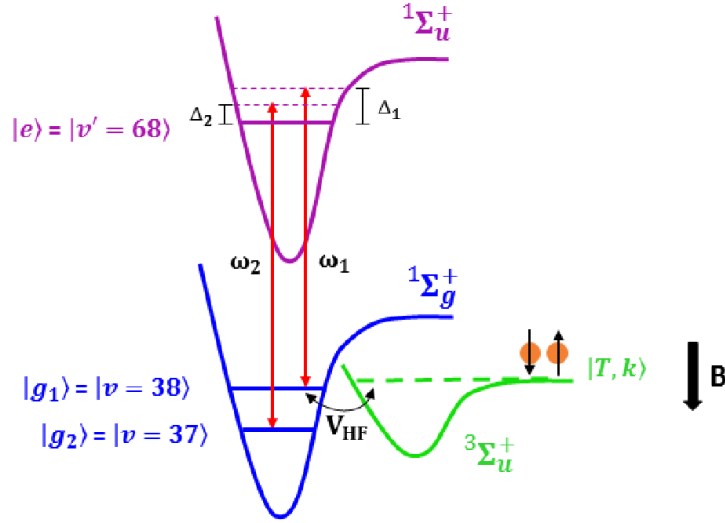


FIGURE 3.1: Basic level scheme for the two-field optical technique. Optical fields of frequencies ω_1 (detuning Δ_1) and ω_2 (detuning Δ_2), respectively, couple two singlet ground molecular states $|g_1\rangle$ and $|g_2\rangle$ to the singlet excited molecular state $|e\rangle$; V_{HF} is the hyperfine coupling between the incoming atomic pair state in the open triplet channel $|T, k\rangle$ and $|g_1\rangle$, which is responsible for a magnetically controlled Feshbach resonance.

loss through destructive quantum interference as discussed below. In a magnetic field B , the triplet continuum $|T, k\rangle$ tunes downward $\propto 2\mu_B B$, where μ_B is the Bohr magneton, $\mu_B/h \simeq h \times 1.4 \text{ MHz/G}$. The hyperfine coupling V_{HF} between $|T, k\rangle$ and $|g_1\rangle$ produces a Feshbach resonance. For our experiments with ${}^6\text{Li}$, $|g_1\rangle$ and $|g_2\rangle$ are the $v = 38$ and $v = 37$ ground vibrational states and $|e\rangle$ is the $v' = 68$ excited vibrational state, which decays at a rate $\gamma_e = 2\pi \times 11.8 \text{ MHz}$.

3.2 Bare-state basis and continuum-dressed state basis

In previous calculations by our group [49, 53], interaction of the colliding atom pair with the optical fields is described in the “bare” state basis, Fig. 3.2a, with singlet states, $|g_1\rangle$, $|g_2\rangle$, and $|e\rangle$, and triplet continuum states $|T, k\rangle$. For our calculations, we employ instead the continuum-dressed state basis, Fig. 3.2b. The bare states $|g_1\rangle$ and $|T, k\rangle$, are replaced by the dressed bound state $|E\rangle$ and the Feshbach resonance

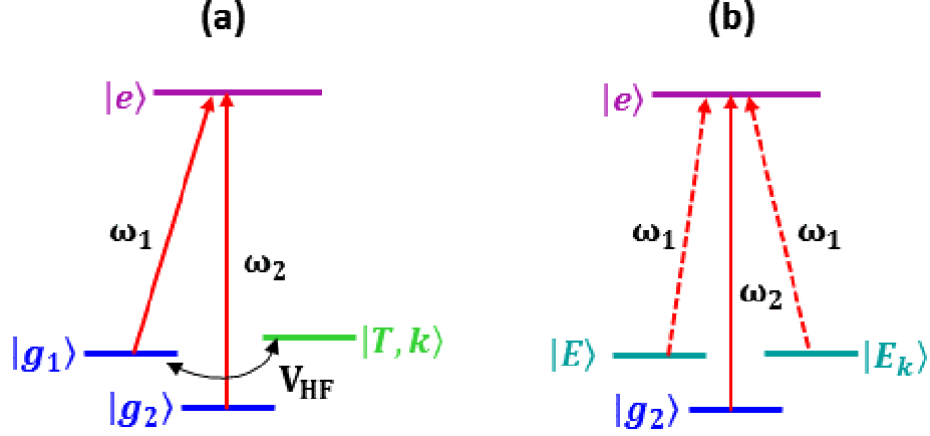


FIGURE 3.2: Level schemes in (a) “bare-state” and (b) “continuum-dressed-state” bases. $|g_1\rangle$, $|g_2\rangle$, and $|e\rangle$ are the bare molecular states in the energetically closed (singlet) channel. $|T, k\rangle$ is a bare continuum state in the open (triplet) channel. The hyperfine interaction V_{HF} couples the bare molecular state $|g_1\rangle$ and the continuum states $|T, k\rangle$, creating the “continuum-dressed” bound state $|E\rangle$ and the (Feshbach resonance) scattering state $|E_k\rangle$.

scattering state $|E_k\rangle$, chapter 2. The optical field with frequency ω_1 couples the dressed-bound state $|E\rangle$ and the dressed-continuum state (Feshbach resonance scattering state) $|E_k\rangle$ to the singlet excited state $|e\rangle$, since both states contain singlet $|g_1\rangle$ contributions. The second optical field with frequency ω_2 couples the singlet state $|g_2\rangle$ to the excited state $|e\rangle$. These dressed states already contain the hyperfine coupling constant V_{HF} , permitting consistent adiabatic elimination of the excited state amplitude $|e\rangle$, even for broad Feshbach resonances where V_{HF} is large. The new model shows that the light-shifts arising from the Ω_1 beam have a different relative momentum (k) dependence for broad resonances than for narrow resonances. Further, it reproduces previous calculations [9, 49, 53] that are valid only for narrow resonances and avoids predictions for the loss rate of a spurious broad resonance at the resonance magnetic field B_{res} that arises when narrow resonance results are incorrectly applied to broad resonances.

3.3 Optical control: Continuum-dressed basis

In this section, we solve the time dependent Schrödinger equation using the continuum-dressed state basis states, which was determined in chapter 2. In the absence of optical fields, the unperturbed Hamiltonian of the four-level system, Fig. 3.2b, in the continuum-dressed state basis can be written as,

$$H_0 = E|E\rangle\langle E| + E_{g_2}|g_2\rangle\langle g_2| + E_e|e\rangle\langle e| + \sum_{all\ k'} E_{k'}|E_{k'}\rangle\langle E_{k'}|, \quad (3.1)$$

where $|E_{k'}\rangle$ is an atom pair dressed continuum scattering state, $|E\rangle$ is the dressed bound state due to the coupling of the bare bound singlet Feshbach state $|g_1\rangle$ with the bare triplet continuum scattering states $|T, k'\rangle$, $|g_2\rangle$ is a lower lying molecular bound singlet state that has no coupling to $|T, k'\rangle$, and $|e\rangle$ is the singlet excited state.

For the perturbation arising from the optical transition, we can assume that the ground singlet states $|g_1\rangle$ and $|g_2\rangle$ have identical spin structure, as the optical transitions $|g_1\rangle \rightarrow |e\rangle \rightarrow |g_2\rangle$ do not change the electron-nuclear spin state. In the rotating wave approximation, the Hamiltonian due to the presence of optical fields is

$$H'_{opt} = -\frac{\hbar\Omega_1}{2} e^{-i\omega_1 t} |e\rangle\langle g_1| - \frac{\hbar\Omega_2}{2} e^{-i\omega_2 t} |e\rangle\langle g_2| + h.c., \quad (3.2)$$

where ω_1 and Ω_1 are the angular and Rabi frequencies of the optical field that couples $|g_1\rangle$ to $|e\rangle$, and ω_2 and Ω_2 are the angular and Rabi frequencies of the optical field that couples $|g_2\rangle$ to $|e\rangle$, respectively.

In thermal equilibrium, for $H'_{opt} = 0$, let $|E_k\rangle$ be the *input* scattering Feshbach resonance state. For H_0 in the diagonal basis with $H'_{opt} \neq 0$, the time-dependent scattering state then takes the form,

$$|\psi_{E_k}(t)\rangle = c_E(t)|E\rangle + c_2(t)|g_2\rangle + c_e(t)|e\rangle + c(k, t)|E_k\rangle + \sum_{k' \neq k} c(k', t)|E_{k'}\rangle, \quad (3.3)$$

where $c_T(k, t)$ is the amplitude for the input Feshbach resonance scattering state $|E_k\rangle$. For box normalized continuum states,

$$\langle E|E_k\rangle = 0, \langle E|E\rangle = 1, \langle E_k|E_{k'}\rangle = \delta_{k'k}.$$

From the time-dependent Schrödinger equation,

$$(H_o + H'_{opt})|\psi_{E_k}(t)\rangle = i\hbar \partial_t |\psi_{E_k}(t)\rangle, \quad (3.4)$$

we solve for the coefficients in $|\psi_{E_k}(t)\rangle$ by taking the projections of Eq. 3.4 on the basis states. For $|E\rangle$, this gives using Eq. 3.2

$$\begin{aligned} i\hbar \dot{c}_E &= \langle E|(H_o + H'_{opt})|\psi_{E_k}(t)\rangle = E c_E + \langle E|H'_{opt}|\psi_{E_k}(t)\rangle, \\ i\hbar \dot{c}_E &= E c_E - \frac{\hbar \Omega_1^*}{2} e^{i\omega_1 t} \langle E|g_1\rangle c_e. \end{aligned} \quad (3.5)$$

Similarly, taking projection of $|g_2\rangle$, $|E_{k'}\rangle$, and $|e\rangle$ on Eq. 3.4 with Eq. 3.2, we obtain

$$i\hbar \dot{c}_2 = E_{g_2} c_2 - \frac{\hbar \Omega_2^*}{2} e^{i\omega_2 t} \langle E|g_1\rangle c_e, \quad (3.6)$$

$$i\hbar \dot{c}(k') = E_{k'} c(k') - \frac{\hbar \Omega_1^*}{2} e^{i\omega_1 t} \langle E_{k'}|g_1\rangle c_e, \quad (3.7)$$

$$\begin{aligned} i\hbar \dot{c}_e &= E_e c_e - \frac{\hbar \Omega_1}{2} e^{-i\omega_1 t} \left[\langle g_1|E\rangle c_E + \sum_{\text{all } k'} \langle g_1|E_{k'}\rangle c(k') \right] \\ &- \frac{\hbar \Omega_2}{2} e^{-i\omega_2 t} c_2 - i \frac{\hbar \gamma_e}{2} c_e. \end{aligned} \quad (3.8)$$

In Eq. 3.8, a decay term $-\gamma_e c_e/2$ is added to the \dot{c}_e equation, describing the radiative decay of the excited state to the ground vibrational manifold.

In the limit, $r \rightarrow \infty$, the asymptotic (triplet) scattering state must be an eigenstate of H with a total energy $E_k = E_T + \hbar^2 k^2/m$, where $E_T = -a_{HF}/2 - 2\mu_B B$ is

the energy of the triplet state and $\hbar^2 k^2/m$ is the relative kinetic energy between an atom pair. Therefore, we seek solutions where $c(k', t) = b(k') \exp(-iE_k t/\hbar)$, where b_i are slowly varying amplitudes. Forcing $c_e = b_e \exp[-i(\omega_1 + E_k/\hbar)t]$ removes all time-dependent phase factors in Eq. 3.7, yielding

$$i\hbar \dot{b}(k') = (E_{k'} - E_k) b(k') - \frac{\hbar \Omega_1^*}{2} \langle E_{k'} | g_1 \rangle b_e. \quad (3.9)$$

Similarly, using $c_e = b_e \exp[-i(\omega_1 + E_k/\hbar)t]$ and $c_E = b_E \exp(-iE_k t/\hbar)$ in Eq. 3.8, and forcing $c_2 = b_2 \exp[i(\omega_2 - \omega_1 - E_k/\hbar)t]$ to eliminate the resulting time-dependent exponential factors, gives,

$$\begin{aligned} i\hbar \dot{b}_e &= (E_e - E_k - \hbar\omega_1) b_e - i \frac{\hbar\gamma_e}{2} b_e - \frac{\hbar \Omega_2}{2} b_2 \\ &- \frac{\hbar \Omega_1}{2} \left[\langle g_1 | E \rangle b_E + \sum_{\text{all } k'} \langle g_1 | E_{k'} \rangle b(k') \right]. \end{aligned} \quad (3.10)$$

From Eq. 3.5 and Eq. 3.6, we get

$$i\hbar \dot{b}_E = (E - E_k) b_E - \frac{\hbar \Omega_1^*}{2} \langle E | g_1 \rangle b_e \quad (3.11)$$

$$i\hbar \dot{b}_2 = [E_{g_2} - E_k - \hbar(\omega_1 - \omega_2)] b_2 - \frac{\hbar \Omega_2^*}{2} b_e \quad (3.12)$$

3.3.1 Adiabatic approximation

In this section, we will find all the amplitudes b_i in terms of input amplitude $b(k)$. As the large hyperfine coupling constant is already included in the basis set, for Ω_1 not too large compared to the excited state decay rate, we can adiabatically eliminate the excited state amplitude b_e . Hence, substituting $\dot{b}_e = 0$ in Eq. 3.10 gives

$$\begin{aligned} \left[(E_e - E_k - \hbar\omega_1) - i \frac{\hbar\gamma_e}{2} \right] b_e &= \frac{\hbar \Omega_2}{2} b_2 \\ &+ \frac{\hbar \Omega_1}{2} \left[\langle g_1 | E \rangle b_E + \sum_{\text{all } k'} \langle g_1 | E_{k'} \rangle b(k') \right]. \end{aligned} \quad (3.13)$$

From Eq. 3.13 we can see b_e tracks $b(k')$, b_E , and b_2 . Further, we assume $\dot{b}_i = 0$ for the slowly varying amplitudes, similar to the method employed in Ref. [49]. Hence substituting $\dot{b}(k') = 0$, $\dot{b}_E = 0$, and $\dot{b}_2 = 0$ in Eq. 3.9, Eq. 3.11, and Eq. 3.12, respectively, gives

$$b_E = \frac{\hbar \Omega_1^*}{2(E - E_k)} \langle E | g_1 \rangle b_e, \quad (3.14)$$

$$b(k' \neq k) = \frac{\hbar \Omega_1^*}{2(E_{k'} - E_k)} \langle E_{k'} | g_1 \rangle b_e, \quad (3.15)$$

$$b_2 = \frac{\hbar \Omega_2^*}{2[E_{g_2} - E_k - \hbar(\omega_1 - \omega_2)]} b_e. \quad (3.16)$$

Using Eq. 3.14, Eq. 3.15, and Eq. 3.16 in Eq. 3.13, we get

$$\begin{aligned} \left[(E_e - E_k - \hbar\omega_1) - i\hbar\frac{\gamma_e}{2} \right] b_e - \left| \frac{\hbar\Omega_1}{2} \right|^2 \left\{ \frac{|\langle g_1 | E \rangle|^2}{E - E_k} + \sum_{k' \neq k} \frac{|\langle g_1 | E_{k'} \rangle|^2}{E_{k'} - E_k} \right\} b_e \\ - \left| \frac{\hbar\Omega_2}{2} \right|^2 \frac{b_e}{E_{g_2} - E_k - \hbar(\omega_1 - \omega_2)} = \frac{\hbar\Omega_1}{2} \langle g_1 | E_k \rangle b(k). \end{aligned} \quad (3.17)$$

Rewriting Eq. 3.17,

$$b_e = \frac{\hbar\Omega_1}{2} \frac{\langle g_1 | E_k \rangle}{D(E, E_k)} b(k), \quad (3.18)$$

where $D(E, E_k)$ in Eq. 3.18 is given by

$$\begin{aligned} D(E, E_k) = E_e - E_k - \hbar\omega_1 - i\hbar\frac{\gamma_e}{2} - \left| \frac{\hbar\Omega_1}{2} \right|^2 \left\{ \frac{|\langle g_1 | E \rangle|^2}{E - E_k} + \sum_{k' \neq k} \frac{|\langle g_1 | E_{k'} \rangle|^2}{E_{k'} - E_k} \right\} \\ - \left| \frac{\hbar\Omega_2}{2} \right|^2 \frac{1}{E_{g_2} - E_k - \hbar(\omega_1 - \omega_2)}. \end{aligned} \quad (3.19)$$

Substituting Eq. 3.18 in Eq. 3.14 and Eq. 3.15 gives,

$$b_E = \left| \frac{\hbar\Omega_1}{2} \right|^2 \frac{\langle E|g_1\rangle\langle g_1|E_k\rangle}{(E - E_k) D(E, E_k)} b(k), \quad (3.20)$$

$$b(k' \neq k) = \left| \frac{\hbar\Omega_1}{2} \right|^2 \frac{\langle E_{k'}|g_1\rangle\langle g_1|E_k\rangle}{(E_{k'} - E_k) D(E, E_k)} b(k). \quad (3.21)$$

For $k' = k$, Substituting Eq. 3.18 in Eq. 3.9 gives;

$$\dot{b}(k) = \frac{i\hbar |\Omega_1|^2 |\langle g_1|E_k\rangle|^2}{4 D(E, E_k)} b(k) \quad (3.22)$$

3.4 Scattering state wave function

For $r \rightarrow \infty$, the bound state contributions vanish i.e., $\langle r|e\rangle = 0$, $\langle r|g_2\rangle = 0$, and $\langle r|E\rangle = 0$. Hence the scattering state is determined only by the triplet part of the wavefunction. The triplet continuum part of the scattering state takes the form $\Psi_{E_k}(r \rightarrow \infty) \exp(-iE_k t/\hbar)$. Taking the projection of $|r\rangle$ on Eq. 3.3 and removing the time-dependent phase factors by substituting the coefficients c_k and $c_{k'}$ in terms of b_k and $b_{k'}$,

$$\langle r \rightarrow \infty | \Psi_{E_k} \rangle = \Psi_{E_k}(r \rightarrow \infty) = b(k) \langle r \rightarrow \infty | E_k \rangle + \sum_{k' \neq k} b(k') \langle r \rightarrow \infty | E_{k'} \rangle. \quad (3.23)$$

As $r \rightarrow \infty$, from chapter 2, we write the dressed continuum state wave function with box normalization as

$$\langle r \rightarrow \infty | E_{k'} \rangle = \frac{1}{\sqrt{V}} \frac{[\sin(k'r + \Delta(k'))]}{k'r}, \quad (3.24)$$

where the factor $1/\sqrt{V}$ is needed for box normalization, and $\Delta(k')$ is the phase shift induced due to the Feshbach resonance, which can be written as the sum of the resonant part of the phase shift $\tilde{\Delta}(k')$ and the background part of the phase shift

$\delta_{bg}(k')$.

$$\Delta(k') = \tilde{\Delta}(k') + \delta_{bg}(k'). \quad (3.25)$$

Substituting Eq. 3.21 and Eq. 3.24 in Eq. 3.23, we get

$$\begin{aligned} \Psi_{E_k}(r \rightarrow \infty) &= \frac{b(k)}{kr\sqrt{V}} \left[\sin(kr + \Delta(k)) \right. \\ &\quad \left. + \sum_{k' \neq k} \frac{\hbar^2 |\Omega_1^2|}{4} \frac{\langle E_{k'} | g_1 \rangle \langle g_1 | E_k \rangle}{(E_{k'} - E_k) D(E, E_k)} \frac{k}{k'} \sin(k'r + \Delta(k')) \right]. \end{aligned} \quad (3.26)$$

We define the second term in Eq. 3.26 to be $S(k)$,

$$S(k) \equiv \sum_{k' \neq k} \frac{\hbar^2 |\Omega_1^2|}{4} \frac{\langle E_{k'} | g_1 \rangle \langle g_1 | E_k \rangle}{(E_{k'} - E_k) D(E, k)} \frac{k}{k'} \sin(k'r + \Delta(k')). \quad (3.27)$$

$S(k)$ is evaluated by converting the summation into an integral in Eq. 3.27 using,

$$\sum_{k' \neq k} \rightarrow \mathcal{P} \int d^3 \vec{k}' \frac{V}{(2\pi)^3} = \mathcal{P} \int_0^\infty dk' 4\pi k'^2 \frac{V}{(2\pi)^3}. \quad (3.28)$$

where \mathcal{P} denotes the principal part ($k' \neq k$). Using Eq. 3.28 in Eq. 3.27, we obtain

$$S(k) = \mathcal{P} \int_0^\infty dk' 4\pi k'^2 \frac{V}{(2\pi)^3} \frac{\hbar^2 |\Omega_1^2|}{4} \frac{\langle E_{k'} | g_1 \rangle \langle g_1 | E_k \rangle}{(E_{k'} - E_k) D(E, k)} \frac{k}{k'} \sin(k'r + \Delta(k')). \quad (3.29)$$

We define (see chapter 2),

$$\frac{V}{(2\pi)^3} \langle E_{k'} | g_1 \rangle \langle g_1 | E_k \rangle \equiv \langle \tilde{E}_{k'} | g_1 \rangle \langle g_1 | \tilde{E}_k \rangle, \quad (3.30)$$

where $|\tilde{E}_k\rangle$ is the dressed continuum state for continuum normalization, which is independent of V . Using Eq. 3.30 in Eq. 3.29, yields

$$S(k) = \frac{\hbar^2 \Omega_1^2}{4} \frac{2\pi m k}{\hbar^2} \langle g_1 | \tilde{E}_k \rangle \mathcal{P} \int_0^\infty \frac{dk' k' [\sin(kr + \Delta(k'))]}{k'^2 - k^2} \langle \tilde{E}_{k'} | g_1 \rangle. \quad (3.31)$$

Using the effective range expansion for phase shift Δ (chapter 2 Eq. 2.56), we write

$$k' \cot \Delta = -\frac{1}{a} + \frac{r_e}{2} k'^2, \quad (3.32)$$

From Eq. 3.32, we can see that Δ is an odd function in k' , since the right hand side is an even function in k' . Therefore, Eq. 3.24 is an even function in k' , which makes the integrand in Eq. 3.31 an even function in k' . Hence, using $\int_0^\infty = \frac{1}{2} \int_{-\infty}^\infty$ in Eq. 3.31,

$$S(k) = \frac{\hbar^2 \Omega_1^2}{4} \frac{2\pi m k}{\hbar^2} \langle g_1 | \tilde{E}_k \rangle \mathcal{P} \int_{-\infty}^\infty \frac{dk' k' [\sin(k' r + \Delta(k'))]}{k'^2 - k^2} \langle \tilde{E}_{k'} | g_1 \rangle. \quad (3.33)$$

As shown in Appendix A Eq. A.27, the function $e^{\pm i\Delta(k')} \langle \tilde{E}_{k'} | g_1 \rangle$ has no poles on the real axis. Hence, for poles on either the upper half or lower half of the imaginary axis, $k' = \pm iq$, where $q > 0$, and $e^{\pm ik' r}$ takes the form e^{-qr} . Therefore, as $r \rightarrow \infty$, $e^{ik' r} \rightarrow 0$ for poles not on the real axis. Hence, as $r \rightarrow \infty$, only the poles on real axis, $k' = \pm k$, contribute. Therefore,

$$\langle g_1 | \tilde{E}_k \rangle \langle \tilde{E}_{k'} | g_1 \rangle \rightarrow |\langle g_1 | \tilde{E}_k \rangle|^2 \quad \text{for } k' = k \quad (3.34)$$

Substituting Eq. 3.34 in Eq. 3.33,

$$S(k) = \frac{\hbar^2 \Omega_1^2}{4} \frac{2\pi m k}{\hbar^2} |\langle g_1 | \tilde{E}_k \rangle|^2 \mathcal{P} \int_{-\infty}^\infty \frac{dk' k' [\sin(kr + \Delta(k'))]}{k'^2 - k^2}. \quad (3.35)$$

We reduce Eq. 3.35 further by finding the principal part of the integral. We let

$$I(k) \equiv \mathcal{P} \int_{-\infty}^\infty \frac{dk' k' [\sin(k' r + \Delta(k'))]}{k'^2 - k^2}, \quad (3.36)$$

$$I(k) = \text{Im} \left\{ \mathcal{P} \int_{-\infty}^\infty \frac{dk' k' [e^{ik' r + \Delta(k')}] }{k'^2 - k^2} \right\} = \text{Im} \{I_1\}. \quad (3.37)$$

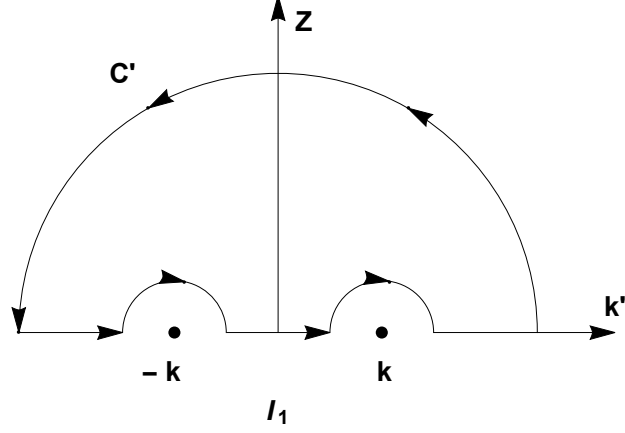


FIGURE 3.3: Contour Integral for I_1

Solving for I_1 using the contour integral method (Fig. B.1),

$$\oint dz = I_1 - \pi i [\text{Res}(-k)] - \pi i [\text{Res}(k)] = 0, \quad (3.38)$$

$$I_1 = \pi i [\text{Res}(-k)] + \pi i [\text{Res}(k)]. \quad (3.39)$$

Using Cauchy residue theorem,

$$I_1 = \lim_{k' \rightarrow -k} \pi i \frac{k'(k' + k)}{(k' - k)(k' + k)} e^{ik'r + \Delta(k')} + \lim_{k' \rightarrow k} \pi i \frac{k'(k' - k)}{(k' - k)(k' + k)} e^{ik'r + \Delta(k')}. \quad (3.40)$$

Eq. 3.40 reduces to,

$$I_1 = i\pi \cos[kr + \Delta(k)]. \quad (3.41)$$

Using Eq. 3.41, Eq. 3.37, and Eq. 3.36 in Eq. 3.35, gives

$$S(k) = \frac{\pi^2 m k \Omega^2}{2} |\langle g_1 | \tilde{E}_k \rangle|^2 \cos[kr + \Delta(k)]. \quad (3.42)$$

Using Eq. 3.42 in Eq. 3.26, we obtain the expression for the wavefunction of the scattering state,

$$\Psi_{E_k}(r \rightarrow \infty) = \frac{b(k)}{kr\sqrt{V}} \left[\sin(kr + \Delta(k)) + \frac{\Omega_1^2}{4} \frac{2\pi^2 m k |\langle g_1 | \tilde{E}_k \rangle|^2}{D(E, E_k)} \cos(kr + \Delta(k)) \right] \quad (3.43)$$

From Eq. 3.43, we can extract the optically induced phase shift. However, the expression for the wavefunction contains the energy denominator $D(E, E_K)$. Before we proceed to deduce the optically induced phase shift, we have to evaluate $D(E, E_K)$, which will be the focus of the next section.

3.5 Evaluating the energy denominator $D(E, E_K)$

In this section, we will evaluate the energy denominator $D(E, E_K)$ in Eq. 3.43. Expressing $D(E, E_k)$ in terms of its real and imaginary parts, we define

$$D(E, E_k) = -D'(E, E_k) - i\hbar\frac{\gamma_c}{2}. \quad (3.44)$$

Comparing Eq. 3.44 and Eq. 3.19,

$$D'(E, E_k) = \hbar\omega_1 - (E_c - E_k) + \left| \frac{\hbar\Omega_2}{2} \right|^2 \frac{1}{E_{g_2} - E_k - \hbar(\omega_1 - \omega_2)} + \left| \frac{\hbar\Omega_1}{2} \right|^2 \left\{ \frac{|\langle g_1|E\rangle|^2}{E - E_k} + \sum_{k' \neq k} \frac{|\langle g_1|E_{k'}\rangle|^2}{E_{k'} - E_k} \right\}. \quad (3.45)$$

We define I_E and I_{E_K}

$$I_E \equiv \frac{|\langle g_1|E\rangle|^2}{E_k - E} = \frac{|\langle g_1|E\rangle|^2}{E_T - E + \frac{\hbar^2 k^2}{m}}, \quad (3.46)$$

$$I_{E_k} \equiv \sum_{k' \neq k} \frac{|\langle g_1|E_{k'}\rangle|^2}{E_{k'} - E_k}, \quad (3.47)$$

where I_E is the dressed bound state contribution as it involves the overlap integral $\langle g_1|E\rangle$ and I_{E_K} is the dressed continuum contribution as it involves the overlap

integral $\langle g_1 | E_k \rangle$. Substituting Eq. 3.46 and Eq. 3.47 in Eq. 3.48, we obtain

$$\begin{aligned}
D'(E, E_k) &= \hbar\omega_1 - (E_e - E_k) + \left| \frac{\hbar\Omega_2}{2} \right|^2 \frac{1}{E_{g_2} - E_k - \hbar(\omega_1 - \omega_2)} \\
&+ \left| \frac{\hbar\Omega_1}{2} \right|^2 (I_{E_k} - I_E)
\end{aligned} \tag{3.48}$$

We define the single photon detuning Δ_e for the $|T\rangle - |e\rangle$ transition as,

$$\Delta_e \equiv \omega_1 - \frac{E_e - E_k}{\hbar}, \tag{3.49}$$

where

$$E_k = E_T + \frac{\hbar^2 k^2}{m} \quad \text{and} \quad E_T = -\frac{a_{HF}}{2} - 2\mu_B B. \tag{3.50}$$

Substituting Eq. 3.50 in Eq. 3.49,

$$\Delta_e = \omega_1 - \frac{E_e + \frac{a_{HF}}{2} + 2\mu_B B}{\hbar} + \frac{\hbar k^2}{m}. \tag{3.51}$$

We can see from Eq. 3.51, Δ_e has the energy E_e in it. However, we would like to define the detunings in terms of only measured quantities. Hence, we define the laser detuning Δ_L for the $|T\rangle - |e\rangle$ transition at a reference B-field B_{ref}

$$\Delta_L \equiv \omega_1 - \frac{E_e + \frac{a_{HF}}{2} + 2\mu_B B_{ref}}{\hbar}. \tag{3.52}$$

Subtracting Eq. 3.52 from Eq. 3.51, we write

$$\Delta_e = \Delta_L - \frac{2\mu_B(B - B_{ref})}{\hbar} + \frac{\hbar k^2}{m} \tag{3.53}$$

We define the two-photon detuning for the $|g_2\rangle - |T\rangle - |e\rangle$ transition as

$$\delta_e \equiv \omega_2 - \omega_1 - \frac{E_k - E_{g_2}}{\hbar} \tag{3.54}$$

Substituting Eq. 3.50 in Eq. 3.54, we obtain

$$\delta_e = \omega_2 - \omega_1 + \frac{\frac{a_{HF}}{2} + 2\mu_B B - E_{g_2}}{\hbar} - \frac{\hbar k^2}{m} \quad (3.55)$$

Similar to Δ_e , we would like to define δ in terms of measured quantities. Therefore, we define the laser detuning Δ_2 for the $|g_2\rangle - |e\rangle$ transition as

$$\Delta_2 \equiv \omega_2 - \frac{E_e - E_{g_2}}{\hbar} \quad (3.56)$$

Using Eq. 3.56 and Eq. 3.51 in Eq. 3.55,

$$\delta_e = \Delta_2 - \Delta_e \quad (3.57)$$

Substituting Eq. 3.53 in Eq. 3.57, yields

$$\delta_e = \Delta_2 - \Delta_L + \frac{2\mu_B(B - B_{ref})}{\hbar} - \frac{\hbar k^2}{m} \quad (3.58)$$

For later use, we define $x = k|a_{bg}|$ and explicitly write the momentum dependence in the single photon detuning Δ_e and two-photon detuning δ_e in terms of x . Therefore, we write

$$\Delta_e(x) = \Delta_L - \frac{2\mu_B(B - B_{ref})}{\hbar} + \frac{\hbar x^2}{m|a_{bg}|^2} \quad (3.59)$$

$$\delta_e(x) = \Delta_2 - \Delta_L + \frac{2\mu_B(B - B_{ref})}{\hbar} - \frac{\hbar x^2}{m|a_{bg}|^2} \quad (3.60)$$

From the definition of the single photon detuning Δ_e (Eq. 3.49) and the two-photon detuning δ_e (Eq. 3.54), we can write the expression for $D'(E, E_k)$ in a simplified form. Substituting Eq. 3.49 and Eq. 3.54 in Eq. 3.48, we have

$$\frac{D'(E, E_k)}{\hbar} = \Delta_e(x) + \frac{\Omega_2^2}{4\delta_e(x)} + \frac{\hbar\Omega_1^2}{4}(I_{E_k} - I_E). \quad (3.61)$$

Next we proceed to evaluate the integrals I_E and I_{E_k} .

3.5.1 Dressed bound state shift I_E

In this section, we will evaluate the dressed bound state shift integral I_E for the broad and narrow Feshbach resonance in ${}^6\text{Li}$. From chapter 2, we know that the probability of the singlet state $|g_1\rangle$ to be in the dressed bound state $|E\rangle$ is given by Eq. 2.90

$$Z = |\langle g_1|E\rangle|^2, \quad (3.62)$$

and the molecular binding energy for $B < B_{res}$ is given by Eq. 2.186

$$E_m = E_T - E. \quad (3.63)$$

We use Eq. 3.62 and Eq. 3.63 to rewrite the expression of I_E in Eq. 3.46 as

$$I_E = \frac{|\langle g_1|E\rangle|^2}{E_T - E + \frac{\hbar^2 k^2}{m}} = \frac{Z}{E_m + \frac{\hbar^2 k^2}{m}} \theta[B_{res} - B], \quad (3.64)$$

where the heavyside theta function $\theta[B_{res} - B]$ imposes the condition that the molecular binding energy exists for only $B < B_{res}$.

As in chapter 2, we define

$$\begin{aligned} \tilde{E}_m &= \frac{E_m}{E_{bg}} \\ E_{bg} &= \frac{\hbar^2}{m a_{bg}^2} \\ x^2 &= k^2 a_{bg}^2 = \frac{\hbar^2 k^2}{m E_{bg}} \\ \epsilon &= \frac{E_{bg}}{2\mu_B \Delta B} \end{aligned} \quad (3.65)$$

Substituting Eq. 3.65 in Eq. 3.64, yields

$$I_E = \frac{2\mu_B \Delta B}{\epsilon} \frac{Z}{\tilde{E}_m + x^2} \theta[B_{res} - B]. \quad (3.66)$$

We define

$$\tilde{I}_E \equiv \frac{1}{2\mu_B\Delta B} I_E = \frac{1}{\epsilon} \frac{Z}{\tilde{E}_m + x^2} \theta[B_{res} - B]. \quad (3.67)$$

For the cases of the broad and narrow resonances in ${}^6\text{Li}$, $\epsilon = 0.00036$ and $\epsilon = 555$, respectively. From chapter 2 Eq. 2.140, we know that $Z \neq 0$ for $B < B_\infty$ and Z is given by

$$Z = \frac{1}{1 + \frac{\mu_B\Delta B}{E_{bg}} \sqrt{\frac{E_{bg}}{E_T - E}} \frac{1}{(1 + \sqrt{\frac{E_T - E}{E_{bg}}})^2}}. \quad (3.68)$$

Using Eq. 3.63 and Eq. 3.65, we rewrite Eq. 3.68

$$Z = \frac{1}{1 + \frac{1}{2\epsilon\sqrt{\tilde{E}_m}(1 + \sqrt{\tilde{E}_m})^2}}, \quad (3.69)$$

From chapter 2 Eq. 2.198, we know that \tilde{E}_m satisfies,

$$\epsilon\tilde{E}_m + \tilde{\Delta}_0 + \frac{\sqrt{\tilde{E}_m}}{1 + \sqrt{\tilde{E}_m}} = 0, \quad (3.70)$$

where $\tilde{\Delta}_0 = (B - B_{res})/\Delta B$. The next step is to evaluate \tilde{I}_E separately for the broad and the narrow Feshbach resonances.

For the broad resonance, $\epsilon \ll 1$ since $\Delta B = 300$ G. Hence, the expression for Z in Eq. 3.69 for $\epsilon \rightarrow 0$ becomes,

$$Z = 2\epsilon \sqrt{\tilde{E}_m} (1 + \sqrt{\tilde{E}_m})^2, \quad (3.71)$$

and Eq. 3.70 for $\epsilon \rightarrow 0$ gives

$$\tilde{E}_m = \frac{1}{\left(1 + \frac{1}{\tilde{\Delta}_0}\right)^2}. \quad (3.72)$$

We use $-\tilde{\Delta}_0 = |\tilde{\Delta}_0|$ for $\tilde{\Delta}_0 < 0$ in Eq. 3.72 and obtain

$$\sqrt{\tilde{E}_m} = \frac{|\tilde{\Delta}_0|}{|1 + \tilde{\Delta}_0|}. \quad (3.73)$$

Using Eq. 3.71 and Eq. 3.73 in Eq. 3.67, we have for the broad resonance,

$$\tilde{I}_E = \frac{2\theta[-\tilde{\Delta}_0]\theta[1 + \tilde{\Delta}_0]}{\tilde{\Delta}_0^2 + x^2(1 + \tilde{\Delta}_0^2)^2} \frac{|\tilde{\Delta}_0|}{|1 + \tilde{\Delta}_0|}, \quad \text{for } \epsilon \ll 1. \quad (3.74)$$

For the narrow resonance, $\epsilon = 555 \gg 1$. Hence, Eq. 3.69 gives $Z \rightarrow 1$ and Eq. 3.70 gives

$$\tilde{E}_m \rightarrow -\frac{\tilde{\Delta}_0}{\epsilon}, \quad \text{for } |\tilde{\Delta}_0| \approx 1; \tilde{\Delta}_0 < 0. \quad (3.75)$$

Substituting Eq. 3.75 in Eq. 3.67, we have for the narrow resonance,

$$\tilde{I}_E = -\frac{\theta[-\tilde{\Delta}_0]}{\tilde{\Delta}_0 - \epsilon x^2}. \quad \text{for } \epsilon \gg 1 \quad (3.76)$$

3.5.2 Dressed continuum state shift I_{E_k}

In this section, we will evaluate I_{E_k} for the case of broad and narrow resonances.

Writing I_{E_k} explicitly from Eq. 3.47,

$$I_{E_k} = \sum_{k' \neq k} \frac{|\langle g_1 | E_{k'} \rangle|^2}{E_{k'} - E_k} = \mathcal{P} \int d^3 \vec{k}' \frac{V}{(2\pi)^3} \frac{|\langle g_1 | E_{k'} \rangle|^2}{E_{k'} - E_k}, \quad (3.77)$$

$$= \mathcal{P} \int dk' 4\pi k'^2 \frac{|\langle g_1 | \tilde{E}_{k'} \rangle|^2}{\frac{\hbar^2}{m}(k'^2 - k^2)}, \quad (3.78)$$

From chapter 2, Eq. 2.143 and Eq. 2.184, we know

$$C(B) = \int_0^\infty 4\pi k^2 dk |\langle g_1 | \tilde{E}_k \rangle|^2 = \epsilon \frac{2}{\pi} \int_0^\infty \frac{dx x^2}{[\tilde{\Delta}_0 - \epsilon x^2]^2 + x^2[1 + \tilde{\Delta}_0 - \epsilon x^2]^2}, \quad (3.79)$$

where $x = k|a_{bg}|$. From Eq. 3.79, we can write

$$|\langle g_1 | \tilde{E}_k \rangle|^2 = \frac{\epsilon |a_{bg}|^3}{2\pi^2} \frac{1}{[\tilde{\Delta}_0 - \epsilon x^2]^2 + x^2 [1 + \tilde{\Delta}_0 - \epsilon x^2]^2}, \quad (3.80)$$

Substituting $|\langle g_1 | \tilde{E}_{k'} \rangle|^2$ in Eq. 3.78 and converting the integral in k' to x' by substituting $x' = k'|a_{bg}|$ and using $\epsilon = E_{bg}/2\mu_B\Delta B$,

$$I_{E_k} = \frac{2}{\pi} \frac{1}{2\mu_B \Delta B} \mathcal{P} \int_0^\infty \frac{dx' x'^2}{(x'^2 - x^2)} \frac{1}{[\tilde{\Delta}_0 - \epsilon x'^2]^2 + x'^2 [1 + \tilde{\Delta}_0 - \epsilon x'^2]^2}. \quad (3.81)$$

As the integral in Eq. 3.81 is even in x' , we rewrite the integral by symmetrizing the limits of integration,

$$I_{E_k} = \frac{1}{\pi} \frac{1}{2\mu_B \Delta B} \mathcal{P} \int_{-\infty}^\infty \frac{dx' x'^2}{(x'^2 - x^2)} \frac{1}{[\tilde{\Delta}_0 - \epsilon x'^2]^2 + x'^2 [1 + \tilde{\Delta}_0 - \epsilon x'^2]^2}. \quad (3.82)$$

We rewrite Eq. 3.82 as,

$$I_{E_k} = \frac{1}{2\mu_B \Delta B} \tilde{I}_{E_k}, \quad (3.83)$$

where \tilde{I}_{E_k} is given by

$$\tilde{I}_{E_k} = \frac{1}{\pi} \mathcal{P} \int \frac{dx' x'^2}{(x'^2 - x^2)} \frac{1}{[\tilde{\Delta}_0 - \epsilon x'^2]^2 + x'^2 [1 + \tilde{\Delta}_0 - \epsilon x'^2]^2}. \quad (3.84)$$

Then Eq. 3.84 takes the form,

$$\tilde{I}_{E_k} = \mathcal{P} \int dx' g_c(x') f_c(\tilde{\Delta}_0, \epsilon, x'), \quad (3.85)$$

where $f_c(\tilde{\Delta}_0, \epsilon, x')$ is given by

$$f_c(\tilde{\Delta}_0, \epsilon, x') = \frac{\epsilon}{\pi} \frac{x'^2}{[\tilde{\Delta}_0 - \epsilon x'^2]^2 + x'^2 [1 + \tilde{\Delta}_0 - \epsilon x'^2]^2}, \quad (3.86)$$

and $g_c(x')$ is given by

$$g_c(x') = \frac{1}{\epsilon(x'^2 - x^2)}, \quad (3.87)$$

We further note from chapter 2 (Eq. 2.184 and Eq. 2.185), that

$$C(B) = \int_{-\infty}^{+\infty} dx' f_c(\tilde{\Delta}_0, \epsilon, x') = 1 - Z(B). \quad (3.88)$$

We will now study the behavior of $f_c(\tilde{\Delta}_0, \epsilon, x')$ in Eq. 3.86 and analyze whether some reasonable approximations can permit us to obtain an analytic form of the complicated integral \tilde{I}_{E_k} . We can see that the value of $f_c(\tilde{\Delta}_0, \epsilon, x')$ is maximum under the conditions,

- i) when $\tilde{\Delta}_0 - \epsilon x'^2 = 0$, which can be satisfied only when $\tilde{\Delta}_0 > 0$, or
- ii) when $1 + \tilde{\Delta}_0 - \epsilon x'^2 = 0$, which can be satisfied only when $1 + \tilde{\Delta}_0 > 0$.

For $\tilde{\Delta}_0 > 0$, we are on the right of the Feshbach resonance in the BCS regime and therefore $Z \rightarrow 0$ and $G \rightarrow 1$. We now evaluate the peak value of the integrand for the two cases. For $\tilde{\Delta}_0 > 0$ and $\tilde{\Delta}_0 - \epsilon x'^2 = 0$,

$$\begin{aligned} x'^2 &= \frac{\tilde{\Delta}_0}{\epsilon}, \\ f_c &\rightarrow \frac{\epsilon}{\pi}. \end{aligned} \quad (3.89)$$

For $1 + \tilde{\Delta}_0 > 0$ and $1 + \tilde{\Delta}_0 - \epsilon x'^2 = 0$,

$$\begin{aligned} x'^2 &= \frac{1 + \tilde{\Delta}_0}{\epsilon}, \\ f_c &\rightarrow \frac{1 + \tilde{\Delta}_0}{\pi}. \end{aligned} \quad (3.90)$$

We now evaluate \tilde{I}_{E_k} for the case of broad Feshbach resonance and narrow Feshbach resonance separately.

For broad Feshbach resonance, $\epsilon \ll 1$. Hence, Eq. 3.90 for the condition $1 + \tilde{\Delta}_0 > 0$ is the dominant case and Eq. 3.89 can be neglected compared to Eq. 3.90. However, the integral in Eq. 3.84 cannot be evaluated for the case $1 + \tilde{\Delta}_0 > 0$ by substituting $\epsilon = 0$, as $f_c(\tilde{\Delta}_0, \epsilon, x')$ exhibits a sharply peaked delta function-like behavior for $\epsilon \rightarrow 0$ as shown in Fig. 3.4. Hence, we use a trick where we evaluate the total integral \tilde{I}_{E_k} for the case $1 + \tilde{\Delta}_0 > 0$ by writing \tilde{I}_{E_k} as

$$\tilde{I}_{E_k} = \tilde{I}_{E_k}^a + \tilde{I}_{E_k}^b.$$

Now we use a two-step approach;

- i) We evaluate the integral $\tilde{I}_{E_k}^a$ near the place where $f_c(\tilde{\Delta}_0, \epsilon, x')$ is sharply peaked by removing $g_c(x')$ outside the integral and evaluating $g_c(x')$ at $x'^2 = \frac{1 + \tilde{\Delta}_0}{\epsilon}$.
- ii) We evaluate the integral $\tilde{I}_{E_k}^b$ at all other places except where $f_c(\tilde{\Delta}_0, \epsilon, x')$ shows the delta function behavior by subtracting the value of the integral $\tilde{I}_{E_k}^a$ evaluated in step 1 from the total integral.

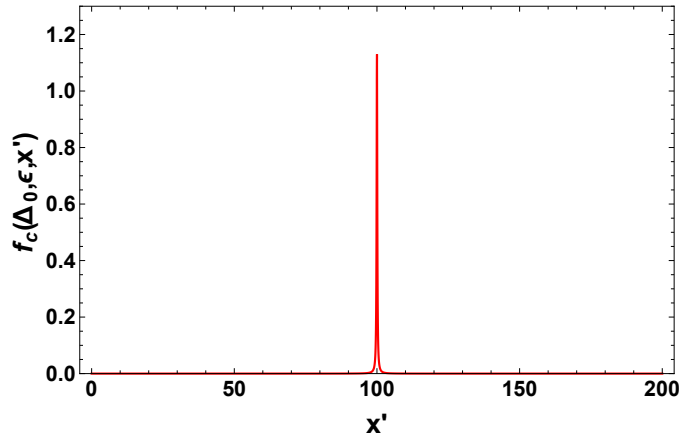


FIGURE 3.4: Plot of $f_c(\tilde{\Delta}_0, \epsilon, x')$ as a function of x for the case $\epsilon \ll 1$ when $\Delta_0 = 2.1$. ϵ is chosen to be $\epsilon = 0.00036$ for this plot as in the case of Broad Feshbach resonance in ${}^6\text{Li}$.

Hence, using the above prescription, from step (i) we have, for $1 + \tilde{\Delta}_0 > 0$,

$$\tilde{I}_{E_k}^a = \theta(1 + \tilde{\Delta}_0) \left[g_c(x') \Big|_{x'^2 = \frac{1 + \tilde{\Delta}_0}{\epsilon}} \int_{-\infty}^{+\infty} dx' f_c(\tilde{\Delta}_0, \epsilon, x') \right]. \quad (3.91)$$

The heaviside step function $\theta(1 + \tilde{\Delta}_0)$ in Eq. 3.91 imposes the condition that $1 + \tilde{\Delta}_0 > 0$. Evaluating $\tilde{I}_{E_k}^a$ in equation Eq. 3.91,

$$\tilde{I}_{E_k}^a = \frac{\theta(1 + \tilde{\Delta}_0)}{1 + \tilde{\Delta}_0 - \epsilon x^2} \int_{-\infty}^{+\infty} dx' f_c(\tilde{\Delta}_0, \epsilon, x'). \quad (3.92)$$

From Eq. 3.88, we know

$$\int_{-\infty}^{\infty} dx' f_c(x') \rightarrow 1, \quad \text{since} \quad Z \rightarrow 0 \quad \text{as} \quad \epsilon \rightarrow 0. \quad (3.93)$$

Using Eq. 3.93 in Eq. 3.92 and taking the limit $\epsilon \rightarrow 0$ gives

$$\lim_{\epsilon \rightarrow 0} \tilde{I}_{E_k}^a = \frac{\theta(1 + \tilde{\Delta}_0)}{1 + \tilde{\Delta}_0}. \quad (3.94)$$

Now using step (ii) outlined above, we get $\tilde{I}_{E_k}^b = \tilde{I}_{E_k} - \tilde{I}_{E_k}^a$,

$$\tilde{I}_{E_k}^b = \mathcal{P} \left\{ \int dx' g_c(x') f_c(\tilde{\Delta}_0, \epsilon, x') - g_c(x') \Big|_{x'^2 = \frac{1 + \tilde{\Delta}_0}{\epsilon}} \int_{-\infty}^{+\infty} dx' f_c(\tilde{\Delta}_0, \epsilon, x') \right\}$$

or

$$\tilde{I}_{E_k}^b = \theta(1 + \tilde{\Delta}_0) P \int_{-\infty}^{\infty} dx' \left[\frac{1}{\epsilon(x'^2 - x^2)} - \frac{1}{1 + \tilde{\Delta}_0 - \epsilon x^2} \right] f_c(x'). \quad (3.95)$$

where the second term in the above integral is the part of the sharp spike evaluated in step 1. Further algebraic reduction of Eq. 3.95 gives,

$$\tilde{I}_{E_k}^b = \frac{\theta(1 + \tilde{\Delta}_0)}{1 + \tilde{\Delta}_0 - \epsilon x^2} P \int_{-\infty}^{\infty} dx' \left[\frac{1 + \tilde{\Delta}_0 - \epsilon x'^2}{\epsilon(x'^2 - x^2)} \right] f_c(x'). \quad (3.96)$$

Now taking the limit $\epsilon \rightarrow 0$ in Eq. 3.96, canceling $1 + \tilde{\Delta}_0$ and using

$$f_c(\epsilon \rightarrow 0, x') = \frac{\epsilon}{\pi} \frac{x'^2}{\tilde{\Delta}_0^2 + (1 + \tilde{\Delta}_0)^2 x'^2}, \quad (3.97)$$

Eq. 3.96 becomes,

$$\lim_{\epsilon \rightarrow 0} \tilde{I}_{E_k}^b = \frac{\theta(1 + \tilde{\Delta}_0)}{\pi} P \int_{-\infty}^{\infty} \frac{dx'}{x'^2 - x^2} \frac{x'^2}{\tilde{\Delta}_0^2 + (1 + \tilde{\Delta}_0)^2 x'^2}. \quad (3.98)$$

The contour integral method as shown in Appendix B Eq. B.15, yields

$$\lim_{\epsilon \rightarrow 0} \tilde{I}_{E_k}^b = \frac{1}{\pi} \frac{\pi |\tilde{\Delta}_0|}{|1 + \tilde{\Delta}_0|} \frac{\theta(1 + \tilde{\Delta}_0)}{\tilde{\Delta}_0^2 + (1 + \tilde{\Delta}_0)^2 x^2}. \quad (3.99)$$

Using Eq. 3.94 and Eq. 3.99, the expression for the integral \tilde{I}_{E_k} for broad Feshbach resonance is given by,

$$\lim_{\epsilon \rightarrow 0} \tilde{I}_{E_k} = \lim_{\epsilon \rightarrow 0} \tilde{I}_{E_k}^a + \lim_{\epsilon \rightarrow 0} \tilde{I}_{E_k}^b = \frac{\theta(1 + \tilde{\Delta}_0)}{1 + \tilde{\Delta}_0} + \frac{|\tilde{\Delta}_0|}{|1 + \tilde{\Delta}_0|} \frac{\theta(1 + \tilde{\Delta}_0)}{\tilde{\Delta}_0^2 + (1 + \tilde{\Delta}_0)^2 x^2}. \quad (3.100)$$

For the narrow resonance, $\epsilon \gg 1$, we can see from Eq. 3.89 and Eq. 3.90, that the result for $\tilde{\Delta}_0 > 0$ is dominant. Although, $f_c(\tilde{\Delta}_0, \epsilon, x')$ does not show a delta function type of behavior for the case $\epsilon \gg 1$, it still has a maximum when the condition $\tilde{\Delta}_0 - \epsilon x'^2 = 0$ is satisfied. Hence, we follow the same recipe used in the case of broad resonance, where we evaluate the integral using a two-step approach.

From step (i) for $x'^2 = \frac{\tilde{\Delta}_0}{\epsilon}$ we have

$$\tilde{I}_{E_k}^a = \theta(\tilde{\Delta}_0) \left[g_c(x') \Big|_{x'^2 = \frac{\tilde{\Delta}_0}{\epsilon}} \int_{-\infty}^{+\infty} dx' f_c(\tilde{\Delta}_0, \epsilon, x') \right], \quad (3.101)$$

$$\tilde{I}_{E_k}^a = \frac{\theta(\tilde{\Delta}_0)}{\tilde{\Delta}_0 - \epsilon x^2} \int_{-\infty}^{+\infty} dx' f_c(\tilde{\Delta}_0, \epsilon, x'). \quad (3.102)$$

We recall from Eq. 3.88,

$$\int_{-\infty}^{+\infty} dx' f_c(\tilde{\Delta}_0, \epsilon, x') = 1 - Z. \quad (3.103)$$

Substituting Eq. 3.103 in Eq. 3.102, we get

$$\lim_{\epsilon \gg 1} \tilde{I}_{E_k}^a = \frac{1}{\tilde{\Delta}_0 - \epsilon x^2} [1 - Z]. \quad (3.104)$$

However, $Z = 0$, for $\tilde{\Delta}_0 > 0$. Hence,

$$\lim_{\epsilon \gg 1} \tilde{I}_{E_k}^a = \frac{\theta(\tilde{\Delta}_0)}{\tilde{\Delta}_0 - \epsilon x^2}. \quad (3.105)$$

Now from step (ii), we have

$$\begin{aligned} \tilde{I}_{E_k}^b &= \tilde{I}_{E_k} - \tilde{I}_{E_k}^a, \\ &= \mathcal{P} \left[\int g_c(x') f_c(\tilde{\Delta}_0, \epsilon, x') dx' - g_c(x') \Big|_{x'^2 = \frac{\tilde{\Delta}_0}{\epsilon}} \int_{-\infty}^{+\infty} dx' f_c(\tilde{\Delta}_0, \epsilon, x') \right] \end{aligned} \quad (3.106)$$

Using Eq. 3.101 and Eq. 3.102 in Eq. 3.106, gives

$$\tilde{I}_{E_k}^b = \theta(\tilde{\Delta}_0) \mathcal{P} \int_{-\infty}^{\infty} dx' \left[\frac{1}{\epsilon(x'^2 - x^2)} - \frac{1}{\tilde{\Delta}_0 - \epsilon x^2} \right] f_c(\tilde{\Delta}_0, \epsilon, x'), \quad (3.107)$$

where the second term in the above integral is the part of the sharp spike evaluated in step 1. Further reduction of Eq. 3.107 gives,

$$\tilde{I}_{E_k}^b = \frac{\theta(\tilde{\Delta}_0)}{\tilde{\Delta}_0 - \epsilon x^2} \mathcal{P} \int_{-\infty}^{\infty} dx' \left[\frac{\tilde{\Delta}_0 - \epsilon x'^2}{\epsilon(x'^2 - x^2)} \right] f_c(\tilde{\Delta}_0, \epsilon, x'). \quad (3.108)$$

From Eq. 3.86, we have

$$f_c(\tilde{\Delta}_0, \epsilon, x') = \frac{1}{\epsilon^2} \frac{\epsilon x'^2}{\pi \left(\frac{\tilde{\Delta}_0}{\epsilon} - x'^2 \right)^2 + \left(\frac{1 + \tilde{\Delta}_0}{\epsilon} - x'^2 \right)^2 x'^2}. \quad (3.109)$$

Substituting Eq. 3.109 in Eq. 3.108,

$$\tilde{I}_{E_k}^b = \frac{\theta(\tilde{\Delta}_0)}{\epsilon^2 \pi (\frac{\tilde{\Delta}_0}{\epsilon} - x^2)} \mathcal{P} \int_{-\infty}^{\infty} dx' \frac{x'^2}{x'^2 - x^2} \frac{(\frac{\tilde{\Delta}_0}{\epsilon} - x'^2)}{(\frac{\tilde{\Delta}_0}{\epsilon} - x'^2)^2 + (\frac{1+\tilde{\Delta}_0}{\epsilon} - x'^2)^2 x'^2}. \quad (3.110)$$

To check whether the integral converges for $\epsilon \gg 1$, we approximate $\tilde{\Delta}_0/\epsilon \rightarrow 0$ and $1 + \tilde{\Delta}_0/\epsilon \rightarrow 0$. Then Eq. 3.110 takes the form

$$\tilde{I}_{E_k}^b = \frac{\theta(\tilde{\Delta}_0)}{\epsilon^2 \pi x^2} \mathcal{P} \int_{-\infty}^{\infty} dx' \frac{x'^2}{x'^2 - x^2} \frac{x'^2}{(1 + x'^2) x'^4}. \quad (3.111)$$

We cancel the terms in the numerator and denominator,

$$\tilde{I}_{E_k}^b = \frac{\theta(\tilde{\Delta}_0)}{\epsilon^2 \pi x^2} \mathcal{P} \int_{-\infty}^{\infty} dx' \frac{1}{(x'^2 - x^2)(1 + x'^2)} \quad (3.112)$$

From Eq. 3.112, we can see that $\tilde{I}_{E_k}^b$ becomes negligible when $\epsilon \gg 1$ (narrow resonance), since the integral is finite and there is a factor of $1/\epsilon^2$ outside the integral. Hence, for narrow resonance $\tilde{I}_{E_k} = \tilde{I}_{E_k}^a$. Therefore,

$$\lim_{\epsilon \gg 1} \tilde{I}_{E_k} = \frac{\theta(\tilde{\Delta}_0)}{\tilde{\Delta}_0 - \epsilon x^2}. \quad (3.113)$$

Summarizing the results for the shift integrals \tilde{I}_{E_k} and \tilde{I}_E for both the broad and the narrow Feshbach resonance,

$$\begin{aligned} \tilde{I}_{E_k} &= \frac{\theta(1 + \tilde{\Delta}_0)}{1 + \tilde{\Delta}_0} + \frac{|\tilde{\Delta}_0|}{|1 + \tilde{\Delta}_0|} \frac{\theta(1 + \tilde{\Delta}_0)}{\tilde{\Delta}_0^2 + (1 + \tilde{\Delta}_0)^2 x^2}, \text{ for } \epsilon \ll 1 \text{ (broad resonance)} \\ &= \frac{\theta(\tilde{\Delta}_0)}{\tilde{\Delta}_0 - \epsilon x^2}, \text{ for } \epsilon \gg 1 \text{ (narrow resonance)} \end{aligned} \quad (3.114)$$

$$\begin{aligned}
\tilde{I}_E &= \frac{2\theta(-\tilde{\Delta}_0)\theta(1+\tilde{\Delta}_0)}{\tilde{\Delta}_0^2+x^2(1+\tilde{\Delta}_0)^2} \frac{|\tilde{\Delta}_0|}{|1+\tilde{\Delta}_0|}, \quad \text{for } \epsilon \ll 1 \text{ (broad resonance)} \\
&= \frac{\theta(-\tilde{\Delta}_0)}{\tilde{\Delta}_0 - \epsilon x^2}, \quad \text{for } \epsilon \gg 1 \text{ (narrow resonance)} \quad (3.115)
\end{aligned}$$

Hence, for the broad Feshbach resonance, for $1 + \tilde{\Delta}_0 > 0$, using Eq. 3.114 and Eq. 3.115,

$$S_B(\tilde{\Delta}_0, x) \equiv \tilde{I}_{E_k} - \tilde{I}_E = \frac{\tilde{\Delta}_0 + (1 + \tilde{\Delta}_0)x^2}{\tilde{\Delta}_0^2 + (1 + \tilde{\Delta}_0)^2 x^2}. \quad (3.116)$$

For the narrow Feshbach resonance, using Eq. 3.114 and Eq. 3.115, and $\theta(\tilde{\Delta}_0) + \theta(-\tilde{\Delta}_0) = 1$, gives

$$S_N(\tilde{\Delta}_0, x) \equiv \tilde{I}_{E_k} - \tilde{I}_E = \frac{1}{\tilde{\Delta}_0 - \epsilon x^2}. \quad (3.117)$$

Before we proceed further, it is important to show that the assumptions that were made in solving I_E and I_{E_k} are valid. Fig. 3.5 shows the comparison between the analytical results for the total shift (Eq. 3.116 and Eq. 3.117) obtained in this section and the exact results evaluated numerically for the total shift using Eq. 3.84 and Eq. 3.67 for the broad and the narrow Feshbach resonances. From Fig. 3.5, it is clear that the analytical results agrees closely with the exact values for both below and above the Feshbach resonance. Also note that for the broad resonance, Fig. 3.5 (top) the analytical and numerical results match even for $1 + \tilde{\Delta}_0 < 0$, although we arrived at an analytical solution by assuming $1 + \tilde{\Delta}_0 > 0$.

Using Eq. 3.67 and Eq. 3.83 in Eq. 3.61, we have

$$\frac{D'(E, E_k)}{\hbar} = \Delta_e(x) + \frac{\Omega_2^2}{4\delta(x)} + \frac{\Omega_1^2}{4} \frac{\hbar}{2\mu_B \Delta B} (\tilde{I}_{E_k} - \tilde{I}_E), \quad (3.118)$$

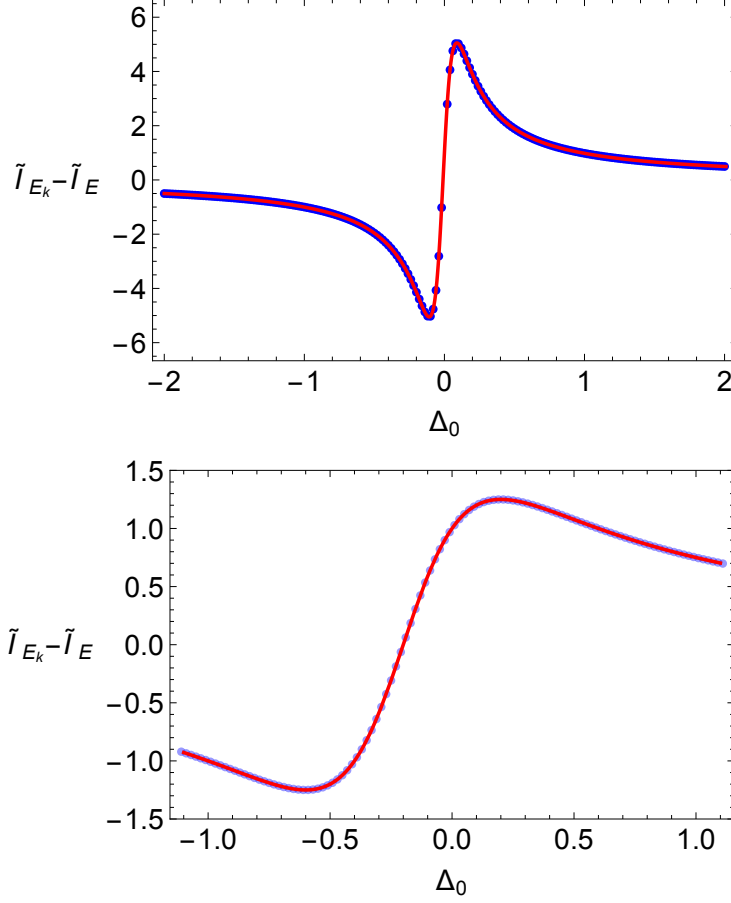


FIGURE 3.5: Comparison between exact shift (blue dots) evaluated numerically from Eq. 3.84 and Eq. 3.67 and analytic shift (red line) evaluated from Eq. 3.116 and Eq. 3.117 for (top) $x = 0.1$ in the case of broad Feshbach resonance ($\epsilon = 0.000361$) and (bottom) $x = 0.05$ in the case of narrow Feshbach resonance ($\epsilon = 555$). The analytic shift matches the exact shift for both $\Delta_0 < 0$ (below resonance) and $\Delta_0 > 0$ (above resonance).

Now we define $S \equiv \tilde{I}_{E_k} - \tilde{I}_E$, and rewrite Eq. 3.118 as

$$\frac{D'(E, E_k)}{\hbar} = \Delta_e(x) + \frac{\Omega_2^2}{4\delta(x)} + \frac{\Omega_1^2}{4} \frac{\hbar}{2\mu_B \Delta B} S(\tilde{\Delta}_0, x), \quad (3.119)$$

where $S(\tilde{\Delta}_0, x)$ is $S_B(\tilde{\Delta}_0, x)$ for the broad resonance (Eq. 3.116) and $S_N(\tilde{\Delta}_0, x)$ for the narrow resonance (Eq. 3.117), respectively. In Eq. 3.119, the momentum dependence $x = k|a_{bg}|$ of the detunings is shown explicitly. Substituting Eq. 3.119 in Eq. 3.44,

we arrive at the final expression for the energy shift function

$$\frac{D(E, E_k)}{\hbar} = -\Delta_e(x) - \frac{\Omega_2^2}{4\delta(x)} - \frac{\Omega_1^2}{4} \frac{\hbar}{2\mu_B \Delta B} S(\tilde{\Delta}_0, x) - i \frac{\gamma_e}{2} \quad (3.120)$$

3.6 Evaluation of the optically induced phase shift ϕ

We recall from Eq. 3.43 that the expression for the wave function of the dressed triplet continuum scattering state is

$$\Psi_{E_k}(r \rightarrow \infty) = \frac{b(k)}{kr\sqrt{V}} \left[\sin(kr + \Delta(k)) + \frac{\Omega_1^2}{4} \frac{2\pi^2 mk |\langle g_1 | \tilde{E}_k \rangle|^2}{D(E, E_k)} \cos(kr + \Delta(k)) \right]. \quad (3.121)$$

To maintain box-normalization of the input state, the output triplet scattering state Eq. 3.43 must take the form

$$\Psi_{E_k}(r \rightarrow \infty) = \frac{1}{\sqrt{V}} \frac{[\sin(kr + \Delta(k) + \phi(k))]}{kr}, \quad (3.122)$$

where $\Delta(k)$ is phase shift induced by the magnetic Feshbach resonance, $\phi(k)$ is the light-induced phase shift, and the total phase shift $\delta(k) \equiv \Delta(k) + \phi(k)$.

Expanding Eq. 3.122,

$$\Psi_{E_k}(r \rightarrow \infty) = \frac{1}{\sqrt{V}kr} [\sin(kr + \Delta(k)) \cos(\phi(k)) + \cos(kr + \Delta(k)) \sin(\phi(k))] \quad (3.123)$$

Comparing Eq. 3.123 with Eq. 3.121,

$$b(k) = \cos[\phi(k)], \quad (3.124)$$

$$b(k) \frac{\Omega_1^2}{4} \frac{2\pi^2 mk |\langle g_1 | \tilde{E}_k \rangle|^2}{D(E, E_k)} = \sin[\phi(k)]. \quad (3.125)$$

Dividing Eq. 3.124 by Eq. 3.125,

$$k \cot[\phi(k)] = \frac{D(E, E_k)}{\frac{\Omega_1^2}{4} 2\pi^2 m |\langle g_1 | \tilde{E}_k \rangle|^2} \quad (3.126)$$

Using $x = k|a_{bg}|$ in the above equation, we have

$$x \cot[\phi(k)] = \frac{D(E, E_k) |a_{bg}|}{\frac{\Omega_1^2}{4} 2\pi^2 m |\langle g_1 | \tilde{E}_k \rangle|^2} \quad (3.127)$$

From Eq. 3.80,

$$\begin{aligned} |\langle g_1 | \tilde{E}_k \rangle|^2 &= \frac{\epsilon |a_{bg}|^3}{2\pi^2} \frac{1}{[\tilde{\Delta}_0 - \epsilon x^2]^2 + x^2 [1 + \tilde{\Delta}_0 - \epsilon x^2]^2}, \\ &= \frac{\epsilon |a_{bg}|^3}{2\pi^2} L(\tilde{\Delta}_0, x), \end{aligned} \quad (3.128)$$

where $L(\tilde{\Delta}_0, x)$

$$L(\tilde{\Delta}_0, x) = \frac{1}{[\tilde{\Delta}_0 - \epsilon x^2]^2 + x^2 [1 + \tilde{\Delta}_0 - \epsilon x^2]^2}. \quad (3.129)$$

In Eq. 3.129, we recall from Eq. 3.65

$$\begin{aligned} \tilde{\Delta}_0 &= \frac{B - B_\infty}{\Delta B}, \\ \epsilon &= \frac{E_{bg}}{2\mu_B \Delta B}, \\ E_{bg} &= \frac{\hbar^2}{ma_{bg}^2}. \end{aligned} \quad (3.130)$$

From the result derived in the previous sections for the energy denominator $D'(E, E_k)$ in Eq. 3.120, we know

$$\frac{D(E, E_k)}{\hbar} = -\Delta_e(x) - \frac{\Omega_2^2}{4\delta(x)} - \frac{\Omega_1^2}{4} \frac{\hbar}{2\mu_B \Delta B} S(\tilde{\Delta}_0, x) - i \frac{\gamma_e}{2}. \quad (3.131)$$

Substituting Eq. 3.131 and Eq. 3.129 in Eq. 3.127, the optically induced phase shift $\phi(x)$ is determined by

$$x \cot[\phi(x)] = -\frac{\tilde{\Delta}_e(x) + \frac{\tilde{\Omega}_2^2}{4\tilde{\delta}(x)} + \frac{\tilde{\Omega}_1^2}{4} \frac{\hbar\gamma_e}{2\mu_B\Delta B} S(\tilde{\Delta}_0, x) + \frac{i}{2}}{\frac{\tilde{\Omega}_1^2}{4} \frac{\hbar\gamma_e}{2\mu_B\Delta B} L(\tilde{\Delta}_0, x)}, \quad (3.132)$$

where the dimensionless frequencies are

$$\tilde{\delta}(x) = \frac{\delta(x)}{\gamma_e}; \quad \tilde{\Delta}_e(x) = \frac{\Delta_e(x)}{\gamma_e}; \quad \tilde{\Omega}_2 = \frac{\Omega_2}{\gamma_e}; \quad \tilde{\Omega}_1 = \frac{\Omega_1}{\gamma_e}.$$

We recall from Eq. 3.51 and Eq. 3.55 that the single photon detuning $\Delta_e(x)$ and two-photon detuning $\delta(x)$ are defined in terms of x as

$$\Delta_e(x) = \Delta_L - \frac{2\mu_B(B - B_{ref})}{\hbar} + \frac{\hbar x^2}{m|a_{bg}|^2} \quad (3.133)$$

$$\delta_e(x) = \Delta_2 - \Delta_L + \frac{2\mu_B(B - B_{ref})}{\hbar} - \frac{\hbar x^2}{m|a_{bg}|^2}, \quad (3.134)$$

where Δ_L (Eq. 3.52) is the laser detuning for the $|T, k\rangle - |e\rangle$ transition defined at a reference magnetic field B_{ref} and Δ_2 (Eq. 3.56) is the laser detuning for the $|g_2\rangle - |e\rangle$ transition.

Eq. 3.132 gives the optically induced light shift in terms of measurable parameters and is the most important result of the continuum-dressed state model. Using Eq. 3.132, we can find the optically induced two-body loss rate, the zero-energy scattering length, and the effective range.

3.7 Evaluation of the total phase shift δ

Our objective is to evaluate the total phase shift δ , which is given by the sum of the light induced phase shift ϕ , and the Feshbach resonance phase shift Δ with no optical fields. Hence,

$$\delta(k) \equiv \Delta(k) + \phi(k) \quad (3.135)$$

From Eq. 3.135, we have

$$k \cot \delta = \frac{k \cot \Delta k \cot \phi - k^2}{k \cot \Delta + k \cot \phi} \quad (3.136)$$

Using $x = k|a_{bg}|$ in the above equation,

$$x \cot \delta = \frac{x \cot \Delta x \cot \phi - x^2}{x \cot \Delta + x \cot \phi}, \quad (3.137)$$

where the phase shift Δ induced by the magnetic Feshbach resonance is given in Appendix A, Eq. A.25 as

$$x \cot \Delta = \frac{\tilde{\Delta}_0 - \epsilon x^2}{1 + \tilde{\Delta}_0 - \epsilon x^2}, \quad (3.138)$$

and phase shift ϕ is derived in the previous section in Eq. 3.132.

In this chapter, the continuum-dressed model was used to derive the expression for the optically induced phase shift ϕ by replacing the bare state basis with the continuum-dressed state basis. In the next chapter, we will use the optically induced phase shift to predict the two-body scattering parameters, including the two-body loss rate constant K_2 , the zero-energy scattering length a , and the effective range r_{eff} .

Continuum-Dressed Model Predictions

In this chapter, I derive expressions for the two-body scattering parameters including the two-body loss rate K_2 , the zero energy scattering length a , and the effective range r_e , from the expression of optically induced phase shift derived in the previous chapter. In addition, we will use the continuum-dressed model to make predictions for K_2 and a near the broad and the narrow Feshbach resonances in ${}^6\text{Li}$ to elucidate the versatility of using our two-field method to control interactions near magnetic Feshbach resonances.

4.1 Two-body loss rate constant K_2

For two-body scattering, the optically induced loss between particles with density n_a and n_b is described by the two-body loss rate constant K_2 ,

$$\dot{n}_a = -(K_2 n_b) n_a \quad (4.1)$$

The two-body loss rate K_2 in the above equation can be written as

$$K_2(k) = v_{rel} \sigma_{inelastic} = \frac{\hbar k}{\mu} \sigma_{inelastic}, \quad (4.2)$$

where v_{rel} is the relative velocity between the two particles, μ is the reduced mass, and $\sigma_{inelastic}$ is the inelastic cross section. Now we proceed to evaluate K_2 by finding the inelastic cross section.

The relative momentum-dependent two-body scattering amplitude is given by

$$f(k) = \frac{1}{2ik}(e^{2i\delta} - 1) = \frac{1}{k \cot \delta(k) - ik}. \quad (4.3)$$

Let

$$k \cot \delta(k) \equiv q'(k) + iq''(k). \quad (4.4)$$

Substituting Eq. 4.4 in Eq. 4.3,

$$f(k) = \frac{1}{q'(k) - i[k - q''(k)]}. \quad (4.5)$$

From the definition of elastic cross section σ_{el} , we know

$$\sigma_{elastic} = 4\pi|f(k)|^2 = 4\pi \frac{1}{[q'(k)]^2 + [k - q''(k)]^2}. \quad (4.6)$$

The total cross section σ_{tot} is given by the optical theorem

$$\sigma_{total} = \frac{4\pi}{k} \text{Im}(f(k)) = \frac{4\pi}{k} \frac{(k - q''(k))}{[q'(k)]^2 + [k - q''(k)]^2}. \quad (4.7)$$

Using Eq. 4.6 and Eq. 4.7, we write the inelastic cross section $\sigma_{inelastic} = \sigma_{total} - \sigma_{elastic}$

$$\sigma_{inelastic} = \frac{4\pi}{k} \text{Im}(f(k)) - 4\pi|f(k)|^2 = \frac{-4\pi}{k} \frac{q''(k)}{[q'(k)]^2 + [k - q''(k)]^2}. \quad (4.8)$$

Substituting Eq. 4.8 in Eq. 4.2 with $\mu = m/2$, yields

$$K_2(k) = \frac{-8\pi\hbar}{m} \frac{q''(k)}{[q'(k)]^2 + [k - q''(k)]^2}. \quad (4.9)$$

Since we derived the expression for the optically induced phase shift ϕ as a function of $x = k|a_{bg}|$, it is useful to write K_2 in terms of x rather than k . Therefore we let

$$\begin{aligned}\tilde{q}(x) &\equiv q(k) |a_{bg}| \\ x \cot \delta(k) &\equiv \tilde{q}'(x) + i\tilde{q}''(x).\end{aligned}\tag{4.10}$$

From Eq. 4.9 and Eq. 4.10, we have

$$K_2(x) = \frac{-8\pi\hbar}{m} |a_{bg}| \frac{\tilde{q}''(x)}{[\tilde{q}'(x)]^2 + [x - \tilde{q}''(x)]^2}.\tag{4.11}$$

The above expression for K_2 assumes that the scattering atoms have a well defined incoming relative momentum k . However, for a thermal cloud of atoms, that is not the case. Hence we need to determine the expression for a momentum averaged K_2 . For simplicity, we assume a classical Boltzmann distribution of relative momentum, which is applicable for the experimental temperatures reported in this thesis. For a classical Boltzmann distribution of relative momentum k we have,

$$\langle K_2(k) \rangle = \int_0^\infty \frac{4\pi k^2 dk}{(k_0\sqrt{\pi})^3} e^{-\frac{k^2}{k_0^2}} K_2(x)\tag{4.12}$$

We know $(\hbar k_0)^2 = 2\mu k_B T = m k_B T$, so that

$$\begin{aligned}\hbar k_0 &\equiv \sqrt{m k_B T} \\ x &= k|a_{bg}| \\ x_0 &= k_0|a_{bg}|\end{aligned}\tag{4.13}$$

Using Eq. 4.13 in Eq. 4.12, we get

$$\langle K_2(k) \rangle = \int_0^\infty \frac{4\pi x^2 dx}{(x_0\sqrt{\pi})^3} e^{-\frac{x^2}{x_0^2}} K_2(x).\tag{4.14}$$

We substitute $x = ux_0$, to arrive at the final expression for the momentum averaged K_2 ,

$$\langle K_2(k) \rangle = \frac{4}{\sqrt{\pi}} \int_0^\infty du u^2 e^{-u^2} K_2(ux_0). \quad (4.15)$$

From Eq. 4.11, natural unit of K_2 is $h|a_{bg}|/m$ and is given in cm^3/s .

4.2 Procedure for calculating K_2

Before I try to plot K_2 for different cases, I will save the reader the trouble of looking at several equations buried in multiple chapters in this thesis. Here, I will summarize the necessary equations and provide a seven step approach for calculating K_2 .

Step 1: Assigning input values. The input parameters can be differentiated into constants that depend on the particular atom under investigation and experimental parameters. The constants are the mass of the atom m , Bohr magneton μ_B , reference magnetic field B_{ref} , resonance magnetic field B_{res} , width of the resonance ΔB , background scattering length a_{bg} , and the linewidth of the optical transition γ_e .

The experimental parameters are temperature T , Rabi frequency Ω_1 for the control laser, Rabi frequency Ω_2 for the EIT laser and the optical detunings. These include the laser detuning Δ_L for the $|T, k\rangle - |e\rangle$ transition, the laser detuning Δ_1 for the $|g_1\rangle - |e\rangle$ transition, and the laser detuning Δ_2 for the $|g_2\rangle - |e\rangle$ transition.

For the broad Feshbach resonance in ${}^6\text{Li}$, we choose $B_{ref} = B_{res} = 832.2$ G and $a_{bg} = -1405 a_0$ and for the narrow Feshbach resonance in ${}^6\text{Li}$, we choose $B_{ref} = B_{res} = 543.2$ G and $a_{bg} = 62 a_0$. The optical transition linewidth γ_e for the singlet molecular transition in ${}^6\text{Li}$ is $2\pi \times 11.8$ MHz.

Step 2: From the input parameters in Step 1, we calculate the following quantities,

$$k_0 = \frac{\sqrt{mk_B T}}{\hbar}$$

$$\begin{aligned}
x &= k_0 |a_{bg}| \\
\tilde{\Delta}_0 &= \frac{B - B_{res}}{\Delta B} \\
\tilde{E}_{bg} &= \frac{\hbar^2}{m a_{bg}^2} \\
\epsilon &= \frac{\tilde{E}_{bg}}{2\mu_B \Delta B} \\
\Delta_e &= \Delta_L - 2\mu_B(B - B_{ref}) + \frac{\hbar^2 x^2}{m |a_{bg}|^2} \\
\delta &= \Delta_2 - \Delta_L + 2\mu_B(B - B_{ref}) - \frac{\hbar^2 x^2}{m |a_{bg}|^2}
\end{aligned}$$

Step 3: From the quantities evaluated in Step (2), we calculate $L(\tilde{\Delta}_0, x)$ and the shift integrals $S_B(\tilde{\Delta}_0, x)$ and $S_N(\tilde{\Delta}_0, x)$.

$$L(\tilde{\Delta}_0, x) = \frac{1}{[\tilde{\Delta}_0 - \epsilon x^2]^2 + x^2 [1 + \tilde{\Delta}_0 - \epsilon x^2]^2}$$

For broad Feshbach resonance,

$$S_B(\tilde{\Delta}_0, x) = \frac{\tilde{\Delta}_0 + (1 + \tilde{\Delta}_0)x^2}{\tilde{\Delta}_0^2 + (1 + \tilde{\Delta}_0)^2 x^2}$$

For narrow Feshbach resonance,

$$S_N(\tilde{\Delta}_0, x) = \frac{1}{\tilde{\Delta}_0 - \epsilon x^2}$$

Step 4: From the shift integrals evaluated in Step (3), we calculate the phase shift due to the magnetic Feshbach resonance Δ , phase shift due to the optical fields

ϕ , and the total phase shift δ .

$$\begin{aligned}
x \cot \Delta &= \frac{\tilde{\Delta}_0 - \epsilon x^2}{1 + \tilde{\Delta}_0 - \epsilon x^2} \\
x \cot \phi &= -\frac{\tilde{\Delta}_e(x) + \frac{\tilde{\Omega}_2^2}{4\delta(x)} + \frac{\tilde{\Omega}_1^2}{4} \frac{\hbar\gamma_e}{2\mu_B\Delta B} S(\tilde{\Delta}_0, x) + \frac{i}{2}}{\frac{\tilde{\Omega}_1^2}{4} \frac{\hbar\gamma_e}{2\mu_B\Delta B} L(\tilde{\Delta}_0, x)} \\
x \cot \delta &= \frac{x \cot \Delta x \cot \phi - x^2}{x \cot \Delta + x \cot \phi}
\end{aligned}$$

Step 5: From Step (4), We calculate the real part $\tilde{q}(x)'$ and imaginary part $\tilde{q}(x)''$ of the total phase shift δ .

$$\begin{aligned}
\tilde{q}'(x) &= \text{Re}[x \cot \delta] \\
\tilde{q}''(x) &= \text{Im}[x \cot \delta]
\end{aligned}$$

Step 6: From $\tilde{q}(x)'$ and $\tilde{q}(x)''$ evaluated in Step (5), we calculate the momentum dependent $K_2(x)$ using the expression,

$$K_2(x) = \frac{-8\pi\hbar}{m} |a_{bg}| \frac{\tilde{q}(x)''}{[\tilde{q}'(x)]^2 + [x - \tilde{q}''(x)]^2},$$

Step 7: Finally, we substitute $x = ux_0$ and evaluate the momentum averaged $\langle K_2(k) \rangle$ from $K_2(x)$ evaluated in Step (6) using the expression,

$$\langle K_2(u) \rangle = \frac{4}{\sqrt{\pi}} \int_0^\infty du u^2 e^{-u^2} K_2(ux_0). \quad (4.16)$$

4.3 Two-body loss rate K_2 near broad Feshbach resonance

In this section, we will study the two-body loss rate K_2 near the broad Feshbach resonance. K_2 is a measure of atom loss due to spontaneous scattering and has the units of cm^3/s . The typical densities of our atom cloud is $\bar{n} \approx 10^{12}/\text{cm}^3$. For a

$K_2 \approx 10^{-11}$ cm³/s, the lifetime of the atoms is 100 ms. With our two-field method, we can reach $K_2 \approx 10^{-11}$ cm³/s as illustrated in the plots below.

The relevant energy states and the detunings required to explain the predictions of the continuum-dressed state model are summarized in Table. 4.1 and Table. 4.2, respectively.

Table 4.1: Energy states for closed channel EIT

States	Definition
$ T, k\rangle$	Triplet continuum scattering state with momentum k .
$ g_1^b\rangle$	Broad singlet ground vibrational state with a hyperfine coupling of $V_{HF} = h \times 131.6$ MHz with $ T, k\rangle$ resulting in the broad Feshbach resonance at 832.2 G.
$ g_1^n\rangle$	Narrow singlet ground vibrational state with a hyperfine coupling of $V_{HF} = h \times 5.9$ MHz with $ T, k\rangle$ resulting in the narrow Feshbach resonance at 543.2 G.
$ g_2\rangle$	Singlet ground vibrational state that is lower in energy than $ g_1\rangle$.
$ e\rangle$	Singlet excited vibrational state.

We start with a simple plot of K_2 vs the single-photon detuning Δ_e near the broad Feshbach resonance at a fixed B-field of 825 G. Fig. 4.1 shows a comparison of the two field loss spectra (red curve) and the single field loss spectra (blue curve) for $\Omega_1 = 1 \gamma_e$, and $\Omega_2 = 1 \gamma_e$, where $\gamma_e = 2\pi \times 11.8$ MHz is the molecular transition linewidth.

Since we are studying the behavior near the broad Feshbach resonance, we take $B_{ref} = B_{res} = 832.2$ G. Therefore, the detuning for the $|T, k\rangle \rightarrow |e\rangle$ transition $\Delta_L = 0$ at $B = 832.2$ G. Note that the single photon detuning $\Delta_e = \Delta_L - 2\mu_B(B - B_{ref})$ can be changed either by changing the magnetic field B or the control laser frequency ω_1 . For the plots shown here for broad Feshbach resonance, we change the control laser frequency ω_1 and hold the magnetic field B constant. We choose the EIT (ω_2) beam

to be resonant for the $|g_2\rangle \rightarrow |e\rangle$ transition i.e., the detuning $\Delta_2 = 0$. The condition for EIT loss suppression is satisfied when two-photon detuning $\delta_e = \Delta_2 - \Delta_e = 0$.

Table 4.2: Zero energy detunings for closed channel EIT

Detuning	Definition
Δ_1	Detuning for the $ g_1\rangle - e\rangle$ transition
Δ_2	Detuning for the $ g_2\rangle - e\rangle$ transition
Δ_L	Detuning for the $ T\rangle - e\rangle$ transition defined at a reference magnetic field B_{ref} .
Δ_e	Single photon detuning, $\Delta_e = \Delta_L - 2\mu_B(B - B_{ref})$
δ_e	Two photon detuning, $\delta_e = \Delta_2 - \Delta_e$

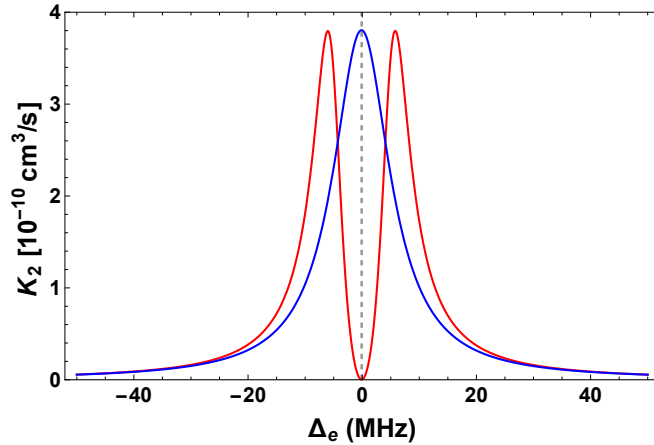


FIGURE 4.1: Two-body loss rate K_2 near the broad Feshbach resonance at $B = 825$ G as a function of single-photon detuning Δ_e by changing the frequency ω_1 of the control laser as predicted by the continuum-dressed state model. The single-field loss (blue) peaks when $\Delta_e = 0$ and two-field loss suppressed (red) when the two-photon detuning $\delta_e = \Delta_2 - \Delta_e = 0$. $T = 10 \mu K$, $\Omega_1 = 1 \gamma_e$, and $\Omega_2 = 1 \gamma_e$, where the molecular transition linewidth $\gamma_e = 2\pi \times 11.8$ MHz.

We use $T = 10 \mu K$ for all the plots so that we are not in the degenerate regime and the relative momentum k of the atoms follows a classical Boltzmann distribution.

The control beam creates atom loss (Fig. 4.1 red) by pumping the free atoms in the triplet continuum $|T, k\rangle$, which is mixed with the broad singlet ground state

$|g_1^b\rangle$ (Table. 4.1), to the singlet excited state $|e\rangle$. For $\Delta_e = 0$, the control beam is resonant for the $|T, k\rangle - |e\rangle$ transition and creates peak atom loss. The control beam does not cause an appreciable light shift of the state $|g_1^b\rangle$ near the broad resonance, since the hyperfine coupling V_{HF} between $|g_1^b\rangle$ and $|T, k\rangle$ is much stronger than Ω_1 .

The EIT beam suppresses atom loss due to destructive quantum interference between the two paths, $|T, k\rangle - |e\rangle$ and $|g_2\rangle - |e\rangle - |T, k\rangle$. This phenomenon of creating a transmission window in an absorption peak is called “electromagnetically induced transparency” (EIT) [55]. Loss suppression is maximum when the two-photon detuning $\delta_e = \Delta_2 - \Delta_e = 0$. Since we chose $\Delta_2 = 0$, maximum loss suppression occurs at $\Delta_e = 0$.

4.3.1 Two-body loss rate K_2 for different Rabi frequencies Ω_2

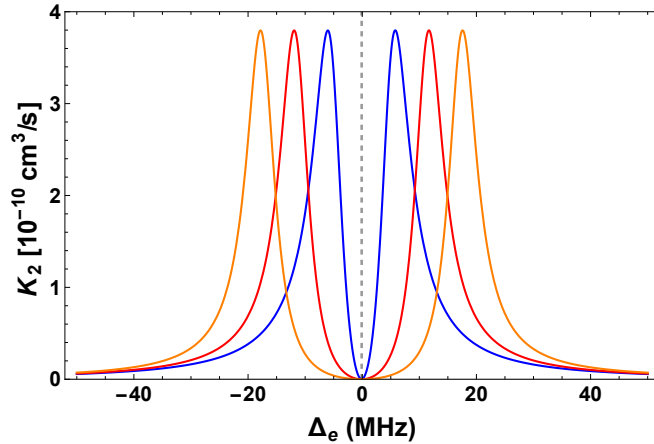


FIGURE 4.2: Two-body loss rate K_2 vs single photon detuning Δ_e for fixed $\Omega_1 = 1 \gamma_e$ and $\Omega_2 = 1 \gamma_e$ (blue), $\Omega_2 = 2 \gamma_e$ (red), and $\Omega_2 = 3 \gamma_e$ (orange). $B = 825 \text{ G}$; $T = 10 \mu\text{K}$. As Ω_2 increases for fixed Ω_1 , the width of the EIT window increases.

Fig. 4.2 shows the effect of changing the Rabi frequency of the EIT beam Ω_2 on loss suppression for three different cases, namely, $\Omega_2 = 1 \gamma_e$, $\Omega_2 = 2 \gamma_e$, and $\Omega_2 = 3 \gamma_e$. We take $\Omega_1 = 1 \gamma_e$ for all three cases. As expected, increasing the Rabi frequency of the Ω_2 beam, increases the width of suppression window and decreases the absolute value of K_2 at two-photon detuning $\delta_e = 0$.

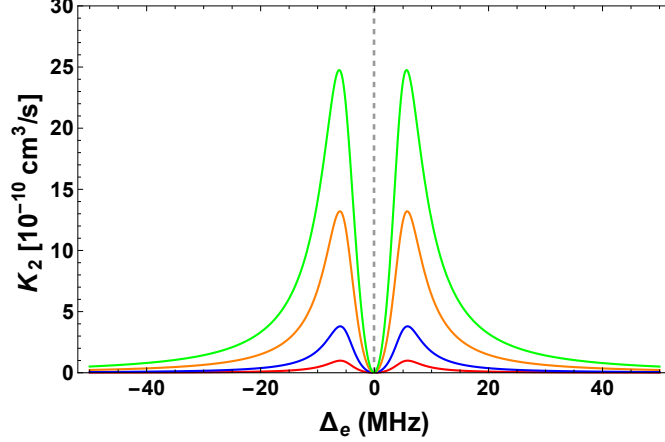


FIGURE 4.3: Two-body loss rate K_2 vs single photon detuning Δ_e for fixed $\Omega_2 = 1 \gamma_e$ and $\Omega_1 = 0.5 \gamma_e$ (red), $\Omega_1 = 1 \gamma_e$ (blue), $\Omega_1 = 2 \gamma_e$ (orange), and $\Omega_1 = 3 \gamma_e$ (green). $B = 825 \text{ G}$; $T = 10 \mu\text{K}$. As Ω_1 increases for fixed Ω_2 , the width of the EIT window decreases.

4.3.2 Two-body loss rate K_2 vs Rabi frequency Ω_1

The effect of changing the Rabi frequency of control laser Ω_1 on loss suppression is shown in Fig. 4.3 for four cases, namely, $\Omega_1 = 0.5 \gamma_e$, $\Omega_1 = 1 \gamma_e$, $\Omega_1 = 2 \gamma_e$, and $\Omega_1 = 3 \gamma_e$. We take $\Omega_2 = 1 \gamma_e$ for all four cases. We can clearly see that increasing Ω_1 increases the absolute value of K_2 and decreases the width of the transparency window.

4.3.3 Two-body loss rate K_2 vs ratio of Rabi frequencies Ω_1/Ω_2

Fig. 4.2 and Fig. 4.3 indicate that the width of the suppression window can be increased by either increasing Ω_2 or decreasing Ω_1 . However, it is important not to misperceive that the *ratio* of Ω_2 and Ω_1 determines the width of the suppression window. This is illustrated in Fig. 4.4 where three different cases, namely, $\Omega_1 = \Omega_2 = 1 \gamma_e$, $\Omega_1 = \Omega_2 = 2 \gamma_e$, and $\Omega_1 = \Omega_2 = 3 \gamma_e$ are plotted. We can clearly see that, although the ratio of Ω_2 and Ω_1 is held constant at 1, as Ω_2 increases, the width of the suppression window increases, indicating that Ω_2 dominates over Ω_1 in determining the width of the EIT window. Hence, in pursuing spectroscopic experiments, when

we are trying to find the loss suppression for the very first time, it is always better to use the maximum intensity available in the EIT beam, thereby maximizing Ω_2 .

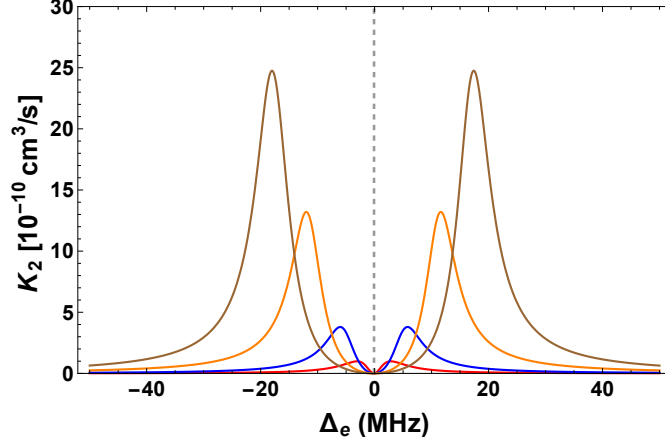


FIGURE 4.4: Two-body loss rate K_2 vs single photon detuning Δ_e for $\frac{\Omega_1}{\Omega_2} = 1$ and $\Omega_1 = \Omega_2 = 0.5 \gamma_e$ (red), $\Omega_1 = \Omega_2 = 1 \gamma_e$ (blue), $\Omega_1 = \Omega_2 = 2 \gamma_e$ (orange), and $\Omega_1 = \Omega_2 = 3 \gamma_e$ (Brown). $B = 825$ and $T = 10 \mu K$. Although the ratio $\frac{\Omega_1}{\Omega_2}$ is held constant at 1, higher Ω_2 increases the width of the EIT window.

4.3.4 Two-body loss rate K_2 vs detuning Δ_2

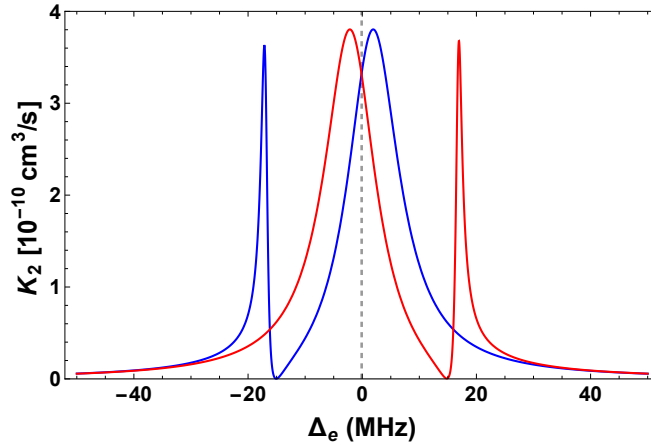


FIGURE 4.5: Two-body loss rate K_2 vs single photon detuning Δ_e at $B = 825$ G for $|\Delta_2| < 2 \gamma_e$. For $\Delta_2 = +15$ MHz, loss suppression occurs at $\delta_e = \Delta_2 - \Delta_e = 0$, i.e., $\Delta_e = 15$ MHz (red) and for $\Delta_2 = -15$ MHz, loss suppression occurs at $\Delta_e = -15$ MHz (blue). $T = 10 \mu K$, $\Omega_1 = 1 \gamma_e$, and $\Omega_2 = 1 \gamma_e$.

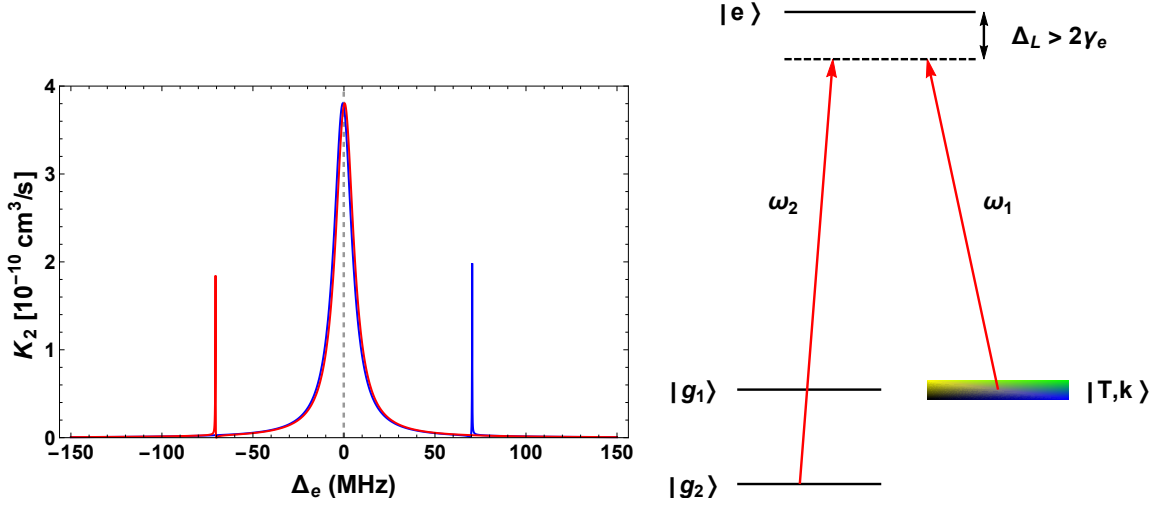


FIGURE 4.6: Two-photon Raman absorption as evidenced by the appearance of two narrow absorption peaks when $|\Delta_2| > 2\gamma_e$. Two-body loss rate K_2 vs single photon detuning Δ_e at $B = 825$ G for $\Delta_2 > 2\gamma_e$. EIT beam no longer suppresses loss in the absorption spectrum but instead causes additional loss due to two-photon Raman absorption. For $\Delta_2 = 60$ MHz, the two-photon absorption peak can be seen for $\Delta_e = 60$ MHz (blue), and for $\Delta_2 = -60$ MHz, the two-photon absorption peak can be seen for $\Delta_e = -60$ MHz (red). $T = 10 \mu K$, $\Omega_1 = 1\gamma_e$, and $\Omega_2 = 1\gamma_e$.

The effect of the detuning of EIT beam Δ_2 on the suppression window is shown in Fig. 4.5. For $|\Delta_2| < 2\gamma_e$, we observe an asymmetric suppression window with respect to the center of the absorption spectra due to EIT. For $\Delta_2 = +15$ MHz, loss suppression occurs at $\delta_e = \Delta_2 - \Delta_e = 0$, i.e., $\Delta_e = 15$ MHz (red) and for $\Delta_2 = -15$ MHz, loss suppression occurs at $\Delta_e = -15$ MHz (blue).

For $\Delta_2 > 2\gamma_e$ (Fig. 4.6), there is no loss suppression in the original absorption spectra due to the EIT beam, Instead the EIT beam produces additional loss at $\delta_e = 0$ through a process called two-photon Raman absorption. For $\Delta_2 = 60$ MHz, the two-photon absorption peak can be seen for $\Delta_e = 60$ MHz (blue), and for $\Delta_2 = -60$ MHz, the two-photon absorption peak can be seen for $\Delta_e = -60$ MHz (red).

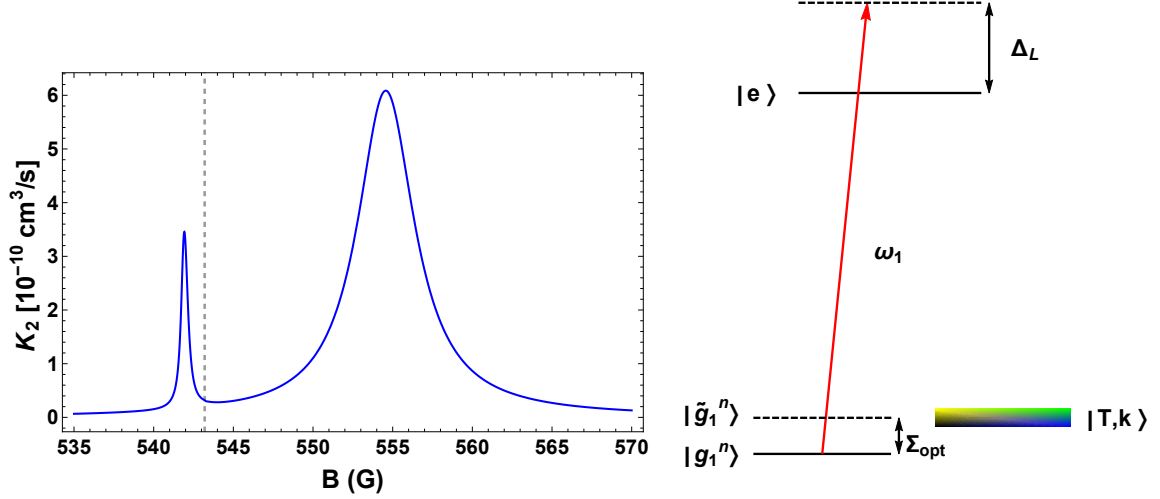


FIGURE 4.7: Shifting the narrow Feshbach resonance using a single optical field. (left) Two-body loss rate constant K_2 as a function of magnetic field near the narrow Feshbach resonance at 543.2 G and (right) corresponding level structure. The control laser Ω_1 is detuned from the $|g_1\rangle - |e\rangle$ transition by $\Delta_L = 31.6$ MHz. Therefore it light shifts the narrow Feshbach resonance state $|g_1\rangle$ at 543.2 G (vertical dashed line) to the left to a new magnetic field $B'_{res} = 541.9$ G. Atom loss occurs when $|T\rangle$ is magnetically tuned to be resonant with the shifted narrow singlet state $|\tilde{g}_1^n\rangle$ giving rise to the narrow peak. The broad peak arises as a result of optical pumping from $|T\rangle$ due to its overlap with broad singlet state $|g_1^b\rangle$. $\Omega_1 = 2\gamma_e$, $\Omega_2 = 0$, and $T = 10 \mu K$.

4.4 Two-body loss rate K_2 near narrow Feshbach resonance

When working near the narrow Feshbach resonance, we take $B_{ref} = B_{res} = 543.2$ G. Therefore, the detuning for the $|T, k\rangle \rightarrow |e\rangle$ transition is $\Delta_L = 0$ at $B_{ref} = 543.2$ G. The detuning for the $|g_1\rangle - |e\rangle$ transition is $\Delta_1 = \Delta_L$.

We begin our discussion with a simple plot of K_2 as a function of magnetic field when a single optical field, the control field (ω_1), illuminates the atoms. Fig. 4.7 (left) shows loss spectra near the narrow Feshbach resonance as a function of magnetic field, when the control beam (ω_1) of Rabi frequency $\Omega_1 = 2\gamma_e$ and detuning $\Delta_L = 31.6$ MHz illuminates the atoms. Fig. 4.7 (right) show the corresponding level scheme. The loss spectra shows two absorption peaks, a broad loss peak at 554 G and a narrow

loss peak at 541.9 G. The dotted line shows the position of the unshifted resonance at 543.2 G.

Near the narrow Feshbach resonance, the hyperfine coupling between the triplet continuum $|T, k\rangle$ and the narrow singlet ground state $|g_1^n\rangle$ (Table. 4.1), is comparable to the Rabi frequency Ω_1 . The control beam strongly mixes the singlet ground state $|g_1^n\rangle$ with the singlet excited state $|e\rangle$, resulting in an energy shifted narrow singlet state $|\tilde{g}_1^n\rangle$ (Fig. 4.7 right). This causes a corresponding shift of the narrow magnetic Feshbach resonance position at $B_{res} = 543.2$ G (vertical dashed line) to a new magnetic field $B'_{res} = 541.9$ G (narrow peak). The shift of the Feshbach resonance in units of frequency is given by $\Sigma_{opt} = 2\mu_B(543.2 - B'_{res})/\hbar = 3.64$ MHz. A red-detuned control beam shifts the resonance to a lower magnetic field and a blue-detuned control beam shifts the resonance to a higher magnetic field.

The control beam creates atom loss by pumping atoms from the triplet continuum $|T, k\rangle$ to the excited singlet state $|e\rangle$. However, near the narrow Feshbach resonance, $|T, k\rangle$ mixes with both the broad singlet state $|g_1^b\rangle$ and the light shifted narrow singlet state $|\tilde{g}_1^n\rangle$ resulting in two absorption peaks, a broad and a narrow peak.

The control beam is resonant with the $|T, k\rangle \rightarrow |e\rangle$ transition when the single-photon detuning $\Delta_e = \Delta_L - 2\mu_B(B - B_{ref}) = 0$. Therefore, maximum loss occurs at $B = B_{ref} + \hbar\Delta_L/2\mu_B = 554$ G, resulting in the broad loss peak.

As the triplet continuum is tuned by changing the magnetic field to resonance with the shifted narrow singlet state $|\tilde{g}_1^n\rangle$, the coupling strength $\langle T, k | \tilde{g}_1^n \rangle$ maximizes resulting in the narrow loss peak.

4.4.1 Shift of the narrow Feshbach resonance vs Rabi frequency Ω_1

Fig. 4.8 shows K_2 as a function of B-field for three different values of the control beam Rabi frequency Ω_1 of the control beam, namely $\Omega_1 = 1\gamma_e, 2\gamma_e,$ and $3\gamma_e$. As Ω_1 increases, the mixing between $|g_1^n\rangle$ and $|e\rangle$ increases, resulting in larger shift of

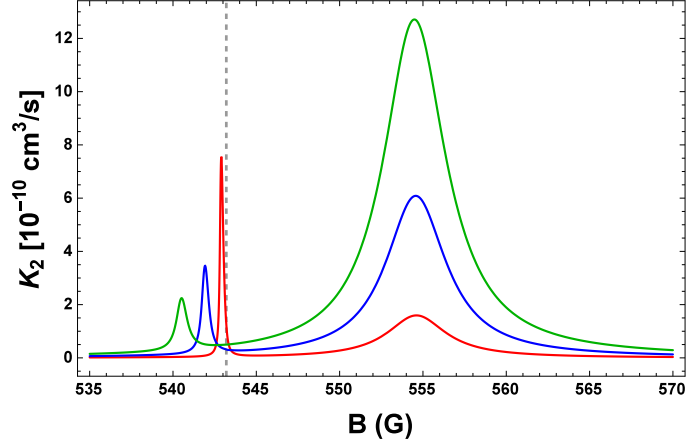


FIGURE 4.8: Shifting the narrow Feshbach resonance at 543.2 G (vertical dashed line) for $\Omega_1 = 1\gamma_e$ (red), $\Omega_2 = 2\gamma_e$ (blue), and $\Omega_2 = 3\gamma_e$ (green). The control laser Ω_1 is detuned from the $|g_1\rangle - |e\rangle$ transition by $\Delta_L = 31.6$ MHz. As Ω_1 increases, the coupling between $|g_1^n\rangle$ and $|e\rangle$ increases, resulting in more shift and reduced K_2 for the narrow peak. For the broad peak, increasing Ω_1 , increases the transition rate resulting in higher K_2 . $\Omega_2 = 0$ and $T = 10\mu K$.

the resonance and reduced coupling strength between $|\tilde{g}_1^n\rangle$ and $|T\rangle$. This is clearly illustrated in Fig. 4.8, where as Ω_1 is increased, it increases the shift of the narrow peak and diminishes the amplitude of K_2 . For the broad loss peak, increase in Ω_1 increases the rate of transition thereby increasing the amplitude of K_2 .

4.4.2 EIT loss suppression near narrow Feshbach resonance

Similar to loss suppression near the broad resonance using the EIT beam, loss suppression near the narrow resonance can be achieved by choosing the correct frequency for the EIT laser. The detuning Δ_2 for the $|g_2\rangle - |e\rangle$ transition can be chosen to suppress loss either at the broad peak or the narrow peak.

Fig. 4.9 shows loss suppression at the broad peak due to the EIT beam for $\Omega_1 = 1\gamma_e$ and $\Omega_2 = 1\gamma_e$. In this case, the EIT beam is on resonance ($\Delta_2 = 0$). Loss suppression occurs when the two-photon detuning $\delta_e = \Delta_2 - \Delta_e = 0$. Since $\Delta_2 = 0$, maximum loss suppression occurs at $\Delta_e = \Delta_L - 2\mu_B(B - B_{ref}) = 0$ i.e., at a magnetic field $B = B_{ref} + \hbar\Delta_L/2\mu_B = 554$ G.

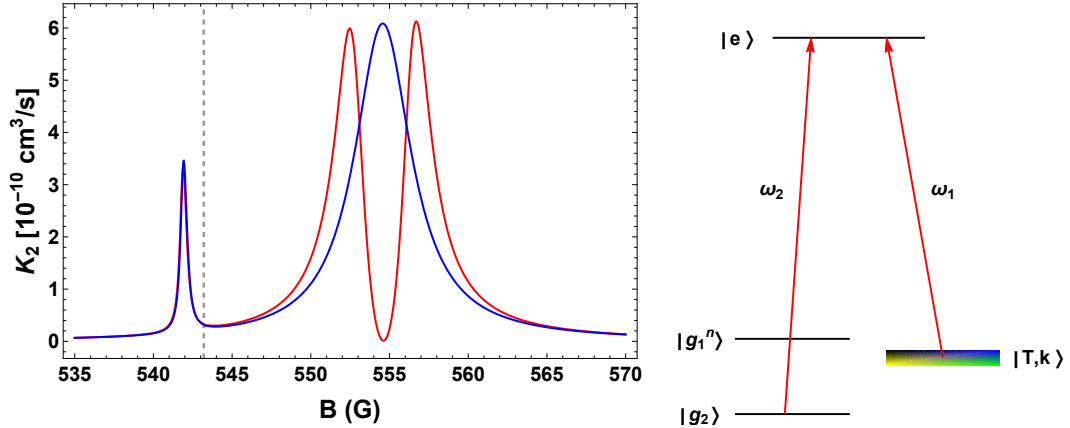


FIGURE 4.9: (left) EIT loss suppression at the broad peak (red) near the narrow Feshbach resonance and (right) corresponding level structure. Vertical dashed line represents unshifted narrow Feshbach resonance at 543.2 G. Single field loss is shown in blue. The frequency ω_2 of the EIT laser is chosen to suppress loss at the broad peak. The control laser Ω_1 is detuned from the $|g_1\rangle - |e\rangle$ transition by $\Delta_L = 31.6$ MHz. The EIT laser is on resonance with the $|g_2\rangle - |e\rangle$ transition i.e., $\Delta_2 = 0$. $\Omega_1 = 2\gamma_e$, $\Omega_2 = 1\gamma_e$, and $T = 10\mu K$.

Fig. 4.10 shows loss suppression at the narrow peak due to the EIT beam for $\Omega_1 = 1\gamma_e$ and $\Omega_2 = 1\gamma_e$. Loss suppression at the shifted narrow peak occurs when the detuning of the EIT beam $\Delta_2 = \Delta_L + \Sigma_{opt}$ (Fig. 4.10 right), where $\Sigma_{opt} = 2\mu_B(543.2 - B'_{res})$. In this case, maximum loss suppression occurs when the two-photon detuning $\delta_e = \Delta_2 - \Delta_e = 0$. Since $\Delta_2 = \Delta_e = \Delta_L + \Sigma_{opt}$, maximum loss suppression occurs when the magnetic field $B = B_{res} - \hbar\Sigma_{opt}/2\mu_B = 541.9$ G.

However, closer examination of the loss suppression spectrum indicates that in addition to suppressing loss through EIT at the narrow loss peak, there is additional loss due to two-photon Raman absorption (Fig. 4.6 explained in section 4.3.4) from the broad Feshbach resonance. The Raman absorption peak is clearly seen in Fig. 4.11 (top-red) where the plot is expanded around the suppression region.

Instead of a simple loss suppression spectrum with an absorption minimum at the point of maximum loss, there is an additional peak (center peak in Fig. 4.11

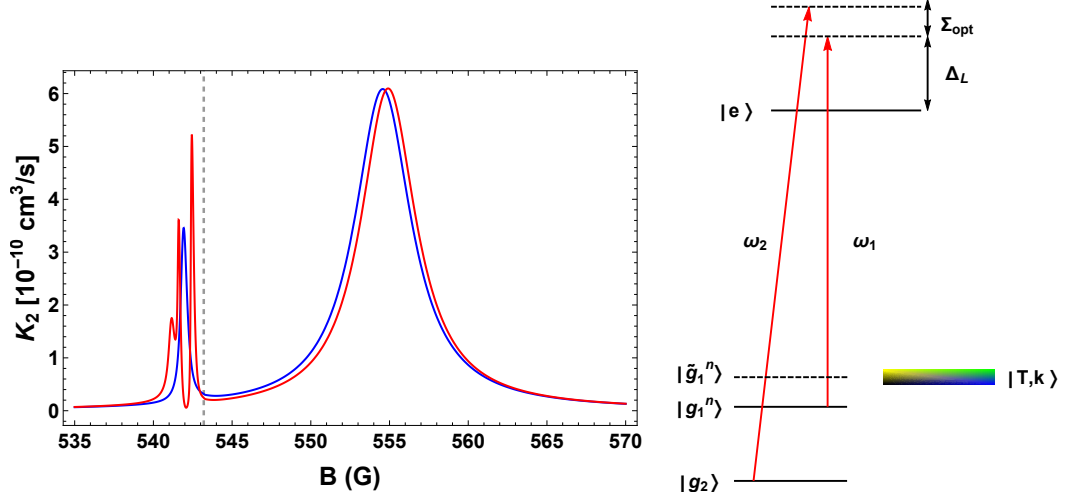


FIGURE 4.10: (Left) EIT loss suppression at the narrow peak near the narrow Feshbach resonance and (Right) corresponding level structure. Vertical dashed line represents unshifted narrow Feshbach resonance at 543.2 G. Single field loss is shown in blue. The control laser Ω_1 is detuned from the $|g_1\rangle - |e\rangle$ transition by $\Delta_L = 31.6$ MHz. The frequency ω_2 of the EIT laser is chosen such that the detuning for the $|g_2\rangle - |e\rangle$ transition $\Delta_2 = \Delta_L + \Sigma_{opt}$ to suppress loss at the narrow peak, where $\Sigma_{opt} = 2\mu_B(543.2 - B'_{res})/\hbar$. $\Omega_1 = 1\gamma_e$, $\Omega_2 = 1\gamma_e$, and $T = 10\mu K$.

(top)) in the spectrum. To further understand this phenomenon, the individual contributions from EIT and Raman absorption were studied. Fig. 4.11 (bottom) shows the contribution of EIT loss suppression (Fig. 4.11 orange) from the narrow Feshbach resonance states and the Raman coupled loss enhancement from the broad Feshbach resonance states (Fig. 4.11 black) separately. From Fig. 4.11, it is clear that the resultant spectrum shown in red (Fig. 4.11 top) is a sum of the EIT spectrum shown in orange (Fig. 4.11 bottom) and the Raman absorption spectrum shown in black (Fig. 4.11 bottom).

4.5 Zero energy scattering length a

In this section, I derive the expression for the zero energy ($k \rightarrow 0$) scattering length that results from a magnetic Feshbach resonance controlled with two optical fields. I list all the relevant equations for the calculation of the scattering length and evaluate

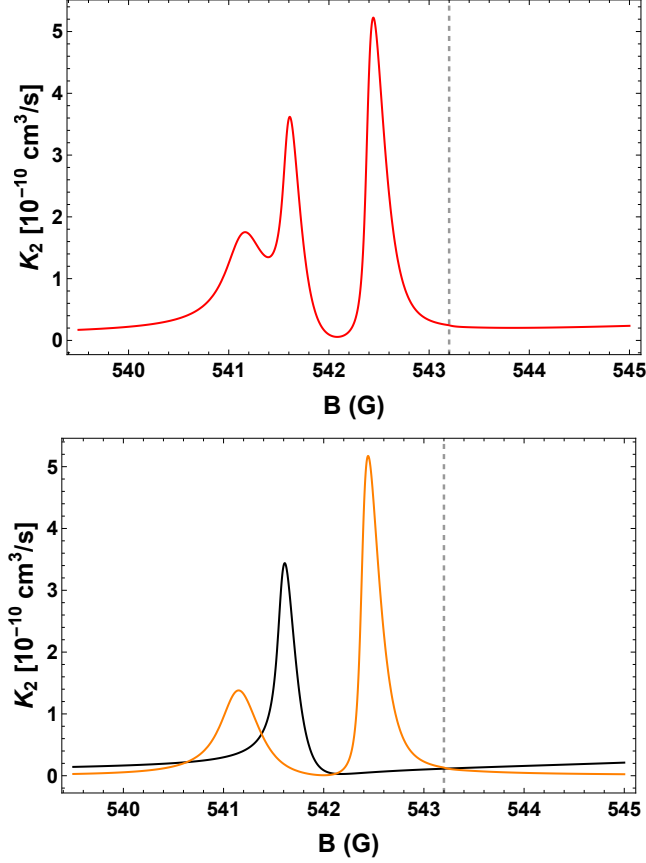


FIGURE 4.11: (top) EIT loss suppression plot in Fig. 4.10 expanded around the suppression region. The additional peak at the center shows a much richer spectrum than a simple EIT spectrum. The additional peak at the center arises due to two-photon Raman absorption from the broad Feshbach resonance as explained in section 4.3.4. (bottom) EIT spectrum from the narrow Feshbach resonance states (orange) and two-photon Raman absorption from the broad Feshbach resonance states (black) shown separately. The plot in red (top) is the sum of the EIT loss suppression spectrum (orange) and two-photon Raman absorption (black) spectrum.

them in the limit $k \rightarrow 0$. From chapter 3 (Eq. 3.138), the phase shift Δ induced due by a magnetic Feshbach resonance for $k \rightarrow 0$ is

$$x \cot \Delta = \frac{\tilde{\Delta}_0}{1 + \tilde{\Delta}_0} = -\frac{|a_{bg}|}{a_{FB}[B]}. \quad (4.17)$$

Hence,

$$\frac{a_{FB}[B]}{|a_{bg}|} = -\frac{1 + \tilde{\Delta}_0}{\tilde{\Delta}_0} = -1 - \frac{1}{\tilde{\Delta}_0}. \quad (4.18)$$

Similarly, for $k \rightarrow 0$, Eq. 3.129 becomes

$$L(\tilde{\Delta}_0, x) = \frac{1}{\tilde{\Delta}_0^2}. \quad (4.19)$$

Then Eq. 3.116 and Eq. 3.117 yield,

$$S_B(\tilde{\Delta}_0, x) = S_N(\tilde{\Delta}_0, x) = \frac{1}{\tilde{\Delta}_0}. \quad (4.20)$$

We recall from chapter 3 (Eq. 3.132 and Eq. 3.137) that the optically induced phase shift ϕ and the total phase shift δ are defined by

$$x \cot[\phi(k)] = -\frac{\tilde{\Delta}_e(x) + \frac{\tilde{\Omega}_2^2}{4\tilde{\delta}_e(x)} + \frac{\tilde{\Omega}_1^2}{4} \frac{h\gamma_e}{2\mu_B \Delta B} S(\tilde{\Delta}_0, x) + \frac{i}{2}}{\frac{\tilde{\Omega}_1^2}{4} \frac{h\gamma_e}{2\mu_B \Delta B} L(\tilde{\Delta}_0, x)}, \quad (4.21)$$

and

$$x \cot \delta = \frac{x \cot \Delta x \cot \phi - x^2}{x \cot \Delta + x \cot \phi}. \quad (4.22)$$

For the case $k \rightarrow 0$, the optically induced phase shift is obtained by substituting Eq. 4.19 and Eq. 4.20 in Eq. 4.21

$$x \cot[\phi(x)] = -\frac{\tilde{\Delta}_e(0) + \frac{\tilde{\Omega}_2^2}{4\tilde{\delta}_e(0)} + \frac{\tilde{\Omega}_1^2}{4} \frac{h\gamma_e}{2\mu_B \Delta B} \frac{1}{\tilde{\Delta}_0} + \frac{i}{2}}{\frac{\tilde{\Omega}_1^2}{4} \frac{h\gamma_e}{2\mu_B \Delta B} \frac{1}{\tilde{\Delta}_0^2}} = -\frac{|a_{bg}|}{a_\phi}, \quad (4.23)$$

$$\frac{a_\phi}{|a_{bg}|} = \frac{\frac{\tilde{\Omega}_1^2}{4} \frac{h\gamma_e}{2\mu_B \Delta B} \frac{1}{\tilde{\Delta}_0^2} \left[\tilde{\Delta}_e(0) + \frac{\tilde{\Omega}_2^2}{4\tilde{\delta}_e(0)} + \frac{\tilde{\Omega}_1^2}{4} \frac{h\gamma_e}{2\mu_B \Delta B} \frac{1}{\tilde{\Delta}_0} - \frac{i}{2} \right]}{\left[\tilde{\Delta}_e(0) + \frac{\tilde{\Omega}_2^2}{4\tilde{\delta}_e(0)} + \frac{\tilde{\Omega}_1^2}{4} \frac{h\gamma_e}{2\mu_B \Delta B} \frac{1}{\tilde{\Delta}_0} \right]^2 + \frac{1}{4}}. \quad (4.24)$$

The total phase shift δ for the case $k \rightarrow 0$ is obtained by using Eq. 4.17 and Eq. 4.23 in Eq. 4.22

$$x \cot \delta = \frac{\left(-\frac{|a_{bg}|}{a_{FB}} \right) \left(-\frac{|a_{bg}|}{a_\phi} \right)}{-\frac{|a_{bg}|}{a_{FB}} - \frac{|a_{bg}|}{a_\phi}} = -\frac{|a_{bg}|}{a_{FB} + a_\phi}. \quad (4.25)$$

Also, as $k \rightarrow 0$, we can write

$$x \cot \delta = -\frac{|a_{bg}|}{a}. \quad (4.26)$$

From Eq. 4.25 and Eq. 4.26, we have the total zero energy scattering length

$$a = a_{FB} + a_\phi. \quad (4.27)$$

Substituting Eq. 4.18 and Eq. 4.24 in Eq. 4.27,

$$\frac{a}{|a_{bg}|} = -1 - \frac{1}{\tilde{\Delta}_0} + \frac{\frac{\tilde{\Omega}_1^2}{4} \frac{\hbar\gamma_e}{2\mu_B\Delta B} \frac{1}{\tilde{\Delta}_0^2} \left[\tilde{\Delta}_e(0) + \frac{\tilde{\Omega}_2^2}{4\delta(0)} + \frac{\tilde{\Omega}_1^2}{4} \frac{\hbar\gamma_e}{2\mu_B\Delta B} \frac{1}{\tilde{\Delta}_0} - \frac{i}{2} \right]}{\left[\tilde{\Delta}_e(0) + \frac{\tilde{\Omega}_2^2}{4\delta(0)} + \frac{\tilde{\Omega}_1^2}{4} \frac{\hbar\gamma_e}{2\mu_B\Delta B} \frac{1}{\tilde{\Delta}_0} \right]^2 + \frac{1}{4}}, \quad (4.28)$$

where $\tilde{\Delta}_e(0)$ is the momentum independent single photon detuning and is defined as $\tilde{\Delta}_e(0) = \Delta_L - 2\mu_B(B - B_{ref})$. Δ_L is the control laser detuning at the reference magnetic field B_{ref} . The momentum independent two-photon detuning $\tilde{\delta}_e(0)$ is defined as $\tilde{\delta}_e(0) = \Delta_e(0) - \Delta_2$, where Δ_2 is the detuning of the EIT laser.

The above equation is the final expression for the total scattering length predicted by the continuum-dressed state model. The first term is a result of the magnetic Feshbach resonance and the second term is the optically induced change. As we can see, when $\Omega_1 \rightarrow 0$, we are left with only the magnetic Feshbach resonance part for the total scattering length.

4.5.1 Zero energy scattering length a near the broad Feshbach resonance

Fig. 4.12 shows scattering length a and the corresponding two-body loss rate constant K_2 as a function of single photon detuning Δ_e using Eq. 4.28 near the Broad Feshbach resonance at 825 G.

The scattering length a without optical fields is shown as the black horizontal line. It is clear that when the two photon detuning $\delta_e = 0$ ($\Delta_2 = \Delta_e = 0$), the loss is minimum and the scattering length using the two-field method (red) is equal to

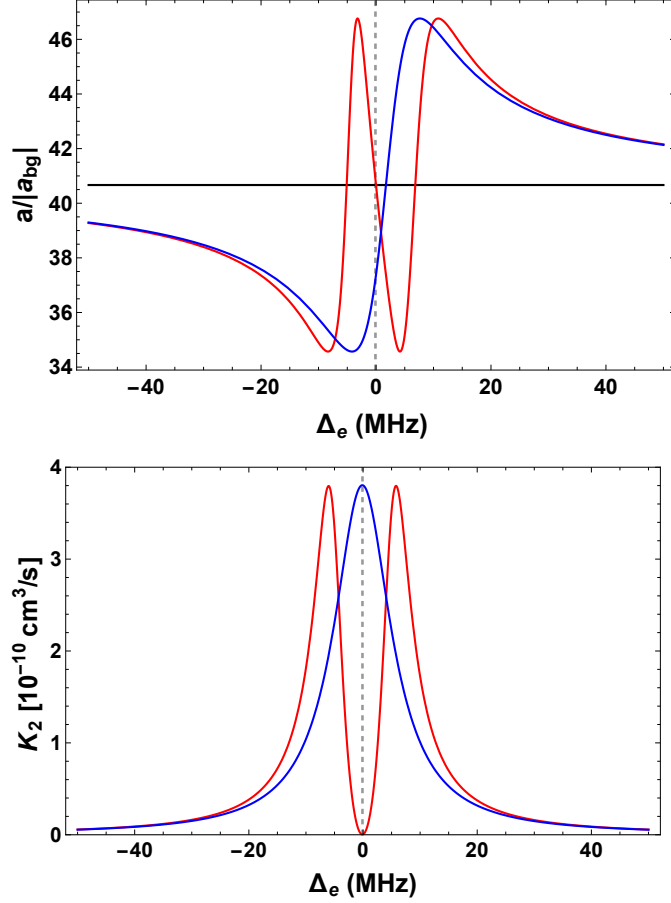


FIGURE 4.12: Zero energy scattering length a (top) and K_2 (bottom) versus single photon detuning Δ_e near the Broad Feshbach resonance at 825 G. Zero energy scattering length due to magnetic Feshbach resonance (black horizontal line), single-field method (blue), and two-field method (red). $T = 10 \mu\text{K}$, $\Omega_1 = 1 \gamma_e$, and $\Omega_2 = 1 \gamma_e$.

the scattering length in the absence of optical fields (black). In other words, at the point of zero loss ($\delta_e = 0$), there is *no* tuning of the scattering length. Although the two-field method does not change the scattering length at the minimum loss point ($\delta_e = 0$), it gives us the flexibility of changing the scattering length considerably about the minimum loss point by making small changes in the frequency ω_1 of the control laser.

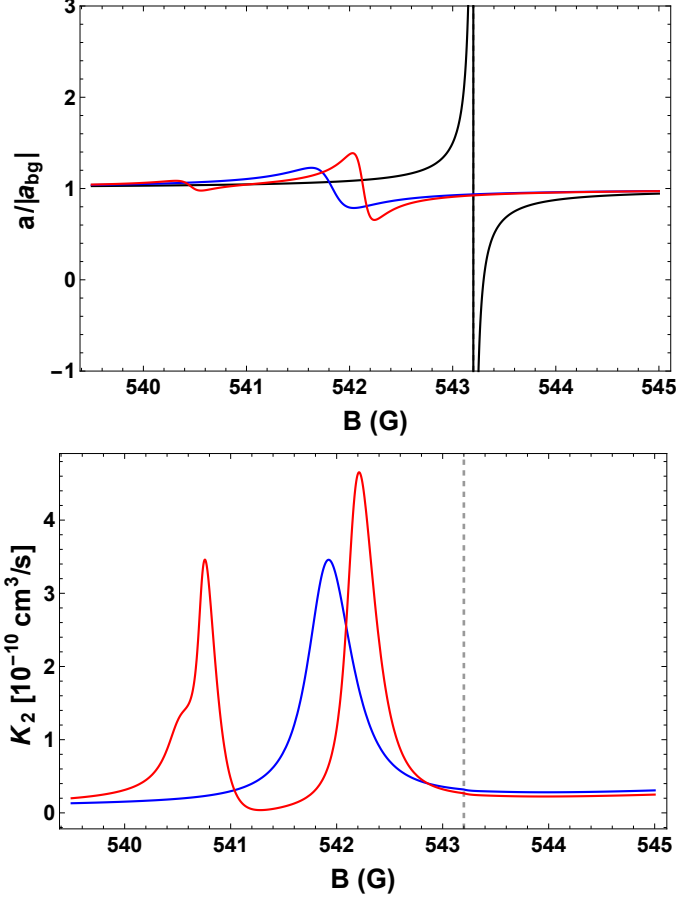


FIGURE 4.13: Zero energy scattering length (top) and corresponding K_2 (bottom) versus B-field near the narrow Feshbach resonance due to magnetic Feshbach resonance (black), single-field method (blue), and two-field method (red). $T = 10 \mu\text{K}$, $\Omega_1 = 1 \gamma_e$, $\Omega_2 = 1 \gamma_e$, and $\Delta_L = 31.6 \text{ MHz}$.

4.5.2 Zero energy scattering length a near the narrow Feshbach resonance

Fig. 4.13 shows scattering length a and the corresponding two-body loss rate constant K_2 as a function of magnetic field near the narrow Feshbach resonance at 543.2 G for the same parameters that were used for Fig. 4.10. The scattering length of the unshifted resonance is shown in black at 543.2 G, which has the typical shape of a magnetic Feshbach resonance. When a single optical field is applied, it results in the shift of the original resonance at 543.2 G to $B'_{res} = 541.9 \text{ G}$ (blue).

As mentioned in section. 4.4, since the shifted narrow singlet state $|\tilde{g}_1^n\rangle$ is an

admixture of $|g_1^n\rangle$ and $|e\rangle$, $|\tilde{g}_1^n\rangle$ loses the pure singlet character of $|g_1^n\rangle$, resulting in much smaller variation in a , between $0.8|a_{bg}|$ and $1.2|a_{bg}|$ (Fig. 4.13 (top) blue) at the shifted narrow resonance $B'_{res} = 541.9$ G. When the ω_2 beam is applied, it mixes the lower vibrational singlet ground state $|g_2\rangle$ with $|\tilde{g}_1^n\rangle$ resulting in suppression of loss due to quantum interference. This also creates two additional artificial resonances (Fig. 4.13 (top) red) on either side of the two-photon resonance at $B = 540.6$ G and $B = 542.4$ G, where the loss is maximum. At the two-photon resonance, similar to the broad Feshbach resonance, the scattering length due to two-field method is equal to the scattering length in the absence of any optical fields.

4.6 Effective range r_e

In this section, we will discuss the advantages of our two-field method to control the effective range in ultracold gases. We will use the total phase shift derived in chapter 3 Eq. 3.137 to calculate the optically induced change in the effective range due to our two-field method.

From the effective range expansion in Eq. 1.2, we know the relationship between the scattering phase shift $\delta(k)$ and the relative momentum k as $k \rightarrow 0$ is given by

$$k \cot \delta(k) \cong -\frac{1}{a} + \frac{k^2}{2} r_e, \quad (4.29)$$

where a is the zero energy s-wave scattering length and r_e is the effective range. Using $x \equiv k|a_{bg}|$, in Eq. 4.29,

$$x \cot \delta(x) = \frac{-|a_{bg}|}{a} + \frac{x^2}{2} \frac{r_e}{|a_{bg}|}. \quad (4.30)$$

From the above equation, we can determine the effective range r_e in terms of $|a_{bg}|$ by expanding the expression for $x \cot \delta(x)$ in Eq. 3.138 in powers of x and computing

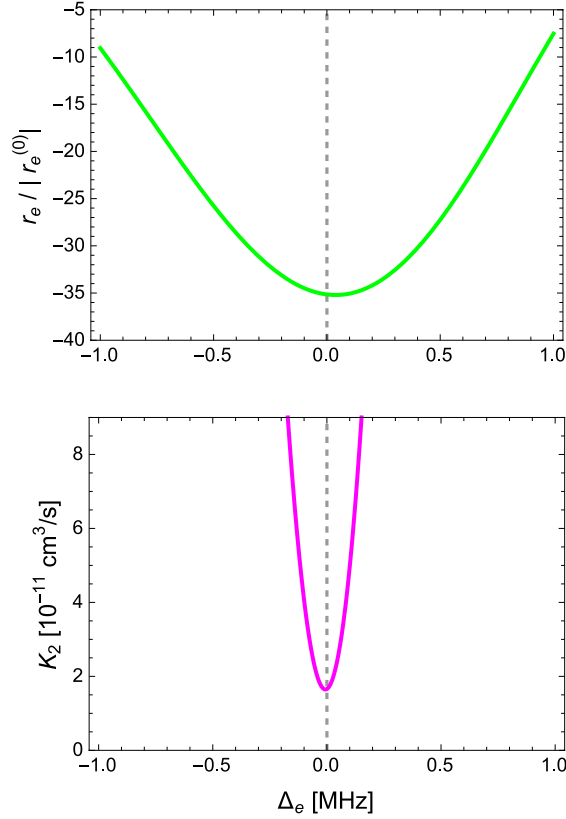


FIGURE 4.14: Effective range versus control beam detuning Δ_e for the two-field method, demonstrating maximum enhancement at the point of minimum loss. $T = 5 \mu\text{K}$; $B = 840 \text{ G}$; $\Omega_1 = 3 \gamma_e$; $\Omega_2 = 0.5 \gamma_e$.

twice the coefficient of the quadratic term in x . In the absence of optical fields, the effective range is given in chapter 2 (Eq. 2.72) as $r_e^{(0)} = -2\epsilon|a_{bg}|$, where ϵ is defined above. For the broad and narrow resonances in the ${}^6\text{Li}$ 1-2 mixture, $r_e^{(0)} \simeq -1 a_0$ and $-7 \times 10^4 a_0$, respectively.

Fig. 4.14 shows $r_e/|r_e^{(0)}|$ for the broad resonance as a function of detuning of the control beam for the two-field method. Note that the effective range is increased in magnitude by a factor of 35 at the point of minimum loss, where K_2 is strongly

suppressed. We can see that the two-field method modifies the effective range of the broad resonances in 1-2 mixture of ^6Li and therefore can be used as a general tool to modify the effective range in ultracold gases.

4.7 Two-field optical method near the narrow Feshbach resonance

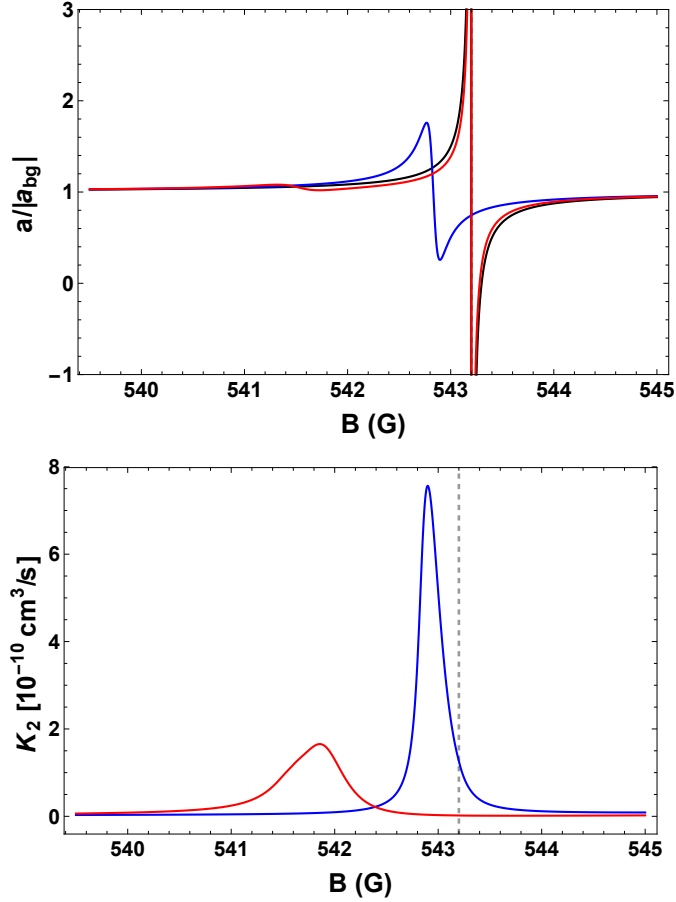


FIGURE 4.15: Using the closed-channel EIT to maximize tunability near a magnetic Feshbach resonance. Zero energy scattering length (top) and corresponding K_2 (bottom) versus B-field near the narrow Feshbach resonance due to magnetic Feshbach resonance (black), single-field method (blue) and two-field method (red). a for two-field method (red) and magnetic Feshbach resonance (black) overlap for $\Delta_2 = 0$, indicating creation of an optically tunable resonance at the original magnetic Feshbach resonance position. $T = 10 \mu\text{K}$, $\Omega_1 = 1 \gamma_e$, $\Omega_2 = 1 \gamma_e$, and $\Delta_L = 31.6$ MHz.

It might seem from the discussion presented in section 4.5, that the two-field

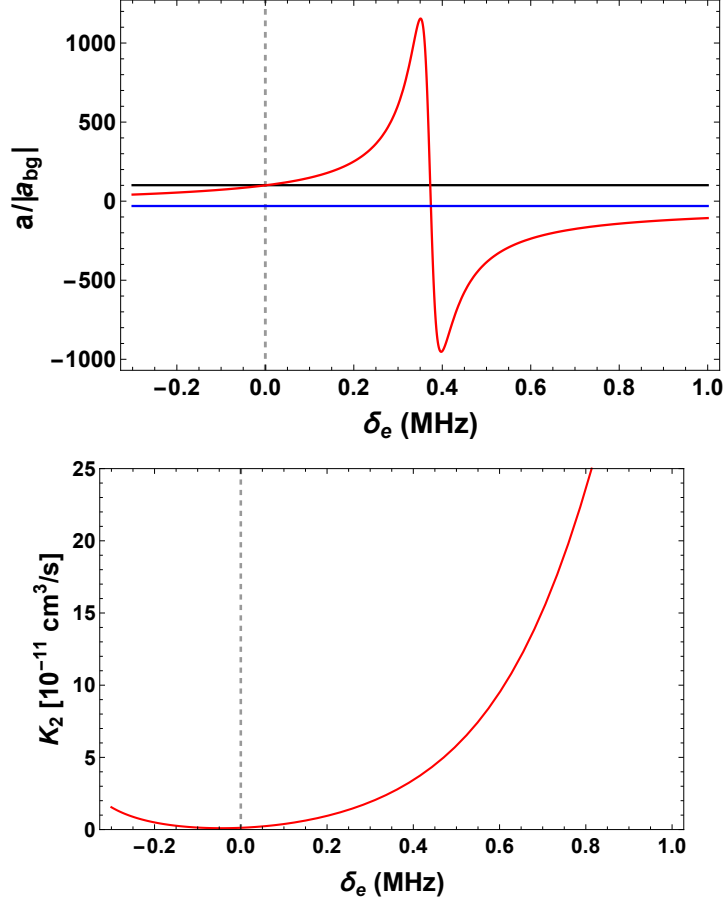


FIGURE 4.16: Using the closed-channel EIT to optically tune interactions by changing laser frequency. Zero energy scattering length a (top) and corresponding K_2 (bottom) versus two-photon detuning δ_e near the narrow Feshbach resonance due to magnetic Feshbach resonance (black), single-field method (blue) and two-field method (red). Scattering length a for two-field method (red) can be tuned from negative to positive value with minimum loss. K_2 for single-field method is off scale and is not shown. $T = 10 \mu K$, $\Omega_1 = 0.1 \gamma_e$, $\Omega_2 = 1 \gamma_e$, and $B = 543.2 \text{ G}$.

method does not provide us any net gain in the tunability of scattering length. This is not true. Fig. 4.15 illustrates the potential of the two-field method when the optimum parameters are chosen. Here, the frequency of the EIT beam is chosen such that it suppresses loss at 543.2 G, i.e., $\Delta_2 = \Delta_1$ as illustrated in Fig. 4.3. The EIT beam completely nullifies the effect of the control beam through destructive quantum interference, snapping the shifted resonance back to 543.2 G. The resonance recreated at 543.2 G using two optical fields is optically tunable, has minimum optical loss, and

has the pure character of the unshifted resonance. Hence the two-field method can allow us to perform many interesting non-equilibrium thermodynamics experiments.

For example, in order to demonstrate spatially varying interactions on an atom cloud, we can do experiments at 543.2 G where the control beam illuminates the entire cloud and the EIT beam illuminates only the center. The center of the atom cloud where both the control beam and the EIT beam overlap will be strongly interacting with minimum loss (Fig. 4.15 red) as the two-field method restores the original resonance at 543.2 G. The regions of the atom cloud where only the control beam is present will be non-interacting (Fig. 4.15 blue) with reduced optical loss because the control beam will have shifted the resonance from 543.2 G. Hence, we can create a strongly interacting system sandwiched between two non-interacting systems using the two-field method.

One of the primary advantages of the two-field method over single field methods is its ability to tune the interactions by changing the laser frequency. This is illustrated in Fig. 4.16 where the scattering length and the corresponding K_2 is shown as a function of the two-photon detuning $\delta_e = \Delta_2 - \Delta_e$ at a fixed magnetic field of 543.2 G. Note the two-photon detuning can be changed by either changing the frequency ω_1 of the control laser or frequency ω_2 of the EIT laser. The vertical dashed line in Fig. 4.16 indicates two-photon detuning $\delta_e = 0$.

Fig. 4.16 (top) shows that the scattering length can be tuned from negative to positive by changing the two-photon detuning near $\delta_e = 0$ with minimal loss as shown by the corresponding K_2 in Fig. 4.16 (bottom). Furthermore, it can be seen from Fig. 4.16 that the two-body interactions can be tuned from weakly-interacting ($a/|a_{bg}| \approx 0$) when $\delta_e = 0$ to strongly interacting ($a/|a_{bg}| = 500$) when $\delta_e = 0.35$ MHz. Therefore, the closed-channel EIT method can provide us an experimental “knob” where a small frequency change of 0.35 MHz can tune the interaction in an ultracold gas from weakly-interacting to strongly interacting.

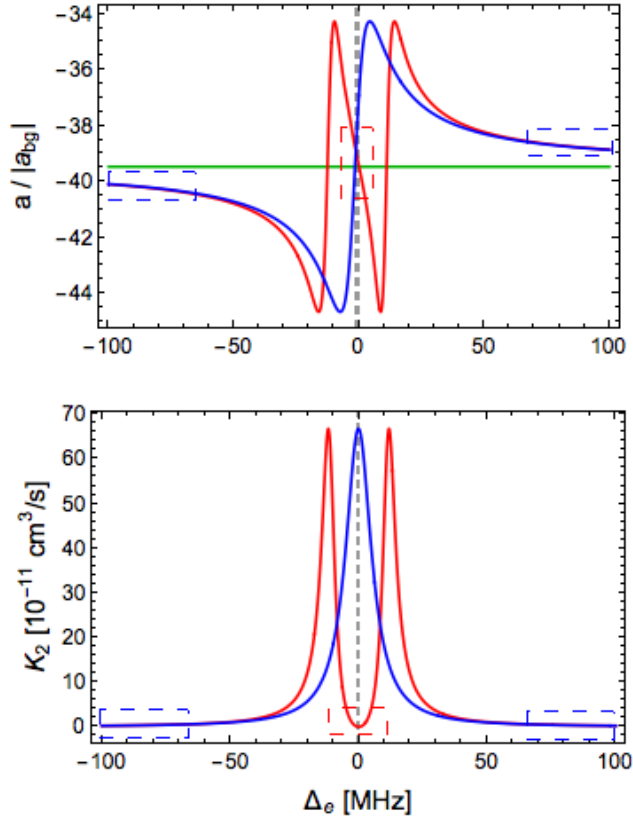


FIGURE 4.17: Zero energy scattering length a (top) and two-body loss rate coefficient K_2 (bottom) as function of ω_1 (detuning Δ_e) for two-field (red) and single-field (blue) methods. Scattering length without optical fields (green); $T = 5 \mu\text{K}$; $B = 840 \text{ G}$; $\Omega_1 = 1 \gamma_e$; $\Omega_2 = 2 \gamma_e$; The minimum point of the red K_2 curve occurs for $\Delta_e = 0$, where the two-photon detuning $\delta = 0$. Red and blue rectangular boxes indicate low loss regions of interest for two-field and single field methods, respectively.

4.8 Two-field optical method near the broad Feshbach resonance

In this section, we will discuss the advantages of closed-channel EIT method near the broad Feshbach resonance. In addition to suppressing atom loss, the closed-channel EIT method has other advantages compared to single-field methods. Using closed-channel EIT, a small frequency change in the frequency of either the ω_1 field or ω_2 field results in large changes in the scattering length. Since single-field methods use large detunings to avoid atom loss, small changes in frequency of the optical

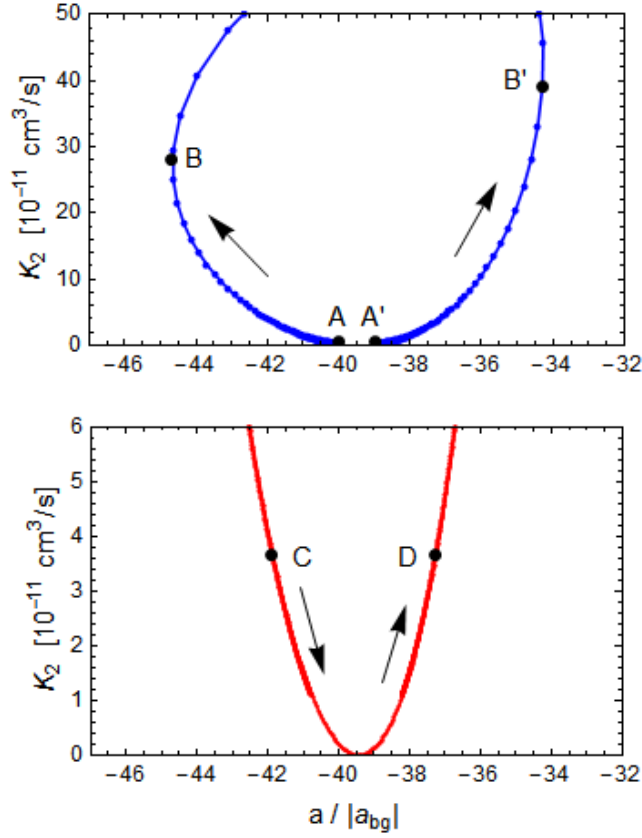


FIGURE 4.18: Two-body loss rate constant K_2 versus zero energy scattering length a for single-field (top) and two-field (bottom) optical methods, using the same parameters as in Fig. 4.17. For the single-field method, tuning from point A to point B requires a change in Δ_e from -100 MHz to -7.5 MHz, where $K_2 = 27 \times 10^{-11} \text{ cm}^3/\text{s}$. In contrast, for the two-field method, tuning from point C to point D requires a change in Δ_e from -4.6 MHz to +4.6 MHz, where $K_2 = 3.6 \times 10^{-11} \text{ cm}^3/\text{s}$.

field will have negligible effect on the scattering length. In contrast to intensity tuning employed in single-field methods, our technique provides a general method of suppressing unwanted changes in the total trapping potential as the two-body parameters are varied. For example, near the broad $|1\rangle - |2\rangle$ Feshbach resonance in ${}^6\text{Li}$ we can tune a by $4.6|a_{bg}|$ with the two-body loss rate constant, K_2 , 7.5 times smaller compared to single-field methods.

Fig. 4.17 shows the zero energy scattering length a and the relative momentum

averaged two-body loss rate constant $\langle K_2 \rangle$ as a function of single photon detuning Δ_e for both two-field (red) and single-field (blue) methods, near the broad Feshbach resonance at 832 G using the continuum-dressed model. We take $B = 840$ G, $T = 5 \mu\text{K}$, $\Omega_1 = 1 \gamma_e$, and $\Omega_2 = 2 \gamma_e$. For the single field method, the region of low loss (blue box) occurs at large detuning where the a varies slowly as a function of Δ_e . This then necessitates large changes in frequency for relatively small changes in scattering length. In contrast, low loss occurs for the two-field method at the two-photon resonance, where the scattering length changes most rapidly with Δ_e (red box). Hence, small changes in the detuning of ω_1 can result in large changes in the scattering length.

To quantify these ideas, we compare single-field methods and closed-channel EIT using our theoretical model to calculate $\langle K_2 \rangle$ for a fixed change $|\Delta a| = 4.6|a_{bg}|$. In Fig. 4.18 (top), the minimum loss point for the single-field method occurs at points A and A' , for large detunings $\Delta_e = \mp 100$ MHz. Tuning to point B (B'), which is $4.6|a_{bg}|$ away on the horizontal axis, is achieved by setting Δ_e to -7.5 MHz (4.5 MHz), where $K_2 = 27 \times 10^{-11} \text{ cm}^3/\text{s}$, ($K_2 = 39 \times 10^{-11} \text{ cm}^3/\text{s}$). In contrast, for the two-field method, we tune through the point of minimum loss from C to D . Here Δ_e changes from -4.6 MHz to $+4.6$ MHz, and at points C and D , $K_2 = 3.6 \times 10^{-11} \text{ cm}^3/\text{s}$, 7.5 times smaller than that of the single-field method, while still achieving the same change in scattering length.

From the above discussion, we see an important advantage of the two-field method: Not only is there a reduction in the loss rate, but the frequency change needed to produce a given change in the scattering length is much smaller than for the single-field method.

4.9 Evaluation of optically induced atom loss from K_2

In our optical control experiments, we illuminate the atoms with optical fields and measure atom loss. However, we only derived the expression for the two-body loss rate constant K_2 using the continuum-dressed state model. Therefore, in order to fit the experimental data with the continuum-dressed state model, we need to derive an expression that relates atom loss and K_2 , which will be the focus of this section.

Let n_\uparrow and n_\downarrow be the density of spin up and spin down atoms in the two hyperfine levels, respectively. Then the loss rate per unit volume can be written as

$$\dot{n}_\uparrow = -n_\downarrow v_r \sigma_{inelastic} n_\uparrow = \dot{n}_\downarrow \quad (4.31)$$

where $n_\downarrow v_r$ is the incoming flux and $n_\downarrow v_r \sigma_{inelastic}$ is the collision rate.

From Eq. 4.2, we know

$$K_2(k) = v_{rel} \sigma_{inelastic} = \frac{\hbar k}{\mu} \sigma_{inelastic}, \quad (4.32)$$

Using Eq. 4.32 in Eq. 4.31, we obtain

$$\dot{n}_\uparrow + \dot{n}_\downarrow = -2K_2(k)n_\uparrow n_\downarrow \quad (4.33)$$

The total loss rate \dot{N} is

$$\dot{N} = \int d^3\vec{r} (\dot{n}_\uparrow + \dot{n}_\downarrow) \quad (4.34)$$

Substituting Eq. 4.33 in Eq. 4.34, we get

$$\dot{N} = -2 \int d^3\vec{r} K_2(k) n_\uparrow n_\downarrow \quad (4.35)$$

For thermal non-degenerate gas that has a classical Boltzmann distribution of relative momentum k , we know from chapter 4 (Eq. 4.12)

$$\langle K_2(k) \rangle = \int_0^\infty \frac{4\pi k^2 dk}{(k_0\sqrt{\pi})^3} e^{-\frac{k^2}{k_0^2}} K_2(k) \quad (4.36)$$

Substituting Eq. 4.36 in Eq. 4.35, yields

$$\dot{N} = -2 \int d^3\vec{r} n_{\uparrow} n_{\downarrow} \int_0^{\infty} \frac{4\pi k^2 dk}{(k_0\sqrt{\pi})^3} e^{-\frac{k^2}{k_0^2}} K_2(k) \quad (4.37)$$

For a 50-50 mixture,

$$n_{\uparrow} = n_{\downarrow} = \frac{n}{2}; n = n_{\uparrow} + n_{\downarrow}. \quad (4.38)$$

Therefore,

$$2 \int d^3\vec{r} n_{\uparrow} n_{\downarrow} = \frac{1}{2} \int d^3\vec{r} n^2 = \frac{1}{2} N \bar{n} = \frac{N^2}{2} \frac{\bar{n}}{N}, \quad (4.39)$$

where \bar{n} is the average density and is given by

$$\bar{n} \equiv \frac{1}{N} \int d^3\vec{r} [n(\vec{r})]^2. \quad (4.40)$$

Substituting Eq. 4.39 in Eq. 4.37, we obtain

$$\dot{N} = \frac{N^2}{2} \frac{\bar{n}}{N} \int_0^{\infty} \frac{4\pi k^2 dk}{(k_0\sqrt{\pi})^3} e^{-\frac{k^2}{k_0^2}} K_2(k) \quad (4.41)$$

Now we let

$$\Gamma \equiv \frac{1}{2} \frac{\bar{n}}{N} \int_0^{\infty} \frac{4\pi k^2 dk}{(k_0\sqrt{\pi})^3} e^{-\frac{k^2}{k_0^2}} K_2(k) \quad (4.42)$$

Substituting Eq. 4.42 in Eq. 4.37, we get

$$\frac{\dot{N}}{N^2} = -\Gamma$$

Integrating both sides and solving for $N(t)$, we get

$$\int_{N_0}^N \frac{dN}{N^2} = -\Gamma \int_0^t dt$$

$$N(t) = \frac{N_0}{1 + N_0\Gamma t} \quad (4.43)$$

$$\frac{N(t)}{N_0} = \frac{1}{1 + N_0\Gamma t}, \quad (4.44)$$

where N_0 is the initial total atom number. We use Eq. 4.44 to compare our experimental atom loss data to the continuum-dressed state model in chapter 6.

In this chapter, the continuum dressed model is used to derive the two-body loss rate constant K_2 , the zero energy scattering length a , and the effective range r_e . Furthermore, it is shown that the two-field method allows us to tune the scattering length and the effective range about the minimum loss region with small changes in laser frequency. It is further illustrated that the two-field method can create spatially selective regions of strong interactions in an otherwise non-interacting system near a magnetic Feshbach resonance. Hence, the two-field method provides a general recipe to pursue non-equilibrium thermodynamic experiments in ultracold gases near a magnetic Feshbach resonance. In chapter 6, the continuum-dressed state model is tested by comparing the calculated K_2 to the experimental data near the broad and the narrow Feshbach resonance in ${}^6\text{Li}$.

Experimental Methods

In this chapter, I will discuss the experimental setup that is used for the two-field optical method to control interactions in ${}^6\text{Li}$. The experiment is done in two steps, namely, (i) creating an ultracold gas of ${}^6\text{Li}$ atoms and (ii) controlling interactions in the ultracold gas using optical fields. The experimental setup for creating an ultracold gas of ${}^6\text{Li}$ atoms is extensively discussed in previous thesis from our group and the recent upgraded experimental setup can be found in Ethan Elliot's thesis [61]. Hence, I will briefly summarize the essential details in this chapter. However, the experimental setup to control interactions in ultracold gas using our two-field method, which is the primary focus of my PhD work, will be discussed in detail.

5.1 Laser cooling and trapping of atoms

In this section, we will discuss the basic technique and the experimental apparatus used in our lab to cool atoms to temperatures near absolute zero. We use a Coherent dye laser that is pumped by a Coherent Verdi laser for our laser cooling and trapping experiments. The Verdi operates at 532 nm with an output power of 6 W. The dye laser is operated at 670.9 nm corresponding to the D_2 line of ${}^6\text{Li}$. We get

approximately 800 mW of power from the dye laser. The beam from the dye laser is processed further to generate all the beams necessary for our cooling and trapping experiments, namely, the “slower” beam, the MOT (Magneto-optical trap) beams and, the “repumper” beams, whose purpose is explained in detailed below. The dye laser is locked to fluorescence signal from a ${}^6\text{Li}$ oven corresponding to the transition from the ground state ${}^2S_{1/2}$ to the ${}^2P_{3/2}$ excited state, which is conventionally called as the D_2 transition of ${}^6\text{Li}$. The transition linewidth for the D_2 transition is 5.9 MHz. The ${}^2S_{1/2}$ ground state of ${}^6\text{Li}$ further splits into $F = 1/2$ and $F = 3/2$ due to hyperfine splitting. The primary objective of our laser cooling and trapping techniques is to produce ultracold atoms in the $F = 1/2$ ground state of ${}^6\text{Li}$.

5.1.1 ${}^6\text{Li}$ oven - Generating the atoms

The first step in producing cold atoms is to generate atoms from an atom source. We produce hot atoms from a lithium oven that is heated to approximately 400°C . We have two ${}^6\text{Li}$ ovens in our lab, namely, the “main” oven and the “reference” oven. The “main” oven supplies the atoms for our experiments. The reference oven generates the fluorescence signal for frequency locking the dye laser. The atoms from the “main” oven enter the ultra-high vacuum chamber for further cooling and trapping.

5.1.2 Zeeman slower and the “slower” beam - Initial cooling

Fig. 5.1 illustrates initial cooling and precooling stages of ${}^6\text{Li}$ atoms. The hot atoms generated in the oven are collimated and enter the region of Zeeman slower (explained below) in the vacuum chamber, where they are illuminated by a “slower” beam. The “slower beam” is a near resonant counter-propagating beam with approximately 140 mW of power and initially slows down the atoms. The reduction in the velocity of the atoms is achieved as the atoms absorb photons in the direction opposite to which they travel and emit photons in random directions. Hence, the net momentum is

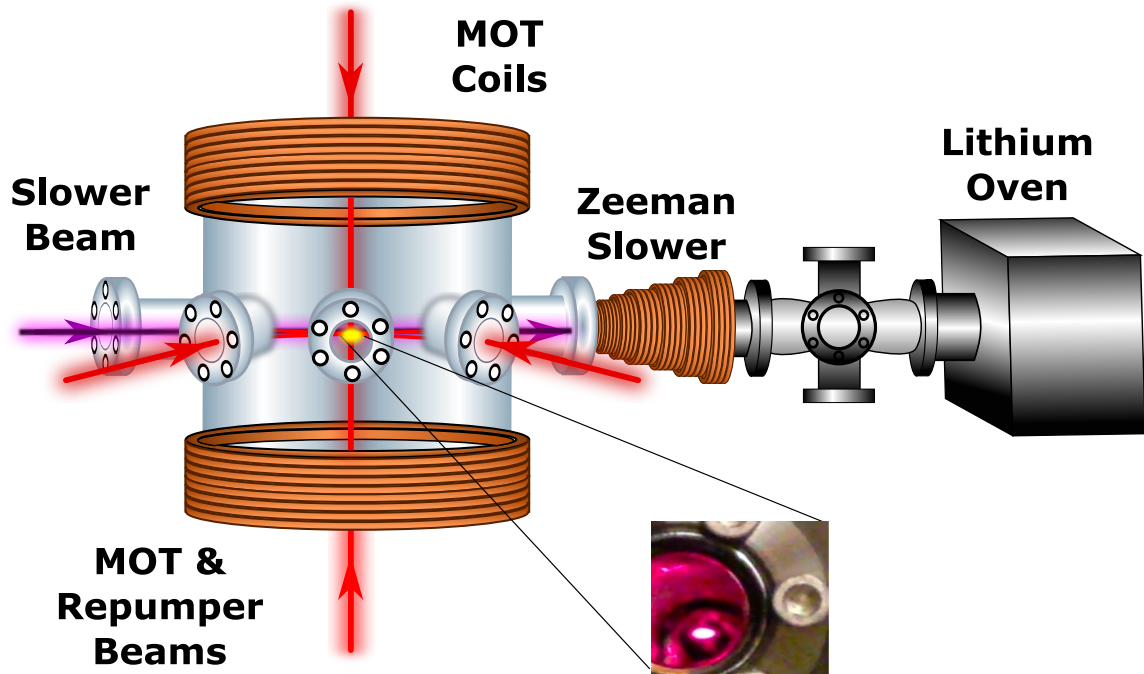


FIGURE 5.1: Experimental setup for initial cooling of ${}^6\text{Li}$ atoms by the Zeeman slower and the slower beam and precooling by the MOT beams, repumper beams and MOT coils. MOT and repumper beams are overlapped and are shown together in red. Inset shows fluorescence from the atoms trapped in the MOT.

reduced in the direction in which the atoms are traveling. Atoms that are initially resonant with the slower beam when moving rapidly, will no longer be resonant as they slow down, becoming “red” detuned due to the Doppler shift. This problem is overcome by the use of Zeeman slower, which is a set of magnetic coils that generates a spatially varying magnetic field in the direction in which the atoms are moving. The magnetic field generated by the Zeeman slower compensates for the Doppler shift by producing a spatially varying Zeeman shift to the energy levels of the atoms. As the atoms exit the Zeeman slower region, the velocity of the atoms is approximately 30 m/s.

5.1.3 Magneto-optical trap - Precooling

After exiting the Zeeman slower region, the atoms enter the main part of the vacuum chamber, where further cooling is achieved by the use of a magneto-optical trap (MOT). The MOT is a combination of optical fields and magnetic fields that provides “precooling” of atoms for our experiments. In addition to cooling the atoms, the MOT provides spatial confinement of atoms. The MOT consists of six optical beams (3 pairs of retro reflected beams) that illuminate the atoms in all three directions providing 3-dimensional cooling. The six beams provide cooling as the atoms absorb photons opposite to the direction in which they are traveling and emit photons in random directions. Therefore, there is a net momentum kick opposite to the velocity of the atoms. As the velocity of the atoms are reduced in all three directions, the atoms become “red” detuned with the MOT beams due to the Doppler shift and can slowly disperse through random walk. This is avoided by the use of MOT magnetic coils that compensates for the Doppler shift by the providing the zeeman shift of the energy levels of the atoms.

The frequency of the MOT beams primarily corresponds to the $F = 3/2$ ground state to the excited state transition. However, the atoms that exit the Zeeman slower region, will populate both the $F = 1/2$ and $F = 3/2$ ground states. The $F = 1/2$ ground state is 228 MHz lower in energy than the $F = 3/2$ ground state. In order to cool the atoms that populate both the ground states, we use an acousto-optical modulator (AOM) to generate an additional optical beam, the “repumper” beam, whose frequency corresponds to the $F = 1/2$ ground state to the excited state transition. The MOT beam and the “repumper” beam are overlapped and their powers are empirically chosen to be in the ratio of 3:1.

The MOT precooling is done in three phases. In the “loading” phase, both the MOT beam and the repumper beam are detuned by about 30 MHz from resonance.

The loading phase will initially load the atoms exiting from the slower region into the MOT. The second phase is the “cooling” phase, where both the MOT beams and the “repumper” beams are tuned to within 3 MHz of resonance. The final phase is the “optical pumping” phase, where the MOT beam is tuned to resonance and the “repumper” is turned off. The optical pumping phase transfers all the atoms in the $F = 3/2$ ground state to the $F = 1/2$ ground state.

At the end of the MOT precooling phase, we have about 300 million atoms in the $F = 1/2$ ground state at a Doppler limited temperature of $140 \mu\text{K}$. Fig. 5.1 (inset) shows fluorescence from the atoms trapped in the MOT.

5.1.4 Far off-resonance trap (FORT) - Evaporative cooling

Fig. 5.2 shows the experimental setup for evaporative cooling of ${}^6\text{Li}$ atoms in a CO_2 optical dipole trap and absorption imaging using a resonant beam. We load the atoms from the MOT into another optical trap, the far off-resonance trap (FORT), for evaporative cooling. The basic principle of the FORT is that an optical beam, far detuned from the resonance frequency of the atoms, will create a dipole force on the atoms that depends on the intensity of the optical beam and the polarizability of the atoms. The interaction energy U_{dip} created by an optical beam of intensity I on an atom of polarizability α is

$$U_{dip} = -\frac{1}{2\epsilon_0 c} \alpha I. \quad (5.1)$$

For large detunings $\Delta \gg \omega_{res}$, the polarizability of an atom α can be written in terms of its static polarizability α_s and resonance frequency ω_{res}

$$\alpha = \frac{\alpha_s}{1 - \omega^2/\omega_{res}^2} \quad (5.2)$$

From Eq. 5.1 and Eq. 5.2, we can see that a blue detuned optical beam ($\omega > \omega_{res}$) will create an repulsive potential and a red detuned optical beam ($\omega < \omega_{res}$) will

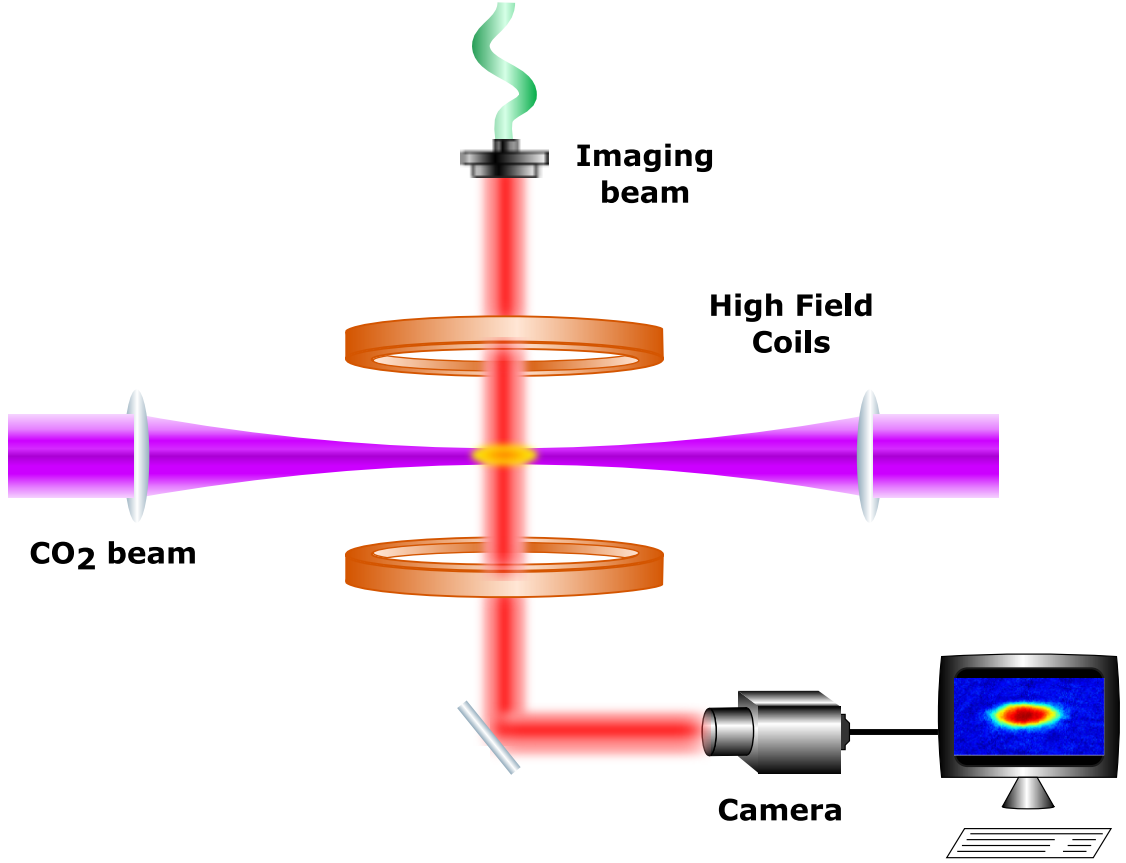


FIGURE 5.2: Experimental setup for evaporative cooling of ${}^6\text{Li}$ atoms in a CO_2 optical dipole trap and absorption imaging using a resonant beam. The high field coils generate the magnetic field required for evaporative cooling at 832.2 G. Atoms are imaged with a CCD camera and processed to generate a false color image.

create an attractive potential. For a cylindrically symmetric gaussian beam, the intensity is

$$I(r, z) = \frac{I_0}{1 + (z/z_0)^2} \exp\left(-\frac{2r^2}{r_0^2}\right), \quad (5.3)$$

where I_0 is the peak intensity, r_0 is the $1/e^2$ intensity radius of the beam, and z_0 is the Raleigh range. Substituting Eq. 5.3 in Eq. 5.2, we arrive at the expression for the spatially varying dipole potential for a Gaussian far off-resonance detuned beam,

$$U_{dip} = \frac{U_0}{1 + (z/z_0)^2} \exp\left(-\frac{2r^2}{r_0^2}\right), \quad (5.4)$$

where U_0 is the maximum trap depth and is defined as

$$U_0 = \frac{\alpha_s I_0}{2 \epsilon_0 c}. \quad (5.5)$$

In our laboratory, we create the FORT by making use of an optical beam generated by a Coherent DEOS CO₂ laser operating at 10.6 μm with an output power of 140 W. After collimating the beam through a telescope, we use a 19 inch focal length lens in front of the main chamber to focus the beam to a $1/e^2$ width of about 60 μm . The power of the focused beam at the atoms is approximately 60 W. This give a peak intensity of 2×10^6 W/cm² corresponding to a maximum trap depth of approximately 1 mK, Eq. 5.5. The CO₂ FORT beam trap provides confinement in all three directions, with tighter confinement in the radial direction and weaker confinement in the axial direction, Fig. 5.3.

The evaporative cooling using the FORT consists of two stages, namely, free evaporation and forced evaporation. In the free evaporation stage, after transferring the atoms from the MOT into the FORT, we wait for a few seconds for the atoms to rethermalize at full trap depth, i.e., maximum intensity of the CO₂ laser. During rethermalization, atoms collide with one another resulting in exchange of energy from hot atoms to cold atoms, ultimately causing the hottest atoms to be kicked out from the FORT.

In the forced evaporation stage of evaporative cooling, the intensity of the CO₂ laser is reduced thereby lowering the trap depth of the FORT. As the trap depth is reduced, the hotter atoms escape from the trap leaving only the colder atoms to remain in the reduced trap depth. This reduced trap depth is called the “lowest-well” trap depth. The lowest-well value and the time to reach the lowest-well value determines the final temperature of our atom cloud. We choose the “lowest-well” trap depth value and the time to reach the lowest-well value, based on the desired final temperature requirements of our atom cloud.

After forced evaporation, the trap depth is again re-raised to a final trap depth. The final trap depth determines the final density of the atomic cloud. Therefore, we adjust the “lowest-well” trap depth value, the lowering time, and the final trap depth value, based on our requirements of temperature and density for the resulting ultracold atomic gas.

For evaporative cooling to efficiently work, the rate of collisions between atoms should be maximized. At zero magnetic field, the $|F = 1/2\rangle$ state is two-fold degenerate with the $|m_f = 1/2\rangle$ and $|m_f = -1/2\rangle$ state. However, at high magnetic fields, this degeneracy is broken resulting in a two component mixture, consisting of the two lowest hyperfine states $|1\rangle$ and $|2\rangle$. The $|1\rangle - |2\rangle$ mixture has a Feshbach resonance at 832.2 G where the scattering length diverges and results in a high collision rate. Therefore, after transferring the atoms from the MOT into the FORT, we sweep the magnetic field to 832.2 G to perform evaporative cooling. However, to perform experiments near the narrow Feshbach resonance at 543.2 G, we cannot utilize the broad Feshbach resonance for evaporative cooling, since sweeping the magnetic field after evaporative cooling at 832.2 G to a value below 700 G results in loss of atoms due to three-body collisions. Therefore, when we perform experiments near the narrow Feshbach resonance, we sweep the magnetic field to 300 G, where the scattering length is about $300 a_0$ to perform evaporative cooling.

5.1.5 Imaging the atom cloud

After evaporative cooling of atoms in the FORT, we turn off the FORT and image the atoms using absorption imaging. Approximately 1 mw of resonant light from the dye laser illuminates the atoms for about $5 \mu\text{s}$. The time between switching off the FORT and the application of the imaging pulse is called the time of flight (TOF). We generally use a TOF of $200 \mu\text{s}$ at full trap depth.

The atoms absorb the resonant light from the imaging pulse and prevent the

light from reaching the CCD array of the Andor camera that is placed behind the atom cloud. As the size of the imaging beam is much larger than the size of the atom cloud, a shadow of the atom cloud is observed in the camera. After taking a background image, with no atoms present, the image of the atoms can be extracted by subtracting the background image from the image where the atoms are present. The subtracted image is further processed to extract the total atom number and the width of the atom cloud. From the total atom number and the width of the atom cloud, the temperature and the density of the atom cloud is calculated.

Fig. 5.3 shows the absorption image of an atom cloud that has been evaporatively cooled at 832 G with a “low-well” value of 0.5 % and a final trap depth of 100 %. The temperature of the atom cloud is $2 \mu\text{K}$. In this section, we discussed the necessary

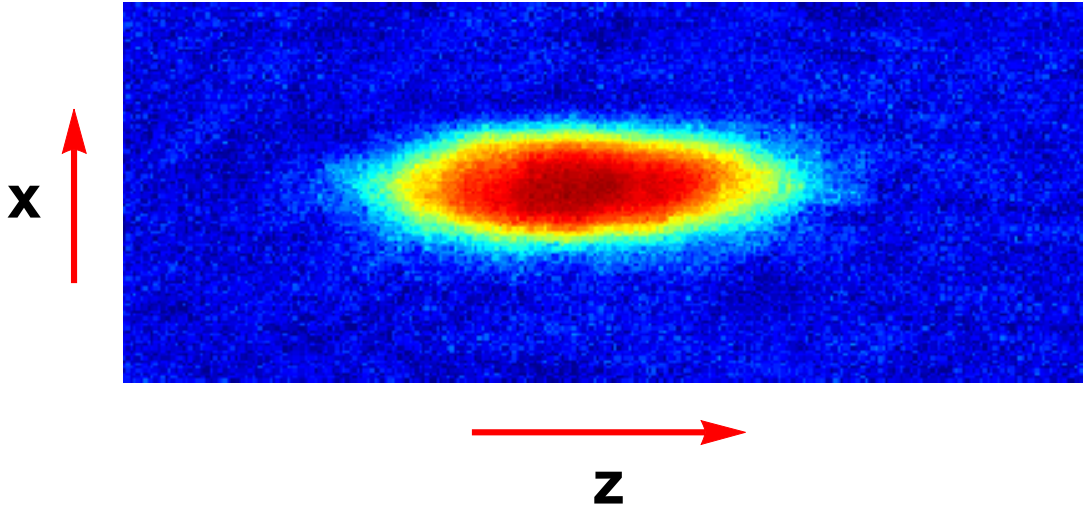


FIGURE 5.3: Absorption image of an atom cloud evaporative cooled at 832 G with a “low-well” value of 0.5 % and a final trap depth of 100 %. The temperature of the atom cloud is $2 \mu\text{K}$. The direction of propagation of the CO_2 optical beam (axial) is labeled as z . The dipole trap provides strong confinement of the the atoms in the radial direction (x and y).

steps involved in producing a cold Fermi gas. In the next section, we will focus on the experimental setup for the two-field method to optically control interaction in

the cold gas.

5.2 Experimental setup for two-field optical method

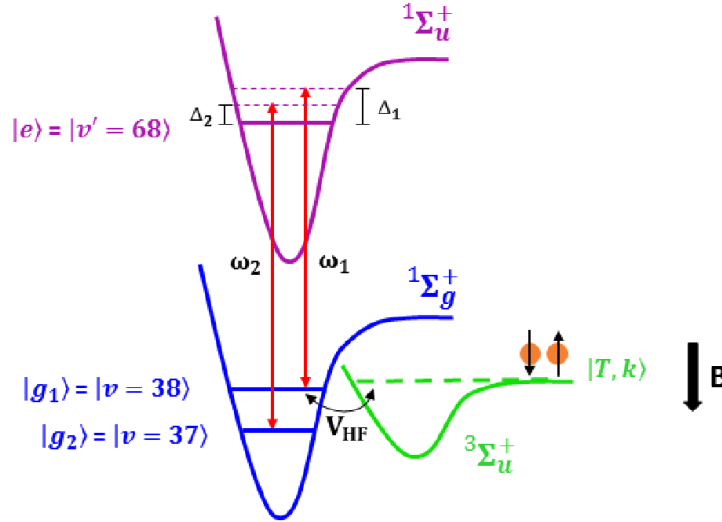


FIGURE 5.4: Basic level scheme for the two-field optical technique. Optical fields of frequencies ω_1 (detuning Δ_1) and ω_2 (detuning Δ_2), respectively, couple two singlet ground molecular states $|g_1\rangle$ and $|g_2\rangle$ to the singlet excited molecular state $|e\rangle$; V_{HF} is the hyperfine coupling between the incoming atomic pair state in the open triplet channel $|T, k\rangle$ and $|g_1\rangle$, which is responsible for a magnetically controlled Feshbach resonance.

I will start this section by briefly summarizing the two-field optical method to control interaction in ${}^6\text{Li}$, Fig. 5.2. We use two optical fields, namely, the control field, with angular frequency ω_1 and Rabi frequency Ω_1 and the EIT field, with angular frequency ω_2 and Rabi frequency Ω_2 . The control field couples the singlet ground state $|g_1\rangle$ to the singlet excited state $|e\rangle$ and the EIT field couples the singlet ground state $|g_2\rangle$ to the singlet excited state $|e\rangle$. The control field creates a light shift of the state $|g_1\rangle$, thereby changing the scattering length by modifying the overlap between the triplet continuum $|T, k\rangle$ and $|g_1\rangle$. However, the control field induces atom loss due to spontaneous scattering of atoms. Therefore, we use a EIT field to suppress spontaneous scattering through destructive quantum interference.

The design of the experimental setup for the two-field optical experiment should include the following requirements,

(i) **Large frequency offset** : The frequency difference between the control and the EIT field is one of the important factors taken into consideration while building the optical system. For the case of ${}^6\text{Li}$, the difference between $|g_1\rangle$ and $|g_2\rangle$ is approximately 57 GHz near 832 G. In the case of small frequency offsets, a simple single laser system with additional frequency generated using a acousto-optical modulator (AOM) or electro-optical modulator (EOM) would suffice. However, frequency differences in the range of tens of GHz requires more complicated setup.

(ii) **Relative frequency stability** : Since we use quantum interference techniques to suppress spontaneous scatter, relative frequency stability between the control and EIT laser limits the effective linewidth of the ground state coherence created by the two-field method. Hence, the relative frequency stability between the control and EIT field is very important.

(iii) **Wide range frequency tunability** : The frequency ω_1 of the control field depends on the magnetic field. Since we want to do experiments both near the broad resonance at 832.2 G and the narrow resonance at 543.2 G, we would like to have an optical system with wide frequency tunability.

5.2.1 *Basic experimental setup*

Based on the above requirements, we designed an optical system that uses three laser sources, namely, a reference laser, a control laser, and a EIT laser. The reference laser provides a stable frequency reference for the control and EIT laser. The control laser provides a stable frequency reference for the control and EIT laser. The control laser generates the optical field for the $v = 38$ to $v' = 68$ transition and the EIT laser generates the optical field for the $v = 37$ to $v' = 68$ transition. The frequency difference between the $v = 38$ to $v' = 68$ and $v = 37$ to $v' = 68$ transition is approximately 57 GHz. In this section, I will discuss the basic experimental setup

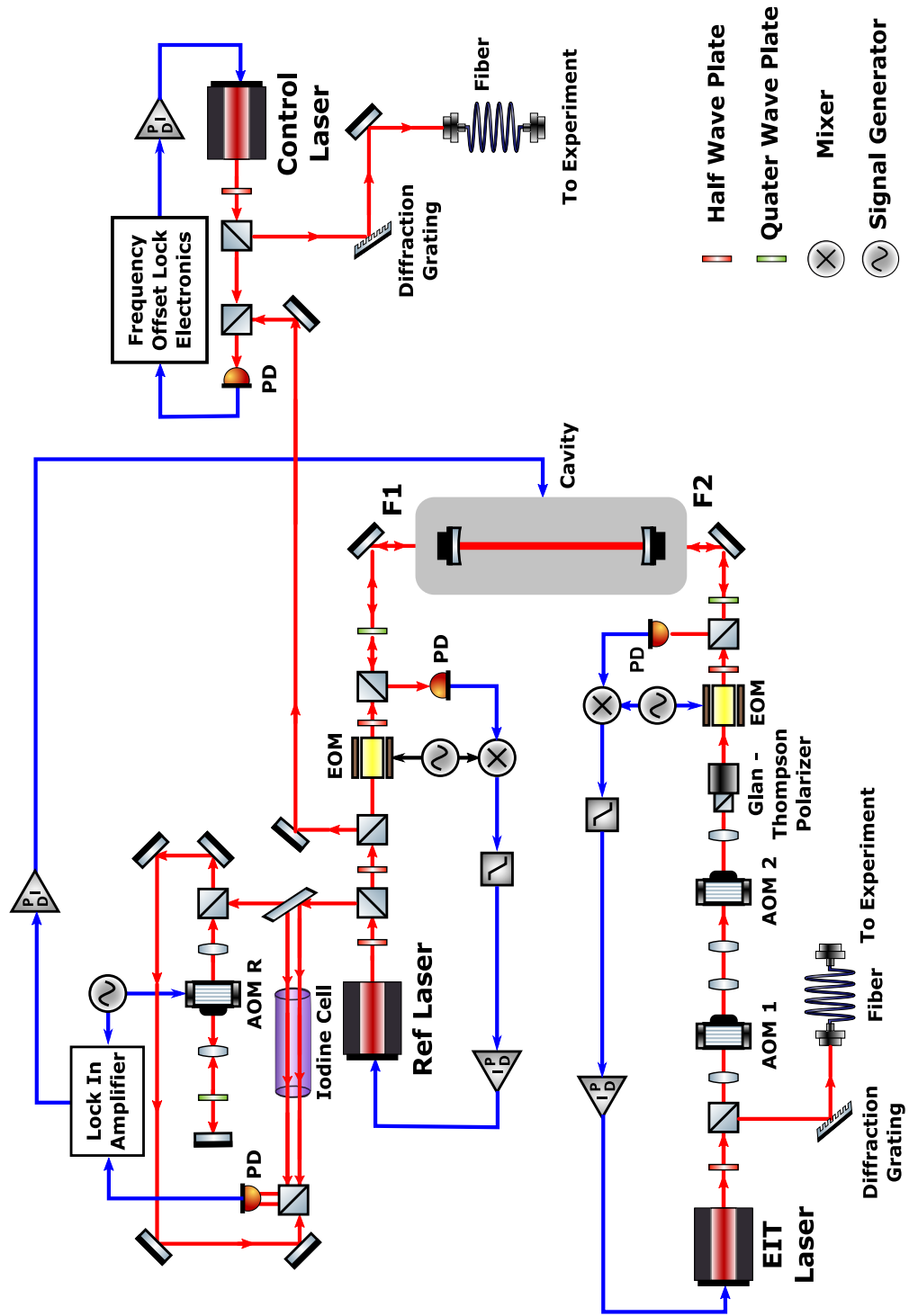


FIGURE 5.5: Experimental setup for two-field optical control. The reference laser and EIT laser is locked to the Fabry-Perot (FP) cavity. The FP cavity is locked to the iodine saturation absorption signal generated by sending part of the beam from reference laser to an iodine gas cell. The control laser is frequency offset locked to the reference laser.

for the two-field method. The different types of frequency stabilization techniques employed in our setup and specific details will be explained in detail below.

The basic setup for generating the optical fields for the two-field optical technique is shown in Fig. 5.5. We use diode lasers (Toptica TA pro) with an output power of approximately 400 mW. The frequencies of the lasers are tuned near the wavelength corresponding to the $v = 38$ to $v' = 68$ transition, namely, 673.2 nm by measuring the frequency using a wavemeter (Toptica WS6-200) with an absolute accuracy of ± 200 MHz. The frequency of the reference laser is stabilized by a Pound-Drever-Hall (PDH) lock to an Fabry Perot (FP) cavity (section 5.2.2). The FP cavity can drift due to mechanical and thermal fluctuations. A part of the beam from the reference laser with an output power of approximately 30 mW is sent into an iodine absorption spectroscopy setup to generate an error signal. The FP cavity is locked to the error voltage generated from the iodine saturation absorption signal.

The main advantage of this setup is that it exploits the high bandwidth lock of the PDH technique to minimize the fast jitter of the diode laser and simultaneously provides an absolute frequency reference.

The control laser with frequency ω_1 is frequency offset locked to the reference laser and generates the optical field for the $v = 38$ to $v' = 68$ transition. The EIT laser with frequency ω_2 is locked to a different mode of the cavity and generates the optical field for the $v = 37$ to $v' = 68$ transition which is approximately 57 GHz higher in frequency from the $v = 38$ to $v' = 68$ transition. The relative frequency jitter between the lasers is $\Delta\nu < 50$ kHz and the absolute frequency stability is < 100 kHz. As the optical linewidth of the molecular transitions is $\gamma_e = 2\pi \times 11.8$ MHz, the absolute stability is not as critical as the relative stability, which limits the effective linewidth of the ground state coherence created by the two-field method.

5.2.2 Frequency stabilization of lasers using PDH lock

In the optical system designed for the two-field optical method, Fig. 5.5, we stabilize the frequency of the reference laser and the EIT laser by locking both the lasers to a FP cavity using a PDH lock. In this section, we will discuss the PDH locking scheme in detail.

A 5 mW beam from the reference laser is used for the PDH locking scheme. The beam enters a electro-optic resonant phase modulator (Thorlabs EO-PM-R-30-C1) with a resonance frequency of 30 MHz. The electro-optic modulator (EOM) phase modulates the laser beam and generates frequency sidebands at +30 MHz and -30 MHz with respect to the laser (carrier) frequency. The EOM is resonantly modulated at 30 MHz using a sinusoidal wave with a peak to peak amplitude of 10 V generated using a Tektronix arbitrary waveform generator (Tektronix AFG3052C). A Glan-Thompson polarizer (Thorlabs GTH5M-B) mounted on a high precision rotational mount (Thorlabs PRM-1) is used in front of the EOM to match the polarization of the beam to the polarization axis of the EOM crystal in order to avoid amplitude modulation. The beam that exits the EOM is then sent through a $\lambda/2$ plate, polarizing beam splitter, and a $\lambda/4$ plate, before it is coupled to a Fabry-Perot cavity (Coherent) with a cavity linewidth of 7 MHz and a free spectral range (FSR) of 1.5 GHz.

The $\lambda/2$ plate after the EOM controls the polarization of the laser beam entering the FP cavity. We choose the polarization of the beam entering the FP cavity to be s-polarized for the reference laser beam. As the phase modulated optical beam with frequency sidebands is incident on the front face $F1$ of the cavity (Fig. 5.5), part of the beam is transmitted into the cavity and part of the beam is reflected. The ratio of the transmitted beam power to the total power is a measure of the coupling efficiency of the cavity. The transmitted beam at the end $F1$ sets up a standing wave

inside the cavity and exits the other end $F2$ of the cavity, when the wavelength λ of the incident light is an integer multiple of the free spectral range i.e., $\lambda = n \times FSR$, where n is an integer. When $\lambda/2 = n \times FSR$, it results in an reflected “leakage” beam that exits the front end $F1$ of the cavity. The cavity is aligned using the input coupling mirrors such that both the initially reflected beam and the “leakage” beam at the end $F1$ are collinear. Both the beams are then focussed on to a high bandwidth (150 MHz) transimpedance amplified photodetector (Thorlabs PDA10A).

Near the cavity resonance, the frequency sidebands in the laser beam are completely reflected from the $F1$ end of the cavity. The “leakage” beam is anti-phase with the reflected beam. Therefore, the carrier frequency component of the reflected beam is completely canceled by the carrier frequency component of the “leakage” beam. However, the sum of the beats generated between the carrier frequency of the “leakage” beam and the upper and lower sidebands of the reflected beam generates a frequency discriminator error signal shown in Fig. 5.6.

The error signal is extracted by mixing the photodetector signal with the modulation signal in a RF mixer (Minicircuits ZAD-1-1-+). A 10 MHz low-pass filter (Minicircuits BLP 10.7) is added to the Intermediate Frequency (IF) port of the mixer to remove high frequency noise. The diode laser is locked to the zero of the error signal using a high bandwidth digital servo system (Toptica Digilock).

If the error signal has a non-zero DC component, it implies the presence of residual amplitude modulation at the EOM. This is rectified by adjusting the Glan-Thompson polarizer in front of the EOM to align the polarization of the laser beam to the polarization axis of the EOM crystal. We were able to achieve a linewidth of about 20 kHz using the PDH technique.

The EIT beam is also locked to the same cavity using the PDH technique, but enters the cavity at the $F2$ end. The EIT beam goes through two Acousto-Optical Modulator’s (AOM), namely, AOM 1 and AOM 2, before entering the cavity at

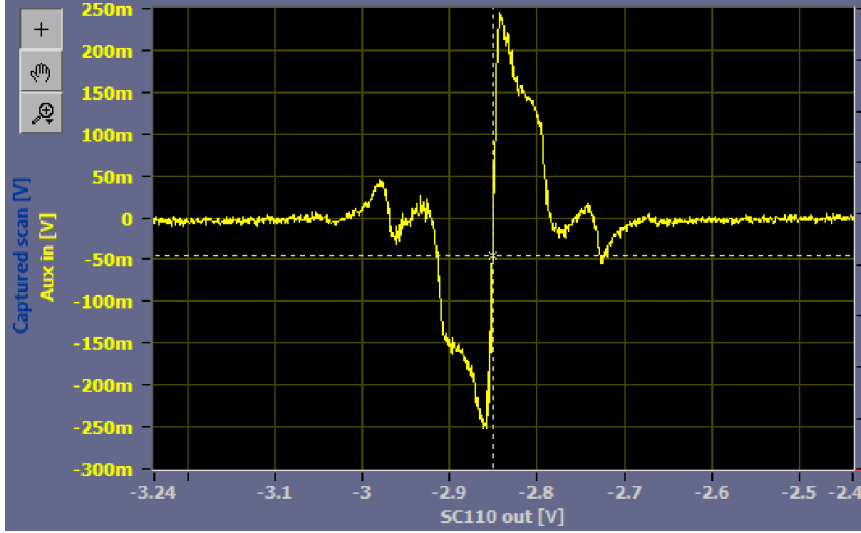


FIGURE 5.6: Frequency discriminator error signal (screenshot) using PDH lock. Error signal voltage vs Laser PZT voltage. 1 V = 500 MHz. The reference laser and the EIT laser is locked to this error signal.

the $F2$ end. AOM 1 (Isomet) downshifts the EIT laser's frequency by 120 MHz and AOM 2 upshifts the frequency by 370 MHz, for a net upshift in frequency of 250 MHz. We choose the polarization of the EIT beam before entering the cavity to be p-polarized. Orthogonal polarizations were chosen for the EIT and reference optical beams to prevent the transmitted EIT beam at the $F1$ end from reaching the photodetector at the $F1$ end that is used to observe the reference laser optical beams and vice versa.

The EIT beam is phase modulated using a resonant EOM with a resonance frequency of 35 MHz. The EIT and reference laser beam are phase modulated at different frequencies (30 MHz and 35 MHz) in order to avoid cross-talk. The EIT laser is locked to a cavity mode which is approximately 57 GHz above the cavity mode to which the reference laser is locked corresponding to the frequency difference between the $v = 37$ to $v' = 68$ and $v = 38$ to $v' = 68$ transition.

A spectrum analyzer is used to record the beat frequency note between the refer-

ence and EIT lasers locked to the same cavity mode using the PDH technique. The FWHM (Full width at half maximum) of the beat note is used to optimize the gain parameters of the Digilock servo system. After locking the lasers to the cavity, the beat note observed in the spectrum analyzer had a FWHM of less than 20 kHz.

5.2.3 Locking the FP cavity using iodine saturation absorption spectroscopy

In the previous section, we discussed the locking of a diode laser to a FP cavity. However, the cavity can drift due to mechanical and thermal fluctuations. In this section, we will discuss the frequency stabilization of an FP cavity using iodine doppler-free saturated absorption spectroscopy.

After locking the reference laser to the cavity, a part of the beam from the reference laser with approximately 30 mW of power is used for saturation spectroscopy. The beam is incident on a 90/10 plate beam splitter which transmits 90% of the power (pump beam) and reflects 10% of the power in two co-propagating beams (probe beams). The probe beams then enter the iodine gas cell and are collected by a balanced photo-detector which subtracts the voltage signal from both the incident probe beams. The pump beam is double passed in an AOM which frequency modulates the pump beam as well as up shifts the frequency by 236 MHz (+118 MHz single-pass). The AOM is modulated using an peak-peak amplitude of 3 V sine wave at 34 KHz generated by an Agilent function generator. The frequency modulated pump beam then counter-propagates with the probe beams and are overlapped with one of the probe beams.

In the absence of the pump beam, the probe beam will be absorbed by iodine molecules with a broad range of velocities and therefore result in Doppler broadening of the absorption peak. The presence of a counter-propagating pump beam overcomes the effect of Doppler broadening by burning a “hole” in the Doppler broadened absorption spectra as the pump and probe beams interacts with the same velocity class

of iodine molecules. The output of the balanced photo-detector and the modulation

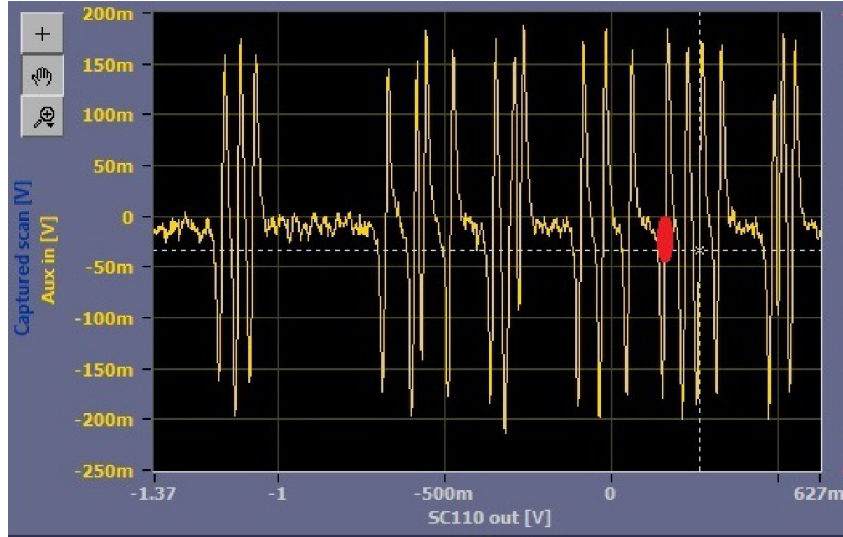


FIGURE 5.7: Frequency discriminator error signal (screenshot) from iodine saturation absorption spectroscopy. Error signal voltage vs Laser PZT voltage. 1 V = 500 MHz. The reference laser is locked to the zero point of the frequency discriminator signal marked with a red dot.

signal is sent into a lock-in amplifier to obtain the frequency discriminator error voltage signal spectrum shown in Fig. 5.7. As seen from the error signal spectrum, there are multiple error signals over a span of 1 GHz since the iodine molecule has a rich spectrum with each error signal corresponding to a transition between rovibrational states. The entire spectrum lies approximately 800 MHz below the $v = 38$ to $v' = 68$ transition. The cavity is locked to the zero of one of the error voltage signal (marked with the red dot in Fig. 5.7) using a home built servo system.

5.2.4 Frequency offset lock between the reference and the control laser

In this section, we will discuss the frequency offset lock [64] between the reference laser and the control laser, which generates the optical field for the $v = 38$ to $v' = 68$ transition. As mentioned in the previous section, the reference laser is locked to the FP cavity which in turn is locked to a iodine peak that lies 800 MHz below the

$v = 38$ to $v' = 68$ transition. Hence, in order for the control laser to generate the optical field for the $v = 38$ to $v' = 68$ transition, the control laser should be locked with an frequency offset of +800 MHz with respect to the reference laser. The basic schematic for the frequency offset lock is shown in Fig. 5.8.

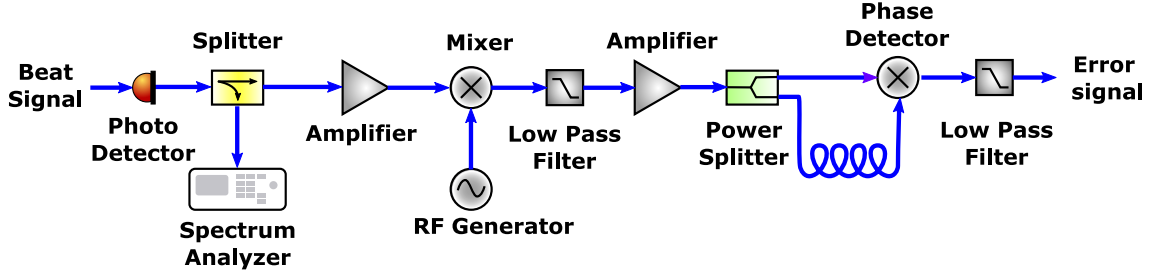


FIGURE 5.8: Basic schematic for the frequency offset lock.

The reference and control laser beams (about 1 mW) are combined using using a 50/50 beam splitter and is made incident on a high bandwidth (1 GHz) transimpedance amplified photodetector (Menlosystems-FPD 310-FV). The photodetector detects the beat frequency signal between the two optical beams. The beat voltage signal from the photodetector is send to a 1×2 power splitter (Minicircuits), which sends part of the beat signal to the spectrum analyzer and rest of the signal to an 40 dB RF amplifier (Minicircuits). The output of the amplifier is send to a mixer which downconverts the beat signal in the 50-100 MHz range by mixing it with an RF signal generated by an RF signal generator. A low pass filter with a cut-off frequency of 100 MHz is connected to the IF output port of the mixer to suppress higher harmonics.

The downconverted beat signal is sent to a 1×2 power splitter. One of the outputs of the power splitter is sent directly to one input port of the phase detector and the other output of the power splitter is sent through a coaxial delay line into the other input port of the phase detector. The phase detector generates an output voltage that depends on the relative phase difference between its two input signals.

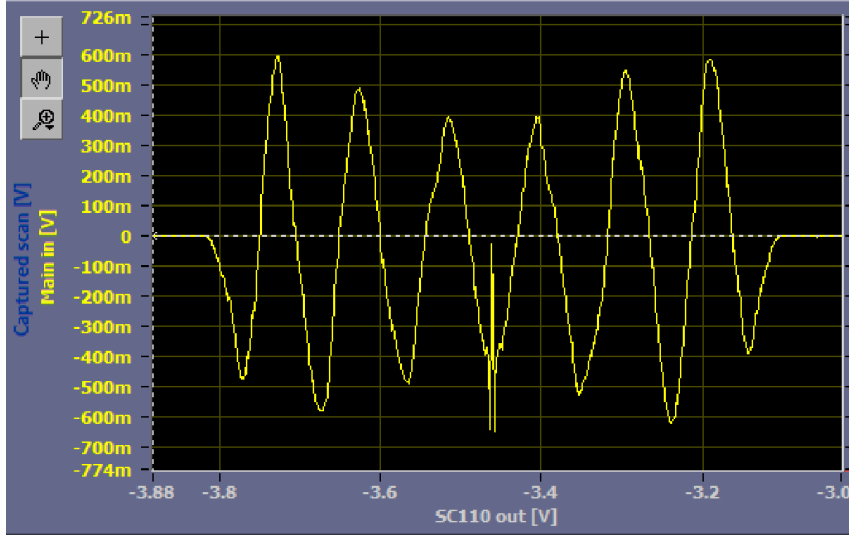


FIGURE 5.9: Frequency discriminator error signal (screenshot) from the frequency offset lock between the reference and the control laser obtained by observing the beat between them. Error signal voltage vs Laser PZT voltage. $1 \text{ V} = 500 \text{ MHz}$. The control laser is locked to this error signal.

The delay line introduces a frequency dependent phase shift. Since the phase shift introduced by the delay line is frequency dependent, the phase detector generates an error voltage that depends on the frequency difference between the reference and the control laser. The frequency discriminator error signal voltage generated by the phase detector as a function of control laser frequency is shown in Fig. 5.9 . A low pass filter with a cut-off frequency of 10 MHz is added at the output of the phase detector to suppress high frequency noise on the error voltage.

The control laser can be locked to several values of the beat frequency by choosing one of the several zero crossings of the error signal. The spacing between the zero crossing depends on the length of the cable and is approximately equal to c/L , where L is the length of the cable and c is the velocity of light. The capture range is then $\approx c/2L$. For our setup, $L = 4$ meters and the capture range is $\approx 37 \text{ MHz}$. Wide frequency tunability of about 250 MHz is achieved by changing the frequency in the RF generator used for down converting the beat signal. The control laser is locked

using a digital servo (Toptica Digilock) system. After locking, the beat note between the reference laser and the control laser observed using the spectrum analyzer has a full-width half maximum of less than 20 kHz (1 s sweep).

5.2.5 Spectral filtering of optical fields

One of the main issues of using a diode laser with a tapered amplifier in our two-field optical control experiments is the wide bandwidth spectral response of the tapered amplifier. Our wavelength of interest for controlling interactions is 672.3 nm and the resonant wavelength for Li atoms is 670.9 nm. As the wavelength to control interactions is approximately 2 nm far from the resonant wavelength, the off-resonant free atom scattering rate from the 672.3 nm is very small, approximately 3 atoms/s. However, during our experiments, when we apply light near 672.3 nm which is non-resonant with the molecular transition to illuminate the atoms, we observe 50% atom loss in 100 ms. This anomaly in increased atom loss rate was later discovered to be due to the wide spectral bandwidth response of the tapered amplifier in our diode lasers.

The tapered amplifier in addition to amplifying the 672.3 nm also transmits a wide range of other wavelengths including the resonant wavelength of 670.9 nm. This severely limits the lifetime of atoms due to both resonant and off-resonant heating. Although the manufacturers data sheet for the tapered amplifier indicates a 30 dB suppression for wavelengths other than the wavelength which is amplified, it is still not sufficient for the purposes of our experiment. For example, at an optical beam intensity of 1×10^3 W/cm², which is typical for all our experiments, a 30 dB suppression of other wavelengths would still transmit about 1 W/cm² of resonant light, which is large enough to cause significant loss. Therefore, it is very important to filter out all other wavelengths except 672.3 nm. This is achieved by the use of a Bragg grating wavelength filter.

A Bragg grating has a periodic variation of refractive index which reflects a particular wavelength at a certain angle of incidence and suppresses all other wavelengths through multipath destructive interference. After frequency stabilization of all the lasers, the control and EIT laser beam are made incident on a Bragg grating wavelength filter. The filter has a bandwidth of approximately 0.1 nm. With the grating filter, we observed only 10% atom loss after 400 ms, when the atoms are illuminated by a non-resonant (molecular) optical beam near 673.2 nm with an intensity of 1×10^3 W/cm².

5.2.6 Illuminating the atoms with optical fields

The reflected optical beam from the Bragg grating passes through an AOM which acts as an optical switch for our experiments. The AOM for the control beam and the EIT beam upshifts the frequency by 118 MHz and 125 MHz, respectively. The control beam and the EIT beam are separately coupled into two polarization maintaining fibers which transport the beams to the main chamber to illuminate the atoms. The optical beam that exits the polarization maintain fiber near the main chamber passes through a polarizing beam splitter where we choose the polarization of the optical beam to be in the direction of the biased magnetic field. Since $v = 37$ to $v' = 68$ transition is much weaker than the $v = 38$ to $v' = 68$ transition, the EIT beam requires more intensity and is therefore focused on to the atoms using a focusing lens with a focal length of 50 cm.

The control beam has an $1/e^2$ radius of $750 \mu\text{m}$. Due to the error in optical alignment, which we discovered only after taking data, the EIT beam was elliptical in all of our experiments with a $1/e^2$ radius of $65 \mu\text{m}$ in one direction and $140 \mu\text{m}$ in the other direction. The beam waist measurement and the alignment of the beam on the atoms were done by imaging the optical beam using the CCD camera that we use to image our atoms.

Prior to concluding this chapter, I will discuss the measurement of some basic quantities such as the trap oscillation frequencies, temperature, density of our ultracold gas, and the transition and Rabi frequencies of the optical fields. I will also discuss the measurement of three-body loss near the narrow Feshbach resonance which we remove from all our loss spectra presented in chapter 6.

5.3 Measurement of density and temperature of the atom cloud

In this section, I discuss the evaluation of density and temperature of our ultracold gas by measuring trap oscillation frequencies.

5.3.1 *Measurement of trap frequencies of atoms in a CO₂ dipole trap*

We measure the the trap oscillation frequencies using parametric resonance, which works on the principle that energy is added to the atoms trapped in an harmonic potential when the trap is modulated at twice the trap oscillation frequency. Previous thesis [61] from our group explains the parametric resonance method of measuring trap oscillation frequencies in detail.

In parametric resonance, the intensity of the optical trap is sinusoidally modulated with a modulation depth of about 5 % and the width of the atom cloud is measured as a function of the modulation frequency. When the modulation frequency equals twice the trap oscillation frequency, there is a increase in the atom cloud width due to the increase in the total energy of the atoms.

After evaporatively cooling the atoms at 300 G, we perform the experiment at 528 G where the $|1\rangle - |2\rangle$ mixture is non-interacting due to the presence of zero-crossing in the scattering length [65]. We modulate the intensity of the optical trap with an sinusoidal wave at an modulation depth of 5 % and image the atoms after a time of flight of 200 μ s. We fit a gaussian function of the form $e^{-((x-x')^2/2\sigma^2)}$ to the spatial profile of the atomic cloud and obtain the width of the atom cloud σ .

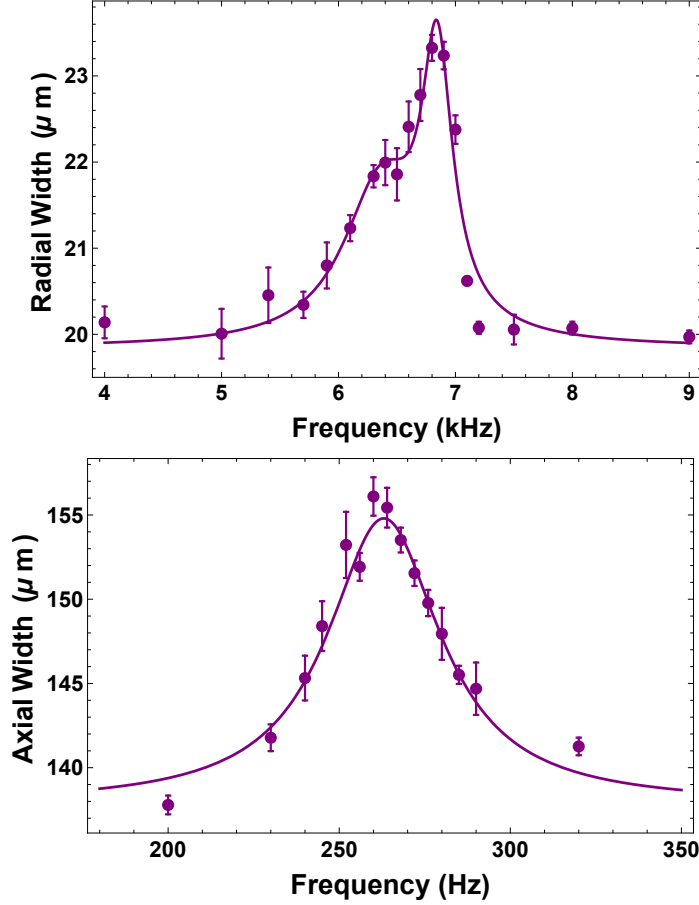


FIGURE 5.10: Parametric resonance to measure trap oscillation frequencies of atoms in an optical dipole trap. Trap oscillation frequency is half the modulation frequency at which the resonance occurs. (top) Measurement of radial trap oscillation frequency. Radial width as a function of modulation frequency. $\omega_x = 3100$ Hz and $\omega_y = 3350$ Hz. (bottom) Measurement of axial trap oscillation frequency. Axial width as a function of modulation frequency. $\omega_z = 130$ Hz.

Fig. 5.10 (top) shows radial cloud width as a function of modulation frequency. The presence of two peaks in Fig. 5.10 (top) implies that our optical dipole trap is not perfectly symmetric in both the radial directions. From Fig. 5.10 (top), we obtain the radial trap frequencies, $\omega_x = 3100$ Hz and $\omega_y = 3350$ Hz, where the smaller of the two frequencies is conventionally called as ω_x . Fig. 5.10 (bottom) shows axial cloud width as a function of modulation frequency. From Fig. 5.10 (bottom), we obtain the axial trap frequency $\omega_z = 130$ Hz.

5.3.2 *Measurement of the trap oscillation frequencies for the combined CO₂ dipole and red trap*

For the CO₂ laser trap alone, the trap frequencies for the x , y and z directions are determined by parametric resonance. However, in our optical control experiment we apply two more optical beams, namely, the control beam and the EIT beam which are red-detuned to the atomic transition. The control and the EIT optical beams can provide additional trapping potential to the atoms thereby changing the trap oscillation frequencies. Therefore it is important to determine the combined trap oscillation frequency of the CO₂ dipole trap and “red” trap. In this section, we determine the trap oscillation frequencies of the combine dipole and red trap using cloud size measurements.

The typical intensities of the control and the EIT beam used in our experiments are 2 W/cm² and 0.5 kW/cm², respectively. The $1/e^2$ intensity radius of the control beam is $\approx 750 \mu\text{m}$. The EIT beam is elliptical due to alignment error with a $1/e^2$ intensity radius of 70 μm in one direction and 160 μm in the other direction. Since the control beam is much larger than the typical axial size of our atom cloud (65-75 μm), the intensity variation of the control beam across the atom cloud is negligible and therefore it cannot create a trapping potential on the atoms. However, the EIT beam which is approximately 250 times more intense than the control beam and comparable in size to the atom cloud can provide additional trapping potential on the atom cloud.

In order to check for changes in the trapping potential due to the EIT beam, we image the atoms in the presence of the EIT beam after abruptly turning off the dipole trap and look for additional confinement by measuring the cloud size. Fig. 5.11 (top) shows the image of the atom cloud with no EIT beam. Fig. 5.11 (bottom) shows the image of the atom cloud in the presence of the EIT beam. By comparing both Fig. 5.11 (top) and Fig. 5.11 (bottom), we can clearly see that the EIT beam creates

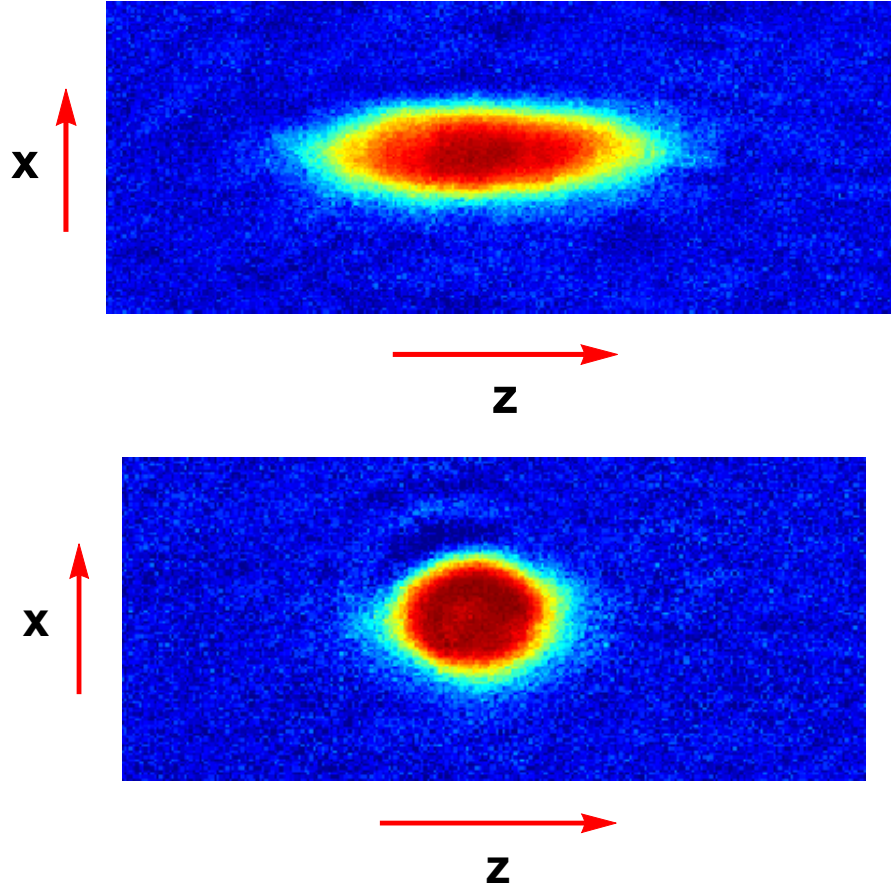


FIGURE 5.11: Atom cloud images in (top) dipole trap (bottom) dipole and red (EIT beam) trap. The EIT beam provides additional confinement in the axial z -direction with negligible confinement in x and y directions. The y direction is not shown in the figure. The CO_2 propagates in the z direction and the EIT beam propagates in the y direction.

additional confinement in the axial direction with negligible confinement in the other two directions.

To determine the correct mean atom density, it is important to measure the ω_z trap frequency including the effect of the EIT beam on the atoms. For the two-beam trap, we find that parametric resonance does not yield a high precision measurement of ω_z . Instead, we use cloud size measurements to find the total trap frequency ω_{zt} , arising from combined the CO_2 laser and EIT beam potentials.

The control beam is turned off throughout the measurement. After forced evaporation in the CO₂ laser trap near 832 G and re-raising the trap to full depth, the EIT beam is adiabatically turned on over 30 ms. Then both the CO₂ laser and EIT beams are abruptly turned off simultaneously and the atoms are imaged after a time of flight of 150 μ s to determine the $1/e$ size σ_{zi} of the cloud just before release. The same procedure is repeated again, but this time, only the EIT (ω_2) beam is abruptly extinguished, so that the atoms are released from the red trap into the CO₂ laser trap, where the axial frequency is $\omega_z < \omega_{zt}$. After a hold time of 200 ms, the atom cloud reaches equilibrium and is imaged to determine its final axial width σ_{zf} in the CO₂ laser trap alone. From σ_{zi} and σ_{zf} , we determine ω_{zt} using energy conservation as follows.

Just before the ω_2 beam is extinguished, the mean z-potential energy per atom is

$$\langle U_z \rangle = \frac{1}{2} m \omega_{zt}^2 \langle z^2 \rangle, \quad (5.6)$$

where the mean cloud size is given by

$$\langle z^2 \rangle = \sigma_z^2. \quad (5.7)$$

As the pressure is isotropic, the total potential energy of the atoms taking into account all three directions is

$$\langle U_{tot} \rangle = \frac{3}{2} m \omega_{zt}^2 \sigma_{zi}^2 \quad (5.8)$$

According to virial theorem [66], the mean internal energy of a unitary gas (near 832 G) is equal to the mean potential energy. Hence the internal energy of the gas at the time of release is also

$$\langle E_{int} \rangle = \frac{3}{2} m \omega_{zt}^2 \sigma_{zi}^2 \quad (5.9)$$

Just after extinguishing the ω_2 beam, the potential energy of the atoms (in the CO₂ laser trap alone) is $\frac{3}{2} m \omega_z^2 \sigma_{zi}^2$, since σ_{zi} has not changed. The total energy of the atoms immediately after the ω_2 beam is turned off is then

$$E_{ti} = \frac{3}{2} m \omega_{zt}^2 \sigma_{zi}^2 + \frac{3}{2} m \omega_z^2 \sigma_{zi}^2 \quad (5.10)$$

According to the virial theorem, after reaching equilibrium, the total energy of the atoms E_{tf} in the CO₂ laser trap alone is twice the mean potential energy,

$$E_{tf} = 3 m \omega_z^2 \sigma_{zf}^2 \quad (5.11)$$

By conservation of energy $E_{ti} = E_{tf}$. Therefore, comparing Eq. 5.10 and Eq. 5.11, we obtain

$$\omega_{zt}^2 = \omega_z^2 \left(2 \frac{\sigma_{zf}^2}{\sigma_{zi}^2} - 1 \right), \quad (5.12)$$

which gives ω_{zt} in terms of the CO₂ laser trap axial frequency, ω_z .

5.3.3 Measurement of temperature of the atom cloud

In this section, we will determine the temperature of the atomic cloud using the measured axial trap frequencies ω_z and the axial cloud size σ_z . For an atom cloud in a harmonic dipole trap with a gaussian spatial profile, the mean total potential energy U_{tot} is given by

$$\langle U_{tot} \rangle = \frac{1}{2} m \omega_x^2 \langle x^2 \rangle + \frac{1}{2} m \omega_y^2 \langle y^2 \rangle + \frac{1}{2} m \omega_z^2 \langle z^2 \rangle, \quad (5.13)$$

where ω_x , ω_y , ω_z are the trap oscillation frequencies and $\langle x^2 \rangle$, $\langle y^2 \rangle$, and $\langle z^2 \rangle$ are the mean cloud size in the x , y , z direction, respectively.

We determine the $1/e$ size of the atomic cloud σ_i by fitting a gaussian function of the form $e^{-((i-i')^2)/2\sigma_i^2}$ to the spatial profile of the atomic cloud. The measured $1/e$

width σ_i is related to the mean cloud size $\langle i^2 \rangle$ by

$$\sigma_i^2 = \langle i^2 \rangle. \quad (5.14)$$

Using Eq. 5.14 in Eq. 5.13,

$$\langle U_{tot} \rangle = \frac{1}{2} m \omega_x^2 \sigma_x^2 + \frac{1}{2} m \omega_y^2 \sigma_y^2 + \frac{1}{2} m \omega_z^2 \sigma_z^2, \quad (5.15)$$

Furthermore, for a harmonic dipole trap of potential energy U_0 ,

$$U_0 = \frac{1}{2} m \omega_x^2 \sigma_x^2 = \frac{1}{2} m \omega_y^2 \sigma_y^2 = \frac{1}{2} m \omega_z^2 \sigma_z^2, \quad (5.16)$$

Substituting Eq. 5.16 in Eq. 5.15, we obtain

$$\langle U_{tot} \rangle = \frac{3}{2} m \omega_z^2 \sigma_z^2, \quad (5.17)$$

For a strongly interacting gas, we know from virial theorem [45], the mean internal energy is equal to the mean potential energy

$$\langle E_{int} \rangle = \langle U_{tot} \rangle = \frac{3}{2} m \omega_z^2 \sigma_z^2, \quad (5.18)$$

Therefore, the total energy of the gas is

$$E_{tot} = \langle E_{int} \rangle + \langle U_{tot} \rangle = 3 m \omega_z^2 \sigma_z^2 = 3 k_B T, \quad (5.19)$$

where T is the temperature of the gas. From Eq. 5.19, we obtain

$$T = \frac{m \omega_z^2 \sigma_z^2}{k_B} \quad (5.20)$$

We use Eq. 5.20 to calculate the temperature of the gas from axial width σ_z and the axial trap frequency ω_z . For the data shown in Fig. 5.12, the measured temperature using Eq. 5.20 is $7.3 \mu\text{K}$.

5.3.4 Measurement of density of the atom cloud

In this section, we will evaluate the density of the atomic gas from the axial width σ_z and trap frequencies ω_x , ω_y , and ω_z . The average density \bar{n} of atoms in an atomic cloud with gaussian atomic spatial profile is given by

$$\bar{n} = \frac{N}{(2\pi)^{3/2} \sigma_x \sigma_y \sigma_z}, \quad (5.21)$$

where N is the total number of atoms and σ_x , σ_y , and σ_z are the $1/e$ widths of the gaussian atomic spatial profile in the x , y , and z direction, respectively.

From Eq. 5.21, we can see that we need information about the total atom number and $1/e$ widths in order to calculate the density of the atomic gas. However, due to strong confinement of the atoms in the radial direction of our CO₂ dipole trap, the widths σ_x and σ_y cannot be reliably measured with the available resolution in our camera system. Therefore, we measure only the width σ_z of the atom cloud in the z -direction (CO₂ laser beam propagation direction) and calculate the widths σ_x and σ_y by measuring the trap oscillation frequencies in all three directions (sec. 5.3.1).

For a harmonic dipole trap, the dipole potential energy U_0 is given by

$$U_0 = \frac{1}{2} m \omega_x^2 \sigma_x^2 = \frac{1}{2} m \omega_y^2 \sigma_y^2 = \frac{1}{2} m \omega_z^2 \sigma_z^2 = k_B T \quad (5.22)$$

From Eq. 5.22, we write the widths σ_x , σ_y , and σ_z in terms of the temperature as

$$\begin{aligned} \sigma_x &= \sqrt{\frac{2 k_B T}{m} \frac{1}{\omega_x}} \\ \sigma_y &= \sqrt{\frac{2 k_B T}{m} \frac{1}{\omega_y}} \\ \sigma_z &= \sqrt{\frac{2 k_B T}{m} \frac{1}{\omega_z}} \end{aligned} \quad (5.23)$$

Using Eq. 5.23 in Eq. 5.21, we obtain

$$\bar{n} = \frac{N\omega_x\omega_y\omega_z}{2\pi^{3/2}} \left(\frac{m}{k_B T} \right)^{3/2} \quad (5.24)$$

We use eq. 5.24 to evaluate the density of the gas from trap frequencies ω_x , ω_y , and ω_z measured in sec. 5.3.1 and temperature T determined in sec. 5.3.3. The typical densities of our atom cloud for the data shown in this thesis are $\approx 10^{-10}\text{cm}^{-3}$.

5.4 Determination of the Rabi frequencies

In order to fit the experimental data using the continuum-dressed state model, we need the Rabi frequencies Ω_1 and Ω_2 of the control and EIT beam, respectively.

We first estimate the Rabi frequency Ω_1 from the predicted electric dipole transition matrix element. In ${}^6\text{Li}$, $|g_1\rangle$ is the ${}^1\Sigma_g^+$ ($N = 0$) $v = 38$, vibrational state, which is responsible for the Feshbach resonance. Starting from that state, the best Franck-Condon factor [67] arises for an optical transition to the excited $A^1\Sigma_u^+$ ($N = 1$) $v' = 68$ vibrational state, which we take as $|e\rangle$. For the $v = 38 \rightarrow v' = 68$ transition, the predicted oscillator strength is $f_{eg} = 0.034$ [67]. We find that the corresponding Rabi frequency is

$$\Omega_1 = 2\pi \times 5.6 \text{ MHz} \sqrt{I},$$

where I is the intensity of the optical beam given in mW/mm^2 .

For the $v = 37 \rightarrow v' = 68$ transition, the predicted oscillator strength is $f_{eg} = 3.8 \times 10^{-5}$ [67]. We find that the corresponding Rabi frequency is

$$\Omega_2 = 2\pi \times 0.17 \text{ MHz} \sqrt{I},$$

where I is the intensity of the optical beam given in mW/mm^2 .

We measure the beam waist ω_0 and power P of the optical beams and calculate the intensity $I = \sqrt{2P/\pi\omega_0^2}$. Using the measured values, we fit all of the data shown

in the chapter 6 using

$$\begin{aligned}\Omega_1 &= 2\pi \times c_1 \text{ MHz } \sqrt{I} \\ \Omega_2 &= 2\pi \times c_2 \text{ MHz } \sqrt{I},\end{aligned}\tag{5.25}$$

and compare the values of c_1 and c_2 to the predicted values of $c_1 = 5.6$ and $c_2 = 0.17$, respectively.

5.5 Measurement of the transition frequencies

In this section, I will discuss the measurement of transition frequencies by laser spectroscopy for the $|v = 38\rangle \rightarrow |v' = 68\rangle$ transition and $|v = 38\rangle \rightarrow |v' = 68\rangle$. The atoms are originally prepared in the triplet continuum state $|T, k\rangle$. However, near the broad Feshbach resonance, as explained in chapter 2, the triplet continuum state $|T, k\rangle$ is mixed with the $|v = 38\rangle$ ground singlet state due to the presence of hyperfine coupling. Therefore, atoms in the triplet continuum state acquires the singlet character of the $|v = 38\rangle$ state and can be pumped to an excited vibrational singlet state in the presence of resonant light. We perform laser spectroscopy near the broad Feshbach resonance at 840 G where the triplet continuum state $|T, k\rangle$ is strongly coupled with the $|v = 38\rangle$ singlet state.

We prepare a 50:50 mixture of ${}^6\text{Li}$ atoms in their two lowest hyperfine states, $|1\rangle$ and $|2\rangle$ in a CO_2 optical trap as explained in section 5.2. Since we are working near the broad Feshbach resonance, we sweep the magnetic field to 832 G to perform evaporative cooling. After forced evaporation, and re-raising the trap to its initial trap depth, we have about 10^5 atoms in each spin state. The magnetic field is then swept to the field of interest where we typically wait for about 2 s for the magnetic field to stabilize. The resonant light for the $|T, k\rangle \rightarrow |v = 38\rangle$ transition from the control laser then illuminates the atoms for 5 ms. The atoms in one of the spin states are imaged after a time of flight of $150 \mu\text{s}$ from which we calculate the total

atom number and the axial width σ_z of the atom cloud as a function of the control laser frequency ω_1 , Fig. 5.12. The frequency corresponding to the maximum atom loss is the transition frequency of the $|T, k\rangle \rightarrow |v = 38\rangle$ transition. Fig. 5.12 shows atom fraction versus single-photon detuning Δ_e , where $\Delta_e = 0$ corresponds to the transition frequency.

With the help of the transition frequencies reported in [62] for their photoassociation experiments, we measured the transition frequency for the $|T, k\rangle \rightarrow |v = 38\rangle$ at 840 G to be

$$\nu(38 \rightarrow 68) = 445.2872 (\pm 0.0002) \times 10^{12} \text{ Hz} \quad (5.26)$$

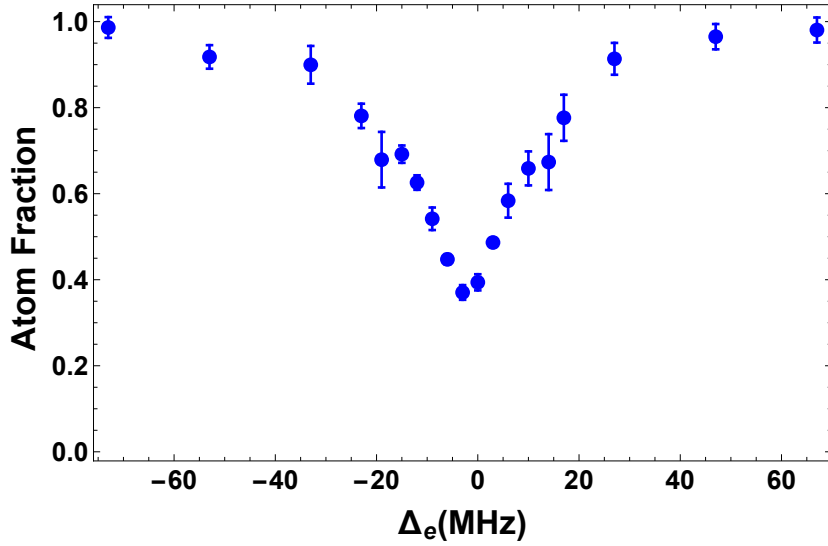


FIGURE 5.12: Single field atom loss spectra as a function of single photon detuning Δ_e by changing the control laser frequency ω_1 at a fixed magnetic field $B = 840$ G. Maximum loss occurs for $\Delta_e = 0$. Temperature $T = 7.3 \mu\text{K}$ and intensity $I = 10 \text{ mW/mm}^2$. Each data point is the average of 5 randomized trials.

The uncertainty in the above measurement is due to the limitation in the absolute accuracy of our wavemeter (± 200 MHz).

Fig. 5.12 shows the normalized atom loss spectra as a function of the single photon detuning by changing the control laser frequency ω_1 . As resonant light from the control laser for the $|T, k\rangle \rightarrow |v = 38\rangle$ transition illuminates the atoms, the

free unbound atoms which are originally in a superposition of $|T, k\rangle$ and $|g_1\rangle$ due to hyperfine mixing near a Feshbach resonance is pumped to the excited singlet molecular state $|e\rangle$. The atoms in the excited state spontaneously decay to *all* allowed lower lying vibrational states thereby incurring atom loss. This process of optically coupling free unbound atoms to a molecular excited bound state is called photoassociation [52]. We can see that maximum atom loss occurs when the single photon detuning Δ_e is tuned to zero.

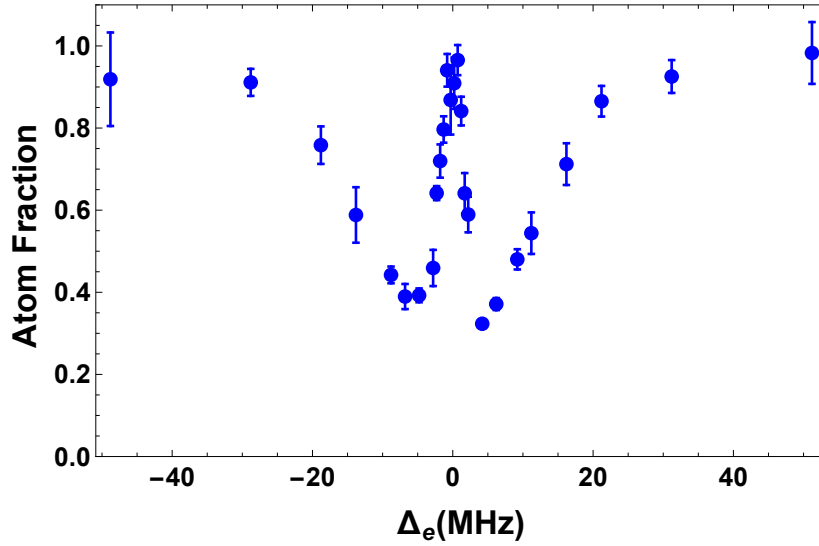


FIGURE 5.13: Loss suppression near the broad Feshbach resonance. Atom loss spectra as a function of single photon detuning Δ_e by changing the control laser frequency ω_1 at a fixed magnetic field $B = 840$ G. The detuning Δ_2 of the EIT beam for the $|g_2\rangle - |e\rangle$ transition is $\Delta_2 = 0$ MHz. Loss suppression occurs when the two-photon resonance condition $\delta_e = \Delta_2 - \Delta_e = 0$ is satisfied i.e., $\Delta_e = 0$ MHz. Intensity of control field and EIT field are 3.5 mW/mm² and 500 mW/mm², respectively

As the energy of the triplet continuum $|T, k\rangle$ tunes downward with B-field by an amount $2\mu_B B$, the resonant frequency for the $|T, k\rangle \rightarrow |v = 38\rangle$ transition tunes with the B-field at the rate of $2\mu_B B/\hbar = 2.8$ MHz/G. The same experiment is repeated at various magnetic fields where atom loss is observed by tuning the control laser frequency ω_1 and we verified that the triplet energy tuning rate is indeed 2.8 MHz/G.

In order to measure the transition frequency for the $|v = 37\rangle \rightarrow |v' = 68\rangle$,

similar to the single field experiment, we initially perform laser spectroscopy. Here, we illuminate the atoms with both EIT and control laser beams and look for loss suppression by changing the frequency ω_2 of the EIT beam with the control laser frequency ω_1 held constant.

With the help of the recently reported results in [68], we measured the transition frequency for the $|v = 37\rangle \rightarrow |v' = 68\rangle$ to be

$$\nu(37 \rightarrow 68) = 445.3442 (\pm 0.0002) \times 10^{12} \text{ Hz} \quad (5.27)$$

The uncertainty in the above measurement is due to the absolute accuracy of our wavemeter (± 200 MHz).

Once we observe loss suppression, we measure the loss suppression spectra at 840 G by changing the control laser frequency ω_1 with the EIT laser frequency ω_2 held constant. Fig. 6.8 show loss suppression spectra near the broad Feshbach resonance at 840 G as a function of single photon detuning by changing the control laser frequency ω_1 . We can see that maximum loss suppression occurs at $\Delta_e = 0$, the center of the absorption peak, validating the transition frequency measured for the $|v = 37\rangle \rightarrow |v' = 68\rangle$ transition.

5.6 Measurement of three-body recombination loss near the narrow Feshbach resonance

One of the main issues working near the narrow Feshbach resonance is the associated three-body recombination loss [59] at 543.2 G, Fig. 5.14. In fact, we use the three-body loss at the narrow Feshbach resonance to identify the exact position of the resonance. In this section, I will discuss about the measurement of three-body loss near the narrow Feshbach resonance which we remove from all our loss spectra presented in chapter 6 for clarity.

The three-body loss occurs in a two component $|1\rangle - |2\rangle$ mixture when three

particles, namely, $|1\rangle$, $|2\rangle$ and either $|1\rangle$ or $|2\rangle$, collide together. This results in the formation of a $|1\rangle - |2\rangle$ quasi-bound molecule, where the extra energy is carried away by the third particle, resulting in atom loss. Since we typically wait for 2 s for our B-field to stabilize, we lose approximately 75 % of the atoms near 543.2 G.

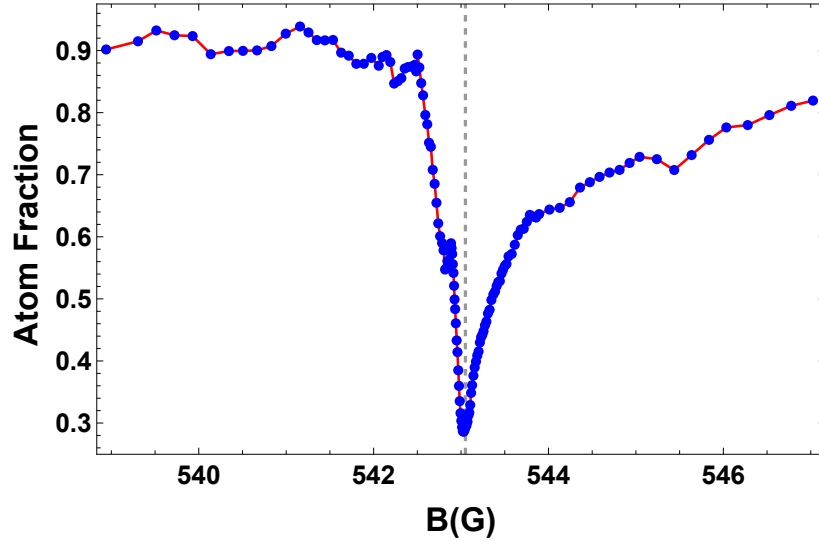


FIGURE 5.14: Three-body recombination loss near the narrow Feshbach resonance at 543.2 G. Atom fraction as a function of magnetic field B for a wait time of 2 s. We remove this loss peak from all loss spectra near the narrow Feshbach resonance by excluding the data points for clarity. Red solid line is guide to the eye.

Atom loss spectra due to three-body loss is shown in Fig. 5.14. The width of the three-body loss peak as seen from Fig. 5.14 for a wait time of 2 s is approximately 0.4 G. This limits our ability to work within 0.4 G of the narrow Feshbach resonance. This problem can be trivially eliminated if we can sweep our B-field quickly, in tens of ms, and not wait 2 s, as all our optical control experiments are done in less than 25 ms. Since the three-body loss is not a fundamental limitation in our experiments, but just a systematic error in all our data, we remove it from all our atom loss spectra shown in chapter 6 by not including the corresponding data points.

In this chapter, I discussed the experimental setup for creating an ultracold gas and for optically controlling interactions using closed channel EIT method. I also

discussed the measurement of physical parameters of the gas such as its density and temperature. Further, I discussed the determination of optical parameters such as the Rabi frequencies, Ω_1 and Ω_2 and measurement of transition frequencies, ω_1 and ω_2 .

In the next chapter, I will discuss the experimental results for the two-field optical control experiment and compare the experimental data with the continuum-dressed state model.

6

Results and Conclusion

In this chapter, I will discuss the experimental demonstration of our two-field optical method to control a magnetic Feshbach resonance and suppress spontaneous scattering through destructive quantum interference. I will show optically induced atom loss spectra near narrow and broad Feshbach resonances. Furthermore, I will fit our data using the continuum-dressed state model and demonstrate the validity of our new theoretical model for both broad and narrow Feshbach resonances.

Fig. 6.1 shows the basic level scheme for the two field optical method. An optical field with frequency ω_1 and Rabi frequency Ω_1 couples the ground vibrational state $|g_1\rangle$ of the singlet $^1\Sigma_g^+$ potential to the excited vibrational state $|e\rangle$ of the singlet $^1\Sigma_u^+$ potential. A second optical field, with frequency ω_2 and Rabi frequency Ω_2 couples a lower lying ground vibrational state $|g_2\rangle$ to the excited vibrational state $|e\rangle$. The control beam results in a light shift of state $|g_1\rangle$ as well as atom loss due to photoassociation from the triplet continuum $|T, k\rangle$, which is hyperfine coupled to $|g_1\rangle$ and hence optically coupled to the excited state $|e\rangle$. The ω_2 beam suppresses atom loss through destructive quantum interference. In a magnetic field B , the triplet continuum $|T, k\rangle$ tunes downward $\propto 2\mu_B B$, where μ_B is the Bohr magneton,

$\mu_B/h \simeq h \times 1.4 \text{ MHz/G}$. The hyperfine coupling V_{HF} between $|T, k\rangle$ and $|g_1\rangle$ produces a Feshbach resonance. For our experiments with ${}^6\text{Li}$, $|g_1\rangle$ and $|g_2\rangle$ are the $v = 38$ and $v = 37$ ground vibrational states. We choose the excited state $|e\rangle$ to be $v' = 68$ as it has the best Franck-Condon overlap with the $v = 38$ ground vibrational state [67]. The excited state decays at a rate $\gamma_e = 2\pi \times 11.8 \text{ MHz}$.

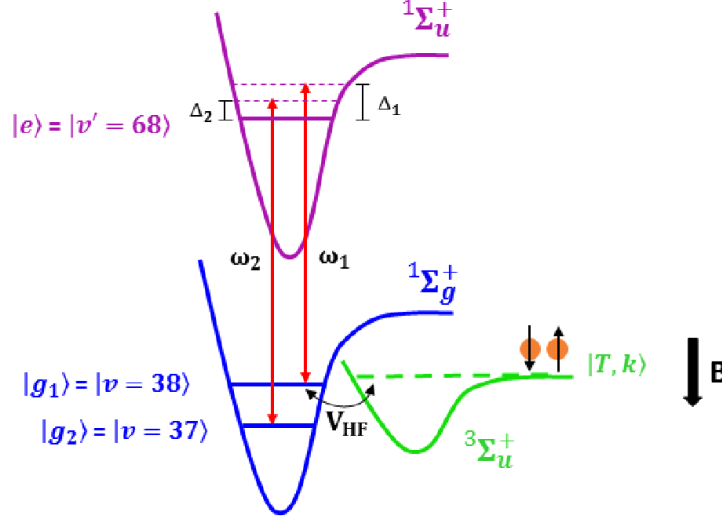


FIGURE 6.1: Basic level scheme for closed-channel EIT technique. Optical fields of frequencies ω_1 (detuning Δ_1) and ω_2 (detuning Δ_2), respectively, couple two singlet ground molecular states $|g_1\rangle$ and $|g_2\rangle$ to the singlet excited molecular state $|e\rangle$; V_{HF} is the hyperfine coupling between the incoming atomic pair state in the open triplet channel $|T, k\rangle$ and $|g_1\rangle$, which is responsible for a magnetically controlled Feshbach resonance.

The detunings of the optical fields that couple state $|g_1\rangle$ and $|g_2\rangle$ to $|e\rangle$ are Δ_1 and Δ_2 , respectively. The single photon detuning of the ω_1 beam for the $|T, k\rangle \rightarrow |e\rangle$ transition is a function of magnetic field and can be defined at a reference magnetic field B_{ref} as $\Delta_e = \Delta_L - 2\mu_B(B - B_{ref})/\hbar$, where Δ_L is the detuning of the optical field when $B = B_{ref}$. The two-photon detuning for the $|T, k\rangle - |e\rangle - |g_2\rangle$ system is $\delta = \Delta_e - \Delta_2$.

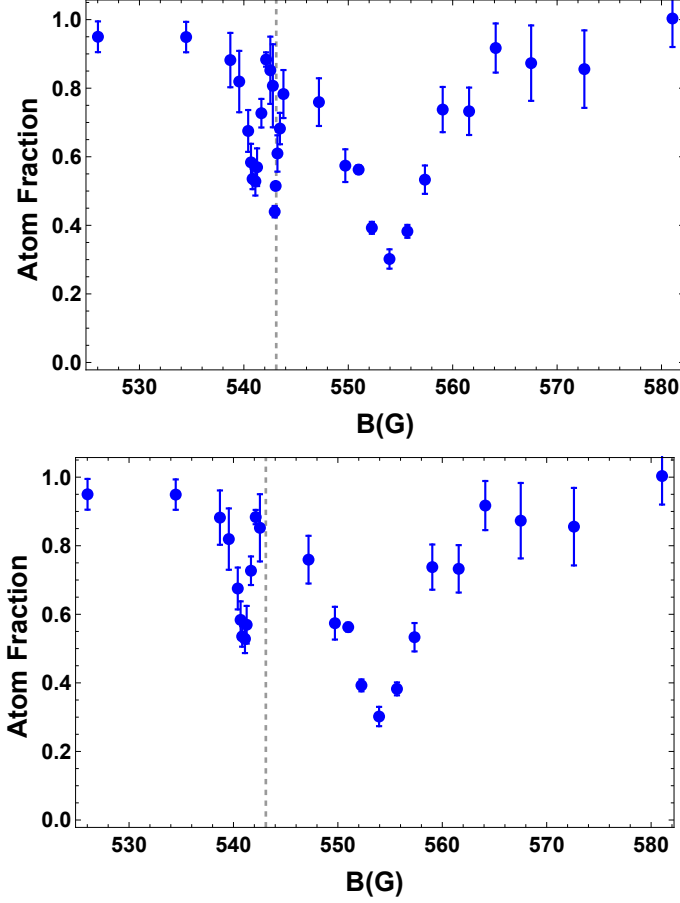


FIGURE 6.2: Single-field loss spectra near the narrow Feshbach resonance (top) with the three body loss peak and (bottom) three body loss peak removed. The position of the three body loss peak (vertical dashed line) is the position of the original narrow Feshbach resonance at $B_{res} = 543.2$ G. The ω_1 field light shifts the position of the narrow Feshbach resonance to $B'_{res} = 541.0$ G illustrated by the narrow loss peak. The large loss peak on the right arises from the broad resonance. Pulse duration $\tau = 5.0$ ms; $T = 5.4 \mu\text{K}$; $\Delta_L = \Delta_1 = 30.2$ MHz; $\Omega_1 = 2.65 \gamma_e$; $\gamma_e = 2\pi \times 11.8$ MHz.

6.1 Shifting the narrow Feshbach resonance using a single-optical field

In this section, I demonstrate that the narrow Feshbach resonance at 543.2 G is shifted using a single optical field. I will show optically induced atom loss spectra as a function of magnetic field to illustrate that by applying the ω_1 field, the narrow Feshbach resonance is shifted from its original position at 543.2 G. The ω_2 optical field is turned off for this experiment.

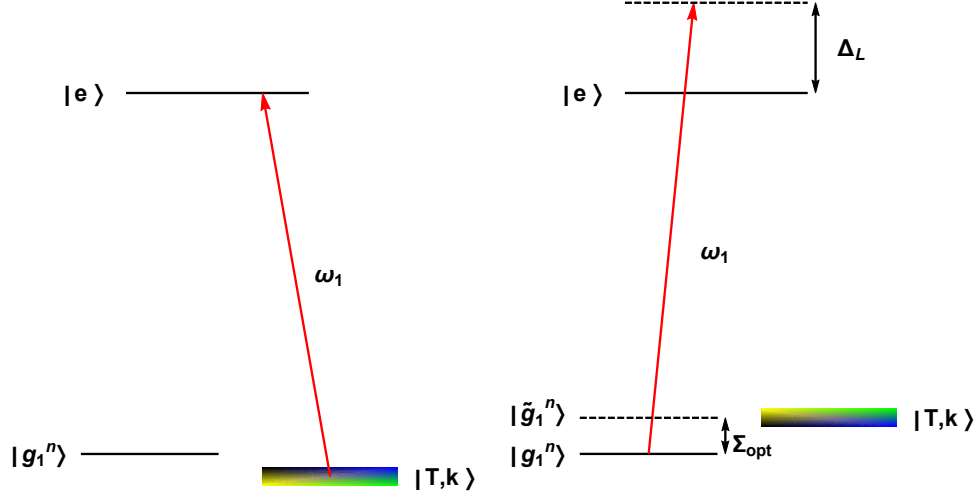


FIGURE 6.3: Level scheme for the single-field optical experiment near the narrow Feshbach resonance. (left) Loss due to broad Feshbach resonance from the $|T, k\rangle \rightarrow |e\rangle$ transition. (right) Loss due to narrow Feshbach resonance from the shifted narrow Feshbach resonance state $|\tilde{g}_1^n\rangle \rightarrow |e\rangle$ transition.

Fig. 6.3 shows the level scheme for the single-field experiment near the narrow Feshbach experiment. Note that near the narrow Feshbach resonance at 543.2 G, optically induced atom loss occurs due to both the broad Feshbach resonance and the narrow Feshbach resonance. The narrow singlet state $|g_1^n\rangle$ is responsible for the narrow Feshbach resonance. The broad singlet state $|g_1^b\rangle$ is mixed with the triplet continuum $|T, k\rangle$ and is not shown in Fig. 6.3

As we are working near the narrow Feshbach resonance, we perform evaporative cooling at 300 G. After forced evaporation at 300 G, the magnetic field is swept to the field of interest and allowed to stabilize for $\simeq 2$ sec. Then the control field ω_1 illuminates the atoms for 5 ms. Atoms are then imaged at the field of interest after a time of flight of $150 \mu\text{s}$ to determine the density profile and the atom number.

The detuning of the control field for the $|T, k\rangle \rightarrow |e\rangle$ is $\Delta_L = 30.2$ MHz, with $\Delta_L \equiv 0$ for $B = B_{ref} = 543.2$ G. The detuning Δ_1 for the $|g_1^n\rangle \rightarrow |e\rangle$ transition is $\Delta_1 = \Delta_L = 30.2$ MHz.

Fig. 6.2 shows the single field atom loss spectra versus magnetic field. The atom loss spectra exhibit three loss peaks:

i) A loss peak at 543.2 G (vertical dotted line) due to three-body recombination loss (see section 5.6). The three-body loss peak occurs at the position of the narrow Feshbach resonance as we wait for 2 s for the B-field to stabilize. We remove the three-body loss peak from all our data for clarity. Fig. 6.2 (bottom) is the same plot as Fig. 6.2 (top) with the three-body loss peak removed.

ii) A narrow peak below 543.2 G. The corresponding level scheme for the loss transition is shown in Fig. 6.3 (right). The ω_1 optical field detuned from the $|g_1^n\rangle \rightarrow |e\rangle$ transition by $\Delta_1 = \Delta_L = 30.2$ MHz light shifts the narrow singlet state $|g_1^n\rangle$ resulting in a shifted narrow singlet state $|\tilde{g}_1^n\rangle$. Atom loss occurs as the magnetic field tunes the triplet continuum near $|\tilde{g}_1^n\rangle$, which is light-shifted in energy, and hence in magnetic field from $B_{res} = 543.2$ G to $B'_{res} = 541.0$ G. Therefore the net shift in the narrow Feshbach resonance is

$$B - B'_{res} = 543.2 - 541.0 = 2.2 \text{ G}$$

The shift in units of frequency is

$$\Sigma_{opt} = \frac{2\mu_B(B_{res} - B'_{res})}{\hbar} = 6.16 \text{ MHz}$$

In this case, the transition strength is resonant, while the ω_1 optical field is off-resonant with the $|T, k\rangle \rightarrow |e\rangle$ transition by $\Delta_L = 30.2$ MHz.

iii) A broad peak arises at 554 G. The corresponding level scheme for the loss transition is shown in Fig. 6.3 (right). Here the ω_1 optical field is resonant with the $|T, k\rangle \rightarrow |e\rangle$ transition when the single photon detuning

$$\Delta_e = \Delta_L - \frac{2\mu_B(B - B_{ref})}{\hbar} = 0.$$

Since we choose $\Delta_L = 30.2$ MHz, maximum atom loss for broad peak occurs at

$$B = B_{ref} + \frac{\Delta_L \hbar}{2\mu_B} = 543.2 + \frac{30.2}{2.8} = 554 \text{ G}.$$

The transition arises from the hyperfine coupling of the triplet continuum $|T, k\rangle$ to broad singlet state $|g_1^b\rangle$, far from the resonance at 832.2 G. Atom loss occurs due to photoassociation of free unbound atom from $|T, k\rangle$ to the excited singlet vibrational state $|e\rangle$.

From Fig. 6.2, we can clearly see that the narrow Feshbach resonance is shifted using a single optical field.

In order to investigate the dependence of the light shift on the Rabi frequency Ω_1 , the experiment is repeated for different values of Ω_1 by changing the intensity of the ω_1 laser.

Single field atom loss spectra versus magnetic field is shown in Fig. 6.4 for three different values of Ω_1 , namely, $\Omega_1 = 2.00 \gamma_e$ (top), $\Omega_1 = 2.65 \gamma_e$ (middle), and $\Omega_1 = 3.1 \gamma_e$ (bottom).

The new resonance position B'_{res} and the corresponding light shift Σ_{opt} is listed for three different values of Ω_1 in Table. 6.1. We can see from Fig. 6.4, as Ω_1 increases, the shift becomes larger due to increased mixing of $|g_1^n\rangle$ with $|e\rangle$. Increasing Ω_1 also reduces the amount of singlet ground state character in the shifted state $|\tilde{g}_1^n\rangle$, thereby reducing the overlap $\langle T, k | \tilde{g}_1^n \rangle$, resulting in reduced loss at the shifted narrow peak. For a $\Omega_1 = 3.1 \gamma_e$ (Fig. 6.4 bottom), the narrow resonance is shifted by 3.0 G, approximately 30 times the width.

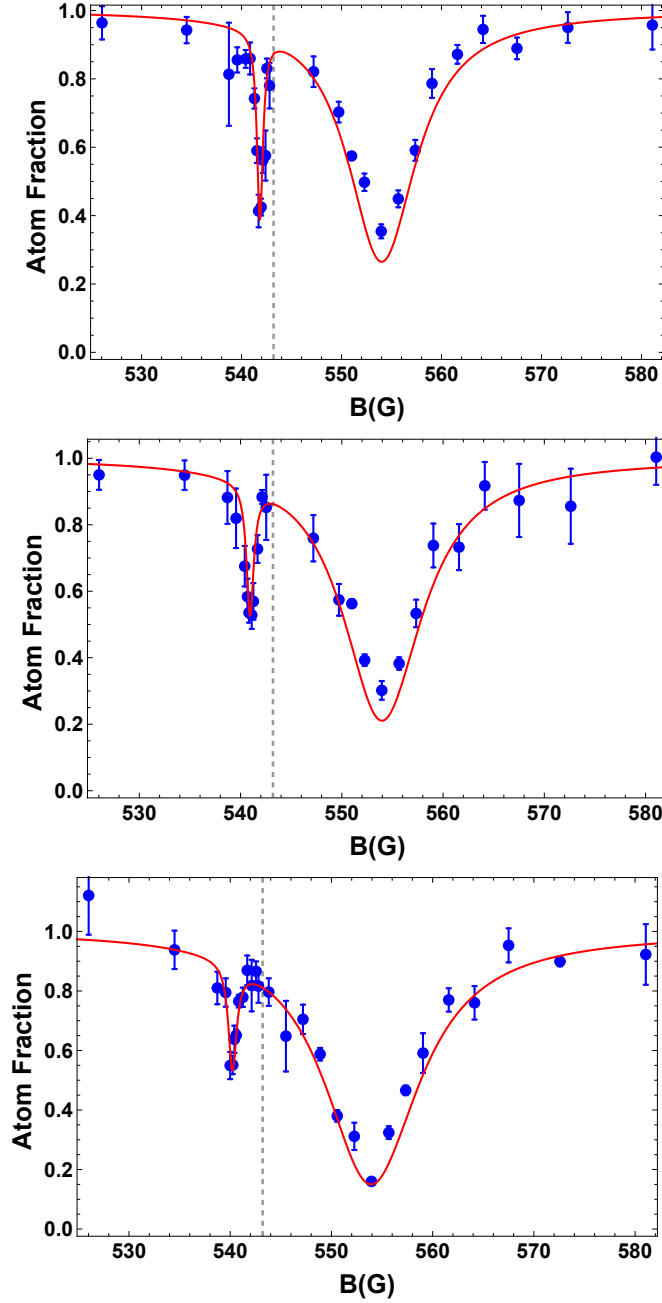


FIGURE 6.4: Shifting the narrow Feshbach resonance at 543.2 G using a single optical field. The large loss peak on the right arises from the broad resonance; The left loss peak arises from the shifted narrow resonance. Vertical dashed line: Position of the unshifted narrow resonance. The background (non-optical) three-body loss near 543.2 G has been suppressed for clarity. Pulse duration $\tau = 5.0$ ms; $T = 5.4 \mu\text{K}$; $\Delta_L = \Delta_1 = 30.2$ MHz; (top) $\Omega_1 = 2.00 \gamma_e$; $B'_{res} = 541.9$ G (middle) $\Omega_1 = 2.65 \gamma_e$; $B'_{res} = 541.0$ G (bottom) $\Omega_1 = 3.10 \gamma_e$; $B'_{res} = 540.2$ G; $\gamma_e = 2\pi \times 11.8$ MHz. Blue dots: Experiment; Solid red curves: Continuum-dressed state model

Table 6.1: Single-field shift of narrow Feshbach resonance

$\Omega_1(\gamma_e)$	$B_{res'}$ (G)	$B'_{res} - B_{res}$ (G)	Σ_{opt} (MHz)
2.00	541.9	1.3	3.64
2.65	541.0	2.2	6.16
3.10	540.2	3	8.40

6.2 Comparison of single-field loss data with the continuum-dressed state model near the narrow Feshbach resonance

We use the continuum-dressed state model (solid red line) to fit the data shown in Fig. 6.4 using Eq. 4.44 in chapter 4,

$$\frac{N(t)}{N_0} = \frac{1}{1 + N_0\Gamma t}, \quad (6.1)$$

where Γ is given in Eq. 4.42.

As discussed in section 5.6, for the Rabi frequency Ω_1 , we use

$$\Omega_1 = 2\pi \times c_1 \text{ MHz } \sqrt{I},$$

where intensity $I = 2P/\pi\omega_0$ in mW/mm² is determined by measuring the power P and the beam waist ω_0 . The continuum-dressed state model simultaneously reproduces the shift of the narrow resonances and the amplitudes of both the narrow and broad resonances using only one fitting parameter c_1 for *all* three spectra in Fig. 6.4.

We obtain a value of

$$\Omega_1 = 2\pi \times 5.1 \text{ MHz } \sqrt{I},$$

which is in good agreement with the predicted value of

$$\Omega_1 = 2\pi \times 5.6 \text{ MHz } \sqrt{I},$$

using the Franck-Condon factors, based on the vibrational wave functions obtained from the molecular potentials [67].

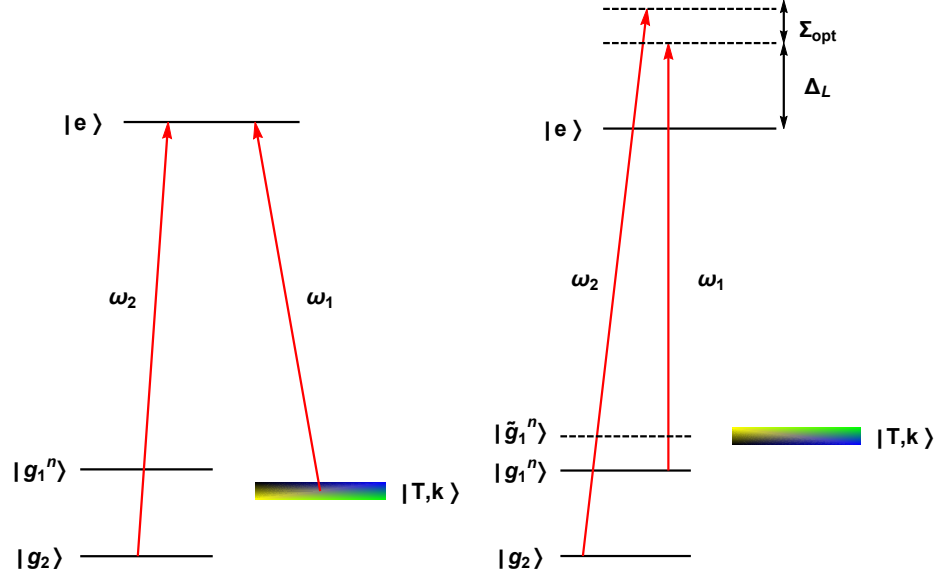


FIGURE 6.5: Level scheme for EIT loss suppression near the narrow Feshbach resonance at (left) the broad peak and (right) the narrow peak.

As the shift depends on Ω_1^2 while the magnitudes of the loss rates depend on the product $\Omega_1^2 |\langle g_1 | E_k \rangle|^2$, the good agreement in the shape of the spectra confirms the transition strengths and momentum-dependent shifts predicted by the continuum-dressed state model.

This is one of the important results reported in this thesis, as it substantiates the validity of the continuum-dressed model to make predictions of two-body scattering parameters in optical control experiments.

6.3 Two-field loss suppression near the narrow Feshbach resonance

In this section, we employ two field optical method and demonstrate that the narrow Feshbach resonance is shifted while suppressing spontaneous scattering using destructive quantum interference. I will show loss suppression spectra near a narrow Feshbach resonance as a function of magnetic field to illustrate both the shift of narrow Feshbach resonance and loss suppression at the shifted position. In order to

suppress atom loss due to spontaneous scattering, we apply a second optical field, with frequency ω_2 and Rabi frequency Ω_2 . The primary objective of this experiment is to suppress atom loss at the shifted narrow Feshbach resonance position.

After sweeping to the magnetic field of interest, the ω_2 beam of intensity of 0.4 kW/cm² is adiabatically turned on over 30 ms. The ω_2 beam creates an optical dipole trap and provides additional confinement in the z-direction, due to its high intensity. This changes the axial trap frequency from 120 Hz to 218 Hz (see section. 5.3.2), with negligible change in the radial trap frequencies. The control beam (ω_1) with Rabi frequency $\Omega_1 = 2.6 \gamma_e$ is then turned on for 5 ms, after which both beams are turned off abruptly.

The level scheme for loss suppression near the narrow Feshbach resonance is shown in Fig. 6.5. The detuning Δ_2 of the ω_2 beam for the $|g_2\rangle \rightarrow |e\rangle$ transition can be chosen to suppress loss either at the broad peak (Fig. 6.5 (left)) or the narrow peak (Fig. 6.5 (right)).

Fig. 6.6 show loss suppression spectra near the narrow Feshbach resonance as a function of the magnetic field. The ω_1 beam shifts the narrow Feshbach resonance from from $B_{res} = 543.2$ G (vertical dashed line) to $B'_{res} = 541.1$ (narrow loss peak) (Fig. 6.6 (top)). Loss suppression occurs when the two-photon resonance condition is satisfied i.e., the two-photon detuning

$$\delta_e = \Delta_2 - \Delta_e = 0.$$

Note that the condition $\delta_e = 0$ can be achieved either by having both Δ_2 and $\Delta_e = 0$ or by having $\Delta_2 = \Delta_e$.

Loss suppression at the broad peak (Fig. 6.6 (top)) occurs when

$$\Delta_2 = \Delta_e = 0.$$

However, this is not interesting as our original goal is to suppress atom loss at the shifted narrow peak at 541.1 G.

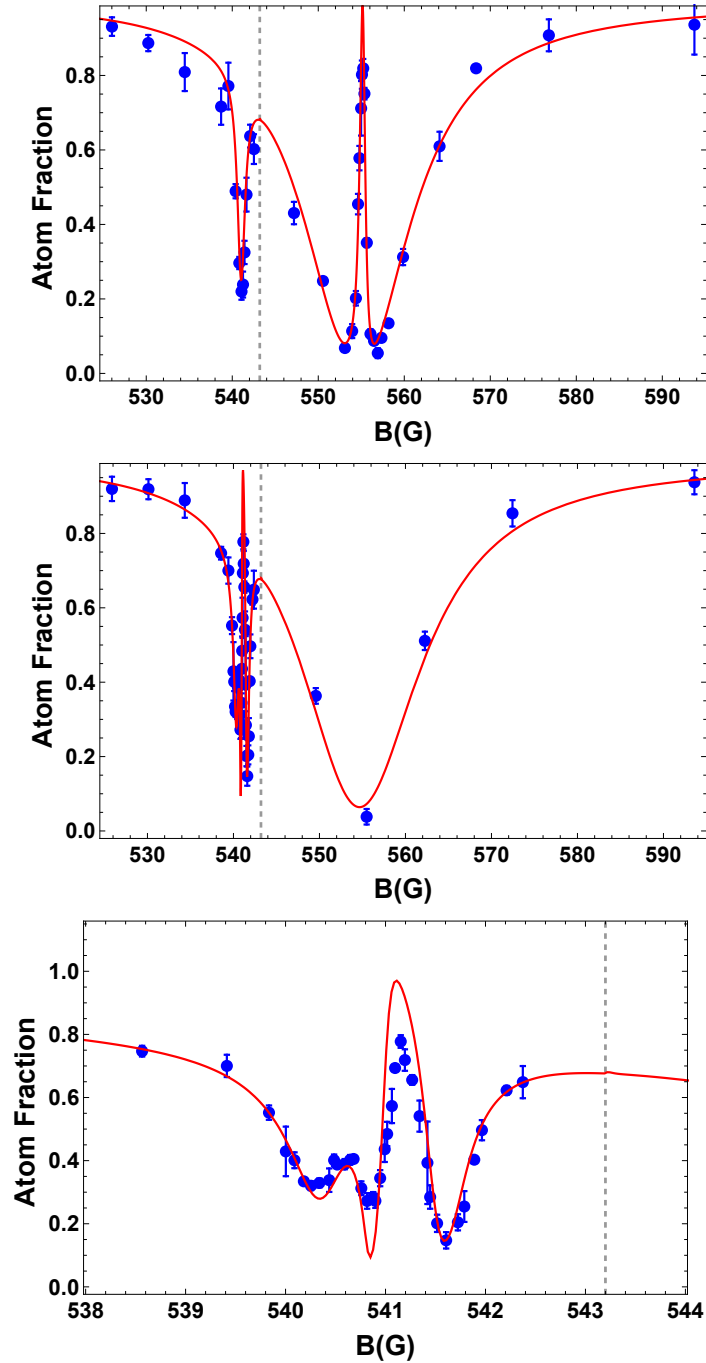


FIGURE 6.6: Loss suppression using the two-field optical technique. The ω_1 beam shifts the narrow Feshbach resonance and the frequency of the ω_2 beam is chosen to suppress loss from (top) the broad resonance (middle) the shifted narrow Feshbach resonance; (bottom) shows an expanded view of (middle) near the loss suppression region. Pulse duration $\tau = 5.0$ ms; $T = 4.5 \mu\text{K}$; $\Omega_1 = 2.6 \gamma_e$; $\Omega_2 = 0.8 \gamma_e$; $\Delta_L = \Delta_1 = 30.2$ MHz; $B'_{res} = 541.1$ G. Vertical dashed line: Position of the unshifted narrow resonance. Solid red curves: Continuum-dressed state model.

Loss suppression at the shifted narrow peak (Fig. 6.6 (middle)) occurs when

$$\begin{aligned}
\Delta_2 = \Delta_e &= \Delta_1 + \Sigma_{opt}. \\
&= \Delta_1 + 2\mu_B (543.2 - B'_{res}). \\
&= 30.2 + 2.8 (543.2 - 541.1) = 36.0 \text{ MHz} \tag{6.2}
\end{aligned}$$

Fig. 6.6 (bottom) shows the same data in Fig. 6.6 (middle), expanded around the loss suppression region. Fig. 6.6 (bottom) clearly shows that atom loss is suppressed at the shifted narrow Feshbach resonance.

As noted in chapter 4 (section. 4.4.2), closer examination of loss suppression of the narrow peak Fig. 6.6 (bottom) reveals a rich spectrum, where we can see a three-peak structure. Unlike a simple loss suppression at the broad peak, where the loss suppression spectra has a minimum loss region in the center of two absorption maximum, we notice an additional peak (center narrow peak). This additional absorption peak arises due to two-photon Raman absorption from the broad Feshbach resonance when the condition $\delta_e = 0$ is satisfied for the case, $\Delta_2 > 2\gamma_e$ (see. section. 4.4.2). For this experiment, $\Delta_2 = 36.0$ MHz (Eq. 6.2) which is greater than $2\gamma_e$.

6.4 Comparison of two-field loss suppression data with the continuum-dressed state model near the narrow Feshbach resonance

We use the continuum-dressed state model (solid red line) to fit the data shown in Fig. 6.6. Similiar to section. 6.2, for the Rabi frequencies Ω_1 and Ω_2 , we use

$$\begin{aligned}
\Omega_1 &= 2\pi \times c_1 \text{ MHz} \sqrt{I_1}, \\
\Omega_2 &= 2\pi \times c_2 \text{ MHz} \sqrt{I_2},
\end{aligned}$$

where intensity $I_1 = 2P_1/\pi\omega_0$ and $I_2 = 2P_2/\pi\omega_0$ are the intensities of the ω_1 field and ω_2 field in mW/mm², respectively. The continuum-dressed state model simultaneously reproduces the shift of the narrow resonance and the amplitudes of both

the narrow and broad resonances by fitting c_1 and c_2 . We obtain a value of

$$\begin{aligned}\Omega_1 &= 2\pi \times 5.45 \text{ MHz} \sqrt{I_1}, \\ \Omega_2 &= 2\pi \times 0.14 \text{ MHz} \sqrt{I_2},\end{aligned}$$

which is in good agreement with the predicted value of

$$\begin{aligned}\Omega_1 &= 2\pi \times 5.6 \text{ MHz} \sqrt{I_1}, \\ \Omega_2 &= 2\pi \times 0.17 \text{ MHz} \sqrt{I_2},\end{aligned}\tag{6.3}$$

using the Franck-Condon factors, based on the vibrational wave functions obtained from the molecular potentials [67].

The better agreement of $c_1 = 5.45$ to the predicted value of 5.6 compared to previous data sets ($c_1 = 5.10$), might be due to the better alignment of the control laser (ω_1) beam on the atoms. The continuum-dressed state model fits the data both in shape and magnitude. We note that the predicted central peaks in Fig. 6.6 (bottom) are somewhat larger than the measured values, which may arise from frequency jitter in the two-photon detuning and intensity variation of the Ω_2 beam across the atom cloud. Furthermore, the continuum-dressed state model also predicts the additional peak in the loss suppression spectra of the narrow peak Fig. 6.6 (bottom) that arises due to two-photon Raman absorption from the broad Feshbach resonance.

The loss spectra clearly demonstrates that the Feshbach resonance is strongly shifted by 2 G and that atom loss is strongly suppressed using our two field optical method. This is one of the primary results of my research work as it demonstrates for the first time, both control of interactions and loss suppression in a ultracold gas using optical techniques.

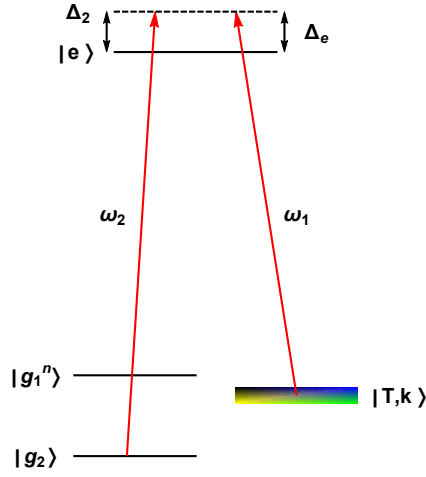


FIGURE 6.7: Level scheme for loss suppression near the broad Feshbach resonance at 840 G

6.5 Two-field loss suppression near broad Feshbach resonance

Loss suppression near a Broad Feshbach resonance in ${}^6\text{Li}$ is particularly difficult due to the large background scattering length of $1405 a_0$. Note that the two body loss rate constant K_2 derived in chapter 4, Eq. 4.11 is proportional to the background scattering length a_{bg} . Therefore, two-body loss is higher for atoms with large background scattering length a_{bg} such as ${}^6\text{Li}$. In this section, I will discuss two field optical experiments that demonstrates loss suppression near the broad Feshbach resonance. I will show loss suppression spectra near the broad Feshbach resonance as a function of the single-photon detuning Δ_e by changing the control laser frequency ω_1 .

Fig. 6.7 show the level scheme for the two field optical experiment near the broad Feshbach resonance. Similar to loss suppression near the narrow Feshbach resonance, we use two optical fields, ω_1 and ω_2 , to suppress loss due to destructive quantum interference. Near the broad Feshbach resonance, there is no contribution from the narrow Feshbach resonance state $|g_1^n\rangle$

Since we are working near the broad Feshbach resonance, we sweep the magnetic field to 832 G to perform evaporative cooling. After forced evaporation, and re-raising the trap to its initial trap depth, we have about 10^5 atoms in each spin state. The magnetic field is then swept to the field of interest where we typically wait for about 2 s for the magnetic field to stabilize. The ω_2 beam of intensity 0.4 kW/cm^2 is adiabatically turned on over 30 ms. The ω_1 beam is then turned on for 5 ms, after which both beams are turned off abruptly.

Fig. 6.8 show loss suppression near the broad Feshbach resonance at 840 G as a function of single photon detuning by changing the control laser frequency ω_1 .

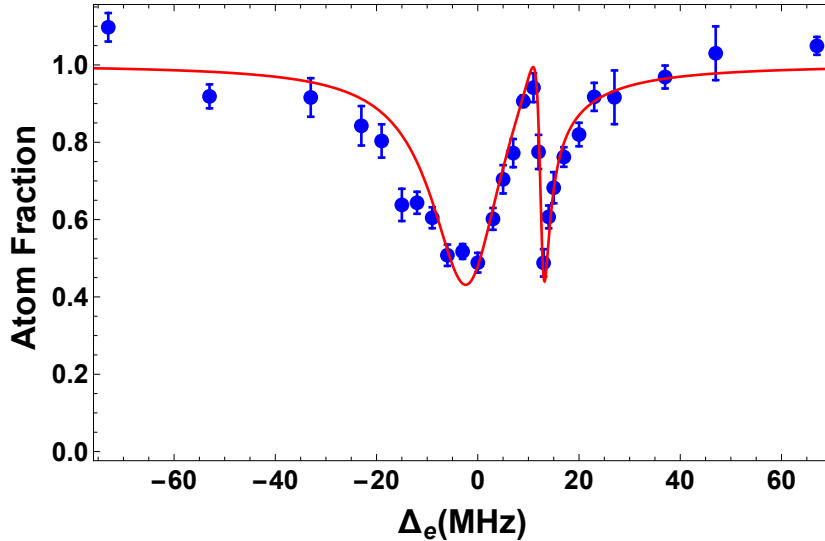


FIGURE 6.8: Two-field optical loss suppression near the broad Feshbach resonance. Atom loss spectra as a function of single photon detuning Δ_e by changing the control laser frequency ω_1 at a fixed magnetic field $B = 840 \text{ G}$. The detuning Δ_2 of the EIT beam for the $|g_2\rangle - |e\rangle$ transition is $\Delta_2 = 10 \text{ MHz}$. Loss suppression occurs when the two-photon resonance condition $\delta_e = \Delta_2 - \Delta_e = 0$ is satisfied i.e., $\Delta_e = 10 \text{ MHz}$. Temperature $T = 14.8 \mu\text{K}$, $\Omega_1 = 1.34 \gamma_e$, and $\Omega_2 = 0.9 \gamma_e$. Each data point is the average of 5 randomized trials. Solid red curves: Continuum-dressed state model.

We chose the detuning Δ_2 of the ω_2 beam for the $|g_2\rangle - |e\rangle$ transition to be $\Delta_2 = 10 \text{ MHz}$. Loss suppression occurs when the frequency of the control laser ω_1 is tuned such that the two-photon detuning $\delta_e = \Delta_e - \Delta_2 = 0$. For this experiment,

since $\Delta_2 = 10$ MHz, the maximum suppression occurs for $\Delta_e = \Delta_2 = 10$ MHz.

Fig. 6.8 clearly illustrates that the two field optical experiment can suppress atom loss even near a broad Feshbach resonance with a large background scattering length.

6.6 Comparison of two-field loss suppression data with the continuum-dressed state model near the broad Feshbach resonance

We use the continuum-dressed state model (solid red line) to compare the data shown in Fig. 6.8. As discussed in section. 6.4, for the Rabi frequencies Ω_1 and Ω_2 , we use

$$\begin{aligned}\Omega_1 &= 2\pi \times c_1 \text{ MHz } \sqrt{I_1}, \\ \Omega_2 &= 2\pi \times c_2 \text{ MHz } \sqrt{I_2},\end{aligned}$$

where intensity $I_1 = 2P_1/\pi\omega_0$ and $I_2 = 2P_2/\pi\omega_0$ are the intensities of the ω_1 field and ω_2 field in mW/mm², respectively. We obtain a value of

$$\begin{aligned}\Omega_1 &= 2\pi \times 5.10 \text{ MHz } \sqrt{I_1}, \\ \Omega_2 &= 2\pi \times 0.14 \text{ MHz } \sqrt{I_2},\end{aligned}$$

which is in good agreement with the predicted value of

$$\begin{aligned}\Omega_1 &= 2\pi \times 5.6 \text{ MHz } \sqrt{I_1}, \\ \Omega_2 &= 2\pi \times 0.17 \text{ MHz } \sqrt{I_2},\end{aligned}\tag{6.4}$$

using the Franck-Condon factors, based on the vibrational wave functions obtained from the molecular potentials [67]. Further, the the value of c_1 obtained by fitting the continuum dressed state model with this data set is consistent with the value obtained from the single-field experiment near the narrow Feshbach resonance (section. 6.1).

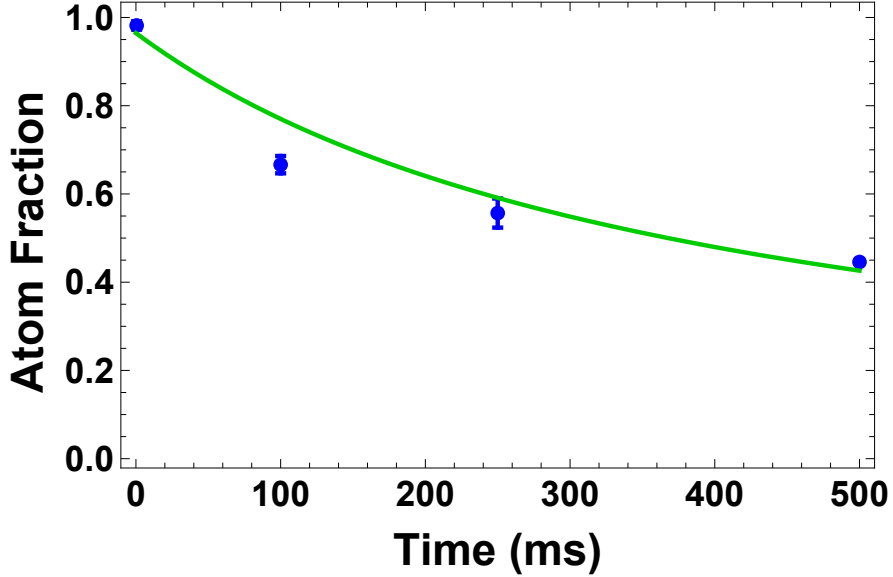


FIGURE 6.9: Number of atoms in state $|1\rangle$ versus time with $\Omega_1 = 0.65\gamma_e$ and ω_1 tuned to cause loss at 841 G. $\Omega_2 = 0.9\gamma_e$ and ω_2 is tuned to suppress loss near 841 G. With $\Omega_1 = 0.65\gamma_e$ and $\Omega_2 = 0$, the corresponding decay time is $\simeq 0.5$ ms. $\gamma_e = 2\pi \times 11.8$ MHz is the radiative decay rate; $T = 4.5\ \mu\text{K}$. Solid green curve: $N(t) = N(0)/(1 + \gamma t)$, where $\gamma = 2.5\ \text{s}^{-1}$.

6.7 Increasing the spontaneous lifetime of atoms near the broad Feshbach resonance

To examine the loss suppression further, we measure the number of atoms as a function of time with the magnetic field tuned to the suppression point. Fig. 6.9 shows the atom fraction as a function of time at the two-photon resonance. Each data point in Fig. 6.9 is obtained by setting the lasers to achieve the two-photon condition at 841 G and then sweeping the magnetic field by about ± 2 G to observe the maximum retrieval fraction. The magnetic field is swept in order to overcome the fluctuations in the magnetic field which can limit the lifetime of the atoms.

The green curve is a fit of the form $N(t) = N(0)/(1 + \gamma t)$, where $\gamma = 2.5\ \text{s}^{-1}$. We observe dramatic suppression of loss using the two-field method, achieving an increase of the inelastic lifetime near the broad resonance of ${}^6\text{Li}$ from 0.5 ms with a

single laser field to 400 ms with the two-field method, despite the large background scattering length of $-1405 a_0$ [69, 70] (Fig. 6.9).

The increase in inelastic lifetime from 5 ms to 400 ms is one of the central achievements of our closed-channel EIT technique, as it demonstrates for the very first time, the feasibility of using optical techniques to control interactions in the timescale of several hundred milliseconds (Fig. 6.9).

6.8 Summary and future experiments

In summary, I have demonstrated new two-field optical techniques, which use quantum interference in the closed-channel to control interactions in an ultracold gas of ${}^6\text{Li}$ atoms. I further illustrated, using our new theoretical model, the advantages of the closed channel EIT method over other optical control methods. One of the major advantages of the closed-channel EIT is the ability to create narrow features in the scattering phase shift enabling large changes in the scattering length with small changes in the optical frequencies. This avoids changes in the net trapping potential on the atoms. Another major advantage of our two-field optical technique is the ability to tune the effective range with minimum atom loss. I also illustrated that near the broad $|1\rangle - |2\rangle$ Feshbach resonance of ${}^6\text{Li}$, the effective range can be changed by a factor of 40 at the minimum loss two-photon resonance.

I have experimentally demonstrated loss suppression and increase in the spontaneous lifetime of atoms from 0.5 ms using single field to 400 ms using two fields near the broad Feshbach resonance despite a huge background scattering length of $-1450 a_0$. I would like to particularly emphasize that this is the very first demonstration of loss suppression in a broad Feshbach resonance. This illustrates the versatile nature of our technique to suppress optical scattering even in the case of very broad Feshbach resonances.

I have demonstrated that the narrow Feshbach resonance can be shifted by 3 G,

nearly 30 times the width of the resonance and the loss strongly suppressed using the closed-channel EIT technique. This is the first demonstration of loss suppression on a Feshbach resonance that is shifted by 2 G.

Furthermore, I have developed a new theoretical model, the continuum-dressed state model, which provides a unified treatment of both broad and narrow Feshbach resonances, resolving a long standing issue for predictions for broad resonances. I further demonstrated that the continuum-dressed state model accurately reproduces all of the light induced level shifts, and the amplitudes, for both the narrow and broad resonances.

The closed-channel EIT method reported in this thesis is an important step forward in using optical techniques to control interactions in ultracold gases as it provides a general prescription to suppress atom loss due to spontaneous scattering. The results presented in this thesis illustrate that loss can be suppressed near any Feshbach resonance, independent of its width, which is a serious shortcoming in other optical techniques.

One of the possible improvements for this method is to achieve loss suppression using an less intense EIT beam that does not create a dipole trapping potential. This can be accomplished by choosing the state $|v' = 62\rangle$ as the excited singlet molecular state $|e\rangle$, since it has a better Franck-Condon overlap with the $|v = 37\rangle$ state. The next major step using this technique would be the experimental measurement of tuning the scattering length and the effective range by measuring the binding energy using radio frequency spectroscopy. The frequency “knob” provided by the closed-channel EIT technique to tune interactions can be used to create exotic atomic clouds with spatially selective regions of strong interactions. The possibilities remain unlimited and I hope that my work presented here will propel this field forward.

Appendix A

Evaluation of phase shift Δ due to magnetic Feshbach resonance

We use Eq. 2.57 to write the total phase shift due to a magnetic Feshbach resonance

$$\Delta = \tilde{\Delta} + \delta_{bg}, \quad (\text{A.1})$$

where $\tilde{\Delta}$ is the phase shift induced by the magnetic Feshbach resonance and δ_{bg} is background phase shift.

For broad Feshbach resonances, where the effective range r_e is small, we can ignore the k^2 terms in the effective range expansion in Eq. 2.21 and write

$$\tan \delta_{bg} = -k a_{bg} \quad (\text{A.2})$$

For $a_{bg} < 0$, we rewrite Eq. A.2

$$\tan \delta_{bg} = -k a_{bg} = k |a_{bg}| = x \quad (\text{A.3})$$

$$\tan \tilde{\Delta} = -\frac{2 \pi^2 m k |\tilde{g}(k)|^2}{E_k - E_{g_1} - \Sigma_E(k)} = \frac{-k |a_{bg}|}{-\tilde{\Delta}_0(x) - \frac{x^2}{1+x^2}} \frac{1}{1+x^2}$$

From Eq. 2.53, we know

$$\tan \tilde{\Delta} = -\frac{2\pi^2 m k |\tilde{g}(k)|^2}{E_k - E_{g_1} - \Sigma_E(k)}. \quad (\text{A.4})$$

From Eq. 2.169 and Eq. 2.174, we know

$$\Sigma_E(k) = -\frac{2\pi^2 m |\tilde{g}(k)|^2}{|a_{bg}|} = -\frac{2\mu_B \Delta B}{1+x^2}. \quad (\text{A.5})$$

From Eq. 2.178, we know

$$E_k - E_{g_1} - \Sigma_E(k) = 2\mu_B \Delta B \left[-\tilde{\Delta}_0 + \epsilon x^2 - \frac{x^2}{1+x^2} \right]. \quad (\text{A.6})$$

Substituting Eq. A.5 and Eq. A.6 in Eq. A.4, we obtain

$$\tan \tilde{\Delta} = \frac{-k|a_{bg}|}{-\tilde{\Delta}_0 + \epsilon x^2 - \frac{x^2}{1+x^2}} \frac{1}{1+x^2}. \quad (\text{A.7})$$

From Eq. 2.179, we know

$$\tilde{\Delta}_0(x) \equiv \tilde{\Delta}_0 - \epsilon x^2. \quad (\text{A.8})$$

Substituting Eq. A.8 in Eq. A.7, yields

$$\tan \tilde{\Delta} = \frac{-k|a_{bg}|}{-\tilde{\Delta}_0(x) - \frac{x^2}{1+x^2}} \frac{1}{1+x^2}. \quad (\text{A.9})$$

Using $x = k|a_{bg}|$ in Eq. A.9,

$$\tan \tilde{\Delta} = \frac{x}{(1+x^2)\tilde{\Delta}_0(x) + x^2} = \frac{x}{\tilde{\Delta}_0(x) + x^2[1 + \tilde{\Delta}_0(x)]}. \quad (\text{A.10})$$

We write the phase shift $\tilde{\Delta}$ in the form

$$\begin{aligned} e^{i\tilde{\Delta}} &= \cos \tilde{\Delta} + i \sin \tilde{\Delta} \\ &= \cos \delta_{bg} [1 + i \tan \delta_{bg}] \\ &= \frac{1 + i \tan \tilde{\Delta}}{\sqrt{1 + \tan^2 \tilde{\Delta}}} \end{aligned} \quad (\text{A.11})$$

Substituting Eq. A.10 in Eq. A.11, we obtain

$$e^{i\tilde{\Delta}} = \frac{1 + \frac{ix}{\tilde{\Delta}_0(x) + x^2[1 + \tilde{\Delta}_0(x)]}}{\sqrt{1 + \frac{x^2}{(\tilde{\Delta}_0(x) + x^2[1 + \tilde{\Delta}_0(x)])^2}}} \quad (\text{A.12})$$

Simplifying Eq. A.12, yields

$$e^{i\tilde{\Delta}} = \frac{\tilde{\Delta}_0(x) + x^2[1 + \tilde{\Delta}_0(x)] + ix}{\sqrt{(\tilde{\Delta}_0(x) + x^2[1 + \tilde{\Delta}_0(x)])^2 + x^2}} \quad (\text{A.13})$$

Similarly, for the background phase shift δ_{bg} , we write

$$e^{i\delta_{bg}} = \cos \delta_{bg} [1 + i \tan \delta_{bg}] \quad (\text{A.14})$$

Substituting Eq. A.3 in Eq. A.14, yields

$$e^{i\delta_{bg}} = \frac{1 + ix}{\sqrt{1 + x^2}} \quad (\text{A.15})$$

Using Eq. A.1, we write

$$e^{i\Delta} = e^{i(\tilde{\Delta} + \delta_{bg})} = e^{i\tilde{\Delta}} e^{i\delta_{bg}} \quad (\text{A.16})$$

Substituting Eq. A.13 and Eq. A.15 in Eq. A.16, we obtain

$$e^{i\Delta} = \frac{\tilde{\Delta}_0(x) + x^2[1 + \tilde{\Delta}_0(x)] + ix}{\sqrt{(\tilde{\Delta}_0(x) + x^2[1 + \tilde{\Delta}_0(x)])^2 + x^2}} \frac{1 + ix}{\sqrt{1 + x^2}} = \frac{N}{D}, \quad (\text{A.17})$$

where N is the numerator and D is the denominator of Eq. A.17, respectively. We reduce the numerator N and denominator D of Eq. A.17 separately. From the numerator of Eq. A.17, we get

$$\begin{aligned} N &= (1 + ix)[\tilde{\Delta}_0(x) + x^2[1 + \tilde{\Delta}_0(x)] + ix] \\ &= \tilde{\Delta}_0(x) + x^2[1 + \tilde{\Delta}_0(x)] + ix + ix[\tilde{\Delta}_0(x) + x^2[1 + \tilde{\Delta}_0(x)] + ix] \\ &= (1 + x^2)\tilde{\Delta}_0(x) + ix[1 + \tilde{\Delta}_0(x) + x^2[1 + \tilde{\Delta}_0(x)]] \\ &= (1 + x^2)[\tilde{\Delta}_0(x) + ix[1 + \tilde{\Delta}_0(x)]] \end{aligned} \quad (\text{A.18})$$

From the denominator of Eq. A.17, we get

$$\begin{aligned}
D &= \sqrt{1+x^2} \sqrt{(\tilde{\Delta}_0(x) + x^2[1 + \tilde{\Delta}_0(x)])^2 + x^2} \\
&= \sqrt{|1+ix|^2 |(\tilde{\Delta}_0(x) + x^2[1 + \tilde{\Delta}_0(x)])^2 + ix|^2} \\
&= \sqrt{|N|^2} = (1+x^2) \sqrt{\tilde{\Delta}_0^2(x) + x^2[1 + \tilde{\Delta}_0(x)]^2}
\end{aligned} \tag{A.19}$$

Substituting, Eq. A.19 and Eq. A.18 in Eq. A.17, we obtain

$$e^{i\Delta} = \frac{(1+x^2)[\tilde{\Delta}_0(x) + ix[1 + \tilde{\Delta}_0(x)]]}{(1+x^2) \sqrt{\tilde{\Delta}_0^2(x) + x^2[1 + \tilde{\Delta}_0(x)]^2}}. \tag{A.20}$$

Cancelling the term $(1+x^2)$ in the numerator and denominator,

$$e^{i\Delta} = \frac{[\tilde{\Delta}_0(x) + ix[1 + \tilde{\Delta}_0(x)]]}{\sqrt{\tilde{\Delta}_0^2(x) + x^2[1 + \tilde{\Delta}_0(x)]^2}} = \cos \Delta + i \sin \Delta. \tag{A.21}$$

From Eq. A.21, we obtain

$$\cos \Delta = \frac{\tilde{\Delta}_0(x)}{\sqrt{\tilde{\Delta}_0^2(x) + x^2[1 + \tilde{\Delta}_0(x)]^2}}, \tag{A.22}$$

and

$$\sin \Delta = \frac{x[1 + \tilde{\Delta}_0(x)]}{\sqrt{\tilde{\Delta}_0^2(x) + x^2[1 + \tilde{\Delta}_0(x)]^2}}. \tag{A.23}$$

Dividing Eq. A.22 by Eq. A.23, we obtain

$$x \cot \Delta = \frac{\tilde{\Delta}_0(x)}{1 + \tilde{\Delta}_0(x)}. \tag{A.24}$$

Using Eq. A.8 in Eq. A.24, yields

$$x \cot \Delta = \frac{\tilde{\Delta}_0 - \epsilon x^2}{1 + \tilde{\Delta}_0 - \epsilon x^2}. \tag{A.25}$$

We use Eq. A.25 to evaluate the total phase shift induced by the magnetic Feshbach resonance.

From Eq. 2.144 and Eq. 2.184, we know

$$\langle g_1 | \tilde{E}_k \rangle = \sqrt{\frac{\epsilon |a_{bg}|^3}{2\pi^2}} \frac{1}{\sqrt{[\tilde{\Delta}_0(x)]^2 + x^2[1 + \tilde{\Delta}_0(x)]^2}}. \quad (\text{A.26})$$

From Eq. A.20 and Eq. A.26, we get

$$e^{i\Delta} \langle g_1 | \tilde{E}_k \rangle = \frac{\epsilon |a_{bg}|^3}{2\pi^2} \frac{\tilde{\Delta}_0(x) + ix[1 + \tilde{\Delta}_0(x)]}{\tilde{\Delta}_0^2(x) + x^2[1 + \tilde{\Delta}_0(x)]^2}. \quad (\text{A.27})$$

Using Mathematica, we find that Eq. A.27 has no poles on the real axis.

Appendix B

Evaluation of contour integral for solving $\tilde{I}_{E_k}^b$ near the broad Feshbach resonance

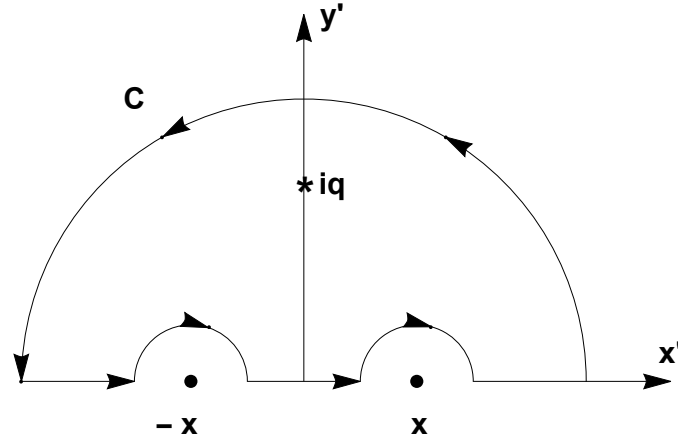


FIGURE B.1: Contour Integral for $I(q, x)$

From Chapter 3 Eq. 3.98, we have

$$\lim_{\epsilon \rightarrow 0} \tilde{I}_{E_k}^b = \frac{\theta(1 + \tilde{\Delta}_0)}{\pi} P \int_{-\infty}^{\infty} \frac{dx'}{x'^2 - x^2} \frac{x'^2}{\tilde{\Delta}_0^2 + (1 + \tilde{\Delta}_0)^2 x'^2}. \quad (\text{B.1})$$

We write

$$I(\tilde{\Delta}_0, x) \equiv P \int \frac{dx'}{(x'^2 - x^2)} \frac{x'^2}{\tilde{\Delta}_0^2 + (1 + \tilde{\Delta}_0)^2 x'^2}. \quad (\text{B.2})$$

Rewriting Eq. B.2,

$$\begin{aligned}
I(\tilde{\Delta}_0, x) &= \frac{1}{(1 + \tilde{\Delta}_0)^2} P \int \frac{dx'}{(x'^2 - x^2)} \frac{x'^2}{\frac{\tilde{\Delta}_0^2}{(1+\tilde{\Delta}_0)^2} + x'^2}. \\
&= \frac{1}{(1 + \tilde{\Delta}_0)^2} I_1(\tilde{\Delta}_0, x),
\end{aligned} \tag{B.3}$$

where

$$I_1(\tilde{\Delta}_0, x) = P \int \frac{dx'}{(x'^2 - x^2)} \frac{x'^2}{\frac{\tilde{\Delta}_0^2}{(1+\tilde{\Delta}_0)^2} + x'^2}. \tag{B.4}$$

We define

$$q^2 \equiv \frac{\tilde{\Delta}_0^2}{(1 + \tilde{\Delta}_0)^2}. \tag{B.5}$$

Substituting Eq. B.5 in Eq. B.4,

$$I_1(\tilde{\Delta}_0, x) = P \int \frac{dx'}{(x'^2 - x^2)} \frac{x'^2}{q^2 + x'^2} = I(q, x) \tag{B.6}$$

We use the contour integral method to solve $I(q, x)$. As illustrated in Fig. B.1, we choose our contour to enclose the upper half plane. Then, from Cauchy's residual theorem, we have

$$I(q, x) - \pi i \operatorname{Res}(-x) - \pi i \operatorname{Res}(x) = 2\pi i \operatorname{Res}(iq). \tag{B.7}$$

The residue for the pole on the real axis $x' = -x$ is

$$\begin{aligned}
\operatorname{Res}(-x) &= \left. \frac{x'^2 (x' + x)}{(x' + x)(x' - x)(x'^2 + q^2)} \right|_{x' \rightarrow -x} \\
&= -\frac{x^2}{2x(x^2 + q^2)}.
\end{aligned} \tag{B.8}$$

The residue for the pole on the real axis $x' = x$ is

$$\begin{aligned} Res(x) &= \frac{x'^2 (x' - x)}{(x' + x)(x' - x)(x'^2 + q^2)} \Big|_{x' \rightarrow x} \\ &= \frac{x^2}{2x(x^2 + q^2)}. \end{aligned} \quad (\text{B.9})$$

The residue for the enclosed pole on the imaginary axis $x' = iq$ is

$$\begin{aligned} I(q, x) &= 2\pi i Res(iq) \\ &= 2\pi i \frac{x'^2 (x' - iq)}{(x' + iq)(x' - iq)(x'^2 + x^2)} \Big|_{x' \rightarrow iq} \\ &= 2\pi i \frac{(iq)^2}{2iq[(iq)^2 + x^2]} = \frac{\pi q}{x^2 + q^2}. \end{aligned} \quad (\text{B.10})$$

Substituting Eq. B.8, Eq. B.9, and Eq. B.10 in Eq. B.7, we obtain

$$I(q, x) = \frac{\pi q}{x^2 + q^2} \quad (\text{B.11})$$

From Eq. B.5, we have

$$q = \frac{|\tilde{\Delta}_0|}{|1 + \tilde{\Delta}_0|} \quad (\text{B.12})$$

Substituting Eq. B.12 in Eq. B.11,

$$I(q, x) = \frac{\pi |\tilde{\Delta}_0|}{|1 + \tilde{\Delta}_0|} \frac{1}{x^2 + \frac{\tilde{\Delta}_0^2}{(1 + \tilde{\Delta}_0)^2}}. \quad (\text{B.13})$$

Using Eq. B.13 and Eq. B.6 in Eq. B.4, yields

$$I(\tilde{\Delta}_0, x) = \frac{\pi |\tilde{\Delta}_0|}{|1 + \tilde{\Delta}_0|} \frac{1}{\tilde{\Delta}_0^2 + x^2 (1 + \tilde{\Delta}_0)^2}. \quad (\text{B.14})$$

Finally, substituting Eq. B.14 in Eq. B.1, we obtain

$$\lim_{\epsilon \rightarrow 0} \tilde{I}_{E_k}^b = \frac{|\tilde{\Delta}_0|}{|1 + \tilde{\Delta}_0|} \frac{\theta(1 + \tilde{\Delta}_0)}{\tilde{\Delta}_0^2 + (1 + \tilde{\Delta}_0)^2 x^2}. \quad (\text{B.15})$$

Bibliography

- [1] C. Chin, R. Grimm, P. Julienne, and E. Tiesinga. Feshbach resonances in ultracold gases. *Rev. Mod. Phys.*, 82:1225, 2010.
- [2] P. O. Fedichev, Y. Kagan, G. V. Shlyapnikov, and T. M. Walraven. Influence of nearly resonant light on the scattering length in low-temperature atomic gases. *Phys. Rev. Lett.*, 77:2913, 1996.
- [3] J. Bohn and P. Julienne. Prospects for influencing scattering lengths with far-off-resonant light. *Phys. Rev. A*, 56:1486, 1997.
- [4] F. Fatemi, K. Jones, and P. Lett. Observation of optically induced Feshbach resonances in collisions of cold atoms. *Phys. Rev. Lett.*, 85:4462, 2000.
- [5] K. Enomoto, K. Kasa, M. Kitagawa, and Y. Takahashi. Optical Feshbach resonance using the intercombination transition. *Phys. Rev. Lett.*, 101:203201, 2008.
- [6] M. Theis, G. Thalhammer, K. Winkler, M. Hellwig, R. Grimm, and J. Hecker Denschlag. Tuning the scattering length with an optically induced Feshbach resonance. *Phys. Rev. Lett.*, 93:123001, 2004.
- [7] Gregor Thalhammer, Matthias Theis, Klaus Winkler, Rudolf Grimm, and Johannes Hecker Denschlag. Inducing an optical feshbach resonance via stimulated raman coupling. *Phys. Rev. A*, 71:033403, 2005.
- [8] R. Yamazaki, S. Taie, S. Sugawa, and Y. Takahashi. Submicron spatial modulation of an interatomic interaction in a Bose-Einstein condensate. *Phys. Rev. Lett.*, 105:050405, 2010.
- [9] D. M. Bauer, M. Lettner, C. Vo, G. Rempe, and S. Dürr. Control of a magnetic Feshbach resonance with laser light. *Nat. Phys.*, 5:339, 2009.
- [10] Zhengkun Fu, Pengjun Wang, Lianghai Huang, Zengming Meng, Hui Hu, and Jing Zhang. Optical control of a magnetic feshbach resonance in an ultracold fermi gas. *Phys. Rev. A*, 88:041601, 2013.
- [11] Logan W. Clark, Li-Chung Ha, Chen-Yu Xu, and Cheng Chin. Quantum dynamics with spatiotemporal control of interactions in a stable Bose-Einstein condensate. *Phys. Rev. Lett.*, 115:155301, 2015.

- [12] Dominik M. Bauer, Matthias Lettner, Christoph Vo, Gerhard Rempe, and Stephan Dürr. Combination of a magnetic feshbach resonance and an optical bound-to-bound transition. *Phys. Rev. A*, 79:062713, 2009.
- [13] H. A. Bethe. Theory of the effective range in nuclear scattering. *Phys. Rev.*, 76:38–50, Jul 1949.
- [14] John M. Blatt and J. David Jackson. On the interpretation of neutron-proton scattering data by the schwinger variational method. *Phys. Rev.*, 76:18–37, Jul 1949.
- [15] A. Jagannathan, N. Arunkumar, J. A. Joseph, and J. E. Thomas. Optical control of magnetic feshbach resonances by closed-channel electromagnetically induced transparency. *Phys. Rev. Lett.*, 116:075301, Feb 2016.
- [16] A. Bulgac and S. Yoon. Large amplitude dynamics fo the pairing correlations in a unitary Fermi gas. *Phys. Rev. Lett.*, 102:085302, 2009.
- [17] A. A. Schwenk and C. J. Pethick. Resonant Fermi gases with a large effective range. *Phys. Rev. Lett.*, 95:160401, 2005.
- [18] Yusuke Nishida and Dean Lee. Weakly bound molecules trapped with discrete scaling symmetries. *Phys. Rev. A*, 86:032706, 2012.
- [19] J. Levinsen, T. G. Tiecke, J. T. M. Walraven, and D. S. Petrov. Atom-dimer scattering and long-lived trimers in fermionic mixtures. *Phys. Rev. Lett.*, 103:153202, 2009.
- [20] S. Jochim, M. Bartenstein, A. Altmeyer, G. Hendl, S. Riedl, C. Chin, J. Hecker Denschlag, and R. Grimm. Bose-einstein condensation of molecules. *Science*, 302(5653):2101–2103, 2003.
- [21] M. W. Zwierlein, C. A. Stan, C. H. Schunck, S. M. F. Raupach, A. J. Kerman, and W. Ketterle. Condensation of pairs of fermionic atoms near a feshbach resonance. *Phys. Rev. Lett.*, 92:120403, Mar 2004.
- [22] S. L. Cornish, N. R. Claussen, J. L. Roberts, E. A. Cornell, and C. E. Wieman. Stable ^{85}Rb bose-einstein condensates with widely tunable interactions. *Phys. Rev. Lett.*, 85:1795–1798, Aug 2000.
- [23] Tino Weber, Jens Herbig, Michael Mark, Hanns-Christoph Nägerl, and Rudolf Grimm. Bose-einstein condensation of cesium. *Science*, 299(5604):232–235, 2003.
- [24] Andrew G. Truscott Randall G. Hulet Kevin E. Strecker, Guthrie B. Partridge. Formation and propagation of matter-wave soliton trains. *Nature*, pages 150–153, 2002.

- [25] L. Khaykovich, F. Schreck, G. Ferrari, T. Bourdel, J. Cubizolles, L. D. Carr, Y. Castin, and C. Salomon. Formation of a matter-wave bright soliton. *Science*, 296(5571):1290–1293, 2002.
- [26] S. T. Thompson, E. Hodby, and C. E. Wieman. Ultracold molecule production via a resonant oscillating magnetic field. *Phys. Rev. Lett.*, 95:190404, Nov 2005.
- [27] M. Gustavsson, E. Haller, M. J. Mark, J. G. Danzl, G. Rojas-Kopeinig, and H.-C. Nägerl. Control of interaction-induced dephasing of Bloch oscillations. *Phys. Rev. Lett.*, 100:080404, Feb 2008.
- [28] M. Fattori, C. D’Errico, G. Roati, M. Zaccanti, M. Jona-Lasinio, M. Modugno, M. Inguscio, and G. Modugno. Atom interferometry with a weakly interacting Bose-Einstein condensate. *Phys. Rev. Lett.*, 100:080405, Feb 2008.
- [29] P. Waldburger, J. G. Danzl, C. Chin, B. Engeser, A. D. Lange, K. Pilch, A. Jaakkola, H.-C. Nägerl, R. Grimm, T. Kraemer, M. Mark. Evidence for Efimov quantum states in an ultracold gas of caesium atoms. *Nature*, 440:315–318, Feb 2006.
- [30] Bo Huang, Leonid A. Sidorenkov, Rudolf Grimm, and Jeremy M. Hutson. Observation of the second triatomic resonance in Efimov’s scenario. *Phys. Rev. Lett.*, 112:190401, May 2014.
- [31] V. Efimov. Energy levels arising from resonant two-body forces in a three-body system. *Physical Letters B*, 33:563–564, Dec 1970.
- [32] J. Kinast, S. L. Hemmer, M. E. Gehm, A. Turlapov, and J. E. Thomas. Evidence for superfluidity in a resonantly interacting Fermi gas. *Phys. Rev. Lett.*, 92:150402, 2004.
- [33] J. Kinast, A. Turlapov, J. E. Thomas, Q. Chen, J. Stajic, and K. Levin. Heat capacity of a strongly interacting Fermi gas. *Science*, 307:1296, 2005. Published online 27 January 2005 (10.1126/science.1109220).
- [34] C. Cao, E. Elliott, J. Joseph, H. Wu, J. Petricka, T. Schäfer, and J. E. Thomas. Universal quantum viscosity in a unitary Fermi gas. *Science*, 331:58, 2011.
- [35] K. M. O’Hara, S. L. Hemmer, M. E. Gehm, S. R. Granade, and J. E. Thomas. Observation of a strongly interacting degenerate Fermi gas of atoms. *Science*, 298:2179, 2002.
- [36] M.W. Zwierlein, J.R. Abo-Shaeer, A. Schirotzek, C.H. Schunck, and W. Ketterle. Vortices and superfluidity in a strongly interacting Fermi gas. *Nature*, 435:1047, 2005.
- [37] C. H. Schunck, M. W. Zwierlein, A. Schirotzek, and W. Ketterle. Superfluid expansion of a rotating Fermi gas. *Phys. Rev. Lett.*, 98:050404, 2007.

- [38] M. W. Zwierlein, A. Schirotzek, C. H. Schunck, and W. Ketterle. Fermionic superfluidity with imbalanced spin populations. *Science*, 311:492, 2006.
- [39] J. Joseph, B. Clancy, L. Luo, J. Kinast, A. Turlapov, and J. E. Thomas. Measurement of sound velocity in a Fermi gas near a Feshbach resonance. *Phys. Rev. Lett.*, 983:170401, 2007.
- [40] M. Bartenstein, A. Altmeyer, S. Riedl, S. Jochim, C. Chin, J. Hecker Denschlag, and R. Grimm. Collective excitations of a degenerate Fermi gas at the BEC-BCS crossover. *Phys. Rev. Lett.*, 92:203201, 2004.
- [41] M. Bartenstein, A. Altmeyer, S. Riedl, S. Jochim, C. Chin, J. Hecker Denschlag, and R. Grimm. Crossover from a molecular bose-einstein condensate to a degenerate Fermi gas. *Phys. Rev. Lett.*, 92:120401, 2004.
- [42] S. Jochim, M. Bartenstein, A. Altmeyer, G. Hendl, S. Riedl, C. Chin, J. Hecker Denschlag, and R. Grimm. Bose-Einstein condensation of molecules. *Science*, 302:2101, 2003.
- [43] J. P. Gaebler J. T. Stewart and D. S. Jin. Using photoemission spectroscopy to probe a strongly interacting fermi gas. *Nature*, 454:744–747, Mar 2008.
- [44] C. A. Regal, C. Ticknor, J. L. Bohn, and D. S. Jin. Creation of ultracold molecules from a Fermi gas of atoms. *Nature*, 424:47, 2003.
- [45] Iacopo Carusotto, Serena Fagnocchi, Alessio Recati, Roberto Balbinot, and Alessandro Fabbri. Numerical observation of hawking radiation from acoustic black holes in atomic bose-einstein condensates. *New Journal of Physics*, 10(10):103001, 2008.
- [46] María I. Rodas-Verde, Humberto Michinel, and Víctor M. Pérez-García. Controllable soliton emission from a bose-einstein condensate. *Phys. Rev. Lett.*, 95:153903, Oct 2005.
- [47] K. Xu, T. Mukaiyama, J. R. Abo-Shaeer, J. K. Chin, D. E. Miller, and W. Ketterle. Formation of quantum-degenerate sodium molecules. *Phys. Rev. Lett.*, 91:210402, Nov 2003.
- [48] Ming-Guang Hu, Ruth S. Bloom, Deborah S. Jin, and Jonathan M. Goldwin. Avalanche-mechanism loss at an atom-molecule efimov resonance. *Phys. Rev. A*, 90:013619, Jul 2014.
- [49] H. Wu and J. E. Thomas. Optical control of the scattering length and effective range for magnetically tunable Feshbach resonances in ultracold gases. *Phys. Rev. A*, 86:063625, 2012.

- [50] John L. Bohn and P. S. Julienne. Prospects for influencing scattering lengths with far-off-resonant light. *Phys. Rev. A*, 56:1486–1491, Aug 1997.
- [51] P. O. Fedichev, Yu. Kagan, G. V. Shlyapnikov, and J. T. M. Walraven. Influence of nearly resonant light on the scattering length in low-temperature atomic gases. *Phys. Rev. Lett.*, 77:2913–2916, Sep 1996.
- [52] William C. Stwalley and He Wang. Photoassociation of ultracold atoms: A new spectroscopic technique. *Journal of Molecular Spectroscopy*, 195(2):194 – 228, 1999.
- [53] H. Wu and J. E. Thomas. Optical control of Feshbach resonances in Fermi gases using molecular dark states. *Phys. Rev. Lett.*, 108:010401, 2012.
- [54] Michael Fleischhauer, Atac Imamoglu, and Jonathan P. Marangos. Electromagnetically induced transparency: Optics in coherent media. *Rev. Mod. Phys.*, 77:633–673, Jul 2005.
- [55] Stephen E. Harris. Electromagnetically induced transparency. *Physics Today*, 50:36, 1997.
- [56] D. M. Bauer. *Optical Control of a Magnetic Feshbach Resonance*. PhD thesis, Max-Planck-Institut für Quantenoptik, Garching and Physik Department, Technische Universität München, August 2009.
- [57] M. Bartenstein, A. Altmeyer, S. Riedl, R. Geursen, S. Jochim, C. Chin, J. Hecker Denschlag, R. Grimm, A. Simoni, E. Tiesinga, C. J. Williams, and P. S. Julienne. Precise determination of ${}^6\text{Li}$ cold collision parameters by radio-frequency spectroscopy on weakly bound molecules. *Phys. Rev. Lett.*, 94:103201, Mar 2005.
- [58] G. Zürn, T. Lompe, A. N. Wenz, S. Jochim, P. S. Julienne, and J. M. Hutson. Precise characterization of ${}^6\text{Li}$ feshbach resonances using trap-sideband-resolved rf spectroscopy of weakly bound molecules. *Phys. Rev. Lett.*, 110:135301, 2013.
- [59] E. L. Hazlett, Y. Zhang, R. W. Stites, and K. M. O’Hara. Realization of a resonant Fermi gas with a large effective range. *Phys. Rev. Lett.*, 108:045304, 2012.
- [60] G. M. Falco and H. T. C. Stoof. Atom-molecule theory of broad Feshbach resonances. *Phys. Rev. A*, 71:063614, 2015.
- [61] E.R. Elliot. *Quantum Transport and Scale Invariance in Expanding Fermi Gases*. PhD thesis, Duke University, April 2014.
- [62] G.B. Partridge. *Pairing of Fermionic ${}^6\text{Li}$ Throughout the BEC-BCS Crossover*. PhD thesis, Rice University, February 2007.

- [63] G. B. Partridge, K. E. Eberhart, R. I. Kamar, M. W. Jack, and R. G. Hulet. Molecular probe of pairing in the BEC-BCS crossover. *Phys. Rev. Lett.*, 95:020404, 2005.
- [64] U. Schnemann, H. Engler, R. Grimm, M. Weidemüller, and M. Zielonkowski. Simple scheme for tunable frequency offset locking of two lasers. *Review of Scientific Instruments*, 70(1), 1999.
- [65] K. M. O'Hara, S. L. Hemmer, S. R. Granade, M. E. Gehm, J. E. Thomas, V. Venturi, E. Tiesinga, and C. J. Williams. Measurement of the zero crossing in a Feshbach resonance of fermionic ${}^6\text{Li}$. *Phys. Rev. A*, 66:041401(R), 2002.
- [66] J. E. Thomas, A. Turlapov, and J. Kinast. Virial theorem and universality in a unitary Fermi gas. *Phys. Rev. Lett.*, 95:120402, 2005.
- [67] R. Côté and A. Dalgarno. Mechanism for the production of ${}^6\text{Li}_2$ and ${}^7\text{Li}_2$ ultra-cold molecules. *J. Mol. Spectr.*, 195:236, 1999.
- [68] Mariusz Semczuk, Will Gunton, William Bowden, and Kirk W. Madison. Anomalous behavior of dark states in quantum gases of ${}^6\text{Li}$. *Phys. Rev. Lett.*, 113:055302, 2014.
- [69] G. Zürn, T. Lompe, A. N. Wenz, S. Jochim, P. S. Julienne, and J. M. Hutson. Precise characterization of ${}^6\text{Li}$ Feshbach resonances using trap-sideband-resolved rf spectroscopy of weakly bound molecules. *Phys. Rev. Lett.*, 110:135301, 2013.
- [70] M. Bartenstein, A. Altmeyer, S. Riedl, R. Geursen, S. Jochim, C. Chin, J. Hecker Denschlag, R. Grimm, A. Simoni, E. Tiesinga, C. J. Williams, and P. S. Julienne. Precise determination of ${}^6\text{Li}$ cold collision parameters by radio-frequency spectroscopy on weakly bound molecules. *Phys. Rev. Lett.*, 94:103201, 2005.

Biography

Arunkumar Jagannathan was born July 2, 1984, in Madras, India. He earned his B.E degree in electronics and communication engineering from Anna University, India. He earned his M.S. in Physics from University of Massachusetts Lowell. His master's research focussed on using terahertz optical techniques to study scattering from rough surfaces. He joined the group of Dr. John Thomas at Duke University in 2010, where he was involved in performing experiments for optically controlling interactions in strongly interacting Fermi gases.